Tailored perovskite-type oxynitride semiconductors and oxides with advanced physical properties

Genehmigte kumulative Dissertation
Vorgelegt von M. Sc. Cora Maren Bubeck aus Göppingen

Zur Erlangung des akademischen Titels *„Doctor rerum naturalium“* (Dr. rer. nat.)

Darmstadt – D17

1. Gutachten: Prof. Dr. Anke Weidenkaff
2. Gutachten: Prof. Dr. Gisela Schütz

TECHNISCHE UNIVERSITÄT DARMSTADT

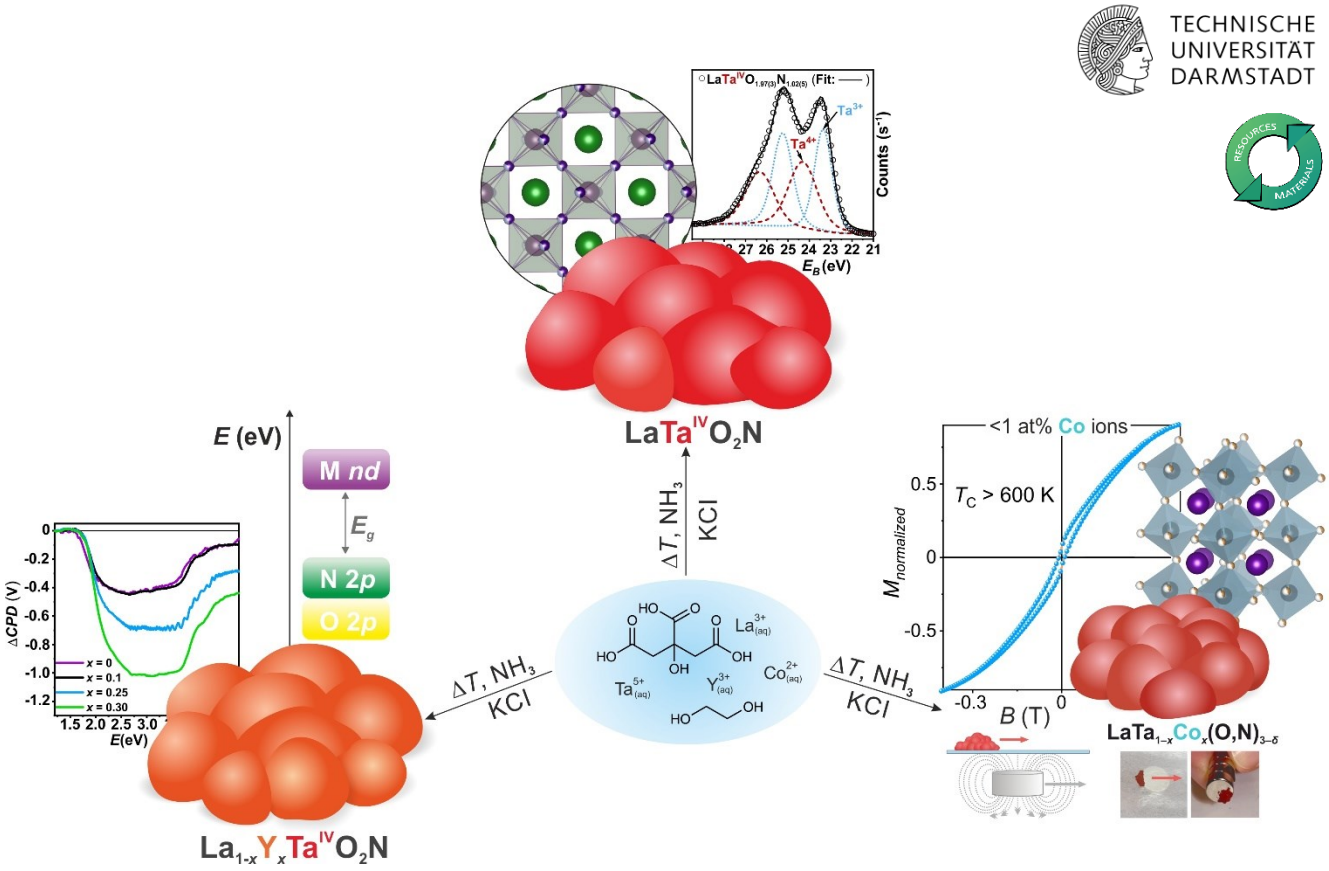

Tailored perovskite-type oxynitride semiconductors and oxides with advanced physical properties

Maßgeschneiderte, perowskitartige Oxynitrid-Halbleiter und Oxide mit zukunftsweisenden, physikalischen Eigenschaften

Dem Fachbereich Material- und Geowissenschaften der TU Darmstadt vorgelegte und genehmigte kumulative Dissertation von M. Sc. Cora Maren Bubeck aus Göppingen.

Zur Erlangung des akademischen Titels *„Doctor rerum naturalium“* (Dr. rer. nat.)

1. Gutachter: Prof. Dr. Anke Weidenkaff
2. Gutachter: Prof. Dr. Gisela Schütz

1. Prüfer: Prof. Dr. Christian Kübel
2. Prüfer: PD Dr. Emanuel Ionescu

Tag der Einreichung: 14.10.2022
Tag der mündlichen Prüfung: 10.02.2023

Darmstadt – D17

Dedicated to my family who supported me my whole life.

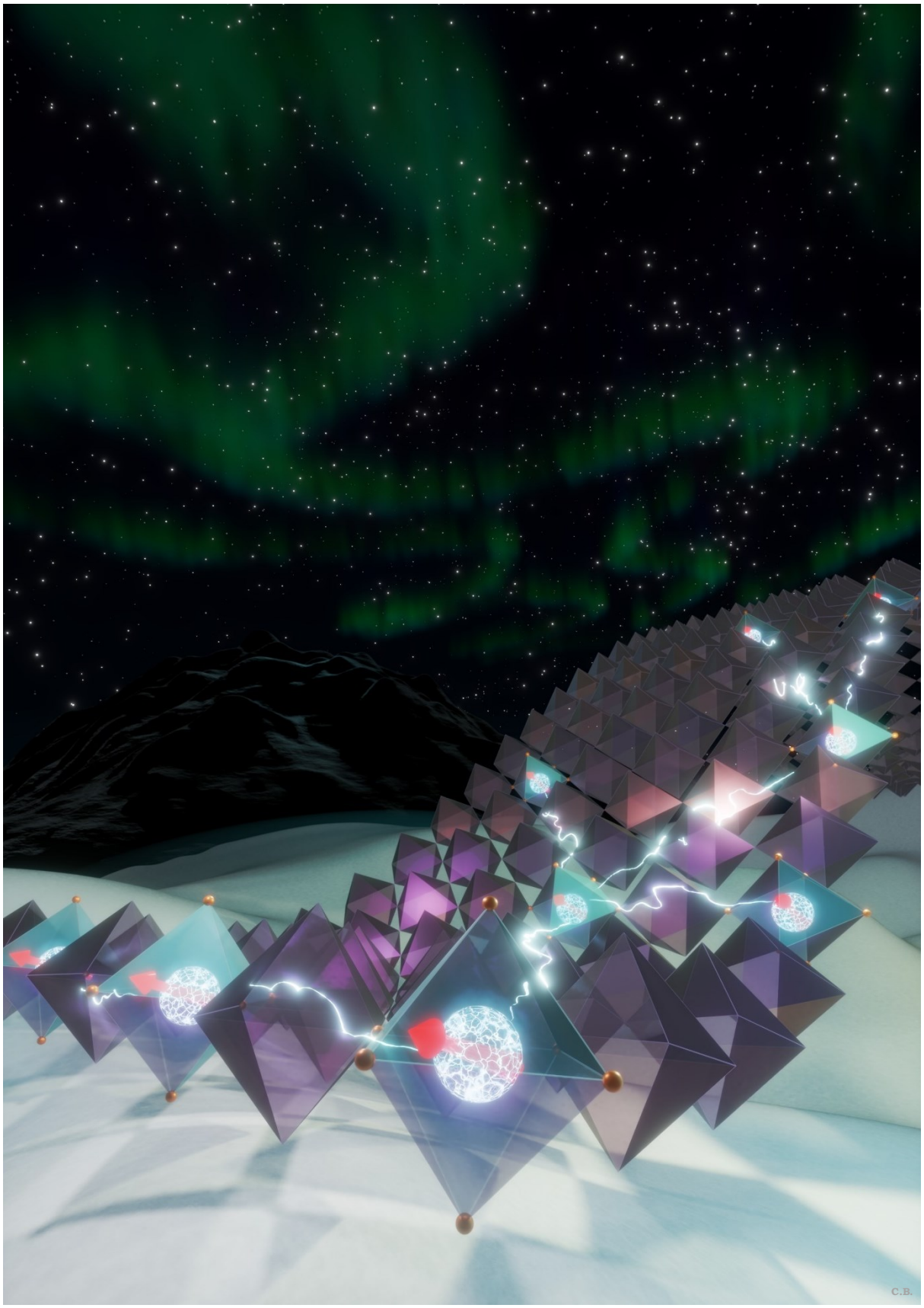

„Das wobei unsere Berechnungen versagen, nennen wir Zufall“
(Albert Einstein)

Abstract

Perovskite materials (ABX_3) reveal a surprisingly large variety of technologically interesting, highly advanced properties for application in solar cells, spin-optoelectronics or magnetic field sensors. In particular, perovskite-type oxynitrides $AB(O,N)_3$ are a well-known class of materials for visible light-driven applications and as inorganic pigments. In the last few decades, their range of applications *e.g.* in solar water splitting (SWS) have been expanded by the discovery of a great number of before unknown materials. However, the formation of such high-applicable materials was not totally clarified and with it the targeted tuning of their physical properties. To tailor the physical properties in perovskite-type oxynitrides substitutions on the *A*- and *B*-site are common, whereas the anionic site (*X*-site) is less explored.

In the first part of the cumulative dissertation, the formation processes of $LaTa^{IV}O_2N$ and $LaTa^{V}ON_2$ from the respective oxide precursors were elucidated. Additionally, the desired oxidation state of Ta and the nitrogen content in the compounds was adjusted. This opened up new perspectives for the understanding of the ammonolysis process in general, which is used for the formation of perovskite-type oxynitrides from oxide precursors. The here synthesized perovskite-type oxynitrides are promising for light-driven applications because of their measured optical bandgap and low optically active defect concentration. Additionally, the range of potentially suited candidates is expanded by degenerated semiconducting oxynitrides.

In the second part, in addition to the nitrogen content and the oxidation state of Ta in $La_{1-x}Y_xTa^{IV}O_2N$ (x = 0, 0.1, 0.25, 0.3, and 1.0) the cationic ratio between Y^{3+} and La^{3+} (*A*-site substitution) was modified. This resulted in controlled physical properties such as an adjusted optical and effective band gap size and a significant charge carrier transport rate. These are important features for SWS and the orthorhombic strain is added to the key descriptors for the band gap size in perovskite-type oxynitrides.

In the third part, instead of an *A*-site substitution a *B*-site substitution of Ta^{z+} for Co^{z+} in $LaTa(O,N)_3$ was applied. This led to the previously unknown perovskite-type oxynitrides $LaTa_{1-x}Co_x(O,N)_{3-\delta}$ (x = 0.01, 0.03, and 0.05). The material exhibited a ferromagnetic order with a Curie temperature exceeding 600 K. The synthesized material corresponds – to the best of one's knowledge – to the first diluted ferromagnetic semiconducting perovskite-type oxynitride. Hence, by substitution of a tiny amount of magnetic *B*-site cations (≤ 1 at%) in the pristine diamagnetic $LaTa(O,N)_3$ physical properties such as ferromagnetism can be tuned.

In the fourth part, through a targeted *B*-site substitution in $La_{0.6}Ca_{0.4}Co_{1-x}Fe_xO_{3-\delta}$ (x =0, 0.3, 0.5, 0.7, 1) physical properties such as CO_2 adsorption abilities, oxygen permeability, and electrical conductivity were tuned. These are – amongst other features – important for the application in carbon capture and utilization. The variation of the Fe/Co ratio led to an improvement of the measured oxygen permeation flux. Furthermore, conducted DFT calculations opened up the possibility to determine the effect of the Fe/Co ratio on the oxygen migration behavior and formation energy of the found oxygen vacancies.

The results shown in this thesis can be used to synthesize further targeted perovskite-type oxynitrides and oxides exhibiting advanced physical properties for future applications.

Zusammenfassung

Perowskitmaterialien (ABX_3) weisen eine überraschend große Vielfalt an technologisch interessanten, hochentwickelten Eigenschaften für die Anwendung in Solarzellen, in Spin-Optoelektronik oder als Magnetfeldsensoren auf. Insbesondere perowskitartige Oxynitride $AB(O,N)_3$ sind eine bekannte Materialklasse für Anwendungen unter Nutzung von sichtbarem Licht und als anorganische Pigmente. In den letzten Jahrzehnten wurde eine Vielzahl an perowskitartigen Materialien mit vielversprechenden, physikalischen Eigenschaften entdeckt und ihr Anwendungsspektrum z.B. in der solaren Wasserspaltung (SWS) erweitert. Allerdings war die Bildung solcher vielseitig, einsetzbaren Materialien und damit die gezielte Modifizierung ihrer physikalischen Eigenschaften nicht vollständig geklärt. Um die physikalischen Eigenschaften in perowskitartigen Oxynitriden anzupassen, sind Substitutionen der *A*- und *B*-Seite der Materialien üblich. Im Gegensatz dazu ist die Substitution der anionischen Seite (*X*-Seite) deutlich weniger gut untersucht.

Im ersten Teil der kumulativen Dissertation wurden die Bildungsprozesse von $LaTa^{IV}O_2N$ und von $LaTa^{V}ON_2$ aus den jeweiligen Oxidpräkursoren aufgeklärt. Zusätzlich wurden der angestrebte Oxidationszustand von Ta und der Stickstoffgehalt in den Verbindungen angepasst. Dies eröffnete neue Perspektiven zum Verständnis des Ammonolyseprozesses im Allgemeinen, der zur Bildung von perowskitartigen Oxynitriden aus Oxidpräkursoren verwendet wird. Zusätzlich sind die hier synthetisierten perowskitartigen Oxynitride vielversprechend für Anwendungen im sichtbaren Licht durch ihre gemessene, optische Bandlücke und geringe, optisch aktive Defektkonzentration. Zusätzlich wurde die Liste der potentiell geeigneten Kandidaten um entartete, halbleitende Oxynitride erweitert.

Im zweiten Teil wurde zusätzlich zum Stickstoffgehalt und den Oxidationsstufen von Ta in $La_{1-x}Y_xTa^{IV}O_2N$ (x = 0, 0,1, 0,25, 0,3 und 1,0) das kationische Verhältnis zwischen Y^{3+} und La^{3+} (*A*-Seitensubstitution) angepasst. Dies ermöglichte kontrollierte, physikalische Eigenschaften wie der angepassten optischen und effektiven Bandlückengröße und einer signifikanten Ladungsträgertransportrate, welche wichtige Eigenschaften für die SWS sind. Hierbei wurde die orthorhombische Verzerrung als wichtige Stellschraube zum Einstellen der Bandlücke identifiziert und implementiert.

Im dritten Teil wurde anstelle einer *A*-Seitensubstitution eine *B*-Seitensubstitution von Ta^{z+} mit Co^{z+} in $LaTa(O,N)_3$ vorgenommen. Dies führte zu dem zuvor unbekannten perowskitartigen Oxynitrid $LaTa_{1-x}Co_x(O,N)_{3-\delta}$ (x = 0,01, 0,03 und 0,05). Das Material weist eine ferromagnetische Ordnung mit einer Curie-Temperatur auf, die 600 K übersteigt. Das synthetisierte Material entspricht - nach bestem Wissen und Gewissen - dem ersten verdünnten, ferromagnetischen, halbleitenden, perowskitartigen Oxynitrid. Durch Substitution einer winzigen Menge von magnetischen *B*-Seitenkationen (≤ 1 at%) im reinen, diamagnetischen $LaTa(O,N)_3$ können daher physikalische Eigenschaften wie der Ferromagnetismus eingestellt werden.

Im vierten Teil wurden durch eine zielgerichtete *B*-Seitensubstitution in $La_{0.6}Ca_{0.4}Co_{1-x}Fe_xO_{3-\delta}$ (x =0, 0,3, 0,5, 0,7, 1) die physikalischen Eigenschaften wie die CO_2 Adsorptionseigenschaften, Sauerstoff-Permeabilität und elektrische Leitfähigkeit modifiziert. Diese Eigenschaften unter vielen anderen sind wichtig für die Anwendung bei der CO_2-Abscheidung und -nutzung. Die Variation des Fe/Co-Verhältnisses führte zu einer Verbesserung der gemessenen Sauerstoff-Permeation. Des Weiteren eröffneten durchgeführte DFT-Berechnungen die Möglichkeit den Effekt des Fe/Co-Verhältnisses auf das Migrationsverhalten des Sauerstoffs und die Bildungsenergie der entdeckten Sauerstoffleerstellen zu bestimmen.

Die in dieser Arbeit gezeigten Ergebnisse können genutzt werden, um weitere perowskitartige Oxynitride und Oxide gezielt zu synthetisieren, die zukunftsweisende, physikalische Eigenschaften für zukünftige Anwendungen aufweisen.

Contents

1. List of publications

Publications related to the cumulative thesis:

1. C. Bubeck, M. Widenmeyer, G. Richter, M. Coduri, E. Goering, S. Yoon and A. Weidenkaff, Tailoring of an unusual oxidation state in a lanthanum tantalum(IV) oxynitride via precursor microstructure design, *Commun. Chem.*, 2019, **2**, 134. DOI: 10.1038/s42004-019-0237-x.

2. C. Bubeck, M. Widenmeyer, A. T. De Denko, G. Richter, M. Coduri, E. Salas Colera, E. Goering, H. Zhang, S. Yoon, F. E. Osterloh and A. Weidenkaff, Bandgap-Adjustment and Enhanced Surface Photovoltage in Y-Substituted $LaTa^{IV}O_2N$, *J. Mater. Chem. A*, 2020, **8**, 11837–11848, DOI: 10.1039/D0TA02136A.

3. C. Bubeck, E. Goering, R. Lawitzki, K. Küster, W. Sigle, M. Widenmeyer, U. Starke, C. Ritter, G. J. Cuello, P. Nagel, M. Merz, S. Schuppler, G. Schütz and A. Weidenkaff, Observation of a possible diluted ferromagnetism above room temperature in cobalt-substituted $LaTa(O,N)_{3-\delta}$, 2022, arXiv:2003.14259.

4. G. Chen, W. Liu, M. Widenmeyer, P. Ying, M. Dou, W. Xie, C. Bubeck, L. Wang, M. Fyta, A. Feldhoff and A. Weidenkaff, High flux and CO_2-resistance of $La_{0.6}Ca_{0.4}Co_{1-x}Fe_xO_{3-\delta}$ oxygen-transporting membranes, *J. Memb. Sci.*, 2019, **590**, 117082, DOI: 10.1016/j.memsci.2019.05.007.

Further non-related publications:

1. M. T. Birch, L. Powalla, S. Wintz, O. Hovorka, K. Litzius, J. C. Loudon, L. A. Turnbull, V. Nehruji, K. Son, C. Bubeck, T. G. Rauch, M. Weigand, E. Goering, M. Burghard and G. Schütz, History-dependent domain and skyrmion formation in 2D van der Waals magnet Fe_3GeTe_2 *Nat. Commun.*, 2022, 13, DOI: 10.1038/s41467-022-30740-7.

Conferences:

1. C. Bubeck, J. Häcker, M. Widenmeyer, W. Xie and A. Weidenkaff, *Bandgap Tuning of Novel Modified Perovskite-type Oxynitrides and Oxyfluoronitrides for Solar Water Splitting Application*. in *EMRS Spring Meeting* (2016). – *Oral Presentation*

2. M. Widenmeyer, X. Xiao, J. Häcker, C. Bubeck, W. Xie and A. Weidenkaff, *Modified Novel Perovskite-type Oxides and Oxynitride Fluorides for Thermolelectric and Solar Water Splitting Applications*. in *Jahrestagung der DGK* (2016). – *Poster Presentation*

3. C. Bubeck, M. Widenmeyer and A. Weidenkaff, *Photoelectrocatalytic Anion Substituted Perovskite Phases (PAP)*. in *DFG SPP 1613 Project Meeting* (2016). – *Poster Presentation*

4. C. Bubeck, M. Widenmeyer and A. Weidenkaff, *Photoelectrocatalytic Anion Substituted Perovskite Phases (PAP)*. in *DFG SPP 1613 Project Meeting* (2017). – *Poster Presentation*

5. C. Bubeck, M. Widenmeyer, G. Richter, M. Coduri, E. Salas Colera, S. Yoon, F. Osterloh and A. Weidenkaff, *Perovskite-type Oxynitrides $LaTaO_2N$ and $LaTaON_2$ – Synthetic Strategies*. in *NanoGe Proceedings - Fallmeeting* (2018). doi:10.29363/nanoge.fallmeeting.2018.041 – *Oral Presentation/Conference Abstract*

6. C. Bubeck, M. Widenmeyer, A. T. De Denko, G. Richter, M. Coduri, E. S. Colera, E. Goering, S. Yoon, F. E. Osterloh and A. Weidenkaff*, Producing unusual Ta^{4+} in perovskite-type oxynitrides*. in *EMRS Spring Meeting* (2019). – *Oral Presentation*

2. The publication of the individual chapters in scientific journals

Chapters 6, 7, and 9 of the cumulative thesis correspond to publications, which have been published in scientific journals. The author contributions for each paper are written in chapter 2.1 and are listed in the respective chapters in the order according to the publisher's guidelines (see www.nature.com and www.rsc.org, section “author responsibilities”).

Chapter 6: Tailoring of an unusual oxidation state in a lanthanum tantalum(IV) oxynitride *via* precursor microstructure design

Chapter 7: Bandgap-Adjustment and Enhanced Surface Photovoltage in Y-Substituted $LaTa^{IV}O_2N$

Chapter 8: Observation of a possible diluted ferromagnetism above room temperature in cobalt-substituted $LaTa(O,N)_{3-\delta}$

Chapter 9: High flux and CO_2-resistance of $La_{0.6}Ca_{0.4}Co_{1-x}Fe_xO_{3-\delta}$ oxygen-transporting membranes

2.1. Author Contributions

2.1.1. Tailoring of an unusual oxidation state in a lanthanum tantalum(IV) oxynitride *via* precursor microstructure design

C. B. developed the parameters for the synthesis of the oxide precursors and the perovskite-type oxynitrides and the *in situ* and *ex situ* ammonolysis study. C.B. performed and pre-evaluated the PXRD, SEM, DRS and TGA measurements. C.B., M.W. and A.W. collectively elaborated the analysis of the synthesis, *in situ* and *ex situ* ammonolysis data. G.R. and C.B. analysed the XPS data. M.W. and M.C. collected the HR-PXRD data at the ESRF. C.B., M.W., S.Y. and M.C. analysed the HR-PXRD data, which had been refined by C.B. and M.W. C.B. and E.G. measured and analysed together the SQUID data. C.B. wrote the paper with input from M.W., G.R., M.C. and S.Y. and A.W. provided final contributions to the conclusions.

2.1.2. Bandgap-Adjustment and Enhanced Surface Photovoltage in Y-Substituted $LaTa^{IV}O_2N$

C. B. developed and synthesized the oxide precursors and perovskite-type oxynitrides, and performed and analyzed *in situ* ammonolysis, PXRD, DRS and TGA. M. W. and A. W. contributed to the discussion of the analysis. A. D. and F. O. performed and interpreted the SPS results with input from C. B. and M. W. M. C. and M. W. measured together HR-PXRD, whereas the data were refined by C. B. C. B., M. W., S. Y., and M. C. further interpreted the resulting Rietveld refinements from HR-PXRD and ND. G. R. and C. B. interpreted together the XPS data. E. S. C. and C. B. elaborated collectively the XANES data measured by E. S. C. E. G. and C. B. measured and interpreted the SQUID data. H. Z. performed and analyzed the DFT calculations with input from C. B. and M. W. C. B. wrote the paper. A. W. provided the research topic and contributions to the conclusions.

2.1.3. Observation of a possible diluted ferromagnetism above room temperature in cobalt-substituted $LaTa(O,N)_{3-\delta}$

C.B. developed and synthesized the LTCO and LTCON powders. C.B. performed and analyzed SEM/EDX, DRS, TGA, PXRD, HT-SQUID and *in situ* ammonolysis. C.B found the magnetism in the perovskite-type oxynitrides, whereas E.G. provided the original interpretation of the HT-ferromagnetism of the compounds. E.G. performed and analyzed the magnetic measurements with data contribution of SQUID measurements from C.B. E.G., C.B., P.N. and S.S performed the XMCD/XAS measurements. The XMCD/XAS data was analyzed by E.G and C.B. G.S., P.N., M.M. and S.S. contributed to the discussion of the XMCD/XAS data. R.L. and C.B. measured and analyzed together TEM/EDX. K.K. performed the XPS measurements and analyzed the data together with C.B. W.S. measured and analyzed together with C.B. and E.G. HR-TEM and additional recorded EDX maps. U.S. provided discussion to the XPS part. M.W. and A.W. contributed to the discussion of the *in situ* ammonolysis. C.B., G.J.C. and M.W. measured together neutron diffraction. C.B. refined and analyzed the ND data. C.R., G.J.C. and M.W. contributed to the discussion of the ND data. C.B. and E.G. wrote together the paper and A.W. provided final contributions to the conclusions.

2.1.4. High flux and CO_2-resistance of $La_{0.6}Ca_{0.4}Co_{1-x}Fe_xO_{3-\delta}$ oxygen-transporting membranes

Guoxing Chen: Synthesis, Oxygen Permeation: formal analysis, validation, methodology, conceptualization, writing (original draft preparation). Wenmei Liu, Maofeng Dou and Maria Fyta: DFT – Formal analysis, validation, methodology, writing (review and editing). Marc Widenmeyer: TGA & XRD: formal analysis, validation, methodology, writing (review and editing). Pingjun Ying and Wenjie Xie: Total conductivity: formal analysis, validation, methodology, writing (review and editing). Cora Bubeck: SEM/EDX: formal analysis, writing (review and editing). Ling Wang: Synthesis: methodology. Armin Feldhoff: writing (review and editing). Anke Weidenkaff: funding acquisition, writing (review and editing) and supervision.

3. Abbreviations and symbols

%	Percent
Δ	Delta (Difference)
∑I	Contribution of ionic character
∢	Angle (°)
□	Vacancy (nitrogen or oxygen)
°C	Degree Celsius
μ_0	Magnetic permeability
μ_B	Bohr magneton
μ_{eff}	Effective magnetic moment
μ_i	Electrochemical potential
µm	Micrometer
†	ESI availabe
A	A-site cation
Å	Ångström
a, b, c (Å)	Unit cell parameters
AFM	Antiferromagnetism
Al	Aluminium
Ar	Argon
As	Arsenic
AT	After temperature
at%	Atomic percent
Atm	Atmosphere
B	B-site cation or magnetic field (T)
Ba	Barium
BET	Brunauer-Emmet-Teller
B_{iso}	Isotropic atomic displacement factor
BT	Before temperature
C	Carbon, Curie constant
Ca	Calcium
CB	Conduction band
CBM	Conduction band minimum
CCU	Carbon capture and utilization
CF	Cryo furnace
cf.	confer
C_i	Concentration of the substance i
Cl	Chlorine
cm	Centimeter
CMR	Colossal magnetoresistance
CN	Coordination number
Co	Cobalt
CPD	Contact potential difference
Cu	Copper
d	Distance
DFT	Density functional theory
DMS	Diluted magnetic semiconductor
DOI	Digital object identifier
DOS	Density of states
DRS	Diffuse reflectance spectroscopy
e.g.	for example
E_B	Binding energy
EDX	Energy dispersive X-ray spectroscopy
E_f	Formation energy
E_g	Electronic bandgap
E_G	Optical bandgap
emu	Electromagnetic units
ESI	Electronic supplementary information
ESRF	European Synchrotron Radiation Facility
E_{tot}	Total energy
eV	Electronvolt
F, F	Faraday's constant, Flourine
Fe	Ferrum
Fig.	Figure
FIZ	Leibniz-Institut für Informationsinfrastruktur
FM	Ferromagnetism
FRM II	Research Neutron Source Heinz Maier-Leibnitz
FTO	Fluorine-doped tin oxide
FU	Formula unit
FWHM	Full width at half maximum
g	Gramm
Ga	Gallium
h	Hour
H	Hydrogen
h·	Electron hole
HAADF	High-angle annular dark-field
H_c	Coercive field
HGE	Hot gas extraction
HR	High resolution
HS	High spin
HT	High temperature
I	Intensity of
I_{AB}	Ionic amount of bond
ICP-OES	Inductively coupled plasma optical emission spectroscopy
ICSD	Inorganic Crystal Structure Database
ILL	Institut Laue-Langevin
IS	Intermediate spin
ITO	Indium-doped tin oxide
J_i	Permeability flux of substance i
K	Potassium, Kelvin
KARA	Karlsruhe Röntgenanlage
k_B	Boltzmann constant
kJ	Kilojoule
KNMFi	Karlsruhe Nano Micro Facility
kV	Kilovolt
La	Lanthanum
LCCF	$La_{0.6}Ca_{0.4}Co_{1-x}Fe_xO_{3-\delta}$
LN→LS	Left north *to* left south
LS	Low spin
LT	Low temperature

LTCO	Lanthanum tantalum cobalt oxide
LTCON	Lanthanum tantalum cobalt oxynitride
LTNON	Lanthanum tantalum nickel oxynitride
m	Meter
M	Transition metal ion
$M(H)$	Magnetic field
m/z	Mass-to-charge
m_{calc}	Calculated mass
$m_{\mathrm{Co\ ion}}$	Magnetic moment per Co ion
mg	Milligramm
MIEC	Mixed ionic electronic conductor
min	Minute
mL	Milliliter
m_l, m_{orb}	Orbital moment
m-$LaTaO_4$	Microcrystalline lanthanum tantalum oxide
mm	Millimeter
Mn	Manganese
mol	*Mol*
M_s	Saturation magnetization
m_s, m_{spin}	Spin moment
M^{z+}	Charged transition metal ion
MΩ	Megaohm
n	Number of atoms per unit cell volume
N	Nitrogen
Nb	Niobium
ND	Neutron diffraction
Ne	Neon
NEB	Nudged elastic band method
n_H	Number of holes
NHE	Normal hydrogen electrode
Ni	Nickel
n-LTO	Nanocrystalline lanthanum tantalum oxide
nm	Nanometer
n-YTO	Nanocrystalline yttrium tantalum oxide
O	Oxygen
O'	Negative charged oxygen
Oe	Oersted
O_O^x	Lattice oxygen
p	Pressure
P	Phosphor
PM	Paramagnetism
PXRD	Powder X-ray diffraction
Q	Formal charge
q_p	Charge
r	Ionic radius
r_A	Effective ionic radius of the *A*-site cation
r_B	Effective ionic radius of the *B*-site cation
R_{Bragg}	Bragg residual factor
rds	Rate-determining step
ref.	Reference
Rh	Rhodium
r_N	Effective ionic radius of the nitrogen anion
RN→RS	Right north *to* right south
r_O	Effective ionic radius of the oxygen anion
R_p	Profile residual factor
RT	Room temperature
R_{wp}	Weighted-profile residual factor
s	Second
S	Siemens
SAED	Selected area electron diffraction
S_{BET}	Specific surface area
Sec.	Section
SEM	Scanning electron microscopy
Si	Silicon
SI	Supporting or supplementary information
sof	site occupancy factor
SPS	Surface photovoltage spectroscopy
sq	Square
SQUID	Superconducting quantum interference device
Sr	Strontium
SSR	Solid state reaction
SWS	Solar water splitting
syn.	Synthetic
t	Tolerance factor
T, T	Absolute temperature, Tesla
Ta	Tantalum
Tab.	*Table*
T_C	Curie temperature
TEM	Transmission electron microscopy
TGA	Thermogravimetric analysis
TGA-MS	Thermogravimetric analysis coupled with mass spectrometry
Ti	Titanium
TM	Transition metal
TR	Transmission
TS	Transition state
UV	Ultra violet
UV–VIS NIR	Ultra violet – visible near infrared
V	Vanadium
V (unit)	Volt
VB	Valence band
VBM	Valence band maximum
V_{cell}	Unit cell volume
$V_{O^{\cdot}}$	Positive charged oxygen vacancy
vol%	Volume percent
vs.	versus
w	Weight
wt%	Weight percent
x	Concentration of *A*- or *B*-site cation

x, y, z (Rietveld)	Atomic positions
XANES	X-ray absorption near edge structure
XAS	X-ray absorption spectroscopy
Xe	Xenon
XMCD	X-ray magnetic circular dichroism
XPS	X-ray photoelectron spectroscopy
Y	Yttrium
z	Defect charge number
ZFC	Zero field cooled
Zn	Zinc
β (°)	Beta (°), angle between unit cell parameters
γ (°)	Gamma (°), angle between unit cell parameters
δ	Delta (vacancy concentration)
ε	Epsilon (orthorhombic strain)
θ	Theta (°), Weiss constant
λ	Lambda (Wavelength)
ν	Local velocity of the inert defect marker
ρ	Density (cm/cm^3)
σ_i	Conductivity
τ_{off}	Photovoltage decay
τ_{on}	Photovoltage generation
χ	Electronegativity
χ(T)	Susceptibility
χ^2	Goodness of fit
χ_A	Electronegativity of ion A
χ_B	Electronegativity of ion B
χ_{dia}	Diamagnetism (emu/mol)
Ω	Ohm (resistivity)

4. Introduction

Perovskites (general composition: ABX_3, where *A* and *B* represent two different cations and *X* an anion) are an emerging class of materials that gained great interest the last few decades. Their extraordinary flexibility in cationic (*A*- and *B*-site) and anionic (*X*-site) substitution leads to a huge number of different perovskites making them suitable for many applications.[1] As examples, the application of hybrid halide perovskites in solar cells[2], perovskite oxides as ferroelectrics[3], and magnetic field sensors[4] are named. Recently, the possible application for organic-inorganic hybrid perovskites in spin-optoelectronic devices[5] was added. Additionally, perovskites seem to be a natural choice also for hydrogen production by solar water splitting as the well-known structure in close conjunction to the huge variety of possible materials opens up a large field of highly interesting applications for perovskite-type materials. However, if a semiconductor for (solar) light-driven applications where a bandgap between 1 eV and 3 eV is needed, perovskite-type oxides are largely lacking.[6] This is owed to the limited bandgap adjustment of perovskite-type oxides by isovalent or heterovalent *A*- and/or *B*-site substitution where the *X*-site is not taken into account. If the anionic or *X*-site substitution is taken into account an additional parameter to adjust further the bandgap size and its' positions can be obtained. This can lead to perovskite-type oxynitrides where the oxygen is partially substituted for nitrogen. By partial *X*-site substitution not only the electronic bandgap size and band positions can be tuned, also the crystallite size, structural stability, and the separation and migration of charge carriers and, hence, the physical properties.[7–9] In Figure 1 a scheme of the changed band positions originating from nitrogen substitution in a typical perovskite-type oxynitride is drawn. Further explanation is given in chapter 5.2.2.

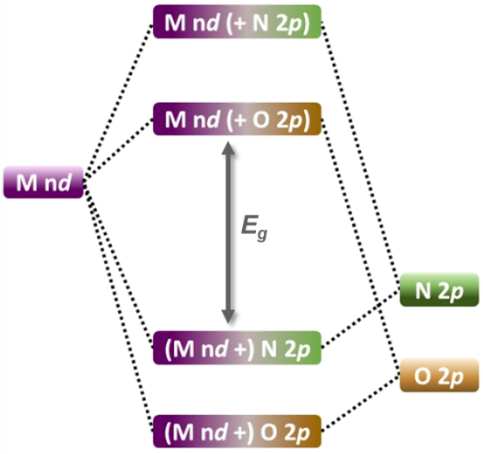

Figure 1. Scheme of band structure in a perovskite-type oxynitride. As example, the band structure of a typical perovskite-type oxynitride containing a d^0-type transition metal is shown. The scheme is drawn after ref. [10].

Because of the much higher variety in bandgap size and band positions, the class of perovskite-type oxynitrides ($AB(O,N)_3$), where oxygen is existing besides nitrogen on the *X*-site, are of special scientific interest. Their physical properties are very promising for future applications in the field of renewable energies (*e.g.* hydrogen production) or as Cd-free yellow-red pigments (*e.g.* $Ca_{1-x}La_xTaO_{2-x}N_{1+x}$).[8,11–14] Furthermore, perovskite-type oxynitrides can be used as memristors (*e.g.* $SrTiO_{3-x}N_y$[15]), as thermoelectrics (*e.g.* $EuTi(O,N)_3$[16]), as dielectrics (*e.g.* $SrTaO_2N$[17]), and for colossal magnetoresistance (*e.g.* $EuMO_{3-x}N_x$[18] with *M* = Nb, Ta, W). In the field of renewable energies, their suitability as photoanodes for solar water splitting (SWS) stands out in particular. [8,19–24] By optimizing the parameters for synthesis, adding co-catalysts or by substituting on the *A*-, *B*-, and *X*-site and

fabricating nanocomposites, effective separation and migration of photogenerated carriers can be achieved.[25] However, for this kind of application many criteria are needed to be taken care of. For example, the suitable bandgap size and energetic band positions are crucial to evolve hydrogen or oxygen during the water splitting process with highest efficiencies.[26] How the bandgap size and band positions influence the suitability for the water splitting process is described further in chapter 5.2.2. In addition to the fitting bandgap sizes and energetic band positions, it was predicted that perovskite-type oxynitrides with a certain structural instability have the best criteria to split water.[8,9,26] Besides $LaTaON_2$[27], one of the most promising candidates is $YTaON_2$[26]. According to Li *et al*.[28], this compound is located at the border of the structural stability field for perovskites. This prediction opened up a new research field in developing before unknown, structurally labile perovskite-type oxynitrides in order to enhance SWS efficiencies.

In chapter 6 it is shown, that by *X*-site substitution the optically active defect concentration and oxidation state of the *B*-site cation in $LaTa(O,N)_3$ can be tuned. The original motivation of this work was the prediction by Li *et al.*[28]. It stated the possible existence of not yet synthesized perovskite-type oxynitrides such as $LaTa^{IV}O_2N$ or $YTa(O,N)_3$.[28] Chapter 6 describes the microstructure-controlled synthesis of the theoretically predicted[28] perovskite-type oxynitride $LaTa^{IV}O_2N$. By tailoring the oxide precursors' microstructure and an adjusted ammonia concentration during ammonolysis, the nitrogen content (*X*-site substitution) and the oxidation state of Ta (from 5+ to 4+) have been controlled. Hence, the formation of $LaTa^{IV}O_2N$ and $LaTa^{V}ON_2$ (topotactic case) from different oxide precursors could be elucidated. In the past, the formation of perovskite-type oxynitrides by ammonolyzing crystalline oxide precursors (topotactic case) was mostly clarified.[29] In contrary, the results shown in this chapter allowed a general understanding in the formation of perovskite-type oxynitrides from nanocrystalline/amorphous oxides in particular and provided a deeper insight in understanding the topotactic case. In addition, the results allow new perspectives in synthesizing further perovskite-type oxynitrides with promising physical properties such as a low optically active defect concentration and suitable bandgap size for light-driven applications.

Until now, often perovskite-type oxynitrides containing transition metal ions on the *B*-site exhibiting a d^0 or a d^{10} electronic configuration are identified as suitable candidates for solar water splitting. [12,30–36] By using *e.g*. a d^1 electronic configuration for the transition metal *B*-site cation in perovskite-type oxynitrides, donor levels close to the conduction band could be formed. For example, reduced Ta species in $Ta^{V}ON$[37,38] or in $LaTa^{V}ON_2$[33] were leading to a fast charge carrier recombination rate and with it to a poor SWS efficiency. However, until now the question remains how *e.g*. a Ta^{4+}-only material is behaving physically and chemically which exhibits just reduced Ta species according to the classical assumption[33]. In chapter 7 amongst other materials, the in chapter 6 described Ta^{4+}-only material $LaTa^{IV}O_2N$ is further investigated with respect to its crystal structure and induced photophysical properties.

Additionally, chapter 7 is a follow-up work of chapter 6 and contains the investigation of the physical properties of the before unknown perovskite-type $La_{1-x}Y_xTa^{IV}O_2N$ (x = 0.1, 0.25, and 0.3) and the respective synthesis. Because of the small ionic radius of Y^{3+}, $YTa(O,N)_3$ is a very instable perovskite-type oxynitride and, therefore, challenging to synthesize – especially in the bulk. In this chapter, the chosen synthesis pathway in order to understand the formability of $YTa(O,N)_3$ was to begin with a well-known perovskite-type oxynitride *e.g*. $LaTa^{V}ON_2$, and to start a partial *A*-site substitution by Y^{3+} for La^{3+}. This applied gradual substitution allowed indeed a deeper understanding in the formation of $YTa(O,N)_3$ and of the perovskite-type oxynitrides $La_{1-x}Y_xTa^{IV}O_2N$ with x = 0.1, 0.25, and 0.3. The variation of the Y content allows to manipulate the orthorhombic strain being an important parameter to adjust the band gap size. In literature the influence of (orthorhombic) strain is only seldomly considered mainly using theoretical methods[39], while experimental verification is typically lacking. For the possible suitability for SWS several characterization methods and DFT calculations were applied. It could be shown that partial Y-substitution enlarges the charge carrier transport rate, which

is an important factor for SWS. Moreover, reduced *B*-site cations such as Ta^{4+} have a significantly weaker impact on the photovoltage and the charge carrier recombination rate than classically assumed. Hence, by applying a targeted *X*- and *A*-site substitution, physical properties for light-driven applications of $La_{1-x}Y_xTa^{IV}O_2N$ (x = 0, 0.1, 0.25, and 0.3) were adjusted.

The large variety of perovskite-type oxynitrides that can be synthesized shows the potential for expanding the possible applications of such materials beyond already known ones[8,12,19–24,40,41]. Until now, in the class of perovskite materials, only perovskite oxides are known as magnetic field sensors or as magneto-optical data storage devices.[4,42] This leads to the question if perovskite-type oxynitrides can exhibit also the desired physical properties for this kind of applications. Therefore, the magnetic properties and with it the Curie temperature (T_C) have to be modified. A fitting of the required physical properties can be achieved by adjusting the composition with *A*-, *B*-, and *X*-site substitution in the perovskite-type materials.[8,29] In the past, one special theory to adjust the T_C was reported: Tomasz Dietl and co-workers predicted the possibility to obtain room temperature (RT) ferromagnetism (FM) in diluted magnetic semiconductors (DMS) *via* introduction of a defined concentration of magnetic ions and/or holes in a materials' matrix.[43] This theory opened up a strong research field in the magnetism community to find a material exhibiting such a desired RT-FM, because, RT-FM DMS systems promise a great advance in spintronics' development.[44] However, until now – to the best of one's knowledge – no sizable room temperature ferromagnetism in diluted magnetic semiconductors could be realized.[45] After revealing for defect-ridden ZnO a ferromagnetism deriving from off-stoichiometric grain boundaries[46–48] the whole scientific field was fallen into oblivion.

Since, *A*- and *X*-site substitutions in the materials' matrix of $LaTa(O,N)_3$ can adjust the physical properties for light-driven applications (chapters 6–7), *B*-site substitutions with magnetic ions such as Co^{z+} may adjust its magnetic properties. In chapter 8 the perovskite-type oxynitrides $LaTa_{1-x}Co_x(O,N)_{3-\delta}$ (x = 0.01, 0.03, 0.05) were synthesized by applying Co-substitution in $LaTa(O,N)_3$. This was leading to a significant ferromagnetic ordering in the materials with a T_C exceeding 600 K ($T_C \geq$ RT) and, hence, to a detailed structural and magnetic investigation. The synthesized materials correspond – to the best of one's knowledge – to the first semiconducting diluted ferromagnetic perovskite-type oxynitrides and may resurrect the scientific field for DMS which had fallen out of favor. This before unknown physical property of a perovskite-type oxynitride promises to expand the number of possible applications for this materials class in the field of spintronics.

As mentioned above, hydrogen production and storage is very important in the field of renewable energies.[49–51] Because, hydrogen is seen as a key player in order to reduce carbon dioxide emission and climate change.[50] It can be used in manifold ways *e.g*. as a renewable energy source substituting electricity, as fuel, and as production chemical for organic chemistry.[50,52,53] Additionally, hydrogen can help to avoid heavily CO_2-containing air which is produced by the steel industry.[54] Currently, the major disadvantage of hydrogen-based technologies is the preferred production of so called "grey hydrogen" – according to the German National Hydrogen Strategy – from steam reforming which is accompanied by significant CO_2 emissions.[55] To overcome this set of problems and to replace methane steam reforming, several electrolysis-based technological approaches are in discussion.[50,51,54,56] The alkaline water electrolysis is the most mature technology.[57,58] However, its' application and upscaling is currently limited, as the demand for the required relatively large quantities of precious metals (oxides) already exceeds the available resources resulting in high production costs.[57,58] Therefore, the proton exchange membrane-based electrolysis which is running under acidic conditions was moving in the focus of the scientific community.[59] It also enables higher operation pressures[59] and thus has the potential to reduce operating costs for subsequent hydrogen storage. However, the current issue by using a precious metal as a catalyst – here platinum group or precious metals – still remains.[59,60] Further approaches revealed lately the high-temperature solid-state electrolysis of steam – basically a reverse mode operation of a solid-state fuel cell – as the latest technology in the field of electrolysis.[61]

Here, the so-called mixed ionic electronic conducting (MIEC) perovskite-type oxides moved closer into the scientific focus.[62]

In order to reduce CO_2 in the atmosphere, oxygen-containing perovskites such as $La_{0.6}Ca_{0.4}Co_{0.8}Fe_{0.2}O_{3-\delta}$[63–65] or $SrFe_{0.8}Nb_{0.2}O_{3-\delta}$[66] were found to be suitable as MIEC oxygen transporting membranes exhibiting a high oxygen permeation and CO_2[64] tolerance for carbon capture and utilization (CCU)[65] – an additional application in the field of energy conversion reducing CO_2 in air. To achieve the desired physical behavior and with it the functional performance, cationic substitution in perovskite-type oxides ABO_3 has been proven to be useful for selected oxynitrides $AB(O,N)_3$ as well, in particular by a targeted *B*-site substitution. As many functional oxide materials contain the critical element Co (*e.g.* Li_xCoO_2[67] in lithium ion batteries or $(Ba,Sr)Co_{0.8}Fe_{0.2}O_{3-\delta}$[64,68] in oxygen transporting membranes) a targeted *B*-site substitution is interesting not only to improve functional performance, but also material's sustainability. Hence, well-known perovskite-type oxides such as $La_{0.6}Ca_{0.4}Co_{0.8}Fe_{0.2}O_{3-\delta}$[63–65] could be a promising candidate for a *B*-site substitution with Fe^{z+}. In chapter 9 by a partial substitution of Co for Fe in $La_{0.6}Ca_{0.4}Co_{1-x}Fe_xO_{3-\delta}$ the oxygen migration behavior could be positively influenced. The resulted measured oxygen permeation flux was three times higher than reported in literature and demonstrated that $La_{0.6}Ca_{0.4}Co_{1-x}Fe_xO_{3-\delta}$ is a promising candidate for high-temperature oxygen separation applications.

To conclude, by a targeted *A*-, *B*-, and *X*-site substitution in $LaTa(O,N)_3$ it is possible to tailor important physical properties. While *A*- and *X*-site substitutions lead to an adjustment of the properties for light-driven applications, a specific *B*-site substitution with a tiny amount of magnetic ions (≤1 at%) leads to before unknown and highly interesting ferromagnetic properties. Whereas a targeted *B*-site substitution in $La_{0.6}Ca_{0.4}Co_{1-x}Fe_xO_{3-\delta}$ leads to an adjusted CO_2 tolerance and total conductivity as important parameters in oxygen transporting membranes. Therefore, the in this thesis shown results can be used to develop further promising perovskite-type oxynitride family members with advanced physical properties and for an improvement of already known perovskite-type oxides.

5. Fundamentals

In the following chapter 5, specific fundamentals are treated to grant a deeper understanding of the chapters 6–9. For example, the crystal structure, electronic structure, and synthesis of perovskite-type oxynitrides – particularly of $LaTa(O,N)_3$ and of $YTa(O,N)_3$ – are described. For further basic theory, reference is made to the relevant textbook literature.

5.1. Crystal structures

5.1.1. Perovskite-type oxynitrides

The composition of perovskite-type oxynitrides is described as $AB(O,N)_3$ where *A* and *B* represent two different cations on two different crystallographic positions. On the anionic site, nitrogen and oxygen are sharing the same crystallographic positions[15,69] with the coordination number (*CN*) of *CN* = 2. The cation, which is located on the *A*-site, normally exhibits a relatively large ionic radius (*e.g*. Ca^{2+}, Sr^{2+}, Ba^{2+}, and La^{3+})[8,11,26,29,70] with a nominal charge of either 2+ or 3+ and a *CN* = 12[1]. Typical *A*-site cations correspond to the alkali, alkaline earth, and rare earth elements.[1] In contrast to the "*A*-site cation" the cation, that is located on the *B*-site corresponds to the transition metals[1]. It exhibits a smaller ionic radius with a higher charge such as 3+ or 5+ (*e.g*. Ti^{3+} and Ta^{5+})[8,9,26,40]. The *B*-site cation is 6-fold coordinated by anions in an octahedral environment.[70] In Figure 2 as an example of a crystal structure of a perovskite-type oxynitride, $LaTaON_2$ is shown.

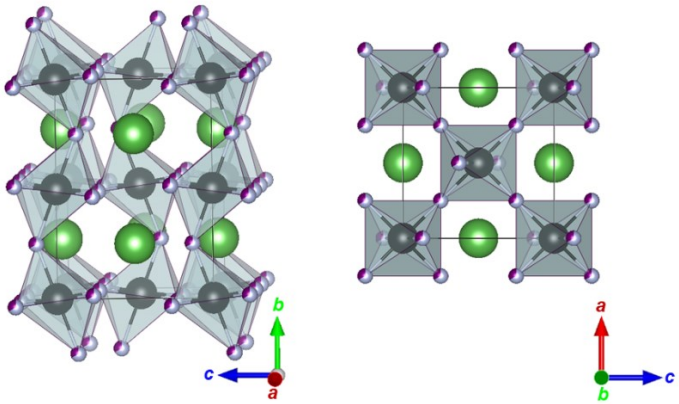

Figure 2. Section of crystal structure of a perovskite-type oxynitride. As example, the perovskite-type oxynitride $LaTaON_2$ in the orthorhombic space group type *Imma*[19,71] is shown. The large green ions represent the *A*-site cations, here, La^{3+} whereas the black ions represent the *B*-site cations, here, Ta^{5+}. The purple/white ions represent the anions with statistical distribution of ⅔ of nitrogen (white) and ⅓ of oxygen (purple) according to the anionic composition of $LaTaON_2$.

The extraordinary flexibility of the perovskite structure is leading by cationic (*A*- and *B*-site substitutions) and/or anionic substitutions (*X*-site substitutions) to a large variety of different perovskite-type materials.[8,15,45,64,69,72,73] By using these ionic substitutions the crystallographic strain[8] and octahedral distortion can be changed, which are affecting the resulting materials' properties. In addition to the octahedral distortion, different symmetries are obtained by ionic substitutions: Perovskite-type oxynitrides often crystallize *e.g*. in orthorhombic or cubic space group types.[1,8,26] Which symmetry is the most stable one for a certain perovskite-type oxynitride is related to the structural stability, which is explained in chapter 5.1.3.

5.1.2. Lanthanum tantalates and yttrium tantalates

Lanthanum tantalum oxides ($La_xTa_yO_z$) crystallize in many symmetries such as in orthorhombic or monoclinic ones (Figure 3a). For example, lanthanum tantalate ($LaTaO_4$) – with the general composition of ABX_4 – can crystallize in an orthorhombic space group type (*e.g.* $A2_1am$[74]) or in a monoclinic one ($P2_1/c$[75]).

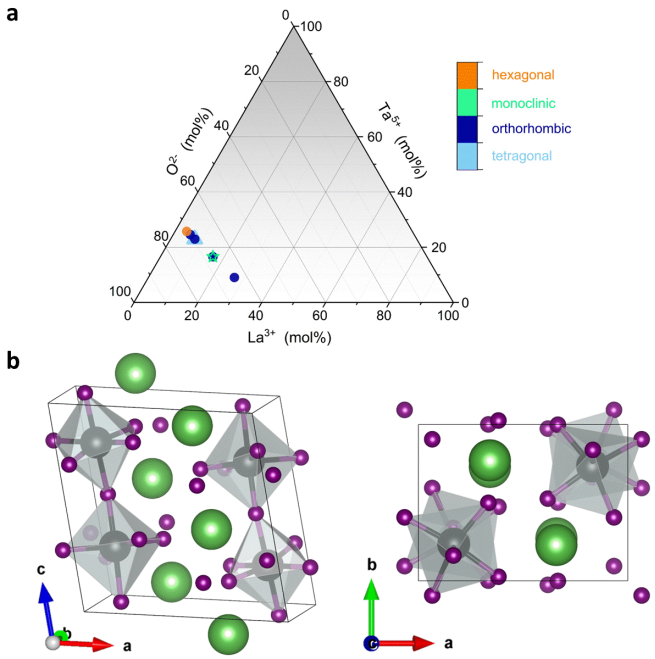

Figure 3. Phase diagram and section of the crystal structure of $LaTaO_4$ crystallized in $A2_1am$. a, Ternary phase diagram of lanthanum tantalum oxides. To collect the crystal symmetry and composition data the ICSD database of the FIZ Karlsruhe[76] was used. b, Section of the crystal structure of lanthanum tantalate. The green ions represent lanthanum, the black ions represent tantalum and the purple ions represent oxygen. The black lines represent the unit cell.

In this work, monoclinic $LaTaO_4$ ($P2_1/c$) was used as oxide precursor to synthesize the perovskite-type oxynitride $LaTaON_2$ (chapter 6). Therefore, in the following the crystal structure of $LaTaO_4$ is treated in general. For $LaTaO_4$ several polymorphs are existing.[77–79] These polymorphs are temperature-dependent.[79] At temperatures between ~200 °C[74] and 1300 °C[75,78] orthorhombic space group types such as *Pbca*, $Cmc2_1$[77,79] or $A2_1am$[74] are favored. Above 1300 °C[75,78] and below ~200 °C[74] $LaTaO_4$ crystallizes in a monoclinic space group type ($P2_1/c$). If crystallizing in the orthorhombic space group types, the *A*-site cation (La^{3+}) is 8-fold coordinated by oxygen ions (*X*-site ions).[74] In contrary, the *B*-site cation (Ta^{5+}) is 6-fold coordinated by oxygen ions in an octahedral environment (Figure 3b).[80] In the monoclinic space group type of $LaTaO_4$, the coordination number of Ta^{5+} remains equal. The coordination number of La^{3+} increases from 8 to 9 by conversion into the monoclinic structure type.[74,79] However, both structure types (monoclinic and orthorhombic) can be regarded as derived from an aristotype phase (*e.g.* with space group type *Cmcm*) through octahedral tilting.[78] The octahedra of the orthorhombic phase tilt along the *a*-axis in-plane, whereas the octahedra of the monoclinic phase tilt along the *c*-axis out-of-plane.[78] In contrast to $LaTaO_4$, yttrium tantalate ($YTaO_4$) can crystallize in monoclinic structure types such as $I2_1/a$, $P2_1/a$ or tetragonal ones.[81,82] In the monoclinic structure type, Y^{3+} is 8-fold coordinated by oxygen ions and Ta^{5+} 6-fold coordinated in an octahedral environment.[82] By *A*-site substitutions in $LaTaO_4$ with Y^{3+} for La^{3+} the crystal structure can be changed from $P2_1/c$ to $P2_1/a$[8], since, the effective ionic radii of both ions differ from each other.

5.1.3. Structural stability of perovskite-type oxynitrides

The structural instability of perovskites can be described by the tolerance factor t[28], which is an extension of the Goldschmidt's tolerance factor[83] (t) and given in equation (1) for the composition ABO_3 as:

$$t = \frac{r_A + r_O}{\sqrt{2}(r_B + r_A)} \tag{1}$$

Where r_A is the effective ionic radius of the A-site cation, r_B is the effective ionic radius of the B-site cation, and r_O is the effective ionic radius of the oxygen anion. The effective ionic radii can be derived *e.g.* from Shannon.[84] In the case of ABO_2N, the tolerance factor can be estimated by the following equation (2) where the effective ionic radius r_N of the nitrogen is coming into account:

$$t = \frac{[(r_A + r_O)^8(r_A + r_N)^4]^{1/12}}{\sqrt{2}[(r_B + r_O)^4(r_B + r_N)^2]^{1/6}} \tag{2}$$

If the composition $ABON_2$ is the case, equation (3) has to be used:

$$t = \frac{[(r_A + r_O)^4(r_A + r_N)^8]^{1/12}}{\sqrt{2}[(r_B + r_O)^2(r_B + r_N)^4]^{1/6}} \tag{3}$$

The stated equations (2) and (3) are reported in ref. [28] by Li *et al.* and were used to determine if an oxynitride phase can exist in the perovskite structure. The stability field for the perovskite structure of oxynitrides depends on the size of A-site and B-site cations and the composition of the anionic site (O : N ratio). The stability field for perovskite-type oxynitrides is according to literature in the range of $0.87794 \geq t \leq 1.03807$ by using the effective ionic radii reported by Shannon.[28,84] However, the t values and the stability range vary on the applied model.[28,85] In the stated prediction[28] several perovskite-type oxynitride phases are not yet synthesized, but should be synthesizable in general. For example $YTaON_2$, which was predicted to be suitable for one-photon water splitting by Castelli *et al.*[26], has the tolerance factor $t = 0.912$ and is not yet synthesized. In Figure 4 – as an example – the respective tolerance factors for partially Y-substituted $LaTa(O,N)_3$ are shown and reveal the increasing structural instability as a perovskite phase by increasing yttrium content.

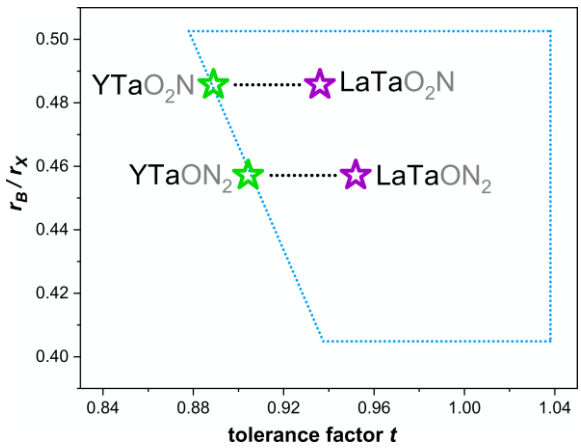

Figure 4. Stability field of the perovskite structure for oxynitrides. The borders of the perovskite structure (dashed blue line) and the tolerance factors t (green and purple stars) are calculated as described in ref. [28]. It is shown, that the structural stability from $LaTa(O,N)_3$ is decreasing by increasing Y-substitution to $YTa(O,N)_3$.

5.2. Physical properties

5.2.1. The electronic structure

In the following, the electronic structure of perovskite oxides (ABO_3) containing d^0 transition metal (M) ions as B-site cations is described. In perovskite oxides the valence band maximum (VBM) is formed by non-bonding[1] O 2p orbitals (Figure 5).

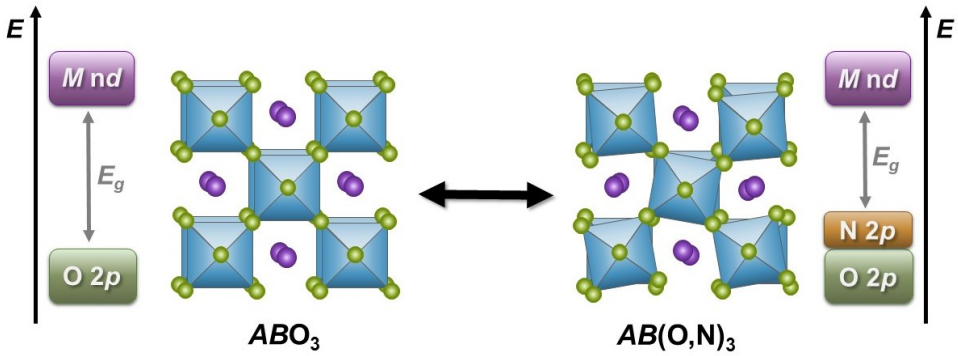

Figure 5. Schematic electronic band diagram. On the left-hand side the schematic bandgaps of ABO_3 and on the right-hand side of $AB(O,N)_3$ are shown. Additionally, the crystal structure of an ideal cubic perovskite oxide and the crystal structure of a perovskite-type oxynitride are shown, where the octahedra are distorted because of nitrogen substitution.

The O 2p orbitals are non-bonding because they are not hybridized with the d-orbitals of the B-site cation. In contrast, the conduction band minimum (CBM) is formed by the empty dt_{2g} orbitals of M (B-site cation).[1,86] These orbitals are antibonding because of their π* interactions with the O 2p orbitals.[1,86] The electronic bandgap (E_g) is defined as the energy difference between the VBM and CBM and is typically large for insulating perovskite oxides such as $SrTiO_3$[1] (E_g = 3.40 eV[87]). The electronic structure can be modified by substitutions of ions in the materials matrix' leading to structural distortions (*e.g.* changes in bond lengths and bond angles).[88] For example, by substituting a B-site cation with a more electronegative one, the covalency of the B–O bond increases.[19] Besides, the B–O bond length decreases. This leads to an expansion of the electron cloud (nephelauxetic effect[80]) and, hence, to an increasing width of the conduction band (CB). Additionally, the B-site cation shifts its' energetic position closer to the valence band (VB) and near the Fermi level.[88] In cubic perovskite oxides the B–O–B bond angles with 180° have the strongest orbital overlap.[1] Hence, by changing the B–O–B bond angles through B-site substitutions from 180°, the orbital overlaps between the B-site cation and oxygen on the X-site are reduced.[89–91] A weaker orbital overlap is observed and, therewith, a narrowing of the CB (d-states).[89–91]

Additionally, the X-site substitution has an impact on the electronic structure of perovskites. By substitution of oxygen for nitrogen on the X-site the electronic bandgap narrows in the resulting perovskite-type oxynitride $AB(O,N)_3$ (Figure 5). The decrease of the bandgap size can be explained by the lower electronegativity χ of N (χ = 3.04) in comparison to O (χ = 3.44) leading to a higher covalency in the B–N bond.[19] Hence, the width of the CB increases and the electronic bandgap size decreases. Supplementary, the lower electronegativity of N locates the N 2p orbitals energetically above the O 2p orbitals[88] (Figure 5). This shifts the VBM to higher energies leading to a narrowing of the electronic bandgap. However, in some perovskite-type materials the band gap size is increasing by substituting oxygen for nitrogen: *e.g.* from $EuTiO_3$ to $EuTi(O,N)_{3\pm\delta}$.[16] This originates by two effects in the material: first, the resulting Eu^{3+} ion in $EuTi(O,N)_{3\pm\delta}$ is leading to structural distortions and, second, the 4f orbitals in the material are shifting through nitrogen substitution.[16] Furthermore, for metallic $SrMoO_3$ a band gap widening by nitrogen substitution to semiconducting $SrMo(O,N)_3$ is observed.[92,93]

Therefore, the electronic structure can be additionally adjusted by the variation of the O : N ratio in perovskite-type oxynitrides. In contrast to the *B*–*X* interactions, the *A*–*X* interactions seem to have a minor impact on the electronic structure of perovskites.[1,8] However, in special cases they can lead to an energy lowering of the VB and formation of partially occupied antibonding bands.[1]

5.2.2. Role of the electronic structure for SWS

The suitable bandgap size and energetic positions of the electronic bands are crucial for light-driven applications. Castelli *et al.*[26] predicted by computational theory the suitability of cubic perovskite-type oxynitrides for one-photon water splitting in correlation with their bandgap size and energetic band positions. This is understandable, since the water redox potential with +1.23 eV versus normal hydrogen electrode (NHE) at pH = 0 is well-defined[94]. Therefore, the energetic level potentials of the electronic bands have to fit in respect to the water redox potential. In Figure 6 schematic band diagrams with two different cases are shown.

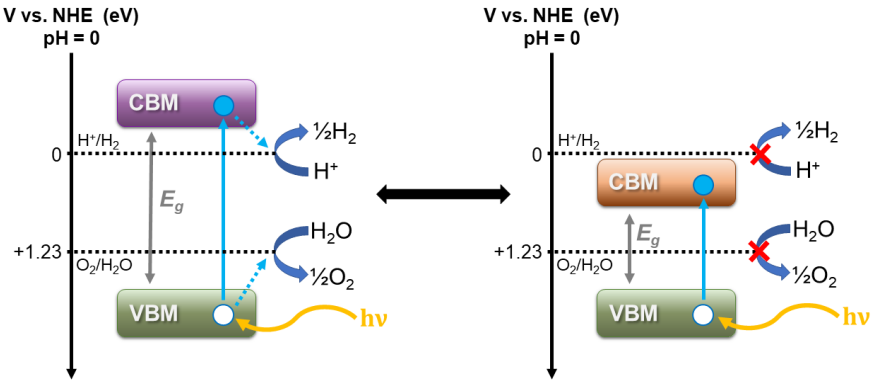

Figure 6. Schematic band diagram. On the left-hand side schematic band diagram of a semiconducting perovskite with energetically well-positioned CBM and VBM in respect to the water redox potential. By photoexcitation of an electron from the VBM into the CBM the band positions and bandgap size are fitting well for splitting water into hydrogen and oxygen. On the right-hand side neither the bandgap size nor the energetic band positions are fitting for solar water splitting.

On the left-hand side, the electronic band positions of CBM, VBM, and bandgap size are fitting energetically for the water splitting process. On the right-hand side, neither the electronic band positions nor the bandgap size are fitting energetically leading to an inhibition of the redox reaction.

Several features can influence if the bandgap size and band positions are fitting for the SWS reaction: *e.g.* Lohaus *et al.*[95] found existing polaron states shrinking the band gap size from 2.2 eV to 1.75 eV in hematite which should be originally suitable for water splitting reactions. Hence, the CBM is shifting about 0.4 eV below the hydrogen potential leading to a poor efficiency for hydrogen evolution.[95] Another influence to the efficiency of a perovskite-type material for SWS can originate from octahedral distortion (*cf.* chapter 5.2.1) or octahedral strain[8] and O/N ordering[39] which can influence the bandgap size and the positions of CBM and VBM. In chapter 7 (and ref. [8]) the decrease of orthorhombic strain in $La_{1-x}Y_xTaO_2N$ leads to a widening of the bandgap from 1.90 eV to 1.96 eV by increasing Y content. Additionally, the O : N ratio can play a role: in chapter 6 (and ref. [19]) it is shown that the bandgap size decreases from 1.9 eV to 1.8 eV by increasing nitrogen content from $LaTaO_2N$ to $LaTaON_2$. Further, recombination centers[8] and defects (as stated above polarons in hematite[95]) can influence the bandgap size. The recombination centers are leading to a poor photocatalytic activity *e.g.* for $BaNbO_2N$[96], $BaTaO_2N$[97], and $Ba_5Nb_{4-x}Ta_xO_{15}$[98].

5.2.3. Magnetism in perovskite-type materials

The magnetism in perovskites is closely related to localized *d*-electrons.[1] In the following, the magnetism in perovskite oxides is discussed: Amongst others, at low temperatures (LT) localized and ordered electron spins in perovskite oxides can lead either to ferromagnetism (FM) or antiferromagnetism (AFM).[6] A typical LT-FM perovskite oxide is $YTiO_3$[99], whereas, typical LT-AFM perovskite oxides are $LaMnO_3$[100], $LaVO_3$[101] or $LaFeO_3$[100]. At high temperatures (HT) the localized electron spins are normally disordered, resulting in paramagnetism (PM).[6] The magnetic behavior in perovskite oxides is mainly described by structural distortions originating by introduced "Jahn Teller ions" (orbital degenerated ions).[6,102] These structural distortions can lead to a symmetry lowering, besides a crystal field splitting.[1,102] By a crystal field splitting in an octahedral ligand field, the five degenerated *d*-orbitals of a transition metal ion (*e.g.* Co^{2+}, d^7 configuration) split into a threefold-degenerated level (t_{2g}) and a two-fold degenerated level (e_g) (Figure 7).[102,103]

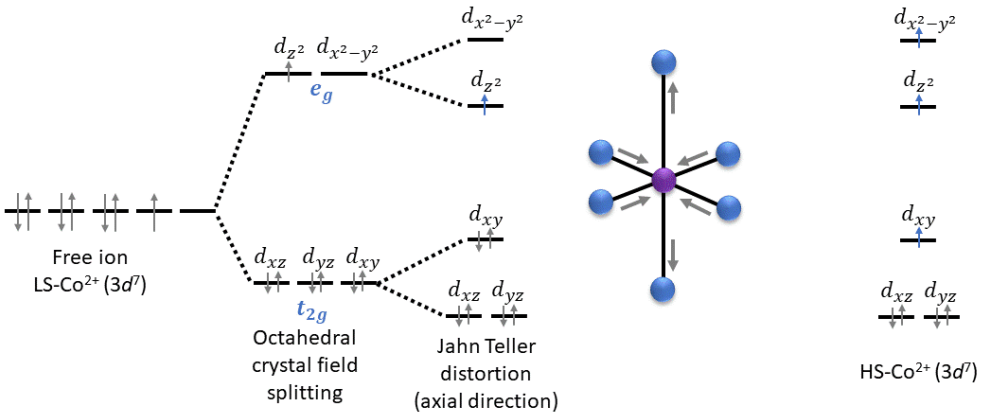

Figure 7. Octahedral crystal field splitting. The scheme of the octahedral crystal field splitting on the left-hand side is drawn after references [1,102,104,105]. In the middle, the octahedral axial stretching because of Jahn Teller distortion of a six-fold coordinated Jahn Teller ion (LS-Co^{2+}) in an octahedral ligand field is shown. On the right-hand side the HS-Co^{2+} configuration with its' three unpaired electrons is shown.

The degenerated t_{2g} and e_g levels can be filled up with electrons by applying the Hund's rules. [1,102,103] In comparison to free ions, the energy levels between the different electronic configurations in perovskites are not that widely separated.[1] Consequently, this results in Coulomb interactions, and accordingly to octahedral distortions such as octahedral axial stretching (filled d_{z^2} orbitals, see Figure 7) or axial compression (filled $d_{x^2-y^2}$ orbitals).[1,102] This effect is called the Jahn Teller effect.[105] In Figure 7, Co^{2+} in the so-called low spin (LS) configuration is shown. Because, the tetragonal distortion of the octahedron provides an energy gain for Co^{2+} – see lowered energy level of the filled d_{z^2} orbital – this distortion is favored.[105] In contrast, in Figure 7 on the right-hand side the HS-configuration of Co^{2+} is shown that exhibits three unpaired electrons. Besides the LS configurations, also high spin (HS) configurations of transition metal ions exhibiting d^4, d^7, and d^9 configurations can exist.[105] These HS configurations exhibit the maximum of possible unpaired electron spins. The crystal field theory and the ligand field theory originate from the same concept.[105] Since in LS complexes the number of unpaired electron spins is reduced in comparison to the HS complexes, a reduced magnetic moment is observed. For example for LS-Co^{2+} 1.73 μ_B/Co^{2+} instead of 3.88 μ_B/Co^{2+} of HS-Co^{2+} is observed.[105,106]

For perovskite oxides such as LT-AFM $LaMnO_3$[100] the mechanism that leads to its' magnetic behavior is explained by a superexchange.[102] This is an antiferromagnetic coupling between the Mn^{3+} ions through an oxygen ion (Figure 8).[102,107]

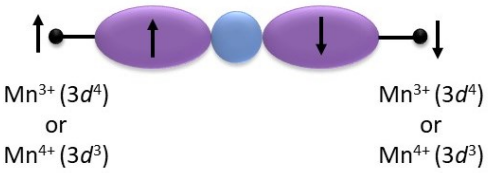

Figure 8. Superexchange. The scheme of a superexchange[102,107] mechanism in LT-AFM $LaMnO_3$.

In contrast, the magnetism in perovskite-type oxynitrides is rarely investigated and not clarified.[45,108] This may be due to their limited number and difficulties in synthesis.[108,109] In comparison to the colossal magnetoresistance (CMR) at RT in the double-perovskite oxide Sr_2FeMoO_6[110] for perovskite-type oxynitrides mostly limited magnetic properties[111,112] are reported. Until now, they revealed either LT-CMR (LT-FM), LT-AFM, or Pauli paramagnetism.[72,73,92,111–114]

5.2.4. Mixed ionic-electronic conductors

Mixed ionic-electronic conductors (MIEC) with perovskite-type structure gained great interest the last few decades as very efficient separators for oxygen from gas mixtures.[63–66,115,116] More applications in which they can be used are as cathode materials in solid-oxide fuel cells, CCU, in the conversion of hydrocarbons to synthesis gas, and in the production of oxygen-enriched air.[64,115,117–120] In Figure 9 the oxygen enrichment of air or another gas mixture by a perovskite-type MIEC membrane is drafted. How the oxygen transport is working by using a MIEC membrane is explained in chapter 5.2.5.

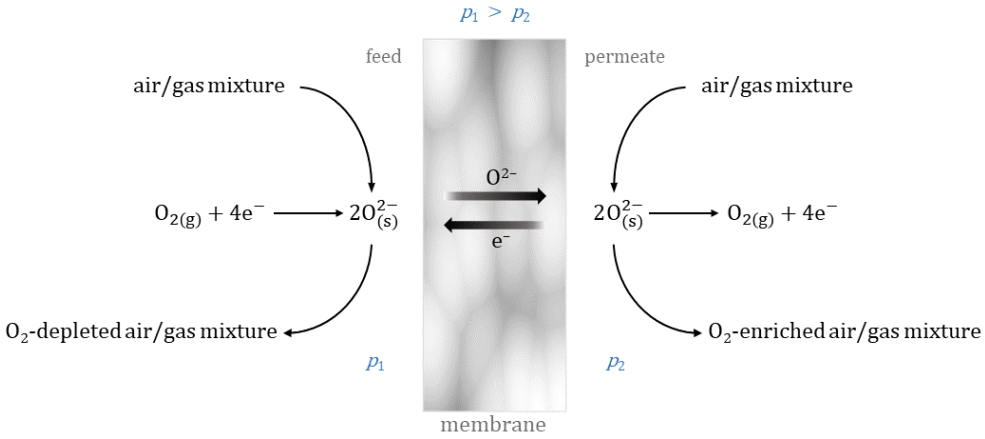

Figure 9. Function of a MIEC. Schematic oxygen enrichment by a perovskite-type mixed-ionic conducting membrane drawn after ref. [117]. At elevated temperatures by setting a differential pressure the oxygen can be transported through the perovskite-type MIEC membrane from p_1 to p_2 ($p_1 > p_2$). For charge neutrality electrons diffuse in the opposite direction as O^{2-}.

There are several advantages of perovskites as MIEC membranes: two of them are 100 % selectivity for molecular oxygen and requiring a lower pressure difference making them work at elevated temperatures.[117] However, by using gas mixtures containing *e.g.* CO_2 another parameter is coming into account: the CO_2 tolerance[64] of the membrane is one of the most important factors if the membrane should work with a high oxygen permeation flux. Therefore, a special composition and structure to tune the right physical properties is needed which is described in chapter 9.

As stated in chapter 4 the tuning of physical properties in perovskites is achieved by *A*-, *B*-, or *X*-site substitutions. According to literature[121] the *A*-site substitution (*e.g.* Ba for La) can have an impact on the coefficients of oxygen diffusion and surface exchange in MIECs. Whereas a *B*-site substitution has a little impact on the rate-determining step and a larger impact on semi-permeation flux performances.[122] Hence, the oxygen diffusion and oxygen diffusion kinetics on the MIEC membrane's surface depend strongly on the nature of the *A*- and *B*-site cations.[121–123]

5.2.5. Oxygen transport

The oxygen transport or oxygen migration through a perovskite-type oxide was found to be influenced mainly by the oxygen vacancy formation.[64,124] Further, the transport of oxygen is controlled by surface exchange and bulk diffusion.[63,125] In the following, the oxygen transport is described as in references [63,124,126,127]:

First, gaseous O_2 adsorbs on the materials surface and is undergoing a surface reaction to oxide ions in the first bulk layer of the membrane. This reaction is described in the Kröger-Vink notation in equations (4) and (5).[124] For further information to the Kröger-Vink notation reference is made to the relevant text book literature.

$$\frac{1}{2}O_2 \rightleftharpoons O' + h^{\cdot} \qquad \text{(pre-equilibrium)} \tag{4}$$

$$O' + V_O^{\cdot\cdot} \rightleftharpoons O_O^x + h^{\cdot} \qquad \text{(rate-determining step)} \tag{5}$$

In both equations, O′ represents the negative charged oxygen ion adsorbed on the surface, $V_O^{\cdot\cdot}$ is the double positive charged oxygen vacancy, O_O^x the lattice oxygen, and $h^{\cdot}$ is an electron hole.[63] In equation (4) the adsorbed oxygen is in equilibrium with the surface (charge exchange step). Equation (5) is the next reaction step and determines the rate (rate-determining step = rds) how fast oxygen can be incorporated as stated in literature[124]. If the concentration of oxygen vacancies ($V_O^{\cdot\cdot}$) reaches a high level on the surface, the reaction is drifting to the right side of the equilibrium and, hence, to a favored incorporation of adsorbed oxygen (O′) into the materials lattice. The overall oxygen incorporation equation[63,124] is depicted in equation (6):

$$\frac{1}{2}O_2 + V_O^{\cdot\cdot} \rightleftharpoons O_O^x + h^{\cdot} \tag{6}$$

After the oxygen is incorporated into the materials lattice, bulk diffusion of the oxygen takes place. The bulk diffusion mainly involves the transfer of oxygen vacancies, interstitial oxygen, and charge.[63] The transfer rate of oxygen can be expressed by the Nernst-Planck equation[63]:

$$J_i = \frac{\sigma_i}{z_i^2 F^2} \nabla \mu_i + C_i \nu \tag{7}$$

In equation (7), J_i is the permeability flux of substance i ($mol \cdot cm^{-2} \cdot s^{-1}$), z is the defect charge number, F is the Faraday's constant, σ_i is the conductivity ($S \cdot cm^{-1}$), μ_i is the electrochemical potential, C_i is the concentration of the substance i ($mol \cdot cm^{-3}$), and ν is the local velocity of the inert defect marker ($cm \cdot s^{-1}$).[63] More exactly how the oxygen transport is working and which factors are influencing and are important is described in chapter 9.

5.3. Methods for perovskite-type oxynitride preparation

5.3.1. Solid state method for oxide preparation

One method to prepare oxide precursors is by using a solid state reaction (SSR). This method contains the homogeneous mixing by grinding of several transition metal binary oxides (*e.g.* La_2O_3 and Ta_2O_5) with flux (*e.g.* KCl or $CaCl_2$) prior to thermal treatment.[11,12,24] The thermal treatment of the oxides' mixture requires high temperatures leading to well-crystalline oxides[11,128–130] because of the high melting points of the binary oxides.

5.3.2. Soft chemistry methods for oxide preparation

5.3.2.1. Pechini method for oxide preparation

Another method to prepare oxide precursors is the Pechini method.[19,131] The Pechini method is sol-gel-related and leads depending of the calcination temperature to nanocrystalline, nearly amorphous oxide precursors.[19,131–133] In Figure 10 the first two reaction steps of the Pechini method[131] are shown.

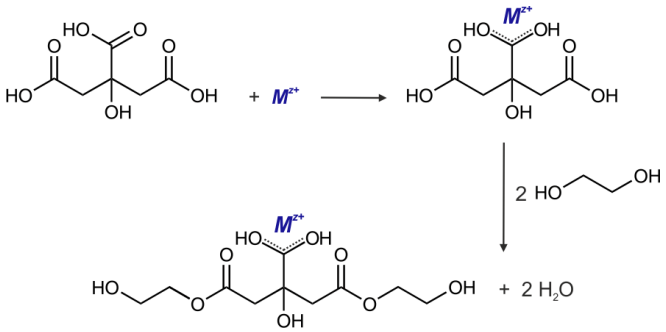

Figure 10. Scheme of the first two reaction steps of the Pechini method. The first two steps of the reaction mechanism are drawn after ref. [132]. For better visibility the metal ion M^{z+} (*A*- or *B*-site cation) is marked in blue.

In the beginning, citric acid and metal ions M^{z+} (*A*- and *B*-site cations) are mixed together in an aqueous solution. The citric acid is acting as a complexing agent for the metal ions.[134] Normally, two citric acid molecules are needed to complex one metal ion[134]. However, by a mixture of *A*- and *B*-site cations in an aqueous solution "double-cored complexes" can be observed. These complexes contain one *A*-site cation and one *B*-site cation complexed together with three citric acid molecules[134]. After the complexation ethylene glycol is added. This leads to a polyesterification under a condensation reaction.[132] Very small colloids consisting of agglomerated short polymers dispersed in an aqueous medium are obtained.[135] This colloidal suspension is called as sol.[135] By a subsequent thermal treatment and evaporating the solvent, the colloids condensate further to a dry three-dimensional network[136], where the pores are partially collapsed. The resulting three-dimensional network is called as xerogel.[134] Xerogels obtained by the Pechini method are black in color.[19] By an additional thermal treatment, the organic residues can be burned away and the pure oxide is obtained.[8,19]

5.3.2.2. The co-precipitation method

The co-precipitation method can be used to synthesize perovskite-type oxide nanoparticles which should be suitable as MIEC membranes.[64] These nanoparticles achieved by co-precipitation can also be used as drug delivery systems and for other applications.[137] The co-precipitation method is more

sol-gel-related than the Pechini method (chapter 5.3.2.1). For more information on the common reaction mechanism of the sol-gel synthesis, reference is made to specific literature[134,135,137].

5.3.3. The ammonolysis of oxides

After preparation of the oxide precursors thermal ammonolysis can be applied to obtain perovskite-type oxynitrides. By using that method, the oxides' surface reacts with flowing ammonia ($NH_{3(g)}$) at high temperatures leading to a nitridation of the oxide.[138] As an example, the reaction of $La_2Ta_2O_{8(s)}$ with $NH_{3(g)}$ to the respective perovskite-type oxynitride $LaTaON_{2(s)}$ is shown in reaction equation (1). The reaction conditions are taken from ref. [139].

$$La_2Ta_2O_{8(s)} + 4\,NH_{3(g)} \xrightarrow{900\,°C - 1000\,°C,\ Flux} 2\,LaTaON_{2(s)} + 6\,H_2O_{(g)} \qquad (1)$$

Ammonia as nitriding agent is used, because neither pure $N_{2(g)}$ nor $N_{2(g)}/H_{2(g)}$ mixtures provide the same efficiency in nitridation.[138] In comparison to the stable $N_{2(g)}$ (high dissociation enthalpy of 226 kcal·mol^{-1}[138]), the decomposition products of ammonia (nitriding species[140]) exhibit a much higher reactivity. At high temperatures – *e.g.* above 1000 °C – gaseous ammonia decomposes into $N_{2(g)}$ and $H_{2(g)}$.[141–143] Therefore, ammonia also provides reducing conditions during the nitriding process. Below 1000 °C its' nitrogen adducts such as $N_2H_{4(g)}$ and others besides $H_{2(g)}$ are present.[140,141] However, the decomposition of ammonia is pressure-dependent – *e.g.* starting decomposition at around 450 °C at 1 Atm – and impurity-dependent.[142–144] Because the ammonolysis process is a solid-gas-interface reaction, nitrogen concentration gradients from surface into the bulk in the particles can be found.[19,45] To avoid such inhomogeneous nitrogen concentration several ammonolysis cycles can be applied.[8] Another way, to get a homogenous product is the usage of flux (*e.g.* KCl).[145] This can prevent also a high defect concentration[145] in the material giving a fine-tuning of the materials' properties.

In this work, the three different oxide preparation methods, which are stated above (5.3.1 and 5.3.2) are used. In Figure 11 mainly the resulting oxide precursors by Pechini method (5.3.2.1) were ammonolyzed to the respective perovskite-type oxynitrides. The following chapters 6–9 give further explanations to the respective materials synthesis and formation processes.

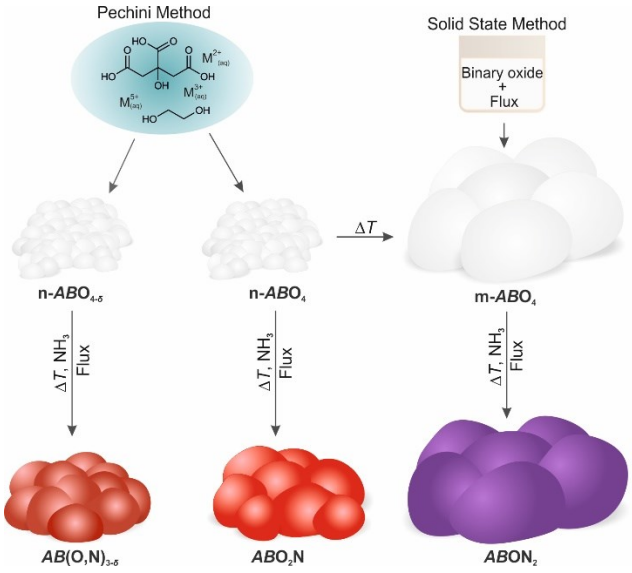

Figure 11. Synthesis scheme of perovskite-type oxynitrides. In this scheme the synthesis paths used in the thesis are shown and point to the importance of the oxide precursor microstructure for the resulting perovskite-type oxynitride product (for further information, see chapter 6–8).

5.4. References

[1] T. Wolfram, S. Ellialtioglu, *Electronic and Optical Properties of* d-*band Perovskites*, Cambridge University Press, **2006**.

[2] A. Kojima, K. Teshima, Y. Shirai, T. Miyasaka, *J. Am. Chem. Soc.* **2009**, *131*, 6050–6051.

[3] W. Li, L. J. Ji, *Science (80-.).* **2018**, *361*, 132.

[4] Y. Wei, H. Gui, Z. Zhao, J. Li, Y. Liu, S. Xin, X. Li, W. Xie, *AIP Adv.* **2014**, *4*, 127134.

[5] J. Wang, C. Zhang, H. Liu, R. McLaughlin, Y. Zhai, S. R. Vardeny, X. Liu, S. McGill, D. Semenov, H. Guo, et al., *Nat. Commun.* **2019**, *10 : 129*, DOI 10.1038/s41467-018-07952-x.

[6] J. Varignon, M. Bibes, A. Zunger, *Nat. Commun.* **2019**, *10*, 1–11.

[7] G. Zhang, G. Liu, L. Wang, J. T. S. Irvine, *Chem. Soc. Rev.* **2016**, *45*, 5951–5984.

[8] C. Bubeck, M. Widenmeyer, A. De Denko, G. Richter, M. Coduri, E. Salas Colera, E. Goering, H. Zhang, S. Yoon, F. Osterloh, et al., *J. Mater. Chem. A* **2020**, *8*, 11837–11848.

[9] I. E. Castelli, J. M. García-Lastra, F. Hüser, K. S. Thygesen, K. W. Jacobsen, *New J. Phys.* **2013**, *15*, 105026.

[10] M. Hojamberdiev, K. Kawashima, *Energy Reports* **2020**, *6*, 13–24.

[11] L. Zhang, Y. Song, J. Feng, T. Fang, Y. Zhong, Z. Li, Z. Zou, *Int. J. Hydrogen Energy* **2014**, *39*, 7697–7704.

[12] M. Jansen, H. P. Letschert, *Nature* **2000**, *404*, 980–982.

[13] S. Chang, J. Yu, R. Wang, Q. Fu, X. Xu, *ACS Nano* **2021**, *15*, 18153–18162.

[14] T. Sakata, R. Yoshiyuki, R. Okada, S. Urushidani, N. Tarutani, K. Katagiri, K. Inumaru, K. Koyama, Y. Masubuchi, *Inorg. Chem.* **2021**, *60*, 4852–4859.

[15] A. Shkabko, M. H. Aguirre, I. Marozau, T. Lippert, A. Weidenkaff, *Appl. Phys. Lett.* **2009**, *95*, 152109.

[16] L. Sagarna, K. Z. Rushchanskii, A. Maegli, S. Yoon, S. Populoh, A. Shkabko, S. Pokrant, M. Ležaić, R. Waser, A. Weidenkaff, *J. Appl. Phys.* **2013**, *114*, 0–10.

[17] Y. Masubuchi, S.-K. Sun, S. Kikkawa, *Dalt. Trans.* **2015**, *44*, 10570–10581.

[18] A. Fuertes, *Prog. Solid State Chem.* **2018**, *51*, 63–70.

[19] C. Bubeck, M. Widenmeyer, G. Richter, M. Coduri, E. Goering, S. Yoon, A. Weidenkaff, *Commun. Chem.* **2019**, *2*, 134.

[20] C. M. Leroy, A. E. Maegli, K. Sivula, T. Hisatomi, N. Xanthopoulos, E. H. Otal, S. Yoon, A. Weidenkaff, R. Sanjines, M. Grätzel, *Chem. Commun.* **2012**, *48*, 820.

[21] A. E. Maegli, E. H. Otal, T. Hisatomi, S. Yoon, C. M. Leroy, N. Schäuble, Y. Lu, M. Grätzel, A. Weidenkaff, *Energy Procedia* **2012**, *22*, 61–66.

[22] S. Pokrant, A. E. Maegli, G. L. Chiarello, A. Weidenkaff, *Chimia (Aarau).* **2013**, *67*, 162–167.

[23] T. Yajima, F. Takeiri, K. Aidzu, H. Akamatsu, K. Fujita, W. Yoshimune, M. Ohkura, S. Lei, V. Gopalan, K. Tanaka, et al., *Nat. Chem.* **2015**, *7*, 1017–1023.

[24] M. Yang, J. Oró-Solée, J. A. Rodgers, A. B. Jorge, A. Fuertes, J. P. Attfield, *Nat. Chem.* **2011**, *3*, 47–52.

[25] S. Jiang, Y. Liu, J. Xu, *Mater. Adv.* **2021**, *2*, 1190–1203.

[26] I. E. Castelli, D. D. Landis, K. S. Thygesen, S. Dahl, I. Chorkendorff, T. F. Jaramillo, K. W. Jacobsen, *Energy Environ. Sci.* **2012**, *5*, 9034–9043.

[27] H. Huang, J. Feng, H. Fu, B. Zhang, T. Fang, Q. Qian, Y. Huang, S. Yan, J. Tang, Z. Li, et al., *Appl. Catal. B Environ.* **2018**, *226*, 111–116.

[28] W. Li, E. Ionescu, R. Riedel, A. Gurlo, *J. Mater. Chem. A* **2013**, *1*, 12239–12245.

[29] H. Kageyama, K. Hayashi, K. Maeda, J. P. Attfield, Z. Hiroi, J. M. Rondinelli, K. R. Poeppelmeier, *Nat. Commun.* **2018**, *9*, DOI 10.1038/s41467-018-02838-4.

[30] T. Yajima, F. Takeiri, K. Aidzu, H. Akamatsu, K. Fujita, W. Yoshimune, M. Ohkura, S. Lei, V. Gopalan, K.

Tanaka, et al., *Nat. Chem.* **2015**, *7*, 1017–1023.

[31] S. G. Ebbinghaus, H. P. Abicht, R. Dronskowski, T. Müller, A. Reller, A. Weidenkaff, *Prog. Solid State Chem.* **2009**, *37*, 173–205.

[32] M. Yang, J. Oró-Solé, J. A. Rodgers, A. B. Jorge, A. Fuertes, J. P. Attfield, *Nat. Chem.* **2011**, *3*, 47–52.

[33] M. Hojamberdiev, M. F. Bekheet, J. N. Hart, J. J. M. Vequizo, A. Yamakata, K. Yubuta, A. Gurlo, M. Hasegawa, K. Domen, K. Teshima, *Phys. Chem. Chem. Phys.* **2017**, *19*, 22210–22220.

[34] F. Tessier, P. Maillard, F. Cheviré, K. Domen, S. Kikkawa, *J. Ceram. Soc. Japan* **2009**, *117*, 1–5.

[35] T. Hisatomi, J. Kubota, K. Domen, *Chem. Soc. Rev.* **2014**, *43*, 7520–7535.

[36] J. Seo, T. Hisatomi, M. Nakabayashi, N. Shibata, T. Minegishi, M. Katayama, K. Domen, *Adv. Energy Mater.* **2018**, *8*, 1800094.

[37] K. Maeda, H. Terashima, K. Kase, M. Higashi, M. Tabata, K. Domen, *Bull. Chem. Soc. Jpn.* **2008**, *81*, 927–937.

[38] K. Maeda, M. Higashi, D. Lu, R. Abe, K. Domen, *J. Am. Chem. Soc.* **2010**, *132*, 5858–5868.

[39] N. Vonrüti, U. Aschauer, *Phys. Rev. Mater.* **2018**, *2*, 105401.

[40] A. E. Maegli, S. Pokrant, T. Hisatomi, M. Trottmann, K. Domen, A. Weidenkaff, *J. Phys. Chem. C* **2014**, *118*, 16344–16351.

[41] M. Liu, W. You, Z. Lei, T. Takata, K. Domen, C. Li, *Chinese J. Catal.* **2006**, *27*, 556–558.

[42] M. Shang, C. Zhang, T. Zhang, L. Yuan, L. Ge, H. Yuan, S. Feng, *Appl. Phys. Lett.* **2013**, *102*, 2–5.

[43] T. Dietl, H. Ohno, F. Matsukura, J. Cibert, D. Ferrand, *Science (80-.).* **2000**, *287*, 1019–1022.

[44] T. Dietl, *Nat. Mater.* **2010**, *9*, 965–974.

[45] C. Bubeck, E. Goering, R. Lawitzki, K. Küster, W. Sigle, M. Widenmeyer, U. Starke, C. Ritter, G. J. Cuello, P. Nagel, et al., *arXiv:2003.14259* **2022**.

[46] B. B. Straumal, A. A. Mazilkin, S. G. Protasova, A. A. Myatiev, P. B. Straumal, G. Schütz, P. A. Van Aken, E. Goering, B. Baretzky, *Phys. Rev. B - Condens. Matter Mater. Phys.* **2009**, *79*, 205206.

[47] T. Tietze, P. Audehm, Y. C. Chen, G. Schütz, B. B. Straumal, S. G. Protasova, A. A. Mazilkin, P. B. Straumal, T. Prokscha, H. Luetkens, et al., *Sci. Rep.* **2015**, *5 : 8871*.

[48] Y. C. Chen, E. Goering, L. Jeurgens, Z. Wang, F. Phillipp, J. Baier, T. Tietze, G. Schütz, *Appl. Phys. Lett.* **2013**, *103*, 162405.

[49] A. Khosravi, R. N. N. Koury, L. Machado, J. J. G. Pabon, *Energy* **2018**, *148*, 1087–1102.

[50] M. Amin, H. H. Shah, A. G. Fareed, W. U. Khan, E. Chung, A. Zia, Z. U. Rahman Farooqi, C. Lee, *Int. J. Hydrogen Energy* **2022**, *47*, 33112–33134.

[51] K. Christopher, R. Dimitrios, *Energy Environ. Sci.* **2012**, *5*, 6640–6651.

[52] H. Shui, Z. Cai, C. C. Xu, *Energies* **2010**, *3*, 155–170.

[53] O. V. Marchenko, S. V. Solomin, *Int. J. Hydrogen Energy* **2015**, *40*, 3801–3805.

[54] S. Griffiths, B. K. Sovacool, J. Kim, M. Bazilian, J. M. Uratani, *Energy Res. Soc. Sci.* **2021**, *80*, DOI 10.1016/j.erss.2021.102208.

[55] BMWI, *Fed. Minist. Econ. Aff. Energy (BMWI), Berlin* **2020**, 1–32.

[56] K. Agbossou, R. Chahine, J. Hamelin, F. Laurencelle, A. Anouar, J. M. St-Arnaud, T. K. Bose, *J. Power Sources* **2001**, *96*, 168–172.

[57] C. K. Kjartansdóttir, L. P. Nielsen, P. Møller, *Int. J. Hydrogen Energy* **2013**, *38*, 8221–8231.

[58] A. N. Colli, H. H. Girault, A. Battistel, *Materials (Basel).* **2019**, *12*, 1–17.

[59] M. F. Ahmad Kamaroddin, N. Sabli, T. A. Tuan Abdullah, S. I. Siajam, L. C. Abdullah, A. Abdul Jalil, A. Ahmad, *Membranes (Basel).* **2021**, *11*, 1–27.

[60] S. D. Ghadge, P. P. Patel, M. K. Datta, O. I. Velikokhatnyi, P. M. Shanthi, P. N. Kumta, *J. Power Sources*

2018, *392*, 139–149.

[61] S. E. Yoon, S. H. Song, J. Choi, J. Y. Ahn, B. K. Kim, J. S. Park, *Int. J. Hydrogen Energy* **2014**, *39*, 5497–5504.

[62] J. Kim, A. Jun, O. Gwon, S. Yoo, M. Liu, J. Shin, T. H. Lim, G. Kim, *Nano Energy* **2018**, *44*, 121–126.

[63] W. Bai, J. Feng, C. Luo, P. Zhang, H. Wang, Y. Yang, Y. Zhao, H. Fan, *Int. J. Hydrogen Energy* **2021**, *46*, 36257–36290.

[64] G. Chen, W. Liu, M. Widenmeyer, P. Ying, M. Dou, W. Xie, C. Bubeck, L. Wang, M. Fyta, A. Feldhoff, et al., *J. Memb. Sci.* **2019**, *590*, 117082.

[65] G. Chen, F. Buck, I. Kistner, M. Widenmeyer, T. Schiestel, A. Schulz, M. Walker, A. Weidenkaff, *Chem. Eng. J.* **2020**, *392*, DOI 10.1016/j.cej.2019.123699.

[66] J. Yi, M. Schroeder, M. Martin, *Chem. Mater.* **2013**, *25*, 815–817.

[67] K. Mizushima, P. C. Jones, P. J. Wiseman, J. B. Goodenough, *Solid State Ionics* **1981**, *3–4*, 171–174.

[68] J. Hoon Park, J. Pyo Kim, S. Hwan Son, *Energy Procedia* **2009**, *1*, 369–374.

[69] A. Shkabko, M. H. Aguirre, I. Marozau, M. Doebeli, M. Mallepell, T. Lippert, A. Weidenkaff, *Mater. Chem. Phys.* **2009**, *115*, 86–92.

[70] L. Katz, R. Ward, *Inorg. Chem.* **1964**, *3*, 205–211.

[71] S. H. Porter, Z. Huang, P. M. Woodward, *Cryst. Growth Des.* **2014**, *14*, 117–125.

[72] S. Yoon, K. Son, S. G. Ebbinghaus, M. Widenmeyer, A. Weidenkaff, *J. Alloys Compd.* **2018**, *749*, 628–633.

[73] S. Yoon, A. E. Maegli, L. Karvonen, A. Shkabko, S. Populoh, K. Gałązka, L. Sagarna, M. H. Aguirre, P. Jakes, R. A. Eichel, et al., *Zeitschrift fur Anorg. und Allg. Chemie* **2014**, *640*, 797–804.

[74] F. Vullum, F. Nitsche, S. M. Selbach, T. Grande, *J. Solid State Chem.* **2008**, *181*, 2580–2585.

[75] T. A. Kurova, V. B. Aleksandrov, *Dokl. Akad. Nauk SSSR* **1971**, *201*, 1095–1098.

[76] "ICSD web version 4.4.0," can be found under https://icsd.fiz-karlsruhe.de/search/basic.xhtml, **2020**.

[77] R. J. Cava, R. S. Roth, *J. Solid State Chem.* **1981**, *36*, 139–147.

[78] K. J. Cordrey, M. Stanczyk, C. A. L. Dixon, K. S. Knight, J. Gardner, F. D. Morrison, P. Lightfoot, *Dalt. Trans.* **2015**, *44*, 10673–10680.

[79] M. Nyman, M. A. Rodriguez, L. E. S. Rohwer, J. E. Martin, M. Waller, F. E. Osterloh, *Chem. Mater.* **2009**, *21*, 4731–4737.

[80] A. L. Tchougréeff, R. Dronskowski, *Int. J. Quantum Chem.* **2009**, *109*, 2606–2621.

[81] D. Nishio-Hamane, T. Minakawa, Y. Ohgoshi, *J. Mineral. Petrol. Sci.* **2013**, *108*, 335–344.

[82] L. H. Brixner, *J. Electrochem. Soc.* **1983**, *130*, 2435.

[83] V. M. Goldschmidt, *Naturwissenschaften* **1926**, *14*, 477–485.

[84] R. D. Shannon, *Acta Crystallogr. Sect. A* **1976**, *32*, 751–767.

[85] R. Ubic, K. Tolman, K. Chan, N. Lundy, S. Letourneau, W. M. Kriven, *J. Alloys Compd.* **2013**, *575*, 239–245.

[86] H. W. Eng, P. W. Barnes, B. M. Auer, P. M. Woodward, *J. Solid State Chem.* **2003**, *175*, 94–109.

[87] Y. Xu, M. Schoonen, *Am. Mineral.* **2000**, *85*, 543–556.

[88] A. Maegli, S. Yoon, E. Otal, L. Karvonen, P. Mandaliev, A. Weidenkaff, *J. Solid State Chem.* **2011**, *184*, 929–936.

[89] J. Hwang, Z. Feng, N. Charles, X. R. Wang, D. Lee, K. A. Stoerzinger, S. Muy, R. R. Rao, D. Lee, R. Jacobs, et al., *Mater. Today* **2019**, *31*, 100–118.

[90] S. A. Akhade, J. R. Kitchin, *J. Chem. Phys.* **2012**, *137*, DOI 10.1063/1.4746117.

[91] I. H. Inoue, O. Goto, H. Makino, N. E. Hussey, M. Ishikawa, *Phys. Rev. B* **1998**, *58*, 4372–4383.

[92] D. Logvinovich, J. Hejtmánek, K. Knížek, M. Maryško, N. Homazava, P. Tomeš, R. Aguiar, S. G. Ebbinghaus, A. Reller, A. Weidenkaff, *J. Appl. Phys.* **2009**, *105*, 023522.

[93] D. Logvinovich, R. Aguiar, R. Robert, M. Trottmann, S. G. Ebbinghaus, A. Reller, A. Weidenkaff, *J. Solid State Chem.* **2007**, *180*, 2649–2654.

[94] R. van de Krol, M. Gräzel, in *Photoelectrochem. Hydrog. Prod.*, Springer US, **2012**, pp. 13–67.

[95] C. Lohaus, A. Klein, W. Jaegermann, *Nat. Commun.* **2018**, *9*, 4309.

[96] J. Seo, M. Nakabayashi, T. Hisatomi, N. Shibata, T. Minegishi, M. Katayama, K. Domen, *J. Mater. Chem. A* **2019**, *7*, 493–502.

[97] J. Seo, M. Nakabayashi, T. Hisatomi, N. Shibata, T. Minegishi, K. Domen, *ACS Appl. Energy Mater.* **2019**, *2*, 5777–5784.

[98] M. Hojamberdiev, M. F. Bekheet, E. Zahedi, H. Wagata, J. J. M. Vequizo, A. Yamakata, K. Yubuta, A. Gurlo, K. Domen, K. Teshima, *Dalt. Trans.* **2016**, *45*, 12559–12568.

[99] A. C. Komarek, H. Roth, M. Cwik, W. D. Stein, J. Baier, M. Kriener, F. Bourée, T. Lorenz, M. Braden, *Phys. Rev. B - Condens. Matter Mater. Phys.* **2007**, *75*, 224402.

[100] W. C. Koehler, E. O. Wollan, *J. Phys. Chem. Solids* **1957**, *2*, 100–106.

[101] S. Miyasaka, Y. Okimoto, M. Iwama, Y. Tokura, *Phys. Rev. B - Condens. Matter Mater. Phys.* **2003**, *68*, 100406(R).

[102] K. I. Kugel, D. I. Khomskii, *Sov. Phys. Uspekhi* **1982**, *25*, 231–256.

[103] G. A. Gehring, K. A. Gehring, *Reports Prog. Phys.* **1975**, *38*, 1–89.

[104] D. H. Kim, N. M. Aimon, L. Bi, J. M. Florez, G. F. Dionne, C. A. Ross, *J. Phys. Condens. Matter* **2013**, *25*, 026002.

[105] E. Riedel, *Allgemeine Und Anorganische Chemie*, De Gruyter, **2010**.

[106] N. Karaman, A. Bayri, S. Ekmekçi, *J. Phys. Conf. Ser.* **2016**, *667*, 012008.

[107] J. B. Goodenough, *Phys. Rev.* **1955**, *100*, 564–573.

[108] S. Mo, Y. Kurauchi, T. Katayama, Y. Hirose, T. Hasegawa, *J. Phys. Chem. C* **2019**, *123*, 25379–25384.

[109] C. Tassel, Y. Kuno, Y. Goto, T. Yamamoto, C. M. Brown, J. Hester, K. Fujita, M. Higashi, R. Abe, K. Tanaka, et al., *Angew. Chemie - Int. Ed.* **2015**, *54*, 516–521.

[110] K. Kobayashi, T. Kimura, H. Sawada, K. Terakura, Y. Tokura, *Nature* **1998**, *395*, 677–680.

[111] M. Yang, J. Oró-Solé, A. Kusmartseva, A. Fuertes, J. P. Attfield, J. P. Attfiel, *J. Am. Chem. Soc.* **2010**, *132*, 4822–4829.

[112] A. B. Jorge, J. Oró-Solé, A. M. Bea, N. Mufti, T. T. M. Palstra, J. A. Rodgers, J. P. Attfield, A. Fuertes, *J. Am. Chem. Soc.* **2008**, *130*, 12572–12573.

[113] Y.-I. Kim, M. Avdeev, *Dalt. Trans.* **2020**, *49*, 6471–6477.

[114] W. Li, A. Gurlo, R. Riedel, E. Ionescu, *Zeitschrift fur Anorg. und Allg. Chemie* **2015**, *641*, 1533–1539.

[115] M. Arnold, H. Wang, A. Feldhoff, *J. Memb. Sci.* **2007**, *293*, 44–52.

[116] H. Cheng, N. Zhang, X. Xiong, X. Lu, H. Zhao, S. Li, Z. Zhou, *ACS Sustain. Chem. Eng.* **2015**, *3*, 1982–1992.

[117] H. Wang, S. Werth, T. Schiestel, J. Caro, *Angew. Chemie - Int. Ed.* **2005**, *44*, 6906–6909.

[118] Z. Shao, S. M. Haile, *Nature* **2004**, *431*, 170–173.

[119] W. Zhu, W. Han, G. Xiong, W. Yang, *Catal. Today* **2005**, *104*, 149–153.

[120] C. Chen, S. Feng, S. Ran, D. Zhu, W. Liu, H. J. M. Bouwmeester, *Angew. Chemie* **2003**, *115*, 5354–5356.

[121] M. Reichmann, P. M. Geffroy, J. Fouletier, N. Richet, T. Chartier, *J. Power Sources* **2014**, *261*, 175–183.

[122] M. Reichmann, P. M. Geffroy, J. Fouletier, N. Richet, P. Del Gallo, T. Chartier, *J. Power Sources* **2015**,

277, 17–25.

[123] Y. Teraoka, T. Nobunaga, N. Yamazoe, *Chem. Lett.* **1988**, *17*, 503–506.

[124] R. Merkle, J. Maier, H. J. M. Bouwmeester, *Angew. Chemie - Int. Ed.* **2004**, *43*, 5069–5073.

[125] H. Li, X. Zhu, Y. Liu, W. Wang, W. Yang, *J. Memb. Sci.* **2014**, *462*, 170–177.

[126] E. Shelepova, A. Vedyagin, V. Sadykov, N. Mezentseva, Y. Fedorova, O. Smorygo, O. Klenov, I. Mishakov, *Catal. Today* **2016**, *268*, 103–110.

[127] C. Li, J. J. Chew, A. Mahmoud, S. Liu, J. Sunarso, *J. Memb. Sci.* **2018**, *567*, 228–260.

[128] K. Ueda, H. Kato, M. Kobayashi, M. Hara, M. Kakihana, *J. Mater. Chem. A* **2013**, *1*, 3667–3674.

[129] W. Si, D. Pergolesi, F. Haydous, A. Fluri, A. Wokaun, T. Lippert, *Phys. Chem. Chem. Phys.* **2017**, *19*, 656–662.

[130] L. Clark, J. Oró-Solé, K. S. Knight, A. Fuertes, J. P. Attfield, *Chem. Mater.* **2013**, *25*, 5004–5011.

[131] M. P. Pechini, *Method of Preparing Lead and Alkaline Earth Titanates and Niobates and Coating Method Using the Same to Form a Capacitor*, **1967**, 3,330,697.

[132] H. Lee, M. Hong, S. Bae, H. Lee, E. Park, K. Kim, *J. Mater. Chem.* **2003**, *13*, 2626–2632.

[133] M. Wang, R. Zuo, S. Qi, L. Liu, *J. Mater. Sci. Mater. Electron.* **2012**, *23*, 753–757.

[134] A. C. Pierre, *Introduction to Sol-Gel Processing*, Springer, **2020**.

[135] J. C. Brinker, G. W. Scherer, *Sol-Gel Science*, Academic Press Inc., **1990**.

[136] A. E. Danks, S. R. Hall, Z. Schnepp, *Mater. Horizons* **2016**, *3*, 91–112.

[137] M. L. Focarete, A. Tampieri, Eds. , *Core-Shell Nanostructures for Drug Delivery and Theranostics*, Woodhead Publishing Series In Biomaterials, **2018**.

[138] R. Marchand, Y. Laurent, J. Guyader, P. L'Haridon, P. Verdier, *J. Eur. Ceram. Soc.* **1991**, *8*, 197–213.

[139] E. Günther, R. Hagenmayer, M. Jansen, *Zeitschrift für Anorg. und Allg. Chemie* **2000**, *626*, 1519–1525.

[140] A. Hellwig, A. Hendry, *J. Mater. Sci.* **1994**, *29*, 4686–4693.

[141] D. Dirtu, L. Odochian, A. Pui, I. Humelnicu, *Cent. Eur. J. Chem.* **2006**, *4*, 666–673.

[142] A. H. White, W. Melville, *J. Am. Chem. Soc.* **1905**, *27*, 373–386.

[143] H. Jacobs, D. Schmidt, in *Curr. Top. Mater. Sci. - Vol. 8* (Ed.: E. Kaldis), North-Holland Publishing Company, **1982**, pp. 383–425.

[144] E. P. Perman, G. A. S. Atkinson, *Chem. News* **1904**, *July 8*, 13–17.

[145] Y. Il Kim, *Ceram. Int.* **2014**, *40*, 5275–5281.

6. Tailoring of an unusual oxidation state in a lanthanum tantalum(IV) oxynitride via precursor microstructure design

Cora Bubeck, Marc Widenmeyer, Gunther Richter, Mauro Coduri, Eberhard Goering, Songhak Yoon, and Anke Weidenkaff

Abstract

Perovskite-type oxynitrides hold great potential for optical applications due to their excellent visible light absorption properties. However, only a limited number of such oxynitrides with modulated physical properties is available to date and therefore alternative fabrication strategies are needed to be developed. Here, we introduce such an alternative strategy involving a precursor microstructure controlled ammonolysis. This leads to the perovskite family member $LaTa(IV)O_2N$ containing unusual Ta^{4+} cations. The adjusted precursor microstructures as well as the ammonia concentration are the key parameters to precisely control the oxidation state and O:N ratio in $LaTa(O,N)_3$. $LaTa(IV)O_2N$ has a bright red colour, an optical bandgap of 1.9 eV and a low (optically active) defect concentration. These unique characteristics make this material suitable for visible light-driven applications and the identified key parameters will set the terms for the targeted development of further promising perovskite family members.

6.1. Introduction

In spite of the growing interest in perovskite materials, the number of oxynitride members is still limited. Most oxynitrides contain metal cations in d^0 or d^{10} electronic configuration[1–8], whereas alternative materials with *B*-site cations in e.g. d^1 configuration such as Ta^{4+} are largely lacking. However, the latter could allow access to different electronic band structures, thus, expanding the applicability of perovskite-type oxynitrides in visible light-driven processes. The negligible number of known perovskite-type oxynitrides might be attributed to the reaction protocols normally used. Currently, the most widely used synthesis technique for this material class is the ammonolysis of oxides[9,10]. This procedure enables tuning of the electronic bandgap *via* (partial) substitution of oxygen by nitrogen[1]. Typically, the bandgap decreases, making the formed perovskite-type oxynitrides $AB(O,N)_3$ interesting for visible light-driven applications[1,4]. An important task in order to identify perovskite-type oxynitrides is the exact determination of the O:N ratio which often causes difficulties[11,12].

The precursors are often mixtures of crystalline binary oxides (e.g. La_2O_3 or Ta_2O_5)[3,4,13] or ternary oxides (e.g. $LaTaO_4$)[14,15], which are either prepared by solid state reactions (SSR) or *via* a Pechini method. The latter allows mild reaction conditions providing excellent product homogeneity[2]. In the case of $LaTa(V)ON_2$, most studies involve a high-temperature treatment of the oxide precursors prior to ammonolysis, leading to high crystallinity of the precursor[13,14,16,17]. The formation of several perovskite-type oxynitrides such as $LaTiO_2N$ and $SrTaO_2N$ from crystalline oxide precursors has been described by a topotactic reaction scheme[18]. In contrast, the reaction behaviour of amorphous/nanocrystalline oxide precursors is still unclear and the detailed ammonolysis mechanism has yet to be clarified[1]. A better understanding and control of essential reaction steps might help to develop new synthesis strategies. Furthermore, a target-oriented electronic configuration of the *B*-site cation and the precise adjustment of the O:N ratio in oxynitrides are the key factors to generate various interesting physical properties.

In this *in situ* and *ex situ* experimental study, we override the above-mentioned strong topotactic relation between oxide precursor and resulting $LaTa(O,N)_3$ formation through a considered selection of well-characterised oxide precursors with different microstructures and an adjusted ammonia concentration. Furthermore, we demonstrate the formation of the $LaTa(IV)O_2N$ utilising nanocrystalline lanthanum tantalum oxide (n-LTO), which exhibits smaller primary particles (nm-range) and a higher specific surface area than microcrystalline $LaTaO_4$ (m-$LaTaO_4$). This adjusted precursor microstructure leads to a favoured Ta reduction in n-LTO. In contrast, ammonolysis of larger primary particles in the µm-range (m-$LaTaO_4$) results in conventional $LaTa(V)ON_2$. Hence, we expand the experimental toolbox by an additional method to access further requested perovskite-type oxynitride family members.

6.2. Results

6.2.1. *In situ* ammonolysis of lanthanum tantalum oxides

First, the reaction steps of the $LaTaO_2N$ (Fig. 1) synthesis were investigated by *in situ* ammonolysis (10 vol% Ar in NH_3) using thermogravimetric analysis (TGA). For a better comparability, similar measurement conditions were selected for both *in situ* and *ex situ* ammonolysis (see below). Nanocrystalline lanthanum tantalum oxide (n-LTO) and microcrystalline $LaTaO_4$ (m-$LaTaO_4$) were synthesised as precursors in order to investigate the effect of the microstructure on the reaction behaviour (synthesis and characterisation details in Supplementary Note 1, Supplementary Fig. 1-5 and Supplementary Tables 1-4).

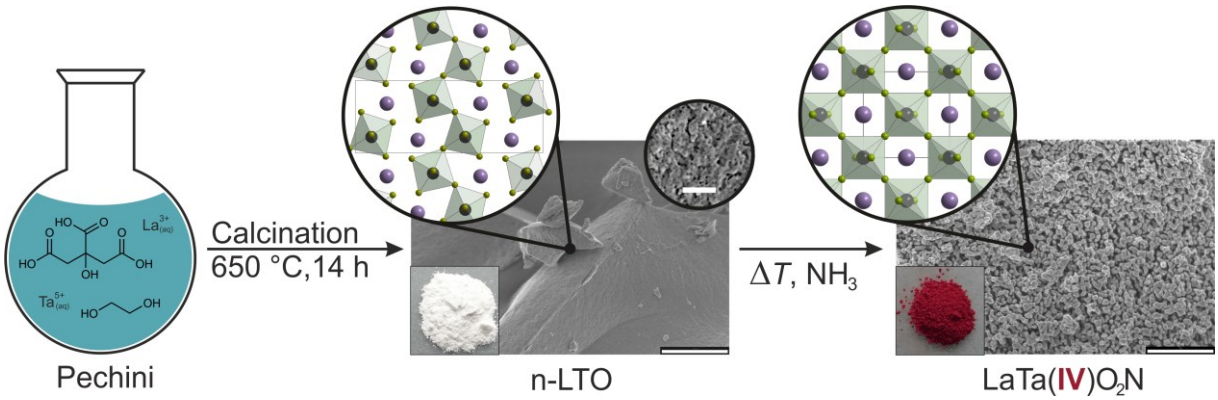

Figure 1. Schematic synthesis path of LaTa(IV)O_2N. Initially, a black xerogel is obtained by a Pechini method. A subsequent low temperature calcination leads to white, nanocrystalline lanthanum tantalum oxide (n-LTO). Finally, ammonolysis of the n-LTO under flowing ammonia at higher temperatures yields the desired bright red LaTa(IV)O_2N. Scalebar of the SEM images: 2 µm, Scalebar of the inset: 100 nm.

The TGA curve of n-LTO during *in situ* ammonolysis (Fig. 2) reveals several mass changes, the origin of which were determined by termination experiments. The initial mass change of -0.7 % in the range of 25 °C to 588 °C (region I) can be assigned to the desorption of residual water or organic contaminants, which is why the precursor remains white (Fig. 2). The subsequent larger mass change of -2.9 % (region II) is accompanied by a local mass minimum at 844 °C. At this temperature, the powder is black and the powder X-ray diffraction (PXRD) pattern shows the onset of crystallisation.

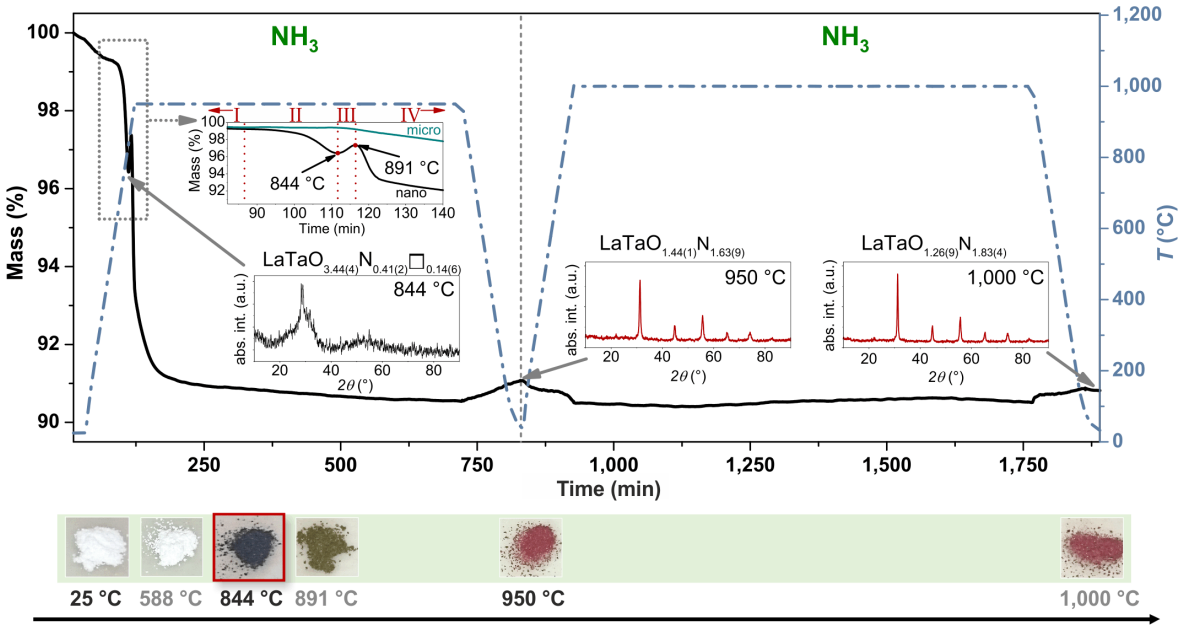

Figure 2. *In situ* TGA ammonolysis of nanocrystalline lanthanum tantalum oxide (n-LTO). *In situ* TGA of the ammonolysis (10 vol% Ar in NH_3) of n-LTO, including respective powder X-ray diffraction (PXRD) patterns and anionic compositions determined *via* hot gas extraction (HGE) after selected termination experiments. The illustrative coloured powders at specific temperatures complement the analysis. The reduction of tantalum at 844 °C is highlighted with a red frame. Additionally, the first four mass changes (region I – IV) during *in situ* ammonolysis of n-LTO are magnified in the inset. The *in situ* ammonolysis results of the microcrystalline $LaTaO_4$ (cyan curve (micro) in the same inset) can be found below.

In addition, hot gas extraction (HGE) reveals a composition of $LaTaO_{3.44(4)}N_{0.41(2)}\square_{0.14(6)}$ (product of the termination experiment at 844 °C) with an assumed ratio of La:Ta:O = 1:1:4 (HGE results are listed in Supplementary Table 5). Therefore, region II (between 588 °C and 844 °C) is characterised by an oxygen vacancy formation with simultaneous nitrogen incorporation. According to literature[19], $LaTaO_4$ crystallises in space group $A2_1am$ up to around 800 °C and exhibits octahedron chains with corresponding interspace (Fig. 1). Therefore, we assume that vacancy formation and nitrogen incorporation takes place in this interspatial region.

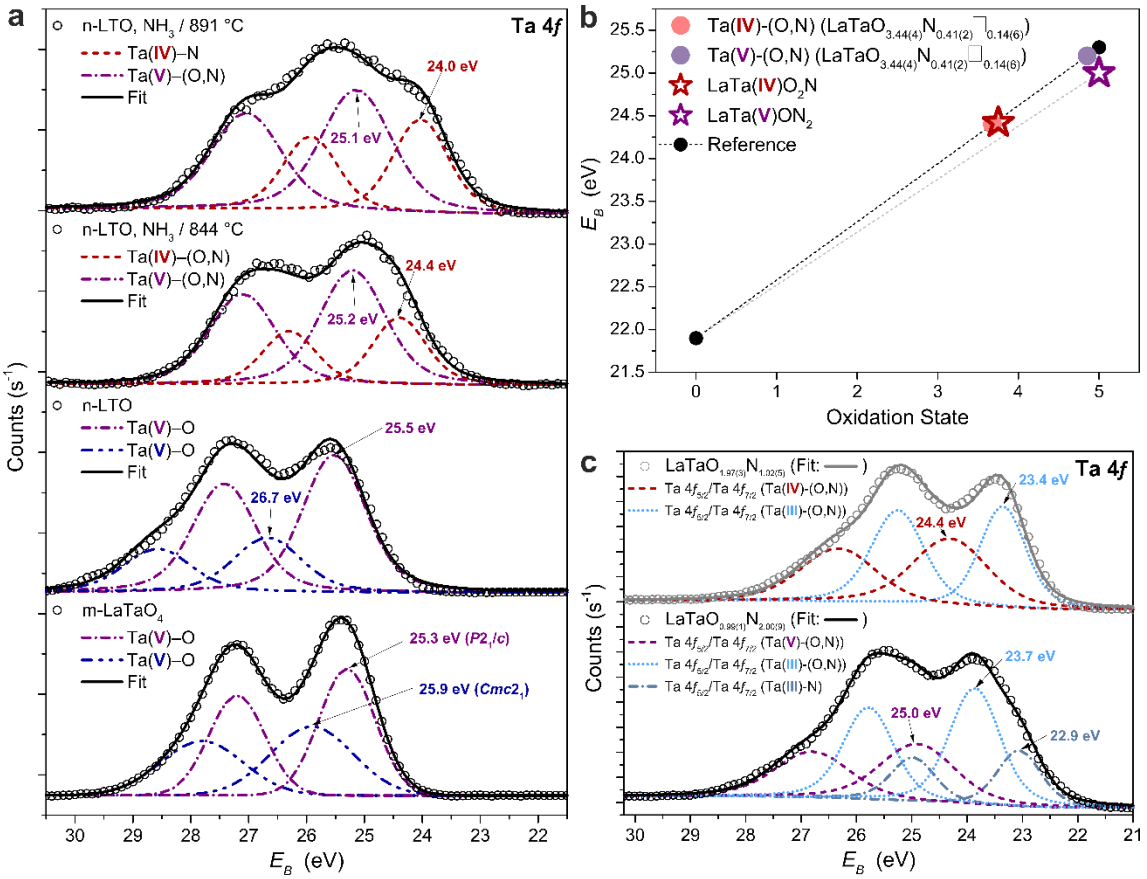

Figure 3. XPS spectra in the Ta 4*f* region and point charge model. a, XPS spectra in the Ta 4*f* region of the intermediates obtained by termination of the *in situ* ammonolysis at 844 °C and 891 °C, as well as of n-LTO and m-$LaTaO_4$ (measurement data: open black circles and solid black line: overall fit). The Ta $4f_{7/2}$ peaks are marked with their respective fitted binding energy and, in case of m-$LaTaO_4$, additionally with the respective space group of the polymorph (cf. SI) **b**, Applied point charge model[20,21] in the Ta 4*f* region of $LaTaO_{3.44(4)}N_{0.41(2)}\square_{0.14(6)}$ (*in situ*), $LaTaO_2N$ (*ex situ*) and $LaTaON_2$ (*ex situ*). The Ta(V)–O binding character of m-$LaTaO_4$ ($P2_1/c$) was used as reference for Ta^{5+}. The black dots represent the reference binding energies of Ta(0) [22] and Ta(V) (measured) connected by the black dashed line. The grey dashed line represents the shifted Ta^{5+} binding energy (from 25.3 eV to 25.0 eV because of N substitution) of $LaTaON_2$ (*ex situ*). **c**, XPS spectra in the Ta 4*f* region of $LaTaO_2N$ and $LaTaON_2$ with the respective fitted binding energies and corresponding binding characters. The open circles represent the measurement data, the solid lines show the overall fit and the dashed lines the fitting results of the respective Ta 4*f* orbitals.

At the same time, the colour-change of the powder from white to black indicates a reduction of the contained Ta. As can be shown by X-ray photoelectron spectroscopy (XPS) (Fig.3), heating to 844 °C in ammonia atmosphere causes the two existing Ta(V)–O binding characters in n-LTO (Fig. 3a, n-LTO) to change their character. The evaluation of the Ta(V)–O binding characters in n-LTO and m-$LaTaO_4$ is described in the Supplementary Note 4. The two new binding energies of the Ta $4f_{7/2}$ orbitals in

$LaTaO_{3.44(4)}N_{0.41(2)}\square_{0.14(6)}$ of E_B (Ta $4f_{7/2}$) = 25.2 eV and E_B(Ta $4f_{7/2}$) = 24.4 eV, respectively, can be derived from the applied peak fittings (Fig. 3a, n-LTO, NH_3/ 844 °C).

Calculations using the equations estimated by Nordling[21] (Supplementary Note 5) suggest that substitution of oxygen with nitrogen at persisting Ta^{5+} causes a chemical shift of 0.3 eV to lower binding energies. The *in situ* observed conversion of n-LTO to $LaTaO_{3.44(4)}N_{0.41(2)}\square_{0.14(6)}$ between 588 °C and 844 °C is accompanied by a Ta $4f_{7/2}$ binding energy shift from 25.5 eV to 25.2 eV for Ta(V)–O by nitrogen incorporation. Therefore, the binding energy E_B(Ta $4f_{7/2}$) = 25.2 eV can be allocated to a Ta(V)–(O,N) binding character since the original binding energy lowers by the expected ΔE_B = 0.3 eV. The other Ta $4f_{7/2}$ binding energy of Ta(V)–O, however, shifts from 26.7 eV in n-LTO to 24.4 eV in $LaTaO_{3.44(4)}N_{0.41(2)}\square_{0.14(6)}$, the difference being much higher than ΔE_B = 0.3 eV. This might be explained by a change of the Ta oxidation state in addition to nitrogen substitution. Therefore, the binding energy at E_B(Ta $4f_{7/2}$) = 24.4 eV can be assigned to a Ta(IV)–(O,N) binding character. The Ta(IV)–(O,N) binding character can be determined by applying the point charge model[20,21] assuming that the atomic potential of Ta remains unaffected by a change of the oxidation state. Ta(0) at E_B(Ta $4f_{7/2}$) = 21.9 eV[22] and Ta(V) at E_B(Ta $4f_{7/2}$) = 25.3 eV in m-$LaTaO_4$ ($P2_1/c$) (instead of E_B(Ta $4f_{7/2}$) = 25.9 eV in m-$LaTaO_4$ ($Cmc2_1$)) were selected as references (Fig. 3b). The selection of the Ta(V) binding energy was based on the similar interatomic distances in and between the $[Ta^{V}O_6]^{7-}$ octahedron together with the amount of neighbouring ions of Ta compared to the respective oxynitride ($[Ta(O,N)_6]^{z-}$ octahedron). Thus, due to the linear relationship between the oxidation state and the binding energy in the point charge model, a Ta oxidation state of 4+ (d^1 electronic configuration) at E_B(Ta $4f_{7/2}$) = 24.4 eV was determined (Fig. 3b).

A further mass change of +1.0 % occurs in the temperature range of 844 °C to 891 °C (region III). Simultaneously, the colour of the powder changes from black to ochre. The weight fractions at 891 °C determined by HGE amount to 13.7 wt% O and 6.7 wt% N (compared to 14.4 wt% O and 1.5 wt% N at 844 °C). However, the total mass increase due to the strong nitrogen enrichment accompanied by only a small oxygen loss cannot be explained by a simple refill of the previously generated oxygen vacancies in "$LaTaO_4$", since the total anionic weight fraction substantially exceeds the calculated maximum value of 16.7 wt% for "$LaTaO_4$" (Supplementary Table 5). Evaluation of the respective powder pattern shows that the ochre-coloured phase is not fully crystallised (Supplementary Note 6 and Supplementary Fig. 6) suggesting the formation of a nitrogen-rich intermediate (proposed composition: $LaTa(O,N,\square)_4:(N_2)_y$). Such intermediates are well-known from reoxidation experiments of several other oxynitrides including $LaTiO_2N$[23]. The XPS measurement (Fig. 3a, n-LTO, NH_3/ 891 °C) again reveals a chemical shift of the Ta $4f_{7/2}$ binding energy from 24.4 eV (Ta(IV)–(O,N)) to 24.0 eV (Ta(IV)–N). This indicates an increased nitrogen content in the chemical environment of Ta and, hence, in the whole sample. The other Ta(V)–(O,N) binding character at E_B(Ta $4f_{7/2}$) = 25.1 eV (previously 25.2 eV) remains unchanged. A further temperature increase to 950 °C (region IV) leads to an abrupt mass change of -6.9 %. During the following 10 h ammonolysis prior to cooling to 25 °C the mass remains near-constant. The respective termination experiment indicates a colour change from ochre to red after the 10 h ammonolysis. HGE of the red phase reveals a composition of $LaTaO_{1.44(1)}N_{1.63(9)}$. This phase is further transformed to red $LaTaO_{1.26(9)}N_{1.83(4)}$ by a second heating cycle under ammonia at 1000 °C for 14 h. Such intermediate compositions during the synthesis of $LaTa(O,N)_3$ are often reported in literature when large amounts of oxide precursors are used or the applied precursor has been crystallised at around 1000 °C before the ammonolysis[24]. Additionally, a large sample amount can cause inhomogeneous exposure to the reducing species during ammonolysis. The positive and negative mass changes observed during the heating and cooling steps seem to be caused by desorption and adsorption of gaseous species (e.g. H_2O and/or NH_3). The nitrogen content of both red phases falls short of that of $LaTaON_2$, revealing that n-LTO is susceptible to the reduction of tantalum (Ta^{5+} to Ta^{4+}). The usage of m-$LaTaO_4$ as a precursor for *in situ* ammonolysis results in $LaTaON_2$, neither involving intermediate phases nor reduction of Ta(V) to Ta(IV) (no black powder indicating a reduction).

Instead, the initial formation of oxygen vacancies (yellow $LaTaO_{3.87(7)}\square_{0.12(3)}$) is followed by a one-step mass change of -5.5 % (onset at 820 °C) indicating the conversion to $LaTaON_2$ (Fig. 4).

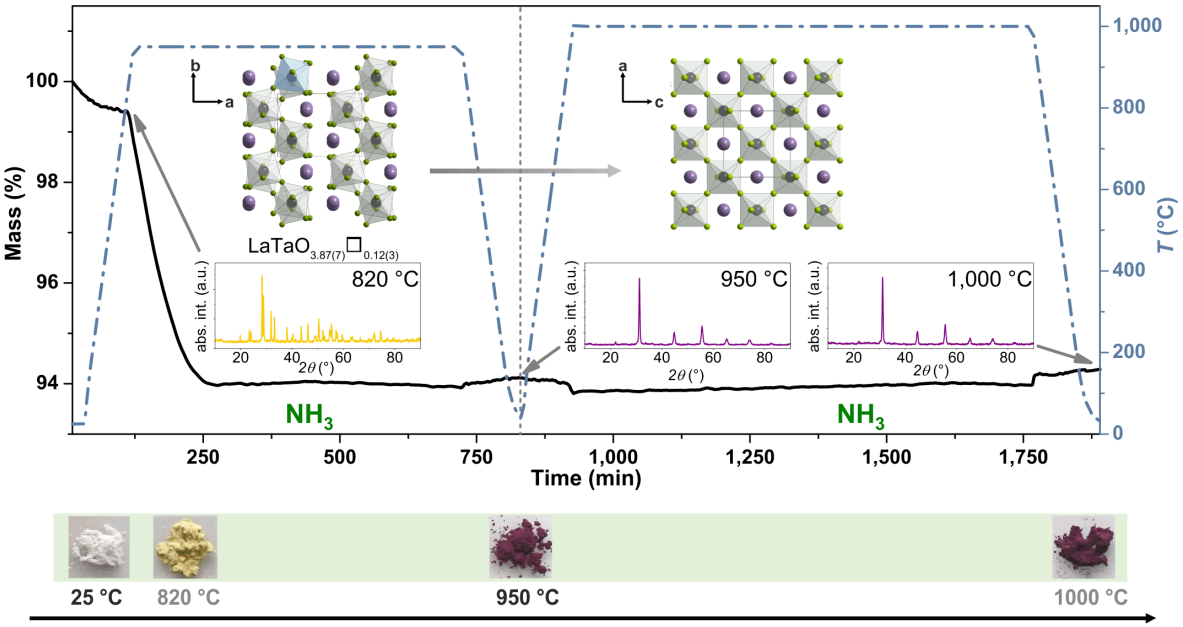

Figure 4. *In situ* TGA ammonolysis of m-$LaTaO_4$. *In situ* ammonolysis (10 vol% Ar in NH_3) of m-$LaTaO_4$. The insets show PXRD patterns at selected termination points and the anionic composition of the product received by termination at 820 °C determined by HGE. The coloured powders of the termination experiments are shown beneath the respective measuring point. The strong topotactic relation between m-$LaTaO_4$ and $LaTaON_2$ is represented by the respectively orientated sections of the crystal structures.

To be more precise, the *in situ* ammonolysis of m-$LaTaO_4$ starts with a mass change of –0.5 % between 25 °C and 820 °C (Fig.4). According to the PXRD results of termination products, the crystal structure of m-$LaTaO_4$ remained unchanged in this temperature range. However, a colour change from white (25 °C) to yellow (820 °C) indicated a change of the chemical composition including oxygen vacancy formation, which was confirmed *via* hot gas extraction (Supplementary Table 5). Further heating to 950 °C led to a change of the powder colour from yellow to purple accompanied by a massive mass change of -5.5 %. The detected mass change is in accordance with the expected mass change of $\Delta m_{calc.}$ = -5.2 % calculated for the formation of $LaTaON_2$ from $LaTaO_4$. Termination experiments at 820 °C and at 950 °C together with hot gas extraction measurements revealed the conversion of microcrystalline $LaTaO_4$ to $LaTaON_2$ above 820 °C by nitrogen incorporation. An isothermal step with a near-constant mass was followed by a second ammonolysis cycle at 1000 °C for 14 h. The PXRD pattern of the final product clearly showed the presence of a perovskite-type phase (insets, Fig.4). The mass changes during these heating and cooling steps might be attributed to the reversible adsorption and desorption of ammonia and water molecules as previously mentioned for n-LTO. We assume that a strong topotactical relation between crystalline ABO_4 and crystalline $ABON_2$ often described in literature[18] also applies to the transformation of m-$LaTaO_4$ to $LaTaON_2$. Based on this assumption, the octahedron chains of defective m-$LaTa(O,\square)_4$ shown in Figure 4 are supposed to create a pattern similar to $LaTaON_2$ by rotating around the *c*-axis. During oxygen vacancy formation and subsequent nitrogen incorporation they connect to the neighbouring chains in a “zipper-type” manner[18]. However, the microstructure of n-LTO is different and exhibits therewith a “soft” topotactic relation to the resulting oxynitride along the interspace of the octahedron chains (Fig.1) inducing a faster reduction of Ta(V) to Ta(IV). Afterwards, a “soft” topotactic reaction with a simultaneous “zipper-type” octahedral connection[18] enables the afore mentioned filling of oxygen vacancies by nitrogen.

The lower nitrogen content of $LaTa(O,N)_3$ in comparison to $LaTaON_2$ when using n-LTO for *in situ* ammonolysis can be explained by the specific surface area and the primary particle size and, thus, the microstructure of the oxide precursors. The specific surface area of n-LTO is S_{BET} = 7 m^2/g (primary particle size: nm-range) and that of m-$LaTaO_4$ S_{BET} = 2 m^2/g (primary particle size: µm-range). Further details about the oxide precursors can be found in Supplementary Note 1. The higher surface area and the smaller primary particle size of the nanocrystalline precursor compared to m-$LaTaO_4$ makes it more susceptible to Ta reduction, since the diffusion of reducing agents is simplified (at higher temperatures NH_3 decomposes into nitrogen- and hydrogen-containing species and molecular hydrogen[9]. A detailed explanation of the interaction of the reducing species with n-LTO can be found in the Supplementary Note 7: Reduction of Ta. This is confirmed by the finding that *in situ* ammonolysis of n-LTO that has been previously converted to m-$LaTaO_4$ also leads to $LaTaON_2$ (Fig. 5and Supplementary Note 2).

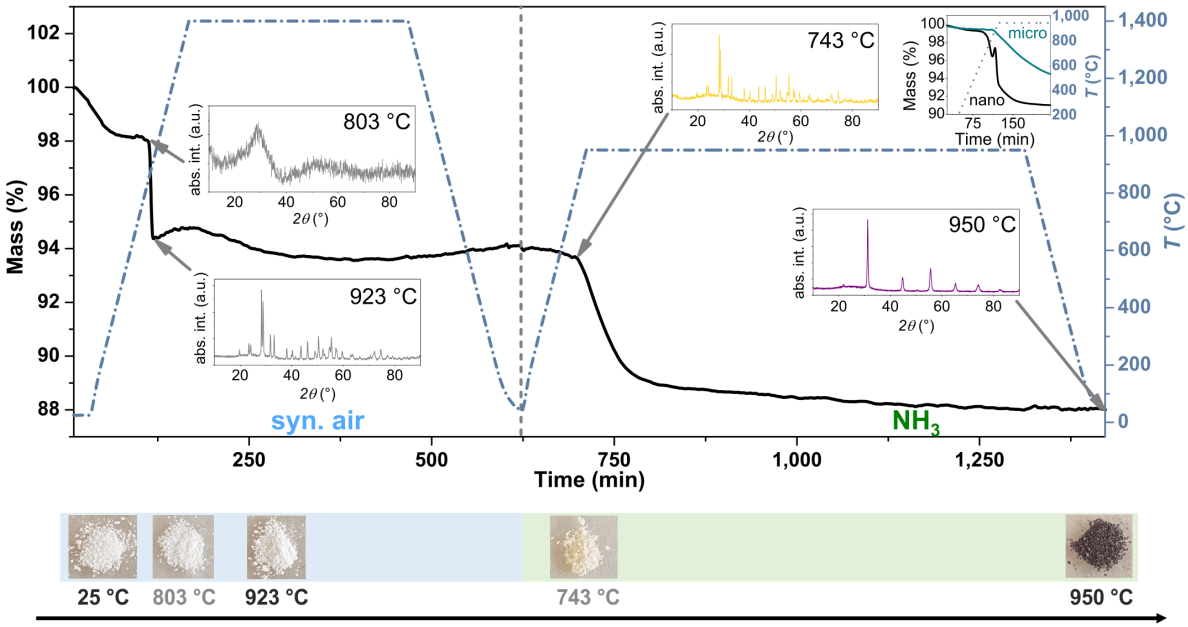

Figure5. Conversion of n-LTO to m-$LaTaO_4$ and subsequent *in situ* TGA ammonolysis to $LaTaON_2$. The first mass change of –1.8 % is caused by desorption of water. The second negative mass change between 803 °C and 923 °C is due to pyrolysis of organic residues from the preceded soft chemistry synthesis. Thermogravimetric measurements coupled with mass spectrometry (TGA-MS) revealed the release of CO_2, NO_2 and organic fragments. The measurement results are displayed in Supplementary Figure 4 and discussed in Supplementary Note 3. The measurement was first carried out in synthetic (syn.) air prior to the ammonolysis step.

Moreover, scanning electron microscopy (SEM) images of the termination products of the annealing process of n-LTO in air prior to *in situ* ammonolysis (Fig. 6a) show a continuous microstructural change with increasing temperature leading to a morphology very similar to m-$LaTaO_4$ (Fig. 6c). In parallel, the onset temperature of the ammonolysis reaction steadily increases from 588 °C to 820 °C with increasing primary particle size and crystallinity (n-LTO to m-$LaTaO_4$, Fig.2, Fig. 5and Fig.6). Hence, a well-designed microstructure allows to enable or supress significant Ta reduction.

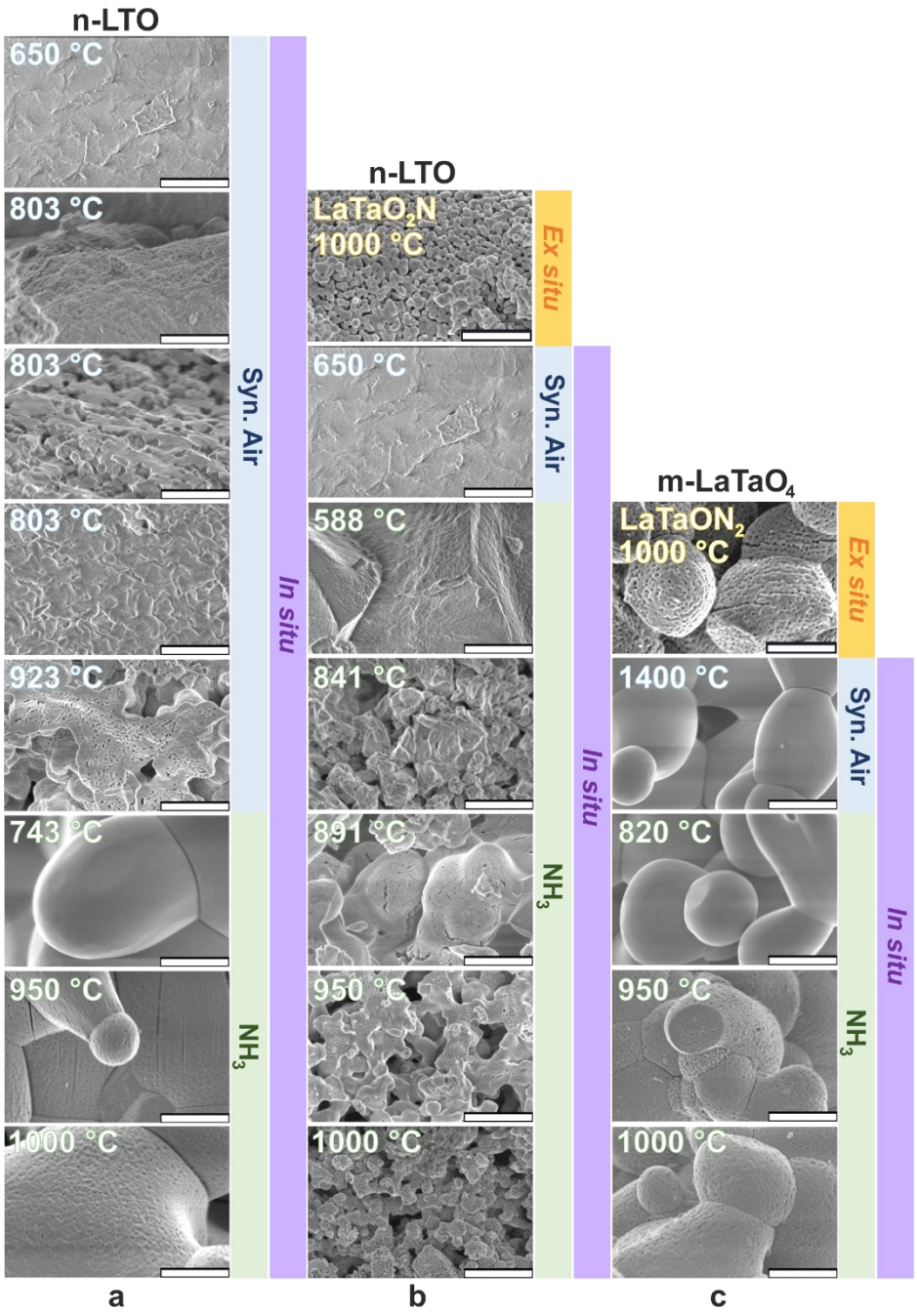

Figure6. SEM images of the termination products of all *in situ* ammonolysis studies. a, Precursor conversion from n-LTO to m-$LaTaO_4$ in synthetic (syn.) air prior to ammonolysis. **b**, SEM images of the termination products of *in situ* ammonolysis of n-LTO and **c**, SEM images of the *in situ* ammonolysis of m-$LaTaO_4$. The temperatures mark the termination temperature at which the products were observed. Scalebar of the SEM images: 1 µm.

6.2.2. *Ex situ* ammonolysis of lanthanum tantalum oxides

Eventually, *in situ* ammonolysis of n-LTO did not deliver $LaTaO_2N$ which might be attributed to the less reductive atmosphere caused by the 10 vol% Ar in NH_3 needed to protect the device. The application of nearly 100 vol% instead of 90 vol% NH_3 in a classical thermal gas flow ammonolysis setup turned the *in situ* into an *ex situ* ammonolysis. The *ex situ* ammonolysis only slightly differs from the *in situ* setup with respect to the sample environment. Using the same temperature profile as in the *in situ*

ammonolysis and an NH_3 flow rate of 300 mL/min we finally converted n-LTO into bright red $LaTaO_{1.98(7)}N_{0.98(5)}$ (S_{BET} = 25 m^2/g) after 10 h at 950 °C *via ex situ* ammonolysis (anionic composition obtained by HGE, Supplementary Table 6). However, when using the microcrystalline instead of the nanocrystalline precursor for *ex situ* ammonolysis with the same temperature profile and ammonia flow as in *in situ* ammonolysis, purple-coloured $LaTaO_{1.05(3)}N_{2.02(3)}$ is obtained (very similar to the *in situ* ammonolysis product). This indicates a very similar parameter selection in *ex situ* and *in situ* ammonolysis. Considering the results of all *in situ* and *ex situ* ammonolysis experiments, we have identified the reduction sensitivity due to microstructural differences and the ammonia concentration as main parameters to adjust the O:N ratio in $LaTa(O,N)_3$.

The aforementioned red $LaTaO_{1.98(7)}N_{0.98(5)}$ and the purple $LaTaO_{1.05(3)}N_{2.02(3)}$ phases prepared by *ex situ* ammonolysis are subjected to a second *ex situ* ammonolysis cycle (same temperature profile as in *in situ* ammonolysis) with KCl flux addition in order to heal possible defects[25]. After the second cycle the compositions slightly change to a bright red $LaTaO_{1.97(3)}N_{1.02(5)}$ (S_{BET} = 8 m^2/g) and to purple $LaTaO_{0.99(1)}N_{2.00(9)}$ (S_{BET} = 3 m^2/g), respectively. $LaTaO_{1.97(3)}N_{1.02(5)}$ ($LaTaO_2N$) reveals less vacancies compared to $LaTaO_{1.98(7)}N_{0.98(5)}$ (obtained from first cycle) indicating a defect healing effect *via* KCl flux. Additionally, a reoxidation study (Supplementary Note 8, Supplementary Fig. 7 and Supplementary Table 7) validated the formation of $LaTaO_2N$.

XPS measurements of $LaTaO_{1.97(3)}N_{1.02(5)}$ and $LaTaO_{0.99(1)}N_{2.00(9)}$ obtained by *ex situ* ammonolysis (Fig. 3c, survey spectra cf. Supplementary Note 9, Supplementary Fig. 8) show significant differences of the Ta oxidation states between both compounds. The data reveal a Ta(IV)–(O,N) binding character with a certain amount of Ta(III)–(O,N) in $LaTaO_{1.97(3)}N_{1.02(5)}$ and a Ta(V)–(O,N) and a Ta(III)–(O,N) binding character in $LaTaO_{0.99(1)}N_{2.00(9)}$ (Fig. 3b and Supplementary Table 8). Since the binding energy at E_B(Ta $4f_{7/2}$) = 24.4 eV in $LaTaO_{1.97(3)}N_{1.02(5)}$ corresponds to that in $LaTaO_{3.44(4)}N_{0.41(2)}\square_{0.14(6)}$, the same binding character due to a similar chemical environment ($[Ta(O,N)_6]^{z-}$ octahedron) can be assumed. However, the fitted binding energy E_B(Ta $4f_{7/2}$) = 25.0 eV in $LaTaO_{0.99(1)}N_{2.00(9)}$ reveals a Ta(V)–(O,N) binding character which can be explained by a simple chemical shift of 0.3 eV to lower binding energies due to nitrogen substitution (m-$LaTaO_4$, E_B(Ta $4f_{7/2}$) = 25.3 eV ($P2_1/c$)). The Ta(III)–(O,N) binding character is the result of the reducing conditions during ammonolysis favouring the reduction of Ta on the surface compared to the bulk. XPS is highly surface-sensitive owing to the small mean free path of photo-emitted electrons.[26] Therefore, the concentrations of Ta(IV)–(O,N) and Ta(V)–(O,N) in the bulk are assumed to be higher than on the surface. The Ta(III)–N binding character in $LaTaO_{0.99(1)}N_{2.00(9)}$ at E_B(Ta $4f_{7/2}$) = 22.9 eV is attributed to the secondary phase TaN since the reference binding energy of this nitride is E_B(Ta $4f_{7/2}$) = 23.0 eV[27]. Additionally, XPS measurements of $LaTaO_2N$ ($LaTaO_{1.97(3)}N_{1.02(5)}$) also confirmed the absence of Ta^{5+} (observed, however, in $LaTaON_2$ ($LaTaO_{0.99(1)}N_{2.00(9)}$) eliminating the possibility of a 1:1 mixture of Ta^{3+} and Ta^{5+} in $LaTaO_2N$.

Investigations of the magnetic properties of $LaTaO_2N$ and $LaTaON_2$ by superconducting quantum interference device (SQUID) measurements were carried out in order to confirm the presence of Ta^{4+} although challenging due to the presence of magnetic impurities such as Ta^{3+} as observed from XPS analysis (Figure 3) and the in general limited knowledge about the magnetism of 5*d* transition metal compounds (compared to their 3*d* counterparts)[28,29]. The respective zero field cooled (ZFC) curves at 500 Oe down to 2 K are shown in Supplementary Note 10 and Supplementary Fig. 9. The low temperature regions (below ~70 K) can be described by a paramagnetic Curie-Weiss-like behaviour with very small effective moments (1.3×10^{-4} μ_B/Ta at 2 K for the $LaTaO_2N$ sample and 9.8×10^{-5} μ_B/Ta for the $LaTaON_2$ sample, respectively) pointing to an activation of magnetic impurity states rather than an intrinsic materials property. The effective magnetic moment is further drastically reduced at increasing temperature. Overall the observed magnetisation is much lower than 1 μ_B/Ta as expected from the simplest paramagnetic model. The small magnetic moment and the fact that Ta is a 5*d* element suggests that the largely extended 5*d* orbitals in $LaTaO_2N$ are strongly hybridised and overlapping with

the O/N 2*p* orbitals[30] leading to weakly localised electrons hampering the up-built of a significant magnetisation. It is well-known for 3*d* transition metal containing perovskites ABO_3 and ABF_3 that with decreasing electronegativity of the anion the hybridisation (or in other words the covalency of the *B*–*X* bond) is enhanced resulting in the aforementioned stronger delocalisation of the electrons and hence the spin[30]. We believe the same is valid for 5*d* transition metal containing perovskites. Besides, two further factors could contribute diminishing the effective magnetic moment: i) the spin-orbit coupling being expected to be much stronger in 5*d* than in 3*d* materials, ii) the experimentally observed presence of stretched octahedra (Supplementary Note 11 and Supplementary Table 9e) results in a splitting of the initially degenerated t_{2g} levels. This splitting leads to the formation of four-fold degenerated $5d_{xz}$ and $5d_{yz}$ states lower in energy than the initial state only occupied by one electron, making it difficult to develop magnetic ordering[31].

Phase purity of $LaTaO_2N$ is proven by high resolution (HR)-PXRD. $LaTaON_2$ has already been reported in the space groups *Imma* and *C*2/*m*[17,3132] and both are considered for $LaTaO_2N$ as well. Since we have observed no clear evidence for a monoclinic distortion and the *Imma* space group gives a slightly lower χ^2 residual than *C*2/*m,* we propose *Imma* as space group for $LaTaO_2N$. The same applies to $LaTaON_2$ (Supplementary Fig. 10 and Supplementary Table 9 for complete crystal structure analysis). The unit cell volumes of $LaTaO_2N$ (V_{cell} = 264.78(3) Å^3) and $LaTaON_2$ (V_{cell} = 264.68(2) Å^3) are very similar. The slightly larger unit cell of $LaTaO_2N$ can be explained by the increase of the effective ionic radius of Ta from 0.64 Å (Ta^{5+})[34] to 0.68 Å (Ta^{4+})[34] after ammonolysis. This expansion is mostly compensated by the different O:N ratio. The partial replacement of the larger nitrogen (1.46 Å)[34] by the smaller oxygen (1.40 Å)[34] leads to a contraction of the unit cell. Furthermore, $LaTaO_2N$ is phase pure, while in $LaTaON_2$ a small amount of Ta_3N_5 (*Cmcm*) was detected through HR-PXRD (Supplementary Fig. 10b and Supplementary Table 9d). Since XPS reveals TaN on the surface and HR-PXRD Ta_3N_5 in the bulk, a nitrogen gradient combined with a decreased susceptibility for the reduction of Ta (from Ta^{5+} to Ta^{3+}) can be assumed. However, TaN can also be amorphous or the amount below the HR-PXRD detection limit.

Scanning electron microscopy gives insight into the morphology of the oxynitrides synthesised by *ex situ* ammonolysis. $LaTaO_2N$ shows primary particles in the nm-range, while $LaTaON_2$ exhibits porous and sintered particles in the µm-range (Fig. 7a).

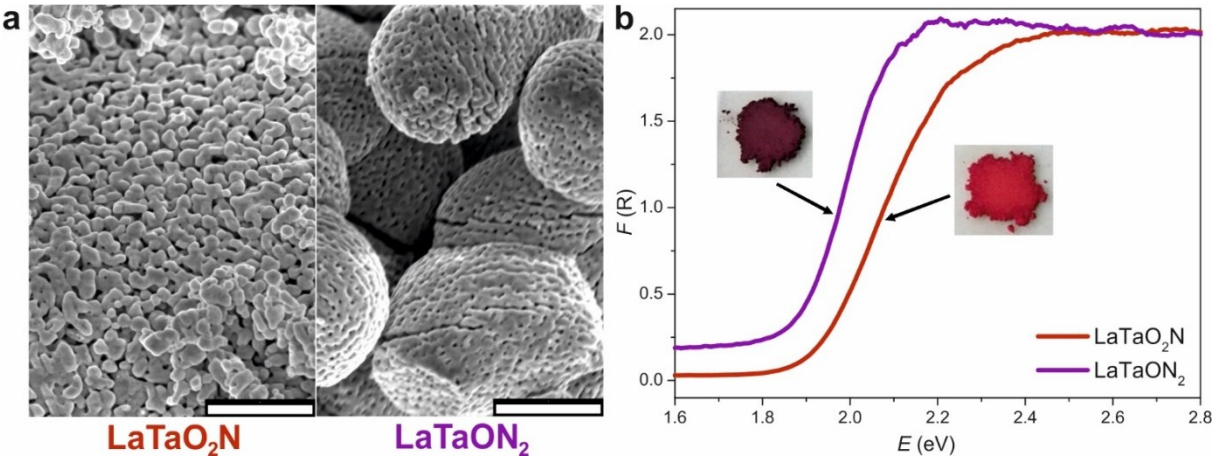

Figure7. SEM images and Kubelka-Munk curves of *ex situ*-prepared $LaTaO_2N$ and $LaTaON_2$. a, SEM images of $LaTaO_2N$ and $LaTaON_2$ show the different morphologies of the materials in the µm-range. Scalebar of the SEM images: 1 µm. **b**, Kubelka-Munk curves of $LaTaO_2N$ and $LaTaON_2$ together with the respective powder images. The bright red colour indicates a much lower optically active defect concentration compared to $LaTaON_2$.

In addition to the determination of the specific surface area (Supplementary Table 10), an increased pore formation in $LaTaON_2$ during ammonolysis can also be confirmed by comparing the SEM images of the oxide with its respective oxynitride. Furthermore, the particle size increases during ammonolysis of n-LTO, whereas using m-$LaTaO_4$ the particle size remains constant (Fig. 6c). The respective SEM images of the oxides can be found in the SI (Supplementary Fig. 2c).

As the colours of the obtained oxynitrides differ from each other, diffuse reflectance spectroscopy (DRS) measurements were performed. The data - converted to Kubelka-Munk[35] curves (Fig. 7b) - show a difference of ΔE_g = 0.1 eV between the optical bandgaps of the $LaTaO_2N$ (1.9 eV) and $LaTaON_2$ (1.8 eV). Detailed investigation shows that the Kubelka-Munk curve of $LaTaO_2N$ converges to zero in contrast to that of $LaTaON_2$, indicating a much lower optically active defect concentration. In addition, after the optical bandgap of E_g = 1.8 eV an intensity increase as observed for $LaTiO_2N$[36], which exhibited undesired defects was not detected for $LaTaO_2N$. $LaTaO_2N$ possess an unusual colour (bright red), which has been expected to be darker (bluish[37]) due to the reduction of Ta^{5+} to Ta^{4+}. Additionally, the larger optical bandgap of $LaTa(IV)O_2N$ compared to $LaTa(V)ON_2$ is noticeable. Based on both observations, we assume a larger crystal field splitting for $LaTaO_2N$ caused by the d^1 state of Ta^{4+}, since Ta is coordinated in a distorted octahedral environment (Jahn-Teller effect[31]) indicated by bond length analysis *via* Rietveld refinements. Specific visible light-driven applications require materials with appropriate defect concentrations[38–40] and suitable bandgaps[41–43]. Therefore, $LaTaO_2N$ could be an interesting candidate for further investigations in this application field.

6.3. Discussion

In this *in situ* and *ex situ* ammonolysis study the key parameters to tailor the oxidation state and to synthesise a perovskite family member $LaTa(IV)O_2N$ containing unusual Ta^{4+} were identified. The oxynitride has an optical bandgap of 1.9 eV, a bright red colour, and a low optically active defect concentration providing promising physical properties for light-driven applications. The formation of $LaTa(IV)O_2N$ is boosted by the oxide precursor's microstructure (primary particle size, specific surface area and crystallinity) and the ammonia concentration (nearly 100 %). In previous studies, the ammonolysis mechanism was already investigated and mostly clarified for the topotactic case. The findings shown here make a substantial contribution to the elucidation of the ammonolysis mechanism in general and to that of amorphous/nanocrystalline oxide precursors in particular. This opens up new perspectives and possibilities for the synthesis of further perovskite-type oxynitrides.

6.4. Methods

6.4.1. Synthesis of $LaTaO_2N$ and $LaTaON_2$

The oxynitrides $LaTaO_2N$ and $LaTaON_2$ were prepared from the respective nanocrystalline and microcrystalline oxide precursors (cf. Supplementary Methods) *via* thermal ammonolysis (synthesis of the respective oxides is described in the SI). The precursor oxides (200 mg) were transferred to an alumina boat and ammonolysed at 950 °C for 10 h with a NH_3 gas flow rate of 300 mL/min (Westfalen AG, > 99.98 %). A second ammonolysis step together with KCl flux (Roth, ≥ 99 %, Ph. Eur.) was carried out in a 1:1 weight ratio of sample and flux at 1000 °C for 14 h.

6.4.2. Sample Characterisation

In order to clarify the phase purity and crystal structure of the produced oxides and oxynitrides, powder X-ray diffraction (PXRD) measurements were carried out on a Rigaku Smartlab powder X-ray diffractometer using Cu-$K\alpha_{12}$ radiation. To avoid a contribution of Cu-K_β radiation a thin nickel foil as filter was used (efficiency is approx. 90 %). The continuous scan covered an angular range of $10° \leq 2\theta \leq 90°$ with an angular step interval of 0.025°. For selected oxide and oxynitride samples additional high-resolution synchrotron radiation PXRD measurements were performed at the beam line ID22 of the European Synchrotron Radiation Facility (ESRF) in Grenoble, France. The powders were filled into 0.7 mm diameter Kapton® capillaries (wavelength, see specific refinements). The collected diffraction data were evaluated *via* Rietveld refinements[44,45] using *FullProf.* 2k[46]. A pseudo-Voigt function was selected to describe the reflection profile and the background was linearly interpolated between a set of background points with refinable heights. The anionic composition of the oxynitrides were fixed according to the respective compositions determined by HGE because the virtually equal form factors make it impossible to discriminate between O^{2-} and N^{3-} by means of X-rays. O and N were statistically assigned to the two independent crystallographic sites.

The chemical composition of the produced samples was investigated *via* inductively coupled plasma optical emission spectroscopy (ICP-OES) using a Spectro Ciros CCD ICP-OES instrument for cations and hot gas extraction technique (HGE) using an Eltra ONH-2000 analyser for the anions.

The investigation of oxynitride formation from nanocrystalline and microcrystalline oxides and the reverse reaction of $LaTaO_2N$ to the corresponding oxide was performed by thermogravimetric analysis (TGA) using a Netzsch STA 449 F3 Jupiter. *In situ* ammonolysis experiments were carried out under flowing NH_3 (80 mL/min NH_3 + 8 mL/min Ar) on alumina plates with a heating rate of 10 °C/min up to 1000 °C. To protect the TGA device from corrosion the measurements were performed in 10 vol% Ar in NH_3. A fast cooling rate of 40 °C/min was used to successfully quench the intermediates since the mass changes observed by TGA and HGE were in good agreement. Reoxidation was carried out on an alumina plate under flowing synthetic air (20.5 vol% O_2 in N_2, Westfalen AG, 50 mL/min) to study the anionic composition of $LaTaO_2N$. The sample was first heated up to 200 °C and maintained at this temperature for half an hour to remove surface adsorbed water. Thereafter, heating was continued up to 1400 °C at a heating rate of 10 °C/min. The temperature was maintained for 2 h in order to achieve full conversion of oxynitride to respective single-phase oxide. TGA-MS to determine possible organic residues in n-LTO was carried out with a Netzsch STA 449C F3 Jupiter coupled with a GAM 200 (InProcess Instruments) mass spectrometer. The oxide was heated to 1200 °C at a rate of 10 °C/min in a crucible under syn. air (20.5 vol% O_2 in N_2, Westfalen AG, 50 mL/min) and then cooled down to 25 °C.

X-ray photoelectron spectroscopy (XPS) on $LaTaO_2N$, $LaTaON_2$, n-LTO, m-$LaTaO_4$ and termination products was carried out to investigate the oxidation states using a Thermo VG Theta Probe 300 XPS system from Thermo Fisher Scientific. The incident beam provided monochromatic and micro-focused Al K_α radiation and a spot size of 400 µm. The powders were fixed on a carbon tape and a flood gun was used to avoid charging effects. For background subtraction a Shirley-type inelastic background was utilised and the zero-shift correction was done by normalizing the measured C 1*s* peak to 284.5 eV. The peak fitting was implemented by carefully considering quantum mechanical requirements for the intensity and energy relations of Ta $4f_{7/2}$ and Ta $4f_{5/2}$ orbitals with ΔE_B = 1.91 eV[22] and identical full width at half maximum (FWHM) for both orbital contributions.

The morphology of the produced oxynitrides and oxides was analysed *via* scanning electron microscopy (SEM) (ZEISS GeminiSEM 500, 5 kV). The in-lens detector was used for imaging.

UV-visible diffuse reflectance spectra (DRS) were obtained using a Carry 5000 UV–VIS NIR spectrophotometer. The baseline was measured with $BaSO_4$. The spectra were recorded in the range of 200 nm to 800 nm. The Kubelka-Munk[35] conversion was applied to the obtained reflectance spectra and the optical bandgap was estimated by extrapolating the onset of absorption to the abscissa.

The specific surface area was obtained *via* nitrogen sorption, first annealing the samples at 120 °C to remove adsorbed water. Adsorption and desorption isotherms were collected at liquid nitrogen temperature using an Autosorb-1-MP (Detection limit: $S_{BET} > 1\ m^2/g$) from Quantachrome Instruments. The specific surface area was determined *via* the Brunauer-Emmet-Teller[47] (BET) method.

SQUID measurements to investigate the magnetic behaviour of Ta in $LaTaO_2N$ and $LaTaON_2$ were carried out with a commercial VSM MPMS3 Superconducting Quantum Interference Device (SQUID) from Quantum Design. For zero field cooling (ZFC) measurements the magnetic field was set to 500 Oe.

6.5. Data Availability

The authors declare that all other data supporting the findings of this study are available within the paper and its Supplementary Information. Reprints and permissions information is available online at www.nature.com/reprints. Correspondence and requests for materials should be addressed to A.W.

6.6. Acknowledgements

The authors thank Mrs. Annette Fuchs, Prof. Dr. Joachim Maier and Prof. Dr. Bettina Lotsch (Max Planck Institute for Solid State Research, Stuttgart), Mr. Peter Schützendübe (Max Planck Institute for Intelligent Systems, Stuttgart), and Mr. Samir Hammoud (Max Planck Institute for Intelligent Systems, Stuttgart) for nitrogen sorption, DRS, XPS, and chemical analysis, respectively, and Alan Fernandes-Dias for producing the microcrystalline oxide precursor. We also thank Dr. Benjamin Balke (Fraunhofer Research Institution Materials Recycling and Resource Strategies, Hanau), Dr. Andrea Knöller, Dr. Angelika Veziridis (Institute for Materials Science, University of Stuttgart), MSc. Sven Fecher (Max Planck Institute for Solid State Research, Stuttgart), and Jun.-Prof. Hongbin Zhang (Department of Materials and Earth Sciences, Technische Universität Darmstadt) for fruitful discussions. The authors acknowledge the financial support of the European Synchrotron Radiation Facility, Grenoble, France and the synchrotron radiation beam time. This work was supported by the Deutsche Forschungsgemeinschaft within the priority program SPP 1613 "Solar H_2" (WE 2803/7-1).

6.7. Author Contributions

C. B. developed the parameters for the synthesis of the oxide precursors and the perovskite-type oxynitrides and the *in situ* and *ex situ* ammonolysis study. C.B. performed and pre-evaluated the PXRD, SEM, DRS and TGA measurements. C.B., M.W. and A.W. collectively elaborated the analysis of the synthesis, *in situ* and *ex situ* ammonolysis data. G.R. and C.B. analysed the XPS data. M.W. and M.C. collected the HR-PXRD data at the ESRF. C.B., M.W., S.Y. and M.C. analysed the HR-PXRD data, which had been refined by C.B. and M.W. C.B. and E.G. measured and analysed together the SQUID data. C.B. wrote the paper with input from M.W., G.R., M.C. and S.Y. and A.W. provided final contributions to the conclusions.

6.8. Competing Interests

The authors declare no competing interests. All authors approved the submission of the manuscript.

6.9. References

1. Yajima, T. *et al.* A labile hydride strategy for the synthesis of heavily nitridized $BaTiO_3$. *Nat. Chem.* **7**, 1017–1023 (2015).

2. Ebbinghaus, S. G. *et al.* Perovskite-related oxynitrides - Recent developments in synthesis, characterisation and investigations of physical properties. *Prog. Solid State Chem.* **37**, 173–205 (2009).

3. Yang, M. *et al.* Anion order in perovskite oxynitrides. *Nat. Chem.* **3**, 47–52 (2011).

4. Jansen, M. & Letschert, H. P. Inorganic yellow-red pigments without toxic metals. *Nature* **404**, 980–982 (2000).

5. Hojamberdiev, M. *et al.* Elucidating the impact of A-site cation change on photocatalytic H_2 and O_2 evolution activities of perovskite-type $LnTaON_2$ (Ln = La and Pr). *Phys. Chem. Chem. Phys.* **19**, 22210–22220 (2017).

6. Tessier, F., Maillard, P., Cheviré, F., Domen, K. & Kikkawa, S. Optical properties of oxynitride powders. *Ceram. Soc. Japan* **117**, 1–5 (2009).

7. Hisatomi, T., Kubota, J. & Domen, K. Recent advances in semiconductors for photocatalytic and photoelectrochemical water splitting. *Chem. Soc. Rev.* **43**, 7520–7535 (2014).

8. Seo, J. *et al.* Efficient solar-driven water oxidation over perovskite-type $BaNbO_2N$ photoanodes absorbing visible light up to 740 nm. *Adv. Energy Mater.* **8**, 1800094 (2018).

9. Kageyama, H. *et al.* Expanding frontiers in materials chemistry and physics with multiple anions. *Nat. Commun.* **9**, 772 (2018).

10. Fuertes, A. Synthetic approaches in oxynitride chemistry. *Prog. Solid State Chem.* **51**, 63–70 (2018).

11. Suemoto, Y. *et al.* Intergrowth between the oxynitride perovskite $SrTaO_2N$ and the Ruddelsten-Popper phase Sr_2TaO_3N. *Inorg. Chem.* **57**, 9086–9095 (2018).

12. Kikkawa, S., Hosono, A. & Masubuchi, Y. Remarkable effects of local structure in tantalum and niobium oxynitrides. *Prog. Solid State Chem.* **51**, 71–80 (2018).

13. Zhang, L. *et al.* Photoelectrochemical water oxidation of $LaTaON_2$ under visible-light irradiation. *Int. J. Hydrogen Energy* **39**, 7697–7704 (2014).

14. Si, W. *et al.* Investigating the behavior of various cocatalysts on $LaTaON_2$ photoanode for visible light water splitting. *Phys. Chem. Chem. Phys.* **19**, 656–662 (2017).

15. Weidenkaff, A. Preparation and application of nanostructured perovskite phases. *Adv. Eng. Mater.* **6**, 709–714 (2004).

16. Ueda, K., Kato, H., Kobayashi, M., Hara, M. & Kakihana, M. Control of valence band potential and photocatalytic properties of $Na_xLa_{1-x}TaO_{1+2x}N_{2+2x}$. *J. Mater. Chem. A* **1**, 3667–3674 (2013).

17. Clark, L., Oró-Solé, J., Knight, K. S., Fuertes, A. & Attfield, J. P. Thermally robust anion-chain order in oxynitride perovskites. *Chem. Mater.* **25**, 5004–5011 (2013).

18. Ebbinghaus, S. G., Aguiar, R., Weidenkaff, A., Gsell, S. & Reller, A. Topotactical growth of thick perovskite oxynitride layers by nitridation of single crystalline oxides. *Solid State Sci.* **10**, 709–716 (2008).

19. Vullum, F., Nitsche, F., Selbach, S. M. & Grande, T. Solid solubility and phase transitions in the system $LaNb_{1-x}Ta_xO_4$. *J. Solid State Chem.* **181**, 2580–2585 (2008).

20. Briggs, D. & Grant, J. T. *Surface analysis by auger and X-ray photoelectron spectroscopy*. (IM Publications, 2003).

21. Nordling, C. ESCA : Elektronen-Spektroskopie für chemische Analyse. *Angew. Chemie* **4**, 144–153 (1972).

22. Moulder, J. F., Stickle, W. F., Sobol, P. E. & Bomben, K. D. *Handbook of X-ray photoelectron spectroscopy*. (Perkin-Elmer Corporation Physical Electronics Division, 1992).

23. Logvinovich, D. *et al.* Synthesis and physical chemical properties of Ca-substituted $LaTiO_2N$. *Prog. Solid State Chem.* **35**, 281–290 (2007).

24. Park, N. Y. & Kim, Y. Il. Morphology and band gap variations of oxynitride $LaTaON_2$ depending on the ammonolysis temperature and precursor. *J. Mater. Sci.* **47**, 5333–5340 (2012).

25. Kim, Y. Il. Effects of KCl flux on the morphology, anion composition, and chromaticity of perovskite oxynitrides, $CaTaO_2N$, $SrTaO_2N$, and $LaTaON_2$. *Ceram. Int.* **40**, 5275–5281 (2014).

26. Henderson, G. S., de Groot, F. M. F. & Moulton, B. J. A. X-ray absorption near-edge structure (XANES) spectroscopy. *Rev. Mineral. Geochemistry* **78**, 75–138 (2014).

27. Zaman, A. & Meletis, E. Microstructure and mechanical properties of TaN thin films prepared by reactive magnetron sputtering. *Coatings* **7**, 209, 1–16 (2017).

28. Erickson, A. S. *et al.* Ferromagnetism in the Mott insulator Ba_2NaOsO_6. *Phys. Rev. Lett.* **99**, 016404 (2007).

29. Wang, X. Y., Avendaño, C. & Dunbar, K. R. Molecular magnetic materials based on 4d and 5d transition metals. *Chem. Soc. Rev.* **40**, 3213–3238 (2011).

30. Varignon, J., Bibes, M. & Zunger, A. Origins vs. fingerprints of the Jahn-Teller effect in d-electron ABX_3. 1–26 Available at: http://arxiv.org/abs/1906.07587.

31. Kugel, K. & Khomskiĭ, D. The Jahn-Teller effect and magnetism: transition metal compounds. *Sov. Phys. Uspekhi* **25**, 231–256 (1982).

32. Günther, E., Hagenmayer, R. & Jansen, M. Strukturuntersuchungen an den Oxidnitriden $SrTaO_2N$, $CaTaO_2N$ und $LaTaON_2$ mittels Neutronen- und Röntgenbeugung. *Z. Anorg. Allg. Chem.* **626**, 1519–1525 (2000).

33. Cordes, N. & Schnick, W. Ammonothermal synthesis of crystalline oxonitride perovskites $LnTaON_2$ (Ln = La, Ce, Pr, Nd, sm, Gd). *Chem. Eur. J.* **2**, 11410–11415 (2017).

34. Shannon, R. D. Revised effective ionic radii and systematic studies of interatomic distances in halides and chalcogenides. *Acta Crystallogr. Sect. A* 751–767 (1976).

35. Kortüm, G., Braun, W. & Herzog, G. Principles and techniques of diffuse-reflectance spectroscopy. *Angew. Chemie Int. Ed.* **2**, 333–341 (1963).

36. Maegli, A. E. *et al.* Perovskite-type $LaTiO_2N$ oxynitrides for solar water splitting: Influence of the synthesis conditions. *Energy Procedia* **22**, 61–66 (2011).

37. Siegrist, T., Cava, R. J. & Krajewski, J. J. Reduced alkaline earth tantalates. *Mater. Res. Bull.* **32**, 881–887 (1997).

38. Zhang, G., Liu, G., Wang, L. & Irvine, J. T. S. Inorganic perovskite photocatalysts for solar energy utilization. *Chem. Soc. Rev.* **45**, 5951–5984 (2016).

39. Xiao, M., Wang, S., Thaweesak, S., Luo, B. & Wang, L. Tantalum (oxy)nitride: narrow bandgap photocatalysts for solar hydrogen generation. *Engineering* **3**, 365–378 (2017).

40. Osterloh, F. E. & Parkinson, B. A. Recent developments in solar water-splitting photocatalysis. *MRS Bull.* **36**, 17–22 (2011).

41. Castelli, I. E. *et al.* New cubic perovskites for one- and two-photon water splitting using the

computational materials repository. *Energy Environ. Sci.* **5**, 9034–9043 (2012).

42. Rajeshwar, K., McConnell, R. & Licht, S. *Solar hydrogen generation*. (Springer Berlin Heidelberg, 2008).

43. Lohaus, C., Klein, A. & Jaegermann, W. Limitation of Fermi level shifts by polaron defect states in hematite photoelectrodes. *Nat. Commun.* **9**, 4309 (2018).

44. Rietveld, H. M. Line profiles of neutron powder-diffraction peaks for structure refinement. *Acta Crystallogr.* **22**, 151–152 (1967).

45. Rietveld, H. M. A profile refinement method for nuclear and magnetic structures. *J. Appl. Crystallogr.* **2**, 65–71 (1969).

46. Rodriguez-Carvajal, J. FullProf. 2k, version 5.30, ILL. *2012* **version 5.**, (2012).

47. Brunauer, S., Emmett, P. H. & Teller, E. Adsorption of gases in multimolecular layers. *J. Am. Chem. Soc.* **60**, 309–319 (1938).

6.10. Supplementary Information

6.10.1. Supplementary Methods

6.10.1.1. Synthesis of microcrystalline $LaTaO_4$ (m-$LaTaO_4$)

The microcrystalline $LaTaO_4$ (m-$LaTaO_4$) was synthesised via solid-state reaction (SSR) (Supplementary Fig. 1). 0.0025 mol Ta_2O_5 (Alfa Aesar, 99.9 %), 0.0025 mol La_2O_3 (REacton®, 99.9 %) and 0.01 mol KCl (Roth, ≥ 99 %, Ph.Eur.) were mixed in an agate mortar for 10 min. The mixture was transferred to an alumina crucible, heated to 1400 °C for 5 h and naturally cooled to ambient temperature. The obtained crystalline powder was washed twice with demineralised water and once with ethanol and dried at 80 °C.

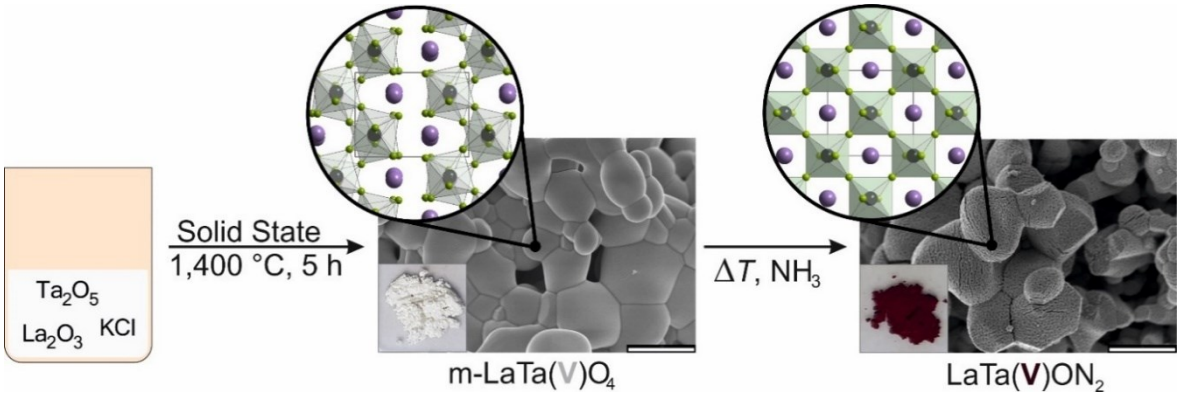

Supplementary Figure 1. Schematic synthesis path to La(V)TaON$_2$. The production of LaTa(V)ON$_2$ comprises the synthesis of m-$LaTaO_4$ by solid state reaction (SSR) and the subsequent ammonolysis to LaTa(V)ON$_2$. The ammonolysis temperature program was adopted from the LaTa(IV)O$_2$N synthesis. Scalebar of the SEM images: 2 µm.

6.10.1.2. Synthesis of nanocrystalline lanthanum tantalum oxide (n-LTO)

0.01 mol $TaCl_5$ (Alfa Aesar, 99.99 %) was loaded into a Schlenk flask under argon atmosphere to avoid hydrolysis of the Ta-compound. 50 mL of dried ethanol was added. A similar way to dissolve $TaCl_5$ has been already reported for the precursors synthesis of $Ba_3Ta_5O_{14}N$ and $LaBa_2Ta_5O_{13}N_2$[1] as well as for many other Ta-containing compounds[2–4]. Water-free citric acid (Sigma Aldrich, ≥ 99.0 %) was added in a 3-fold molar excess. A stoichiometric amount of $La(NO_3)_3{\cdot}6H_2O$ (Sigma Aldrich, 99.99 %) was weighed into a second Schlenk flask and citric acid was added in the same molar ratio as for the Ta-compound. The mixture was dissolved in 10 mL of dried methanol. After complexation of both metal cations at room temperature, the solutions were combined in one Schlenk flask and stirred under reflux for 3 h at 80 °C with addition of a 15-fold molar excess of ethylene glycol (Merck, EMPLURA®). The dispersion was transferred to a crystallising dish and heated for 10 h at 120 °C followed by a thermal treatment at 300 °C for 5 h. The resulting black xerogel was calcined in an alumina crucible for 14 h at 650 °C to obtain the white nanocrystalline oxide precursor.

6.10.2. Supplementary Discussion

6.10.2.1. Supplementary Note 1: PXRD, SEM investigations and DRS of nanocrystalline n-LTO and m-$LaTaO_4$

The powder X-ray diffraction (PXRD) patterns in Supplementary Figure 2a,b verified the expected level of crystallinity after synthesis in both cases. Since the nanocrystalline nature of n-LTO calcined at 650 °C does not allow an identification of the crystal structure, a reference was not inserted (Supplementary Fig. 2a). In contrast to the nanocrystalline precursor, m-$LaTaO_4$ revealed two polymorphs ($P2_1/c$ and $Cmc2_1$) *via* Rietveld refinements (Supplementary Fig. 2b and Supplementary Table 1a-c).

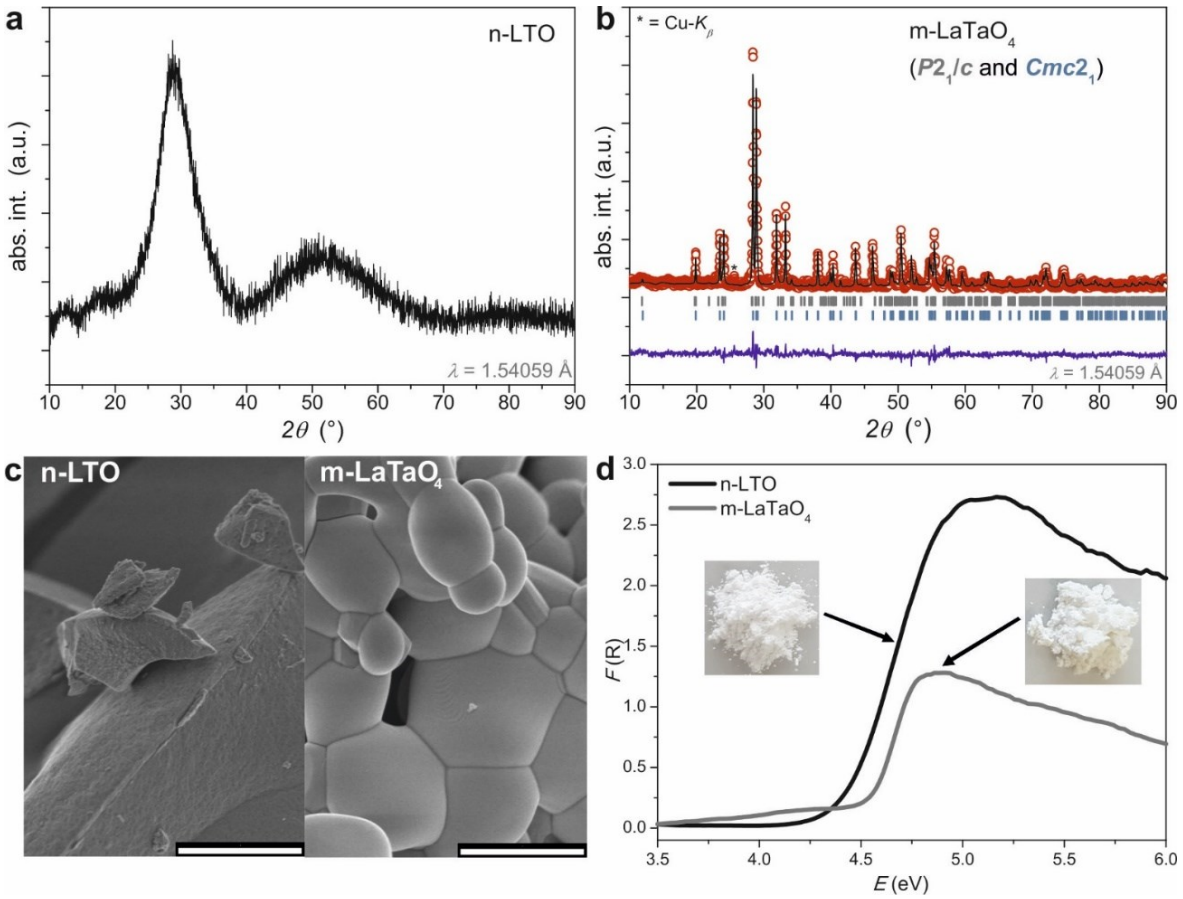

Supplementary Figure 2. XRD patterns, SEM images and DRS curves of as-prepared oxides. a, PXRD pattern of n-LTO synthesised by a soft chemistry route and **b**, Rietveld refinements of m-$LaTaO_4$ synthesised by SSR. Both polymorphs are labelled with ticks ($P2_1/c$ (grey colour) and $Cmc2_1$ (blue colour)). **c**, SEM images of n-LTO and m-$LaTaO_4$. Scalebar of the SEM images: 2 µm. **d**, Kubelka-Munk plot of n-LTO calcined at 650 °C and of m-$LaTaO_4$ synthesised by SSR.

The weight fractions of La, Ta and O obtained via inductively coupled plasma optical emission spectroscopy (ICP-OES) and hot gas extraction (HGE) were in good accordance with the expected values for $LaTaO_4$ for both oxides (Supplementary Table 2). The scanning electron microscopy (SEM) image of n-LTO indicated very small particles in the nm-range (Supplementary Fig. 2c and Fig. 1). In comparison to n-LTO, m-$LaTaO_4$ exhibited sintered and much larger particles in the µm-range (Supplementary Fig. 2c). The optical bandgap of n-LTO and m-$LaTaO_4$ was investigated by diffuse reflectance spectroscopy (DRS) (Supplementary Fig. 2d). The optical bandgap of 4.4 eV for white n-LTO determined by the tangent method was in good agreement with the white colour and literature data.[5] In contrast, the yellowish white m-$LaTaO_4$ revealed a higher optical bandgap of 4.5 eV and an

intensity increase after the optical bandgap. The difference in the optical bandgap and the curve shape might originate from the slight yellowish colour indicating oxygen vacancies[6] in the microcrystalline oxide. This is supported by the results of the hot gas extraction yielding an oxygen content of 16.5 ± 0.2 wt% instead of the desired 16.9 wt% (Supplementary Table 2).

Supplementary Table 1 a. Refined unit cell parameters of both polymorphs of m-$LaTaO_4$ synthesised *via* SSR.

Unit Cell Parameter	$P2_1/c$		$Cmc2_1$
***a* (Å)**	7.629(4)		3.9271(4)
***b* (Å)**	5.574(3)		14.8095(2)
***c* (Å)**	7.818(4)		5.6118(6)
***β* (°)**	101.46(5)		90
V_{cell} **(Å^3)**	325.8(3)		326.37(6)
Phase fraction (wt.-%)	14(1)		86(2)
R_p **(%)**		9.23	
R_{wp} **(%)**		11.6	
χ^2		1.94	
R_{Bragg} **(%)**	44.0		12.9

Supplementary Table 1 b. Refined atom positions of m-$LaTaO_4$ (*via* SSR) in space group type $P2_1/c$.

Atom	Wyck. Symb.	*x*	*y*	*z*	B_{iso} (Å^2)	sof[1]
La	4*e*	0.35478(4)	0.73924(9)	0.10483(5)	2.0	1
Ta	4*e*	0.21724(4)	0.30578(6)	0.33740(4)	2.0	1
O(1)	4*e*	0.16115[2]	0.15285[2]	0.04289[2]	0.6[2]	1
O(2)	4*e*	0.06283[2]	0.58501[2]	0.21649[2]	0.5[2]	1
O(3)	4*e*	0.37743[2]	0.46925[2]	0.33389[2]	0.5[2]	1
O(4)	4*e*	0.34367[2]	0.00839[2]	0.35912[2]	1.2[2]	1

[1]site occupancy factor, [2]adopted from ref.[7]

Supplementary Table 1 c. Refined atom positions of m-$LaTaO_4$ (*via* SSR) in space group type $Cmc2_1$.

Atom	Wyck. Symb.	*x*	*y*	*z*	B_{iso} (Å^2)	sof[1]
La	4*a*	0	0.16961(3)	0.09685(5)	2.0	1
Ta	4*a*	0	0.41467(3)	0.13325(5)	2.0	1
O(1)	4*a*	0	0.30400[2]	0.40800[2]	0.64[2]	1
O(2)	4*a*	0	0.33100[2]	0.87100[2]	0.64[2]	1
O(3)	4*a*	0	0.47000[2]	0.53200[2]	0.64[2]	1
O(4)	4*a*	0	0.91500[2]	0.25[2]	0.64[2]	1

[1]site occupancy factor, [2]adopted from ref.[8]

Supplementary Table 2. Composition of as-prepared n-LTO and m-$LaTaO_4$ determined *via* ICP-OES and HGE. According to the formula $LaTaO_4$ the desired elemental weight fractions are: La 36.2 wt%, Ta 47.1 wt% and O 16.9 wt%.

Elements	La[1]	Ta[1]	O[2]
Composition of n-LTO	1.00 ± 0.01	1.00 ± 0.01	4.11 ± 0.02[3]
Weight fraction in n-LTO (wt.%)	35.9 ± 0.4	46.8 ± 0.5	17.0 ± 0.2
Composition of m-$LaTaO_4$	1.00 ± 0.01	1.00 ± 0.01	3.95 ± 0.05
Weight fraction in m-$LaTaO_4$ (wt.%)	36.1 ± 0.4	47.1 ± 0.5	16.5 ± 0.2

[1] ICP-OES, [2] HGE, [3] Contains most probably residual carbonate and nitrate analogues according to the TGA-MS measurement (Supplementary Fig. 4)

6.10.2.2. Supplementary Note 2: Conversion of n-LTO to m-$LaTaO_4$

Annealing at 1400 °C transformed n-LTO into a microcrystalline $LaTaO_4$. Two polymorphs (space group types: $P2_1/c$ and $Cmc2_1$) were identified by Rietveld refinements of the high-resolution (HR) synchrotron PXRD data (Supplementary Fig. 3 and Supplementary Table 3a-c).

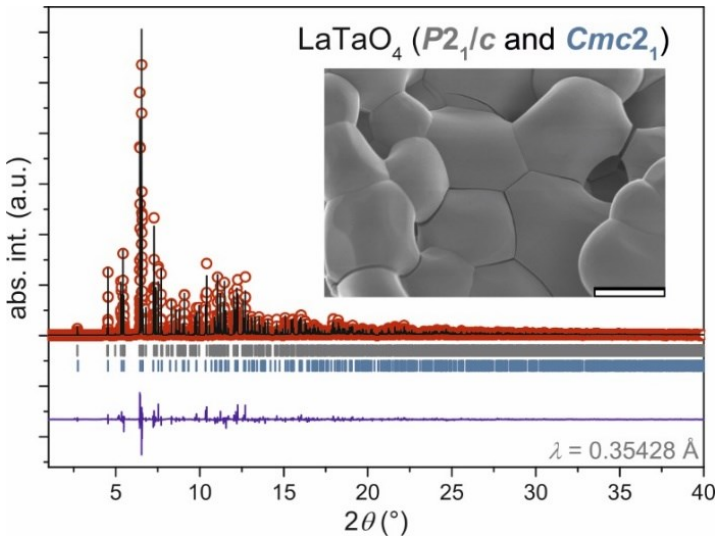

Supplementary Figure 3. Rietveld refinements and SEM image of m-$LaTaO_4$ obtained *via* annealing. The open red circles represent the measured data, the black line the calculated pattern, the blue line the difference, and the vertical tick marks ($P2_1/c$ (grey colour) and $Cmc2_1$ (blue colour)) the expected Bragg reflections. Scalebar of the SEM image: 2 μm.

It is well-known that $LaTaO_4$ easily forms two polymorphs in the space groups $Cmc2_1$ and $P2_1/c$, respectively[9]. Since the interatomic Ta–O distances in $LaTaO_2N$ and $LaTaON_2$ (Supplementary Table 9e) determined by Rietveld refinements are closer to those in m-$LaTaO_4$ ($P2_1/c$) rather than in m-$LaTaO_4$ ($Cmc2_1$) (Supplementary Table 3d), the m-$LaTaO_4$ polymorph in space group $P2_1/c$ was taken as Ta^{5+}-containing reference material for the later XPS investigations. The SEM image depicted a morphology very similar to that of m-$LaTaO_4$ obtained via SSR (Supplementary Fig. 2c, Supplementary Fig. 3). The *in situ* ammonolysis of both, the n-LTO-derived m-$LaTaO_4$ and the m-$LaTaO_4$ obtained by SSR, is compared in section "*In situ* ammonolysis of n-LTO and m-$LaTaO_4$" in the main text.

Supplementary Table 3 a. Refined unit cell parameters of both n-LTO-derived m-$LaTaO_4$ polymorphs.

Unit Cell Parameter	$P2_1/c$	$Cmc2_1$
$\boldsymbol{a}$ **(Å)**	7.6334(4)	3.9321(3)
$\boldsymbol{b}$ **(Å)**	5.5826(3)	14.8070(1)
$\boldsymbol{c}$ **(Å)**	7.8265(4)	5.6184(5)
$\boldsymbol{\beta}$ **(°)**	101.57(3)	90
$\boldsymbol{V_{cell}}$ **(Å^3)**	326.75(3)	327.11(5)
Phase fraction (wt.-%)	59(2)	41(2)
$\boldsymbol{R_p}$ **(%)**	9.12	
$\boldsymbol{R_{wp}}$ **(%)**	12.6	
$\boldsymbol{\chi^2}$	7.91	
$\boldsymbol{R_{Bragg}}$ **(%)**	5.26	6.41

Supplementary Table 3 b. Refined atom positions of n-LTO-derived m-$LaTaO_4$ in space group type $P2_1/c$.

Atom	Wyck. Symb.	x	y	z	B_{iso} (Å^2)	sof[1]
La	4*e*	0.34132(2)	0.77245(4)	0.09567(1)	0.39(3)	1.00(1)
Ta	4*e*	0.16836(1)	0.26501(3)	0.30058(1)	0.14(2)	1.03(1)
O(1)	4*e*	0.16970(2)	0.16334(3)	0.04686(2)	0.7(1)[2]	1
O(2)	4*e*	0.05918(2)	0.59019(3)	0.21127(2)	0.7(1)[2]	1
O(3)	4*e*	0.38449(2)	0.47106(3)	0.32807(2)	0.7(1)[2]	1
O(4)	4*e*	0.33335(2)	0.00577(3)	0.36234(2)	0.7(1)[2]	1

[1]site occupancy factor, [2]constrained

Supplementary Table 3 c. Refined atom positions of n-LTO-derived m-$LaTaO_4$ in space group type $Cmc2_1$.

Atom	Wyck. Symb.	x	y	z	B_{iso} (Å^2)	sof[1]
La	4*a*	0	0.1696(2)	0.170(5)	1.20(6)	1.00(2)
Ta	4*a*	0	0.4151(1)	0.203(5)	0.15(2)	1.02(2)
O(1)	4*a*	0	0.296(2)	0.407(7)	0.7(1)[2]	1
O(2)	4*a*	0	0.337(2)	0.953(6)	0.7(1)[2]	1
O(3)	4*a*	0	0.479(2)	0.535(6)	0.7(1)[2]	1
O(4)	4*a*	0	0.907(2)	0.256(7)	0.7(1)[2]	1

[1]site occupancy factor, [2]constrained

Supplementary Table 3 d. Ta-O distances in the $[TaO_6]^{7-}$ octahedron of n-LTO-derived m-$LaTaO_4$ (space group types: $Cmc2_1$ and $P2_1/c$) determined *via* Rietveld refinements of the HR-PXRD data.

Compound	m-$LaTaO_4$ ($P2_1/c$)	m-$LaTaO_4$ ($Cmc2_1$)
$d_{Ta\text{-}O(1)}$ (Å)	2.067(2)	2.2(8)
$d_{Ta\text{-}O(2)}$ (Å)	1.968(2)	1.6(1)
$d_{Ta\text{-}O(3)}$ (Å)	2.061(2)	1.9(1)
$d_{Ta\text{-}O(4)}$ (Å)	1.978(2)	1.9(9)
$d_{Ta\text{-}O(5)}$ (Å)	1.984(2)	2.0(4)
$d_{Ta\text{-}O(6)}$ (Å)	1.913(2)	2.0(4)
$d_{Ta\text{-}O,\ average}$ (Å)	1.99(5)	1.97(8)

6.10.2.3. Supplementary Note 3: Thermogravimetric Analysis coupled with Mass Spectrometry (TGA-MS)

The TGA-MS study of the conversion of n-LTO to m-$LaTaO_4$ in syn. air revealed the release of H_2O and hydroxyl groups in the first negative mass change up around 700 °C, since only MS signals for $OH^{\bullet+}$(m/z = 17) and H_2O^+ (m/z = 18) were detected. By further heating, fragments of CO_2 (m/z = 12 ($C^{\bullet+}$), m/z = 16 ($O^{\bullet+}$), m/z = 44 (CO_2^+), and m/z = 45 ($^{13}CO_2^+$)) and NO_2 (m/z = 46 (NO_2^+)) and additional CH-fragments (m/z = 13 ($CH^{\bullet+}$) were detected around the inflection point of the second negative mass change of Δm = -4.2 % at 870 °C. This result points to the decomposition of carbonates (most probably partial formation of $La_2(CO_3)_3$ or $La_2O_2CO_3$ due to the basic character of La_2O_3 – typically decomposition around 960 °C even in CO_2 atmosphere is observed[10]) and the release of residual organic compounds and nitrates from the soft chemistry synthesis. The residues arise from the low calcination temperature of only 650 °C required to maintain a suitable microstructure for the formation of $LaTaO_2N$.

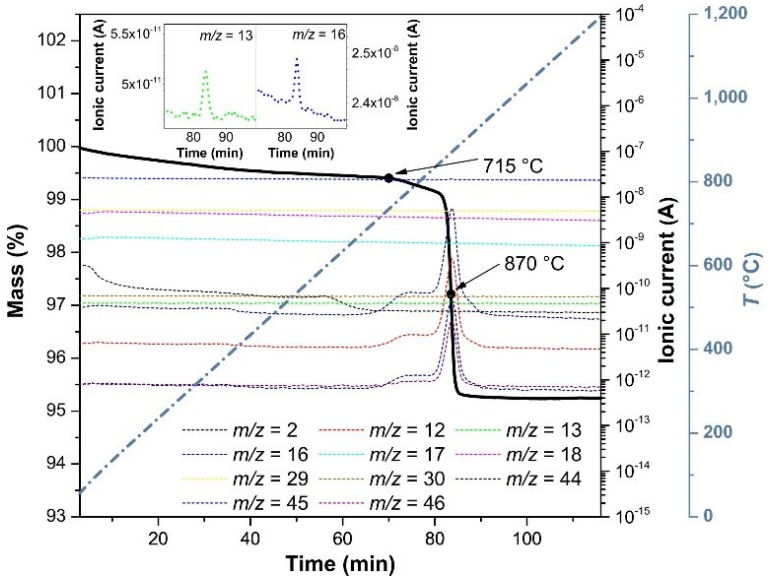

Supplementary Figure 4. TGA-MS study of the conversion of n-LTO to m-$LaTaO_4$. The measurement was done in synthetic air in order to investigate the released gaseous species during the conversion of n-LTO to m-$LaTaO_4$.

6.10.2.4. Supplementary Note 4: Oxidation state of Ta in n-LTO and m-$LaTaO_4$

XPS measurements were performed on m-$LaTaO_4$ originally prepared by thermal treatment of n-LTO at 1400 °C (Supplementary Fig. 5) because the atomic distances in m-$LaTaO_4$ ($P2_1/c$) were similar to $LaTaO_2N$ and $LaTaON_2$.

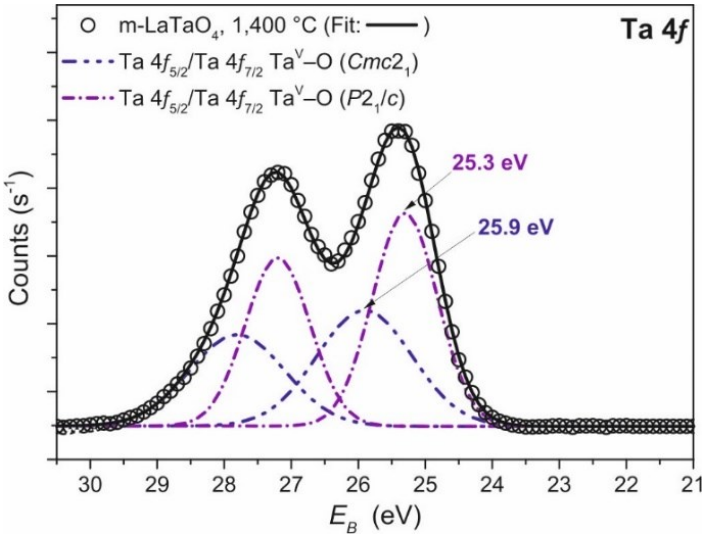

Supplementary Figure 5. XPS spectrum of the Ta 4*f* region of m-$LaTaO_4$ formed from n-LTO. The two polymorphs $Cmc2_1$ and $P2_1/c$ obtained by Rietveld refinements of HR-PXRD data were also visible by XPS. The open circles represent the experimental data and the solid line the overall fit, while the scattered lines are the fitting results of the Ta 4*f* orbitals.

Additionally, the presence of both m-$LaTaO_4$ polymorphs was confirmed via Ta 4*f* XPS data (Supplementary Fig. 5). The XPS spectrum of the Ta 4*f* region was successfully fitted with two binding states. The first binding state at lower binding energies of the Ta $4f_{7/2}$ orbitals was fitted to 25.3 eV. The second binding energy at higher values of the Ta $4f_{7/2}$ orbitals was fitted to a local maximum of 25.9 eV. These binding energies were in good agreement to literature values of Ta^{5+} containing compounds, e.g. $KTaO_3$ (Ta $4f_{7/2}$ = 26.1 eV)[11] or $RhTaO_4$ (Ta $4f_{7/2}$ = 25.8 eV)[12]. This leads to the conclusion that all local Ta $4f_{7/2}$ binding energy maxima of m-$LaTaO_4$ can be assigned to a Ta(V)–O binding character. The weight fractions of the two polymorphs ($Cmc2_1$: 40 wt% $P2_1/c$: 60 wt%) were obtained from the Ta 4*f* peak areas of both Ta(V)–O binding characters. They were in accordance with the results of the Rietveld refinements ($Cmc2_1$: 41(2) wt% $P2_1/c$: 59(2) wt%, Supplementary Table 3a). Therefore, the polymorph with space group $P2_1/c$ shows lower binding energies than the polymorph with space group $Cmc2_1$. The binding energies of the Ta $4f_{5/2}$ and the respective Ta $4f_{7/2}$ orbitals are listed in Supplementary Table 4. The fitted binding energies for n-LTO were not assignable to a certain phase since phase identification via PXRD was not possible (Supplementary Fig. 2a). The XPS spectrum of the Ta 4*f* region of n-LTO is shown in Figure 3a in the main text.

Supplementary Table 4. Binding energies of the Ta $4f_{7/2}$ orbitals and the respective Ta $4f_{5/2}$ orbitals of m-$LaTaO_4$ and n-LTO.

Compound	space group type	$E_{B.Ta\ 4f7/2}$ (eV)	$E_{B.Ta\ 4f5/2}$ (eV)	Binding Character
m-$LaTaO_4$	$P2_1/c$	25.3	27.2	Ta(V)–(O)
	$Cmc2_1$	25.9	27.8	Ta(V)–(O)
n-LTO	–	25.5	27.4	Ta(V)–(O)
	–	26.7	28.6	Ta(V)–(O)

6.10.2.5. Supplementary Note 5: Calculation of the chemical shift for nitrogen substitution

Supplementary Equations (1) and (2) estimated by Nordling[13] were used to determine the chemical shift due to a nitrogen substitution in $LaTaO_4$. The Pauling electron negativities[14] for Ta, O and N were used.

$$I_{AB} = 1 - e^{-0.25(\chi_A - \chi_B)^2} \qquad \text{(Supplementary Equation 1)}$$

$$q_p = Q + \sum I \qquad \text{(Supplementary Equation 2)}$$

With:

I_{AB}	Ionic amount of bond
χ_A	Electronegativity of ion A
χ_B	Electronegativity of ion B
q_p	Charge
Q	Formal charge
$\sum I$	Contribution of ionic character

6.10.2.6. Supplementary Note 6: In situ ammonolysis of m-$LaTaO_4$ and n-LTO

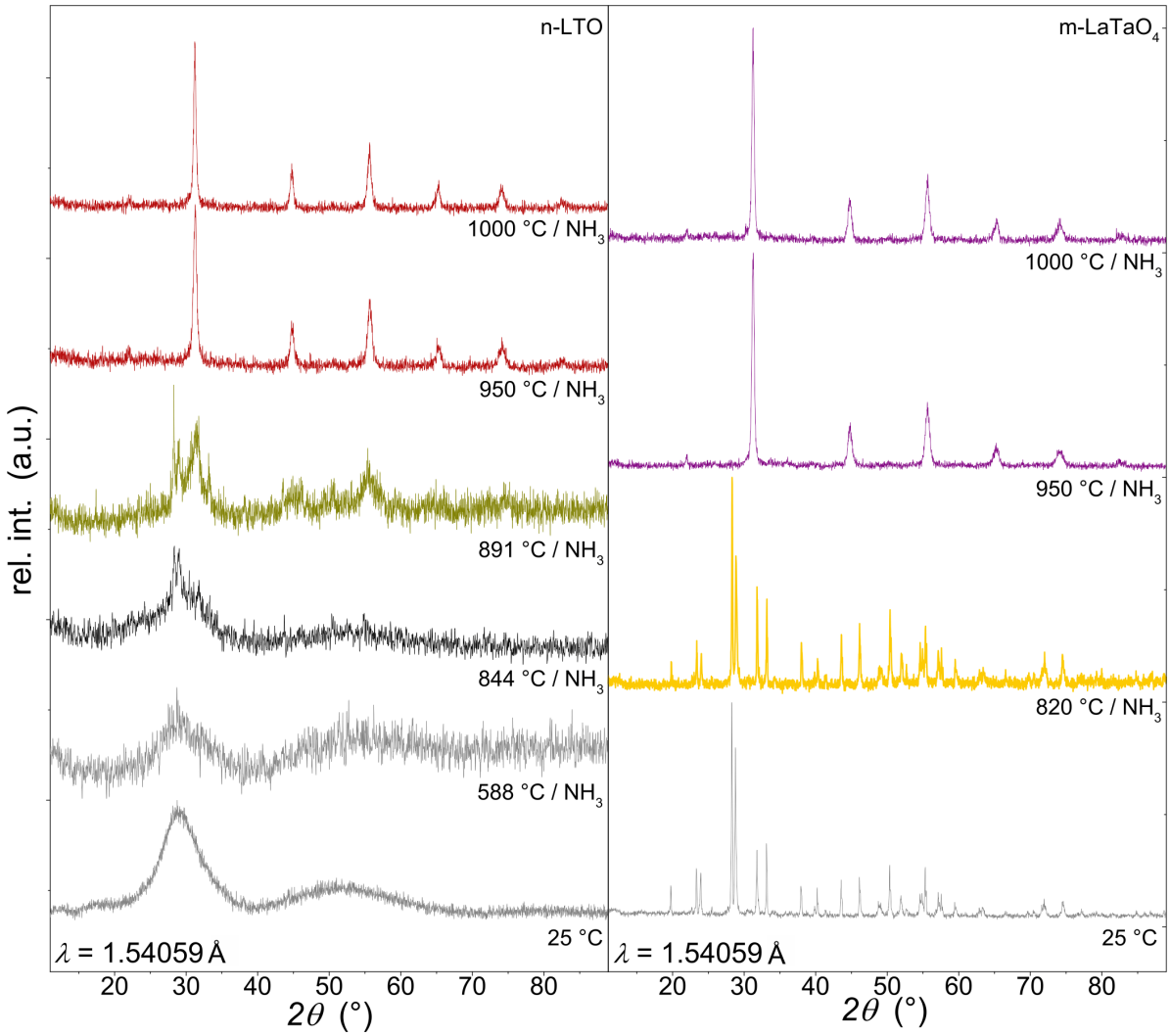

Supplementary Figure 6. PXRD patterns of the products obtained *via* termination experiments. PXRD diffractograms of the during *in situ* ammonolysis obtained termination products of nanocrystalline LTO (n-LTO) (left) and microcrystalline $LaTaO_4$ (m-$LaTaO_4$) (right). The colour of the PXRD patterns reflects the colour of the respective powder. The partially high background of the PXRD patterns might be owed to the small sample amount limited by the size of the ammonolysis crucible.

Supplementary Table 5. HGE results of the *in situ* ammonolysis termination experiments.

Compound	O	N	Vacancies
n-LTO; 844 °C / NH_3	3.44(4)	0.41(2)	0.14(6)
n-LTO; 891 °C / NH_3	3.28(1)	1.82(4)	0.00(5)
n-LTO; 950 °C / NH_3	1.44(1)[1]	1.63(9)[1]	-
n-LTO; 1000 °C / NH_3	1.26(9)[1]	1.83(4)[1]	0.00(2)
n-LTO; 1400 °C / syn. air	3.95(7)	-	0.04(3)
m-$LaTaO_4$; 820 °C / NH_3	3.87(7)	-	0.12(3)
m-$LaTaO_4$; 950 °C / NH_3	1.05(1)[2]	2.35(4)[2]	-
m-$LaTaO_4$; 1000 °C / NH_3	1.04(7)[2]	2.45(9)[2]	-
m-$LaTaO_4$; 1400 °C / syn. air	3.88(1)	-	0.12(1)

[1]perovskite-type phase, [2]perovskite-type phase with N-containing impurity

Supplementary Table 6. Composition of $LaTaO_2N$ and $LaTaON_2$ after the second *ex situ* ammonolysis cycle determined by ICP-OES and hot gas extraction.

Compound	La[1]	Ta[1]	O[2]	N[2]
$LaTaO_2N$	1.00 ± 0.01	1.00 ± 0.01	1.97 ± 0.02	1.02 ± 0.03
$LaTaO_2N$ (wt%)	37.9 ± 0.4	49.6 ± 0.5	8.6 ± 0.1	3.9 ± 0.1
$LaTaON_2$	1.00 ± 0.09	0.99 ± 0.01	0.99 ± 0.02	2.01 ± 0.03
$LaTaON_2$ (wt%)	37.9 ± 0.4	49.4 ± 0.5	4.57 ± 0.07	7.73 ± 0.12

[1] ICP-OES, [2] HGE

6.10.2.7. Supplementary Note 7: Reduction of Ta

The oxide anions surrounding Ta^{5+} in n-LTO were most probably attacked by H• radicals from the gas atmosphere leading to the formation of Ta-O-H groups. This results already in a reduction of Ta. These groups can be further exchanged in a nucleophile attack of the NH_2• radicals leading to the incorporation of N into the material and after internal H atom transfer to the release of H_2O to the flowing gas atmosphere.

6.10.2.8. Supplementary Note 8: Reoxidation of $LaTaO_2N$ to $LaTaO_4$

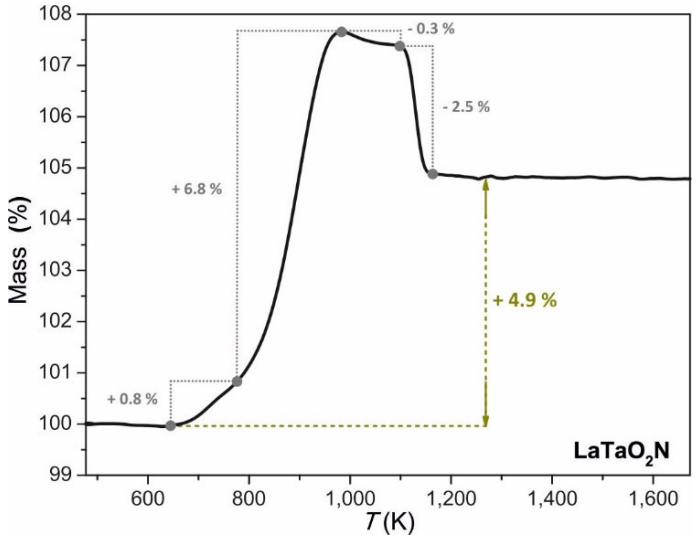

Supplementary Figure 7. TGA of the reoxidation of $LaTaO_2N$ in synthetic air. The observable changes can be assigned to four reaction steps (numbers s. Supplementary Table 7) allowing the determination of the following reaction sequence: 1. chemisorption of oxygen. 2. continued physisorption of oxygen. 3. intermediate formation as with the reoxidation of $BaTaO_2N$[15]. 4. full conversion to microcrystalline $LaTaO_4$. The expected mass change for the reoxidation of $LaTaO_2N$ to $LaTaO_4$ is $\Delta m_{calc.}$ = 4.92 %.

Supplementary Table 7. Results of the reoxidation of $LaTaO_2N$. The mass changes fall into four sections.

$LaTaO_2N \rightarrow LaTaO_4$		
Temperature	Δm_{TGA} (%)	Step
372 °C – 503 °C	0.8	1
503 °C – 710 °C	6.8	2
710 °C – 828 °C	-0.3	3
828 °C – 891 °C	-2.5	4

6.10.2.9. Supplementary Note 9: XPS measurements of novel $LaTaO_2N$, $LaTaON_2$ and m-$LaTaO_4$

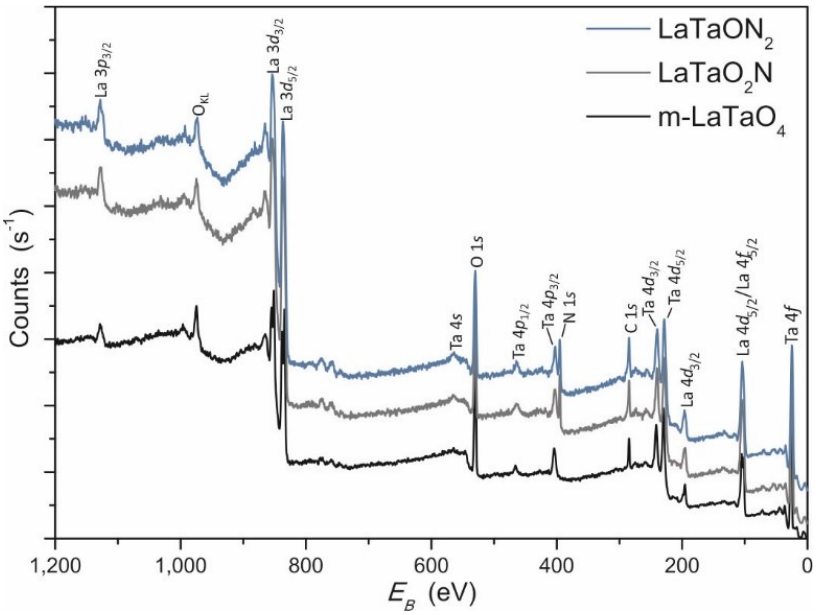

Supplementary Figure 8. XPS survey spectra. Survey spectra of as-prepared m-$LaTaO_4$ (black), *ex situ*-synthesised $LaTaO_2N$ (grey) and $LaTaON_2$ (blue).

Supplementary Table 8. Fitted binding energies of Ta 4*f* orbitals for *ex situ*-synthesised $LaTaO_2N$ and $LaTaON_2$. The binding characters were determined *via* the point charge model and assigned to the compound region where they can occur. Since XPS is surface-sensitive a nitrogen concentration gradient associated with an oxidation state concentration gradient of Ta is not excluded.

Compound	E_B (Ta $4f_{7/2}$) (eV)	E_B (Ta $4f_{5/2}$) (eV)	Binding Character	Compound region
$\mathbf{LaTaO_{2.0(5)}N_{1.0(8)}}$	24.4	26.3	Ta(IV)–(O,N)	Bulk of $LaTaO_2N$
	23.4	25.3	Ta(III)–(O,N)	Surface of $LaTaO_2N$
	25.0	26.9	Ta(V)–(O,N)	Bulk of $LaTaON_2$
$\mathbf{LaTaO_{0.9(9)}N_{2.0(1)}}$	23.7	25.7	Ta(III)–(O,N)	Surface of $LaTaON_2$
	22.9	24.8	Ta(III)–(N)	TaN[16] (impurity)

6.10.2.10. Supplementary Note 10: Magnetic measurements

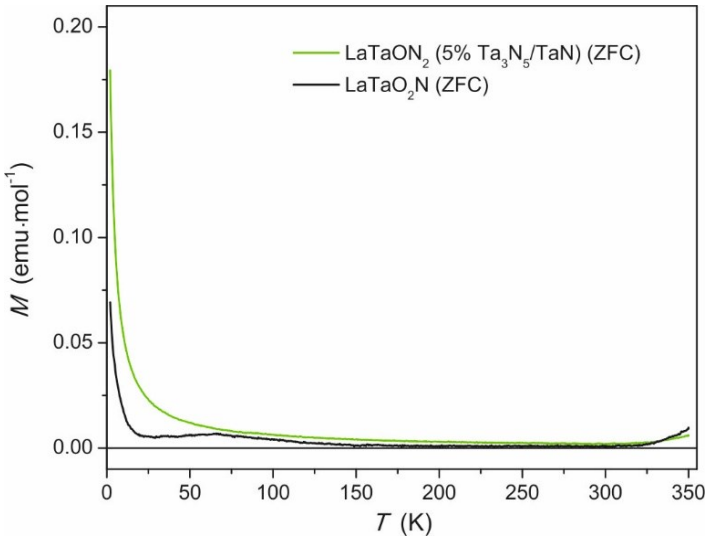

Supplementary Figure 9. Zero field cooled (ZFC) temperature dependent magnetisation curves. The ZFC curves of *ex situ* prepared $LaTaO_2N$ and $LaTaON_2$ were measured.

Zero field cooled curves are measured at a magnetic field of 500 Oe. The resulting curves were corrected by subtracting the present diamagnetism ($LaTa(IV)O_2N$: χ_{dia} = −0.35 emu·mol^{-1} and $LaTa(V)ON_2$ χ_{dia} = −0.10 emu·mol^{-1}). To determine the effective magnetic moments of the $LaTaO_2N$ and $LaTaON_2$ samples supplementary equations (3) and (4) were used[17]. The increase of the magnetisation at very low ($T \lesssim 30$ K) and high temperature (~320 K) is most probably caused by the activation of pinned impurity states. The hump at about 70 K seems to stem from physisorbed O_2[18].

$$\chi(T) = \frac{C}{T+\theta} \qquad \text{(Supplementary Equation 3)}$$

$$C = \frac{n\mu_{eff}^2\mu_0}{3k_B} \qquad \text{(Supplementary Equation 4)}$$

With:

χ	Susceptibility	μ_0	Magnetic permeability
T	Absolute temperature	k_B	Boltzmann constant
C	Curie constant		
θ	Weiss constant		
n	Number of atoms per unit volume		
μ_{eff}	Effective magnetic moment		

6.10.2.11. Supplementary Note 11: Rietveld refinements of $LaTaO_2N$ and $LaTaON_2$

During the Rietveld refinements of the crystal structures of the oxynitrides $LaTaO_2N$ and $LaTaON_2$ the anionic compositions were fixed according to the respective compositions determined before, since the virtually equal form factors make it impossible to discriminate between O^{2-} and N^{3-} by means of X-rays. The anions were statistically assigned to the two independent crystallographic sites.

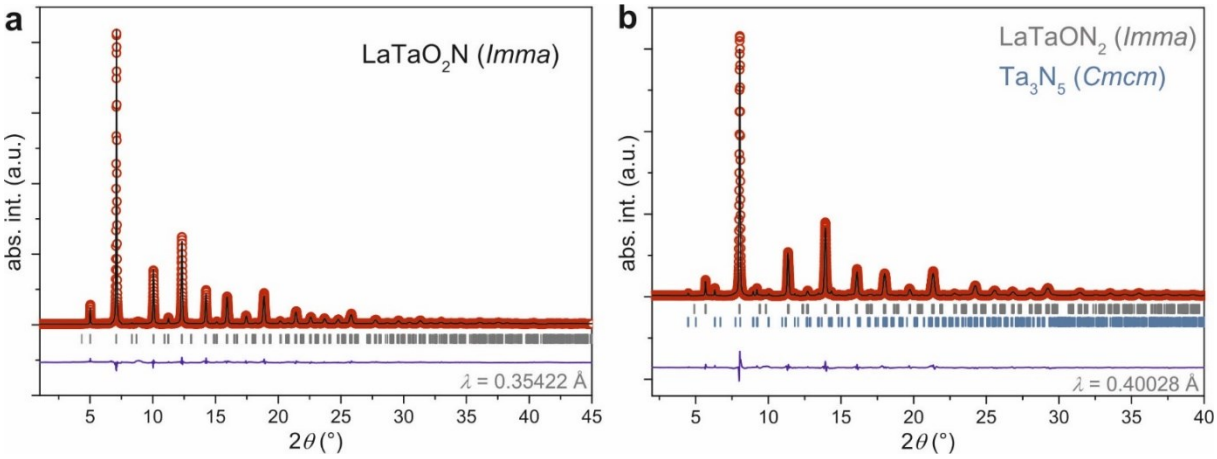

Supplementary Figure 10. Rietveld refinements of HR-PXRD data of novel $LaTaO_2N$ and $LaTaON_2$. a, Rietveld refinements of $LaTaO_2N$ (*Imma*) and **b**, $LaTaON_2$ in space group *Imma* (grey colour). The blue coloured ticks indicate the impurity phase (Ta_3N_5 (*Cmcm*)).

Supplementary Table 9 a. Refined atom positions of $LaTaO_2N$ in space group type *Imma*.

Atom	Wyck. Symb.	*x*	*y*	*z*	B_{iso} (Å^2)	sof[1]
La	4*e*	0	¼	½	0.738(2)	1
Ta	4*a*	0	0	0	0.682(1)	1
O(1)	4*e*	0	¼	0.088(2)	0.5	⅔
N(1)	4*e*	0	¼	0.088(2)	0.5	⅓
O(2)	8*g*	¼	0.967(3)	¼	0.5	⅔
N(2)	8*g*	¼	0.967(3)	¼	0.5	⅓

[1]site occupancy factor

Supplementary Table 9 b. Refined atom positions of $LaTaON_2$ in space group type *Imma*.

Atom	Wyck. Symb.	*x*	*y*	*z*	B_{iso} (Å^2)	sof[1]
La	4*e*	0	¼	½	0.84(5)	1
Ta	4*a*	0	0	0	0.99(6)	1
N(1)	4*e*	0	¼	0.129(7)	0.5	⅔
O(1)	4*e*	0	¼	0.129(7)	0.5	⅓
N(2)	8*g*	¼	0.975(7)	¼	0.5	⅔
O(2)	8*g*	¼	0.975(7)	¼	0.5	⅓

[1]site occupancy factor

Supplementary Table 9 c. Atomic coordinates of Ta_3N_5 in space group type *Cmcm* adopted from Brese *et al.*[19].

Atom	Wyck. Symb.	*x*	*y*	*z*	B_{iso} (Å^2)	occ[1]
Ta	4*c*	0	0.19710	¼	1	¼
Ta	8*f*	0	0.13455	0.55906	1	½
N(1)	4*c*	0	0.76322	¼	1	¼
N(2)	8*f*	0	0.04701	0.11949	1	½
N(3)	8*f*	0	0.30862	0.07378	1	½

[1]occupancy

Supplementary Table 9 d. Unit cell parameters of single phase $LaTaO_2N$, $LaTaON_2$ and the impurity Ta_3N_5.

Unit Cell Parameter	$LaTaO_2N$	$LaTaON_2$	Ta_3N_5 (*Cmcm*)
***a* (Å)**	5.7158(5)	5.7160(3)	3.8907(4)
***b* (Å)**	8.0645(5)	8.0590(4)	10.2186(1)
***c* (Å)**	5.7442(4)	5.7457(3)	10.2782(1)
V_{cell} (Å^3)	264.78(3)	264.68(2)	408.63(8)
Phase fraction (wt.-%)	100	94.62(7)	5.38(7)
R_p (%)	8.33	7.33	
R_{wp} (%)	12.8	10.3	
χ^2	4.78	4.13	
R_{Bragg} (%)	7.12	4.79	33.0

Supplementary Table 9 e. Distances in the $[Ta(O,N)_6]^{z-}$ octahedron of *ex situ* synthesised $LaTaO_2N$ and $LaTaON_2$ determined via Rietveld refinements of the respective HR-PXRD data.

Compound	$LaTaO_2N$	$LaTaON_2$
$d_{Ta\text{-}(O,N)1}$ (Å)	2.0428(2)	2.044(2)
$d_{Ta\text{-}(O,N)2}$ (Å)	2.0428(2)	2.044(2)
$d_{Ta\text{-}(O,N)3}$ (Å)	2.0428(2)	2.044(2)
$d_{Ta\text{-}(O,N)4}$ (Å)	2.0428(2)	2.044(2)
$d_{Ta\text{-}(O,N)5}$ (Å)	2.0799(7)	2.0806(9)
$d_{Ta\text{-}(O,N)6}$ (Å)	2.0799(7)	2.0806(9)
$d_{Ta\text{-}(O,N),average}$ (Å)	2.05(5)	2.05(6)

Supplementary Table 10. Specific surface area. Specific surface areas S_{BET} determined by the BET method.

Compound	S_{BET} (m^2/g)
n-LTO	6.8
m-$LaTaO_4$ (650 °C→1400 °C)	<1
$LaTaO_2N$ (1 Cycle, *ex situ*)	25.0
$LaTaO_2N$ (2 Cycles, *ex situ*)	8.0
m-$LaTaO_4$ (SSR)	2
$LaTaON_2$ (2 Cycles, *ex situ*)	3.2

6.11. Supplementary References

1. Anke, B., Bredow, T., Pilarski, M., Wark, M. & Lerch, M. From $Ba_3Ta_5O_{14}N$ to $LaBa_2Ta_5O_{13}N_2$: Decreasing the optical band gap of a photocatalyst. *J. Solid State Chem.* **246**, 75–80 (2017).
2. Motohashi, T., Hamade, Y., Masubuchi, Y. & Takeda, T. Structural phase transition in the perovskite-type tantalum oxynitrides, $Ca_{1-x}Eu_xTa(O,N)_3$. *Mater. Res. Bull.* **44**, 1899–1905 (2009).
3. Shen, Y., Leckie, R. M., Levi, C. G. & Clarke, D. R. Low thermal conductivity without oxygen vacancies in equimolar $YO_{1.5}$+ $TaO_{2.5}$- and $YbO_{1.5}$+ $TaO_{2.5}$-stabilized tetragonal zirconia ceramics. *Acta Mater.* **58**, 4424–4431 (2010).
4. Shian, S. *et al.* The tetragonal-monoclinic, ferroelastic transformation in yttrium tantalate and effect of zirconia alloying. *Acta Mater.* **69**, 196–202 (2014).
5. Park, N. Y. & Kim, Y. Il. Morphology and band gap variations of oxynitride $LaTaON_2$ depending on the ammonolysis temperature and precursor. *J. Mater. Sci.* **47**, 5333–5340 (2012).
6. Estrada-Urbina, J., Cruz-Alonso, A., Santander-González, M., Méndez-Albores, A. & Vázquez-Durán, A. Nanoscale zinc oxide particles for improving the physiological and sanitary quality of a mexican landrace of red maize. *Nanomaterials* **8**, 247 (2018).
7. Kurova, T. A. & Aleksandrov, V. B. The crystal structure of $LaTaO_4$. *Dokl. Akad. Nauk SSSR* **201**, 1095–1098 (1971).
8. Titov, Y. O. *et al.* Crystal structure of the orthorhombic modification of $LaTaO_4$. *Dopovidi Natsional'noi Akad. Nauk Ukr.* **3**, 140–145 (2003).
9. Cordrey, K. J. *et al.* Structural and dielectric studies of the phase behaviour of the topological ferroelectric $La_{1-x}Nd_xTaO_4$. *Dalt. Trans.* **44**, 10673–10680 (2015).
10. Bakiz, B. *et al.* Carbonatation and decarbonatation kinetics in the La_2O_3-$La_2O_2CO_3$ system under CO_2 gas flow. *Adv. Mater. Sci. Eng.* **2010**, (2010).
11. Bajorowicz, B. *et al.* Perovskite-type $KTaO_3$ – reduced graphene oxide hybrid with improved visible light photocatalytic activity. *RSC Adv.* **5**, 91315–91325 (2015).
12. Moulder, J. F., Stickle, W. F., Sobol, P. E. & Bomben, K. D. *Handbook of X-ray photoelectron spectroscopy*. (Perkin-Elmer Corporation Physical Electronics Division, 1992).
13. Nordling, C. ESCA : Elektronen-Spektroskopie für chemische Analyse. *Angew. Chemie* **4**, 144–153 (1972).
14. Pauling, L. & Pitzer, K. S. The nature of the chemical bond and the structure of molecules and crystals: an introduction to modern structural chemistry. *J. Am. Chem. Soc.* **82**, 4121 (1960).
15. Hellwig, A. & Hendry, A. Formation of barium-tantalum oxynitrides. *J. Mater. Sci.* **29**, 4686–4693 (1994).
16. Zaman, A. & Meletis, E. Microstructure and mechanical properties of TaN thin films prepared by reactive magnetron sputtering. *Coatings* **7**, 209, 1–16 (2017).
17. Cullity, B. D. & Graham, C. D. Diamagnetism and Paramagnetism. in *Introduction to Magnetic Materials* 87–114 (2003).
18. Dubroca, T., Hack, J. & Hummel, R. Comment on 'Unusual magnetic transitions and nature of magnetic resonance spectra in oxide glasses containing gadolinium'. *Phys. Rev. B - Condens. Matter Mater. Phys.* **74**, 026403 (2006).
19. Brese, N. E., O'Keeffe, M., Rauch, P. & DiSalvo, F. J. Structure of Ta_3N_5 at 16 K by time-of-flight neutron diffraction. *Acta Crystallogr. Sect. C Cryst. Struct. Commun.* **47**, 2291–2294 (1991).

7. Bandgap-Adjustment and Enhanced Surface Photovoltage in Y-Substituted $LaTa^{IV}O_2N$

Cora Bubeck, Marc Widenmeyer, Alexandra T. De Denko, Gunther Richter, Mauro Coduri, Eduardo Salas Colera, Eberhard Goering, Hongbin Zhang, Songhak Yoon, Frank E. Osterloh, Anke Weidenkaff

Abstract

Perovskite-type oxynitrides $AB(O,N)_3$ are photocatalysts for overall water splitting under visible light illumination. In the past, structurally labile perovskite-type oxynitrides (*e.g.* $YTaON_2$) were predicted to be highly suitable. In this work, we tackle the challenging $YTa(O,N)_3$ synthesis by Y-substitution in $LaTa^{IV}O_2N$ resulting in phase-pure $La_{0.9}Y_{0.1}Ta^{IV}O_2N$, $La_{0.75}Y_{0.25}Ta^{IV}O_2N$, and $La_{0.7}Y_{0.3}Ta^{IV}O_2N$. By using microcrystalline $YTaO_4$ together with an unconventional ammonolysis protocol we synthesized the highest reported weight fraction (82(2) wt%) of perovskite-type $YTa(O,N)_3$. Ta^{4+} in $La_{1-x}Y_xTa^{IV}O_2N$ was verified by X-ray photoelectron spectroscopy (XPS) and X-ray near edge absorption structure (XANES) analysis. Density functional theory (DFT) calculations revealed a transparent conductor-like behavior explaining the unusual red/orange color of the Ta^{4+}-containing perovskites. In combination with crystal structure analysis the DFT calculations identified orthorhombic strain as the main descriptor for the unexpected trend of the optical bandgap ($E_{G,x=0.3} \approx E_{G,x=0} < E_{G,x=0.1} < E_{G,x=0.25}$). Surface photovoltage spectroscopy (SPS) of particulate $La_{1-x}Y_xTa^{IV}O_2N$ (x = 0, 0.1, 0.25, 0.3) films revealed negative photovoltages at photon energies exceeding 1.75 eV, confirming that these materials are n-type semiconductors with effective bandgaps of ~1.75 eV irrespective of the Y content. The photovoltage values increased with the Y content, suggesting an improved carrier generation and separation in the materials. However, increasing the Y content also slowed down the timescales for photovoltage generation/decay indicating trap states in the materials. Based on our results, we suggest a significantly weaker as classically assumed impact of reduced *B*-site metal cations such as Ta^{4+} on the photovoltage and charge carrier recombination rate.

7.1. Introduction

Among other materials, perovskite-type oxynitrides $AB(O,N)_3$ have attracted much attention particularly as photocatalysts for direct solar water splitting (SWS).[1–10] Their perovskite-type structure is of great scientific and technological interest because it combines distinctive resistance with a large compositional flexibility allowing a controlled variation of the electronic properties. Owing to their SWS-suited optical bandgaps of $E_g \approx 2$ eV, the most thoroughly investigated perovskite-type oxynitrides contain La^{III} on the *A*-site and Ti^{IV} (ref. 11) or Ta^{V} (ref. 12–19) on the *B*-site. In former reports, often reduced transition metal (TM) ions such as reduced Ta species in $Ta^{V}ON$[20,21] or in $LaTa^{V}ON_2$ (ref. 22) were the origin of a fast charge carrier recombination and consequently a poor SWS performance. In such cases the TM ions were handled as defects introducing donor levels close to the conduction band. It was shown that an elimination of these defects enhanced the SWS activity[20,21] and slowed down the charge carrier recombination. However, a still remaining question is how a material and the respective electronic band structure (*e.g.* non-degenerated *vs.* degenerated semiconductor) behave, if only reduced TM ions (*e.g.* Ta^{4+}) as *B*-site cations are present. In accordance with experimental reports,[12,23–25] $LaTaON_2$ was identified as a promising candidate for SWS also by computational analysis of the bandgap.[26–28] However, DFT-based electronic band structure calculations showed that the energetic position of the conduction band minimum (CBM) of $LaTaON_2$ does not ideally fit to the redox potential of the water reduction reaction.[27] Instead, the perovskite-type oxynitride $YTaON_2$, which to the best of one's knowledge has not been synthesized in a single phase yet, seems to be well-suited.[27] In contrast to $LaTaON_2$, its CBM is predicted to be appropriate for the overall water splitting reaction.[27] Y-containing perovskite-type materials are only rarely studied[29–31] due to the presumable instability as reflected by the low tolerance factor *t* as defined by Li *et al.*[32], *e.g.* $t = 0.912$ for $YTaON_2$ and $t = 0.898$ for $YTaO_2N$. Geometric considerations (extension of Goldschmidt's tolerance factor) locate $YTaON_2$ on the border of the existence field of perovskite-type oxynitrides, whereas $YTaO_2N$ is located more or less outside of the existence field.[32] This higher instability, as expressed by the slightly positive heat of formation,[27] combined with the favorable band edge position is supposed to result in an enhanced reactivity as found for other catalytic systems.[33,34] Additionally, the low tolerance factors of $YTaO_2N$ and $YTaON_2$ (ref. 32) require a strong tilting of the octahedral network classically leading to a widening of the optical bandgap and a reduced dispersion of the conduction band.[27,35] This allows the adjustment of the CBM to the requirements of the water splitting reaction as theoretically demonstrated for $YTaON_2$.[27] The predicted metastability with respect to binary oxides and nitrides[27] makes it very challenging to synthesize perovskite-type $YTa(O,N)_3$, since typically a defect-fluorite-type phase $YTa(O,N,\square)_4$ sometimes accompanied by small amounts of perovskite-type phase was observed.[36–39]

We have recently reported on the controlled formation of perovskite-type oxynitrides $LaTa^{IV}O_2N$ and $LaTa^{V}ON_2$ by a precursor microstructure controlled ammonolysis.[14] A similar concept can also be applied to the synthesis of yttrium tantalum oxynitrides. In the literature, the usage of a nanocrystalline oxide precursor (n-YTO) resulted in the formation of a defect-fluorite-type phase[30,36] with a suitable optical bandgap ($E_G \approx 2.2$ eV) but without photocatalytic activity for SWS.[30] The usage of microcrystalline $YTaO_4$ (m-$YTaO_4$) allowed the formation of a low crystallized perovskite-type main phase together with a defect-fluorite-type phase and Ta_3N_5 impurities.[30] Attempts to enhance the crystallinity by raising the ammonolysis temperature resulted in transformation into a defect-fluorite-type main phase.[30] For potential photocatalysts for water splitting and photoanode materials for water oxidation under visible light not only bandgap sizes and band edge positions[40–42] are important, but also the efficiency of charge carrier separation plays an essential role. As one of the advanced analytical tools, surface photovoltage spectroscopy (SPS) is typically applied to investigate the photo-induced charge carrier separation in a material.[43–45] This method provides information about the majority charge carrier type (electron or hole), effective bandgaps, charge transfer timescales, and reversibility.[46,47]

In this work, a precursor microstructure controlled ammonolysis was combined with the gradual substitution of Y^{3+} for La^{3+} to tackle the synthetic challenge of forming $YTa(O,N)_3$. This produced the before unknown perovskite-type oxynitride family members $La_{1-x}Y_xTaO_2N$ (x = 0.1, 0.25, 0.3) and, for x = 1.0, a mixture of a perovskite-type main phase (w = 82(2) wt%) and defect-fluorite-type secondary phase (w = 18(2) wt%). The expected increasing distortion of the octahedral network induced by increasing Y content ($x \leq 0.3$) was confirmed by Rietveld refinements of high-resolution powder X-ray diffraction (HR-PXRD) patterns. However, diffuse reflectance spectroscopy (DRS) revealed a widening of the optical bandgap only up to x = 0.25 indicating that for $La_{1-x}Y_xTaO_2N$ ($x \leq 0.3$) the distortion of the octahedral network is an insufficient descriptor for the bandgap size. Instead it seems that the level of orthorhombic strain ε is crucial for the resulting bandgap. In all synthesized $La_{1-x}Y_xTa^{IV}O_2N$ (x = 0.1, 0.25, 0.3) compounds the presence of Ta^{4+} as the main oxidation state was confirmed *via* X-ray photoelectron spectroscopy (XPS) and X-ray near edge absorption structure (XANES) analysis, respectively. Superconducting quantum interference device (SQUID) measurements were used to characterize the magnetic properties. Density functional theory (DFT) calculations revealed a different band structure for $La_{1-x}Y_xTa^{IV}O_2N$ in comparison to $LaTa^{V}ON_2$ pointing to a transparent conductor-like behavior with a bandgap in the first case. The experimentally determined optical bandgaps of around 1.9 eV and low optically active defect concentrations of $LaTa^{IV}O_2N$[14] and $La_{1-x}Y_xTa^{IV}O_2N$ make these d^1 materials interesting as potential photocatalysts and as model systems to study the influence of reduced *B*-site cations on the photo-induced charge carrier separation processes. SPS measurements revealed a n-type semiconducting behavior of $La_{1-x}Y_xTaO_2N$ upon visible light exposure and similar effective bandgaps regardless of the Y content. However, small Y contents had the fastest reversible charge carrier dynamics whereas higher contents decelerated it. One reason might be the level of tilting of the octahedral network and elongation of the octahedra. Importantly, surface photovoltages of up to −1 V were observed in $La_{1-x}Y_xTa^{IV}O_2N$ ($x \leq 0.3$), demonstrating the possibility of long-lived charge carriers in "Ta^{4+}-only" materials for the first time.

7.2. Results and Discussion

Ex situ ammonolysis of Y-substituted nanocrystalline lanthanum tantalum oxide (n-LTO) (10 mol% Y, 25 mol% Y, and 30 mol% Y) with KCl flux addition leads to red $La_{0.9}Y_{0.1}TaO_2N$, orange $La_{0.75}Y_{0.25}TaO_2N$, and orange $La_{0.7}Y_{0.3}TaO_2N$ after several cycles (Fig. 1).

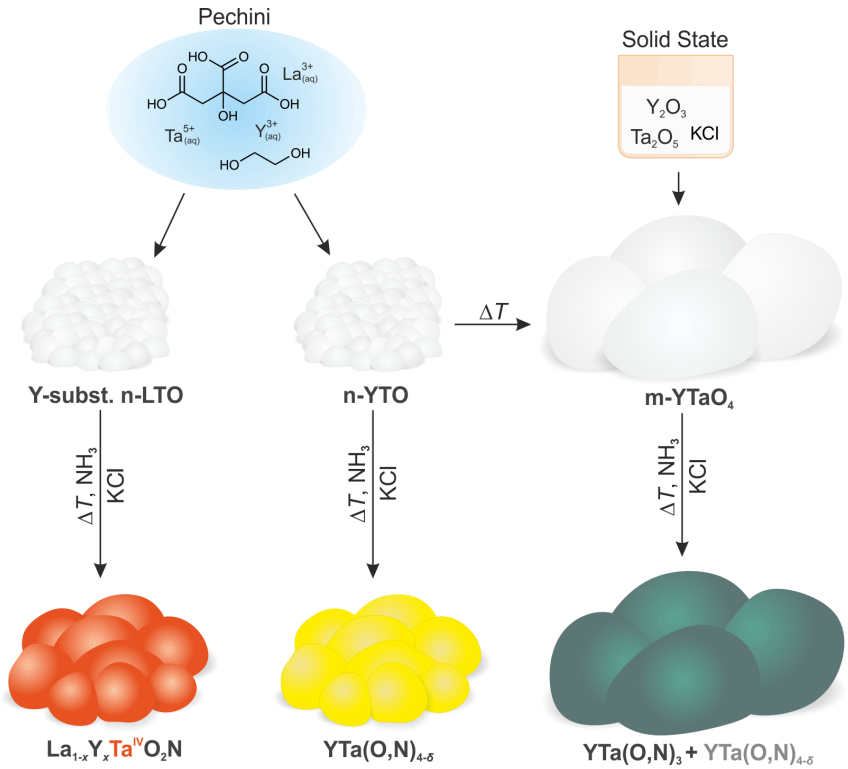

Fig. 1. Schematic synthesis paths from Y-substituted nanocrystalline lanthanum tantalum oxide (Y-subst. n-LTO), nanocrystalline yttrium tantalum oxide (n-YTO), and microcrystalline yttrium tantalate ($m\text{-}YTaO_4$) to the respective oxynitrides.

The characterization of the oxide precursors is described in the ESI (Fig. S1–S4 and Tables S1–S4). The compositions of the oxynitrides were confirmed *via* inductively coupled plasma emission spectroscopy (ICP-OES) and hot gas extraction (HGE). Similar anionic ratios were previously reported for $LaTaO_2N$.[14] In addition, to prove the observed anionic ratio of O : N = 2 : 1 during *in situ* experiments in Y-substituted $LaTaO_2N$ *in situ* ammonolysis with selected termination experiments and a subsequent reoxidation experiment by TGA were performed. The mass changes associated with *in situ* ammonolysis of 10 mol% Y-substituted n-LTO were similar to those previously reported for pure n-LTO[14] (Fig. S5, ESI†). However, the specific surface area of 9 $m^2\ g^{-1}$ for 10 mol% Y-substituted n-LTO compared to 7 $m^2\ g^{-1}$ for n-LTO[14] was apparently high enough to achieve the desired O : N ratio of 2 : 1. This was confirmed *via* HGE measurements. Hence, the earlier assumption that ammonolysis of oxide precursors exhibiting a higher specific surface area leads to oxynitrides with a higher oxygen content[14] could also be demonstrated for 10 mol% Y-substituted $LaTaO_2N$. Additionally, the assumed "soft" topotactic reaction[14] *via* an intermediate in the space group $Cmc2_1$ (alternative description $A2_1am$) which was suggested for $LaTaO_2N$ could be observed for $La_{0.9}Y_{0.1}TaO_2N$. By chemical analysis and PXRD the black colored intermediate at 1187 K in the space group $Cmc2_1$ was identified as $La_{0.9}Y_{0.1}TaO_{2.76(8)}N_{0.48(1)}\square_{0.75(9)}$ (Fig. S5, S6, and Table S5, ESI†). After *in situ* ammonolysis at 1223 K for 10 h and at 1273 K for 14 h, respectively, subsequent reoxidation of $La_{0.9}Y_{0.1}TaO_2N$ to $La_{0.9}Y_{0.1}TaO_4$ was carried out under synthetic air. The observed mass change of +4.94% was close to the calculated value of Δm_{calc} = +5.0% (reoxidation of $La_{0.9}Y_{0.1}TaO_2N$ to $La_{0.9}Y_{0.1}TaO_4$) confirming an O : N ratio of 2 : 1

during *in situ* experiments. For higher Y-substituted n-LTO (25 mol% Y and 30 mol% Y), it was found that repeated ammonolysis cycles at 1273 K for 14 h with KCl flux addition (Fig. 1) were required to achieve single phase oxynitrides. *In situ* ammonolysis studies were not performed in these cases for the protection of the TGA device.

The HR-PXRD patterns of $La_{1-x}Y_xTaO_2N$ (x = 0.1, 0.25, 0.3) revealed that all three compounds were phase pure and adopted the space group *Imma* (Fig. S7(a)–(c) and Table S6, ESI†). $LaTaO_2N$ has already been reported to have the same space group.[14] In addition to HR-PXRD, $La_{0.9}Y_{0.1}TaO_2N$ was also studied by neutron diffraction (ND) in order to receive additional information about the space group and a potential anionic long-range order (Fig. S8 and Table S7, ESI†). The refined ND data could give no indications of an anionic long-range order. The absence of long-range ordering is in agreement with crystal structure data reported in the literature.[48] The analysis of the unit cell parameters and unit cell volume obtained by Rietveld refinements of the HR-PXRD data showed that increasing Y substitution has two clear effects: a continuous decrease of the unit cell volume (Table 1) and a higher level of tilting in the octahedral network (Table S8(a), ESI†) due to the smaller ionic radius[32,49] of Y^{3+}.

Table 1. Unit cell parameters, volumes, and orthorhombic strain ε of $La_{1-x}Y_xTaO_2N$ ($0 \le x \le 0.3$) in the space group *Imma*

Unit Cell Parameter	$LaTaO_2N$[14]	$La_{0.9}Y_{0.1}TaO_2N$	$La_{0.75}Y_{0.25}TaO_2N$	$La_{0.7}Y_{0.3}TaO_2N$
a (Å)	5.7158(5)	5.7093(2)	5.6993(5)	5.7044(2)
b (Å)	8.0645(5)	8.0563(2)	8.0845(3)	8.0908(2)
c (Å)	5.7442(4)	5.7322(2)	5.6901(6)	5.6709(2)
V_{cell} (Å^3)	264.78(3)	263.66(1)	262.18(4)	261.73(2)
ε (-)	0.0025(1)	0.0020(1)	0.0008(1)	0.0029(1)

The enhanced tilting of the $[Ta(O,N)_6]^{z-}$ octahedron due to partial Y^{3+} substitution is well known for $[B(O,N)_6]^{z-}$ (B = Ti, Zr)[31] and can be visualized as a continuous reduction of the average Ta–(O/N)–Ta angles in $La_{1-x}Y_xTaO_2N$ (x = 0.1, 0.25, 0.3) (Table S8(a), ESI†). Moreover, the Ta–(O/N) bond lengths in the axial direction (b-axis) increase with increasing Y content leading to an elongation of the octahedron (Fig. S9 and Table S8(b), ESI†). At the same time, the Ta–(O/N) bond lengths in the equatorial direction (c-axis) decrease with increasing Y^{3+} content (Table S8(b), ESI†). The effects of elongation and distortion can be described by different amplitudes of the R_4^+ mode allowing a distortion of an initially cubic perovskite ($Pm\bar{3}m$) along [111] leading directly to the observed symmetry lowering to *Imma*. Even though there is already a significant tilting level reached, the HR-PXRD data suggest that the solubility limit of Y^{3+} is not yet surpassed up to x = 0.3 in $La_{1-x}Y_xTaO_2N$ (Fig. 2(a)).

For $LaTa^{IV}O_2N$ and $LaTa^{V}ON_2$ (ref. 14), the oxide precursor microstructure played an important role in determining which phase is formed. The same applies for the reaction of nanocrystalline yttrium tantalum oxide (n-YTO) to form its oxynitride. In agreement with literature reports,[30,36,37] it was not possible to prepare perovskite-type $YTa(O,N)_3$ by using n-YTO as the precursor. Even by using an expanded tested parameter array for the ammonolysis temperature (from 973 K to 1373 K) in combination with n-YTO as the precursor, only the formation of a defect-fluorite-type oxynitride phase was possible. In Fig. S10(b), ESI,† the yellowish, defect-fluorite-type $Y_{0.96(2)}Ta_{1.05(2)}O_{0.85(1)}N_{1.38(2)}\square_{1.82(3)}$ synthesized at 1023 K – containing highly reduced Ta – is shown as an example. Because, the here used n-YTO contains smaller crystallites caused by using a calcination temperature of 873 K instead of 1023 K (Si *et al.*[30]) the onset of the applied ammonolysis reaction lowered at least by 50 K. In contrast, by using a microcrystalline yttrium tantalum oxide (m-$YTaO_4$) (Fig. S10(c), ESI†), it was possible to synthesize a well-crystalline perovskite-type main phase $YTa(O,N)_3$ in the space group *Pnma* (w =

82(2) wt%) next to $YTa(O,N,\square)_4$ (w = 18(2) wt%) without XRD-detectable traces of binary nitrides such as Ta_3N_5 (Fig. S10(d), ESI†). In this study, the usage of a microcrystalline precursor in combination with a higher ammonolysis temperature of 1373 K prior to a cycle at 1273 K and a larger ammonia gas flow as in ref. 30 allowed the perovskite-type phase formation. In agreement with the predictions based on the tolerance factor t (ref. 32) mentioned above $YTa(O,N)_3$ crystallized as an orthorhombic perovskite phase but in contrast to $La_{1-x}Y_xTaO_2N$ in the space group *Pnma*. This might be due to either the unknown O : N ratio or the smaller effective ionic radius of Y^{3+} compared to La^{3+}. Regarding the dual phase nature of this sample, the determination of the nitrogen content of the individual phases by chemical analysis is not applicable. By diffraction methods a definitive answer could not be provided, as the X-ray scattering contrast between O^{2-} and N^{3-} is too low and not enough material was available for ND measurements.

An increase of the specific surface area (S_{BET}) was observed for $La_{1-x}Y_xTaO_2N$ (x = 0.1, 0.25, 0.3) by comparing the synthesized oxide precursors (9–14 $m^2\ g^{-1}$) with the respective oxynitrides (18–28 $m^2\ g^{-1}$). SEM images (Fig. 2(b)) depicted morphologies similar to that of $LaTaO_2N$[14] with visibly larger primary particle sizes compared to the respective oxides (Fig. S2(a)–(c), ESI†).

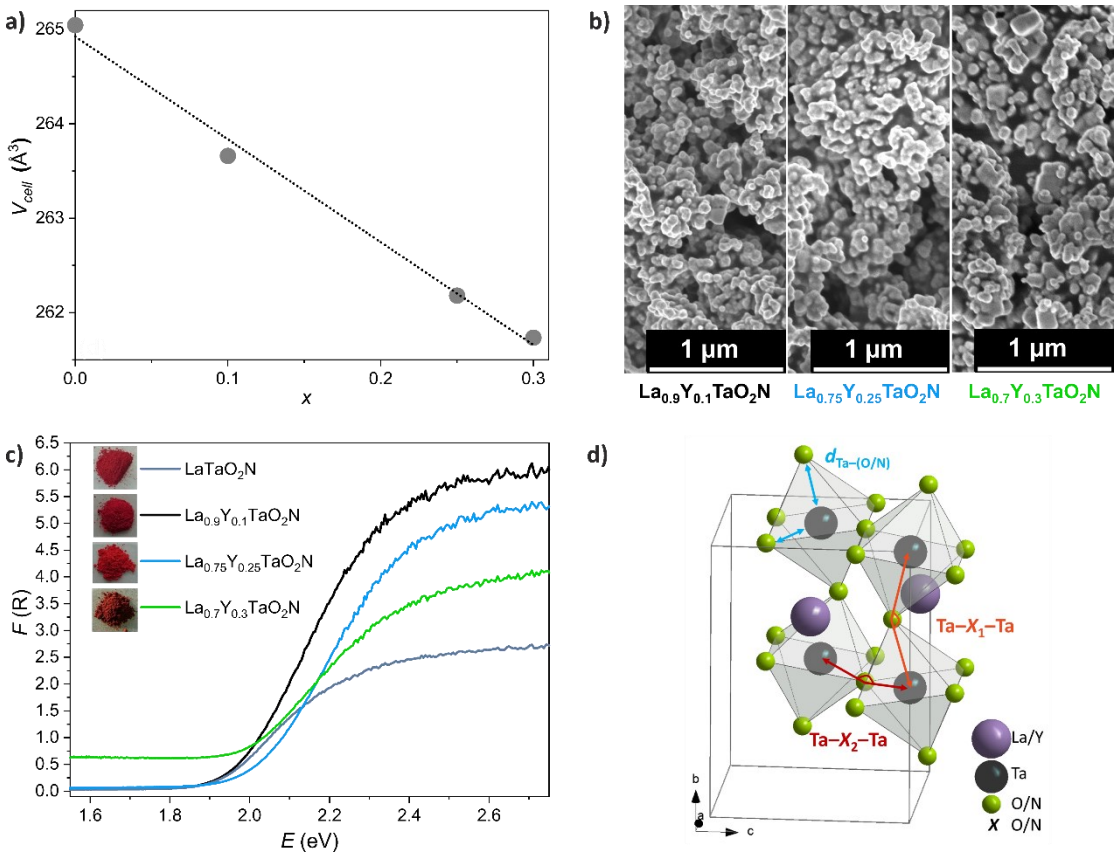

Fig. 2. (a) Vegard's plot of the refined unit cell volume of $La_{1-x}Y_xTaO_2N$ (x = 0.1, 0.25, 0.3); for x = 0 the unit cell volume of $LaTaO_2N$[14] was used as the reference. (b) SEM images of $La_{1-x}Y_xTaO_2N$ (x = 0.1, 0.25, 0.3). (c) DRS spectra of $La_{1-x}Y_xTaO_2N$ (x = 0, 0.1, 0.25, 0.3) plotted as Kubelka–Munk curves together with photographs of the received powders. (d) $La_{1-x}Y_xTaO_2N$ unit cell edges and selected $[Ta^{IV}(O,N)_6]^{z-}$ octahedra with indicated Ta–$X_{1,2}$–Ta angles (with X = O/N) and $d_{Ta-(O/N)}$ distances. The O and N anions are displayed with a reduced radius for visibility reasons.

In addition to the decrease of the unit cell volume and the increase of the distortion of the octahedral network also the observed color change from red to orange (Fig. 2(c)) indicated a widening of the bandgap. DRS measurements and applying the Kubelka–Munk conversion[50] showed a slight change of

the optical bandgap from 1.90 eV ($LaTaO_2N$) to 1.96 eV ($La_{0.75}Y_{0.25}TaO_2N$) with increasing Y substitution. In contrast $La_{0.7}Y_{0.3}TaO_2N$ (E_G = 1.88 eV) did not follow this trend even though the average Ta–(O/N)–Ta angle was further decreased (Table S8(a), ESI†). The samples $La_{0.9}Y_{0.1}TaO_2N$ (E_G = 1.92 eV) and $La_{0.75}Y_{0.25}TaO_2N$ (E_G = 1.96 eV) showed the same high color brilliance as $LaTaO_2N$.[14] In contrast, $La_{0.7}Y_{0.3}TaO_2N$ has a brownish tone originating from optically active defects. The obtained behavior of the bandgap size upon partial Y^{3+} substitution is more complex than initially expected and cannot be simply explained by one effect. In $La_{1-x}Y_xTaO_2N$ (x = 0, 0.1, 0.25, 0.3) multiple effects play a distinctive role: (i) the effect of distortion of the octahedral network (decreasing average Ta–(O/N)–Ta angles (Fig. 2(d) and Table S8(a), ESI†)) typically related to a widening of the bandgap and (ii) the elongation of the octahedra (increasing Ta–(O,N) bond lengths in the axial direction, Table S8(b), ESI†) leading to a smaller bandgap. These counteracting effects can be seen in the unexpected trend $E_{G,x=0.3} \approx E_{G,x=0} < E_{G,x=0.1} < E_{G,x=0.25}$ of the optical bandgap. The above mentioned R_4^+ mode is able to simultaneously describe both structural effects in $La_{1-x}Y_xTaO_2N$ (x = 0, 0.1, 0.25, 0.3). Based on DFT calculations using a fixed, experimentally determined orthorhombic strain only a slight variation of the R_4^+ mode amplitude by about 10% upon partial Y^{3+}-substitution was observed. This is in accordance with the determined alteration of the unit cell parameters, bond angles and lengths of the materials (Tables 1 and S8, ESI†), and the small resulting effect of the distortion of the octahedral network on the bandgap size. However, the experimentally observed changes in the bandgap data require a more complex description. The obtained variation of the unit cell parameters with the Y content x together with the different ionic radii of the A-site cations (r (La^{3+}) and r(Y^{3+})) resulted in an irregular variation of the orthorhombic strain ε – as defined in eqn (1)[51] – of the oxynitrides $La_{1-x}Y_xTaO_2N$ ($x \leq 0.3$) (Table 1).

$$\varepsilon = \left|\frac{(a-c)}{(a+c)}\right| \quad (1)$$

For $La_{1-x}Y_xTaO_2N$ ($x \leq 0.3$) the effect of the strain on the bandgap seems to dominate in comparison to the effects (distortion and elongation) resulting from a change in the amplitude of the R_4^+ mode. A clear correlation between ε and E_G can be obtained in the following way where a larger strain leads to a smaller band gap and *vice versa*. Consequently, $La_{0.7}Y_{0.3}TaO_2N$ has the smallest band gap within the series because it has the largest strain, while for $La_{0.75}Y_{0.25}TaO_2N$ the smallest strain but the largest bandgap is observed. In comparison to perovskite-type oxides ABO_3 the effect of strain on the resulting bandgap in perovskite-type oxynitrides $AB(O,N)_3$ is much more complex and experimentally far less investigated. DFT calculations suggest that the strain is an important parameter for the band structure, since a variation of the strain state can cause a change of the bandgap of more than 1 eV (ref. 52) (for $SrTiO_3$ (ref. 53) in comparison just 0.1 eV). For ABO_3 the application of both compressive and tensile stress results in a reduction of the bandgap.[52] For the oxynitrides such as $LaTiO_2N$, $CaTaO_2N$, $SrTaO_2N$, and $BaTaO_2N$ a multiparameter dependency of the bandgap from the strain is observed by DFT calculations. The application of both strains (compressive or tensile) on these materials can either cause a blue-shift or a red-shift of the bandgap depending on the following parameters: (i) unit cell volume (controlled mainly by the A-site cation), (ii) the energetic position and crystal field splitting of the B-site cations (3d *vs.* 5d) with respect to the O/N 2p orbitals, (iii) direction of applied strain in relation to the crystal axis, (iv) the type and degree of (local) O/N ordering (*cis vs. trans*), and (v) the level of octahedral rotation and the inversely correlated ferroelectric displacements.[52,54] Therefore, more combined theoretical and experimental investigations are required in the future to establish a more generally valid model to describe the interrelation between the strain and bandgap in perovskite-type oxynitrides. Besides the bandgap size also the band edge positions must match with the redox potentials of H_2O for potential SWS catalysts. The conducted electrochemical experiments and calculations (Table S9, ESI†) did not provide a conclusive answer so far to the question whether the band edge positions of $La_{1-x}Y_xTa^{IV}O_2N$ are suitable for SWS. The detailed analysis results can be

found in Table S9, ESI.† Therefore, in the following we focus on the charge carrier separation behavior and the effects of Ta^{4+} on it.

Like the samples $La_{1-x}Y_xTaO_2N$ () the defect-fluorite-type oxynitride $YTa(O,N,\square)_4$ (Table S10, ESI†) also showed a different coloration than expected from the presence of Ta ions below the 5+ state. Nonetheless, the determined optical band gap of E_G = 2.2 eV (Fig. S11, ESI†) was still in agreement with literature reports.[26,30] At lower energies than the optical bandgap no increasing background was observed pointing to a low optically active defect concentration as observed for the La-containing perovskites. In contrast, the color of the mixture of the perovskite-type $YTa(O,N)_3$ phase (greenish black) indicated a high concentration of optically active defects besides an optical bandgap of around 2 eV.

The composition of $La_{1-x}Y_xTaO_2N$ (x = 0.1, 0.25, 0.3) provides two possibilities for the oxidation state of Ta (Fig. 3(a)–(c)).

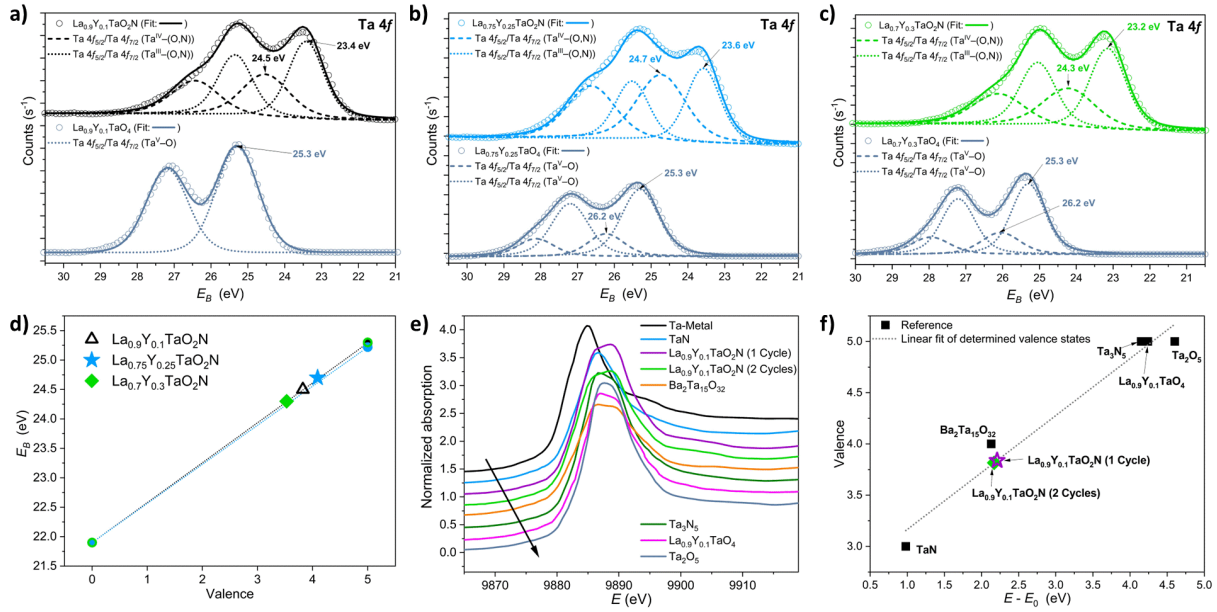

Fig. 3 (a–c) XPS spectra of the Ta 4f region of $La_{1-x}Y_xTaO_2N$ (x = 0.1, 0.25, 0.3). Microcrystalline $La_{0.9}Y_{0.1}TaO_4$ was used as a reference for Ta^{5+} and to determine the chemical shift after ammonolysis. (d) The point charge model[55,56] was applied to the spectra as described in Bubeck *et al.*[14] (e) Normalized X-ray absorption at the Ta L_{III}-edge as a function of energy for all measured compounds and (f) valence determination applying the inflection method: plot of the energy shift with respect to Ta^0 against the valence for all measured compounds.

Either it has an overall oxidation state of 4+ or it is present as 3+ and 5+ in equal shares. For a detailed evaluation of the oxidation state of Ta we analyzed the Ta 4f regions of the XPS spectra. The binding energies of the Ta $4f_{7/2}$ and Ta $4f_{5/2}$ orbitals (Table 2) obtained from the spectra (survey spectra in Fig. S12, ESI†) were consistent with the values determined for the Ta^{4+} compound $LaTa^{IV}O_2N$.[14] As recently reported for $LaTaO_2N$[14] by applying the point charge model,[14,55,56] a chemical shift to lower binding energies by more than 0.3 eV indicates a change of the Ta oxidation state from 5+ to 4+. Therefore, the binding energies of $La_{1-x}Y_xTaO_2N$ (x = 0.1, 0.25, 0.3) are consistent with either a Ta^{IV}–(O,N) or a Ta^{III}–(O,N) binding character (Table 2). The Ta $4f_{7/2}$ binding energies for the Ta^{V}–O binding character of microcrystalline $La_{0.9}Y_{0.1}TaO_4$ ($E_{B,Ta\ 4f7/2}$ = 25.3 eV), $La_{0.75}Y_{0.25}TaO_4$ ($E_{B,Ta\ 4f7/2}$ = 25.2 eV) and $La_{0.7}Y_{0.3}TaO_4$ ($E_{B,Ta\ 4f7/2}$ = 25.3 eV) were used as Ta^{5+} references, respectively (Fig. 3(a)–(c)). In contrast to recent literature reports on $LaTaON_2$ (ref. 12 and 14) and $PrTaO_2N$,[12] our data did not provide any evidence of the presence of Ta^{5+} in $La_{1-x}Y_xTaO_2N$ (x = 0.1, 0.25, 0.3). The $E_{B,Ta(V)\ 4f7/2}$ values reported

there (*e.g.* 28.03 eV,[12] 27.46 eV,[12] and 25.0 eV (ref. 14)) significantly exceed our measurement results. A massive peak broadening or significant double peak splitting described for the above mentioned compounds[12] was not observed either in our measurement data. Thus, the observed anionic composition of $La_{1-x}Y_xTaO_2N$ can be explained by the presence of Ta^{4+} (d^1 state). The slightly lower binding energy of the Ta^{IV}–(O,N) binding character in $La_{0.7}Y_{0.3}TaO_2N$ can be attributed to the higher number of ammonolysis cycles required at 1273 K leading to an enhanced reduction to Ta^{3+} at the surface and nitrogen enrichment[14] in the chemical environment of the $[Ta^{IV}(O,N)_6]^{z-}$ octahedron.

Table 2. Binding energies of the Ta 4f region of $La_{1-x}Y_xTaO_2N$ (x = 0.1, 0.25, 0.3) with the respective binding characters determined *via* the point charge model

Compound	$E_{B,\mathrm{Ta}\ 4f7/2}$ (eV)	$E_{B,\mathrm{Ta}\ 4f5/2}$ (eV)	Binding Character
$La_{0.9}Y_{0.1}TaO_2N$	23.4	25.4	Ta^{III}–(O,N)
	24.5	26.4	Ta^{IV}–(O,N)
$La_{0.75}Y_{0.25}TaO_2N$	23.6	25.5	Ta^{III}–(O,N)
	24.7	26.6	Ta^{IV}–(O,N)
$La_{0.7}Y_{0.3}TaO_2N$	23.2	25.1	Ta^{III}–(O,N)
	24.3	26.2	Ta^{IV}–(O,N)

Additionally, the N and O weight fractions were calculated from the peak areas of the respective fitted orbitals. O/N ratios of 2, 1.92, and 1.79 were determined for 10, 25 and 30 mol% Y-substitution in $La_{1-x}Y_xTaO_2N$, respectively. This matches quite well with the anionic compositions determined *via* reoxidation and HGE measurements (Table S11, ESI†). The determined O/N ratios support the above given interpretation of the shifted binding energy by nitrogen enrichment in the surrounding of Ta. The small deviation from the theoretical O/N ratio of 2 can also be resulting from the overlapping of N 1s, Y 3s, and Ta 4p orbitals.

Given by the small mean free path of photo-emitted electrons (normally between 1 and 10 nm (ref. 57)) XPS is a surface-sensitive method. Therefore, the assumed change of the oxidation state from Ta^{5+} to Ta^{4+} during ammonolysis of the oxide precursors was additionally studied in the bulk *via* XANES at the Ta-L_{III} edge (Fig. 3). As reference materials, well-defined Ta oxidation states of Ta metal, TaN, $Ba_2Ta_{15}O_{32}$, Ta_3N_5, $La_{0.9}Y_{0.1}TaO_4$, and Ta_2O_5 were used for the XANES data analysis. The samples $La_{0.9}Y_{0.1}TaO_2N$ (ammonolyzed once at 1223 K) and $La_{0.9}Y_{0.1}TaO_2N$ (ammonolyzed twice: 1× at 1223 K, 1× at 1273 K + KCl flux addition) were measured and their determined normalized absorption was plotted against the energy (Fig. 3(e)). The Ta-L_{III} absorption edges of both $La_{0.9}Y_{0.1}TaO_2N$ samples are located in-between the Ta-L_{III} absorption edges of the Ta^{3+} and Ta^{5+} reference materials and close to the Ta-L_{III} absorption edge of $Ba_2Ta^{IV}{}_{15}O_{32}$, which have been synthesized according to Siegrist *et al.*[58] As expected, the absorption edge shifted to higher energies with increasing oxidation state of Ta.[59] According to Henderson *et al.*[57] a shift of the *L*-edges by about 1.5 eV per valence is expected. For Si even a shift of 2.2 eV per valence[57] was observed. In our case, a shift of 2.1–2.2 eV with respect to the Ta^0 reference was determined for $La_{0.9}Y_{0.1}TaO_2N$ (1 and 2 cycles). Since the oxidation state or valence state, respectively, is linearly correlated with the energy shift,[57] an oxidation state between +3.8 and +3.9, close to the expected +4, was obtained in the bulk (Fig. 3(f)). Hence, a uniform oxidation state could be demonstrated for the bulk and the surface region. This finding is in good accordance with the anionic ratio of O : N = 2 : 1 obtained from chemical analysis and XPS data. On closer examination of the curve shapes of $La_{0.9}Y_{0.1}TaO_2N$, $Ba_2Ta_{15}O_{32}$, and $La_{0.9}Y_{0.1}TaO_4$, a double structure in the white line is visible. According to Rietveld refinements, Ta is surrounded by six anions in a distorted octahedral coordination suggesting a crystal field splitting. This crystal field splitting becomes obvious in the Ta-L_{III} transition since it probes the (partially) empty 5d states with electrons from the occupied 2p states.[60] Crystal field splitting values of 4 eV (ref. 60) and even 5.5–6 eV (ref. 61) were reported for

Ta^{5+} in $KTaO_3$ and Ta-substituted TiO_2 solid solutions, respectively. For both $La_{0.9}Y_{0.1}TaO_2N$ samples a smaller peak splitting of 2.5 eV was observed. This points to a lower oxidation state since the oxidation state and crystal field splitting energy are correlated.[61] Additionally, distortion in the octahedral environment of the centered cation increases the crystal field splitting according to theoretical models.[57] Since the effective ionic radius of Ta^{4+} ($r_{eff}(Ta^{4+})$ = 0.68 Å (ref. 27)) is larger than that of Ta^{5+} ($r_{eff}(Ta^{5+})$ = 0.64 Å (ref. 27)) and the effective radius of K^+ ($r_{eff}(K^+)$ = 1.64 Å (ref. 27)) is larger than those of La^{3+} and Y^{3+}, the distortion in both $La_{0.9}Y_{0.1}TaO_2N$ samples is expected to be lower than that in $KTaO_3$. This is consistent with our measurements and the fact that $r_{eff}(Ta^{4+}) > r_{eff}(Ta^{5+})$ also explains the different peak splitting values of $La_{0.9}Y_{0.1}TaO_2N$ (2.5 eV) and $La_{0.9}Y_{0.1}TaO_4$ (2.8 eV).

The $5d^1$ electronic configuration of tantalum (Ta^{4+}) was further analyzed *via* SQUID measurements (Fig. S13(a) and (b), ESI†). The obtained $M(H)$ curves reveal different saturation magnetizations of 3.46×10^{-4} emu (x = 0.1) and of 9.19×10^{-4} emu (x = 0.25) which are equivalent to effective magnetic moments of 0.0011 μ_B/Ta (x = 0.1) and 0.0031 μ_B/Ta (x = 0.25), respectively. Additionally, to the paramagnetism, $La_{0.75}Y_{0.25}Ta^{IV}O_2N$ showed a very small ferromagnetic-like contribution. To separate the observed ferromagnetic (FM) contribution, it was subtracted from the low temperature hysteresis of the sample. Similar FM-like contributions were also observed in other bulk non-magnetic materials, with nominal d^0 contribution, which were identified as non-stoichiometric surface states.[62–64] By applying a Brillouin function[65] fit (shown in the insets of Fig. S13(a)–(c), ESI†) to investigate the paramagnetism a magnetic moment of 2.1 μ_B for both samples was estimated. This is in contrast to the calculated small μ_B/Ta values for both samples, showing that just a tiny fraction of the Ta ions show paramagnetism with a moment of 2.1 μ_B. The determined 2.1 μ_B for both samples is consistent with surface related Ta^{3+} impurity ions ($5d^2$ with assumed 2 μ_B/magnetic ion), which were detected by XPS (Fig. 3(a)–(c)). If we assume a 50% presence of Ta^{3+} in the first 0.1 nm of each nanoparticle, we can calculate the surface to volume ratio with which the same reduced total μ_B/Ta is obtained. This results in typical particle sizes in the range of 100–300 nm, consistent with the obtained SEM results in Fig. 2(b). By calculating the quantitative amount of Ta^{3+} and Ta^{4+} for x = 0.1 one Ta^{3+} per 1914 Ta^{4+} ions and for x = 0.25 one Ta^{3+} per 670 Ta^{4+} ions are obtained, respectively. This confirms the small amount of Ta^{3+} and points to the suggested "Ta^{4+}-all" materials and that Ta^{3+} is just located on the samples' surface. A similar nearly non-magnetic behavior was already observed for $LaTa^{IV}O_2N$ and $LaTa^{V}ON_2$ (ref. 14) and, hence, a similar orbital hybridization for $La_{1-x}Y_xTaO_2N$ is assumed. Fixed magnetic calculations at 0 K (Fig. S13(d), ESI†) showed for $LaTa^{V}ON_2$, $LaTa^{IV}O_2N$, and $La_{0.75}Y_{0.25}Ta^{IV}O_2N$ a positive energy upon addition of a magnetic moment pointing to a non-magnetic behavior of the respective oxynitrides.

The simultaneous presence of reduced *B*-site cations with d^1 electron configuration and a significant optical band gap is quite unusual and might point to a transparent conductor-like behavior. Indeed, from the electronic band structure and consequently the density of states (DOS), the existence of metallic Ta 5d states was visible (Fig. S14, ESI†). Such behavior is well known from heavily doped degenerated semiconductors such as transparent conducting fluorine-doped tin oxide (FTO)[66] and indium-doped tin oxide (ITO).[67] Another even closer related example is the red metallic photocatalyst $Sr_{1-x}NbO_3$ (Nb^{4+}) with an optical band gap of 1.9 eV showing a very similar electronic band structure[68] to $La_{1-x}Y_xTaO_2N$. A detailed discussion of the electronic band structure can be found in the ESI, section "Electronic band structure".† The calculated optical conductivity[61] of $La_{1-x}Y_xTaO_2N$ (Fig. 4(a)) agreed as well with this by showing a strong increase of the conductivity at energies below around 0.5 eV pointing to the presence of metallic states. However, at energies higher than 3.5 eV a second increase of the calculated optical conductivity was obtained caused by the absorption of photons with an energy higher than the bandgap. For $LaTa^{V}ON_2$ as expected no absorption was obtained at energies lower than the bandgap in the calculated optical conductivity due to the $5d^0$ electronic configuration of Ta^{5+} (Fig. 4(a)).

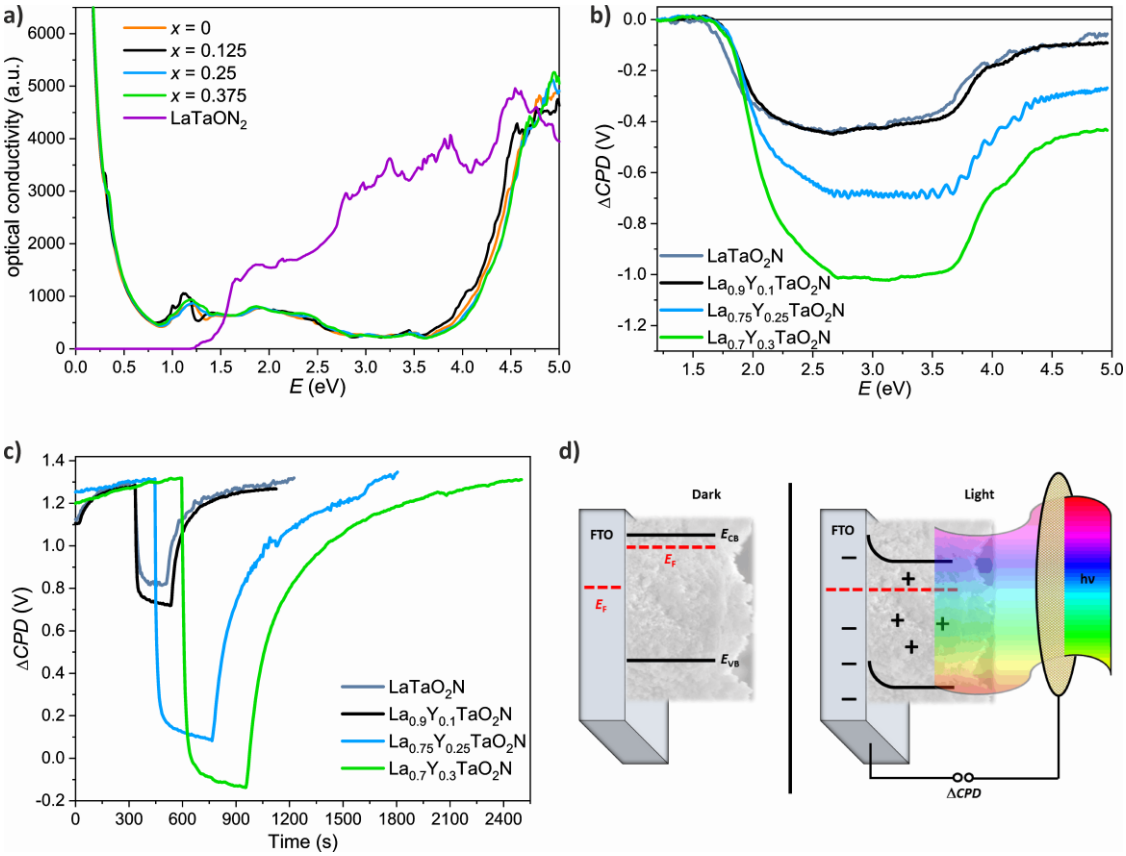

Fig. 4 (a) Calculated optical conductivity of $La_{1-x}Y_xTaO_2N$ (x = 0, 0.125, 0.25, 0.375) and $LaTaON_2$. (b) Surface photovoltage spectra (SPS) of all $La_{1-x}Y_xTaO_2N$ sample films on FTO. ΔCPD denoted the contact potential difference change under illumination, *i.e.* the photovoltage. (c) Chopped light scans of all $La_{1-x}Y_xTaO_2N$ samples under monochromatic illumination at 2.48 eV (on: ~300–600 s; off: ~500–960 s). (d) Energy diagram of the $La_{1-x}Y_xTaO_2N$/FTO interface before and after illumination.

The ability of oxynitrides to separate photogenerated charge carriers under illumination was studied by surface photovoltage spectroscopy (SPS) of 800–1500 nm thick particulate films on fluorine doped tin oxide (FTO) substrates. The SPS data are presented in Fig. 4(b) and (c) (for numerical data and photos of the films see Table S12 and Fig. S15, ESI†). All $La_{1-x}Y_xTaO_2N$ films produced negative photovoltage ranging from −0.44 V to −1.01 V due to electron injection into the FTO substrate (Fig. 4(d)). This indicates that all samples are n-type semiconductors. As can be seen from the exemplary calculated electronic band structure of $LaTa^{V}ON_2$ (Fig. S14(a), ESI†), a direct bandgap was obtained. This is beneficial for light-driven applications and light absorption. In contrast, the band structures of $LaTa^{IV}O_2N$ and $La_{0.875}Y_{0.125}Ta^{IV}O_2N$ (Fig. S14(b) and (c), ESI†) point to a degenerated semiconductor. The maximum photovoltage was reached at 2.75 eV for most materials, which coincides with the maximum spectral emission intensity from the Xe-lamp (Fig. S16, ESI†). The photovoltage value increases in the order $LaTaO_2N$, $La_{0.9}Y_{0.1}TaO_2N$ < $La_{0.75}Y_{0.25}TaO_2N$ < $La_{0.7}Y_{0.3}TaO_2N$, suggesting improved charge carrier separation for the more heavily Y-substituted samples. Based on tangential approximation of the major photovoltage feature, the effective bandgaps ranged from 1.65 eV to 1.78 eV. These values are 0.25 eV to 0.12 eV below the measured optical bandgaps of $E_G \approx 1.9$ eV for $La_{1-x}Y_xTaO_2N$ (x = 0, 0.1, 0.25, 0.3). The difference indicates a small concentration of visible light-active states near the band edges in the materials. These states are observable in SPS even though their concentration is too small to contribute to the visible absorption spectra. After concluding the SPS scan, the films were left in the dark until a stable voltage signal was achieved. Then, chopped light scans were applied under monochromatic illumination at 2.48 eV to examine the reversibility of photo-induced charge separation in each material (Fig. 4(c)). The time constants, τ, in Table S12 (ESI†)

correspond to the amount of time required to achieve 63.21% of the final photovoltage after turning the light on or off. The sample $La_{0.9}Y_{0.1}TaO_2N$ (x = 0.1) had the fastest photovoltage generation/decay (τ_{on} = 7.62 s, τ_{off} = 73 s) compared to *e.g.* the Y-free sample (τ_{on} = 22 s; τ_{off} = 89 s), suggesting that the introduction of a small amount of Y improves the charge carrier transport rate. The τ_{on} and τ_{off} values of the other samples increased with increasing Y content, meaning charge carrier transport became slower. Besides changes in the electronic structure of the material, induced by Y-substitution, other reasons for the increased τ_{on} times could be an increase in the particle packing density in the films, resulting from a change in the particle morphology upon substitution with Y^{3+}, or a change in the concentration of the hole traps at the particle surfaces, allowing faster trapping of photogenerated holes in the Y-substitution materials. A strong surface state-dependent photovoltage formation due to hole trapping has been observed before *e.g.* for Fe_2O_3 nanorod arrays.[69] The larger photovoltage values correspond to an enhanced separation of the photogenerated charge carriers. It has already been reported that the presence of reduced *B*-site metal cations such as Ti^{III} (ref. 70 and 71) or Ta^{IV} (ref. 72) can cause fast recombination of photogenerated electrons and holes significantly decreasing the photovoltage. However, based on the SPS data in Fig. 4(b), the Ta^{4+}-only materials $La_{1-x}Y_xTa^{IV}O_2N$ (x = 0, 0.1, 0.25, 0.3) are able to generate and separate charge carriers based on the photovoltage. A reason for this might be hidden in beneficial effects caused by the octahedral network distortion and elongation of the $[Ta^{IV}(O,N)_6]^{z-}$ octahedra as well as the altered electronic band structure overcompensating the traditionally assumed detrimental effect of Ta^{4+}.

7.3. Conclusion

In conclusion, perovskite-type d^1 materials $La_{0.9}Y_{0.1}Ta^{IV}O_2N$, $La_{0.75}Y_{0.25}Ta^{IV}O_2N$, $La_{0.7}Y_{0.3}Ta^{IV}O_2N$ were produced *via ex situ* ammonolysis of 10 mol%, 25 mol%, and 30 mol% Y-substituted n-LTO – achieved *via* the Pechini method – successfully expanding the applicability of our recently published precursor microstructure controlled ammonolysis. Using n-YTO and m-$YTaO_4$ as precursors allowed synthesizing either a defect-fluorite-type phase $YTa(O,N,\square)_4$ or the highest weight fraction of perovskite-type $YTa(O,N)_3$ known so far next to small amounts of $YTa(O,N,\square)_4$. For visible light-driven energy conversion processes the bandgap size is a crucial material parameter. In this context, a mixture of $YTa(O,N)_3$ and a defect-fluorite phase showed a greenish black color with an optical band gap of around 2 eV and broad range absorption. In contrast, the pure defect fluorite-phase showed a yellowish color with a well-defined optical bandgap of 2.2 eV. In $La_{1-x}Y_xTa^{IV}O_2N$ ($x \leq 0.3$) increasing Y substitution revealed an unexpected trend of the optical bandgap ($E_{G,x=0.3} \approx E_{G,x=0} < E_{G,x=0.1} < E_{G,x=0.25}$) with unusual colors ranging from red to orange. XPS and XANES data revealed that the oxidation state of Ta in $La_{1-x}Y_xTaO_2N$ is predominantly 4+. In accordance, DFT calculations showed the presence of metallic Ta 5d states next to a fundamental bandgap obvious from the calculated optical conductivity. The combination of crystal structure analysis and DFT calculations suggests orthorhombic strain as the main reason for the experimentally observed optical bandgap trends. The octahedral network distortion and elongation of the octahedra play additional roles.

Furthermore, SPS revealed an unexpected, remarkable photovoltage and a visible light-driven charge carrier separation even in the presence of reduced *B*-site cations, namely Ta^{4+} and Ta^{3+}. The increasing partial substitution of Y^{3+} for La^{3+} in $La_{1-x}Y_xTa^{IV}O_2N$ (x = 0, 0.1, 0.25, 0.3) indicated an improved charge carrier generation and separation for the "Ta^{4+}-all" materials on the basis of larger photovoltage values. These results confirm the possibility of photophysical charge separation in degenerate semiconductors with large free carrier concentrations (from Ta^{4+} states).

7.4. Experimental

7.4.1. Synthesis of Y-substituted n-LTO and $La_{1-x}Y_xTaO_2N$

Nanocrystalline Y-substituted n-LTO (x_Y = 10 mol%, 25 mol%, and 30 mol%) and n-YTO precursors were prepared by the same sol–gel-related method as described previously.[14] Y substitution was accomplished by providing an appropriate amount of $Y(NO_3)_3{\cdot}6H_2O$ (Alfa Aesar, 99.9%) according to the mol% fraction (x = 0, 0.1, 0.25, 0.3, 1.0) in addition to $La(NO_3)_3{\cdot}6H_2O$ (Sigma Aldrich, 99.99%) in a second Schlenk flask. Further details about the oxide precursors are summarized in the ESI.† The oxynitrides $La_{1-x}Y_xTaO_2N$ ($x \leq 0.3$) were prepared from the respective nanocrystalline oxide precursors *via* thermal gas flow (*ex situ*) ammonolysis as previously reported in detail:[14] 200 mg of the oxides were transferred into an Al_2O_3 boat and ammonolyzed once at 1223 K for 10 h under flowing NH_3 (300 mL min^{-1}, Westfalen AG, >99.98%). This was followed by repeated *ex situ* ammonolysis cycles with KCl flux addition (weight ratio 1 : 1) at 1273 K for 14 h until phase purity was achieved. The higher the Y substitution, the more ammonolysis steps (up to 10) were required. For the synthesis of yttrium tantalum oxynitrides the precursors n-YTO and m-$YTaO_4$ were used. m-$YTaO_4$ was prepared by a solid state reaction similar to that in Bubeck *et al.*[14] For n-YTO the ammonolysis temperature was varied from 973 K to 1373 K keeping the reaction time constant at 14 h. m-$YTaO_4$ was ammonolyzed first at 1373 K for 10 h, and then for 14 h at 1273 K with KCl flux addition using several repetitions. The ammonia flow rate was in both cases the same as that for $La_{1-x}Y_xTaO_2N$ (300 mL min^{-1}).

Caution: ammonia is a toxic and corrosive gas and have to be handled only by supervised and trained persons in special apparatus not allowing the emission of ammonia into the laboratory atmosphere.

7.4.2. Films of $La_{1-x}Y_xTaO_2N$ for Surface Photovoltage Spectroscopy

Fluorine-doped tin oxide (FTO) substrates (12–14 Ω sq^{-1}, MTI Corporation) were cleaned by sonication in acetone, methanol, isopropanol, and water (purified to about 18 MΩ cm resistivity with a Nano-pure filtration system) for 10 min each, and dried in air. Separate suspensions of the $La_{1-x}Y_xTaO_2N$ powders in water with a concentration of 0.5 mg mL^{-1} were prepared. After sonication for 15 minutes, 0.05 mL of each suspension was drop-coated onto the FTO substrates. The coverage area (0.5 cm × 0.5 cm) was controlled with a polyester masking tape (Cole Parmer). After drying at ambient temperature, the films were heated on a hot plate at 373 K for 90 min in air. Photos of the films are included in the ESI.† The films were between 800 nm and 1500 nm thick as determined with a stylus-type Veeco Dektak profilometer.

7.4.3. Density Functional Theory (DFT) Calculations

The DFT calculations were performed using the full potential local-orbital minimum-basis method as implemented in the FPLO code.[73,74] The exchange-correlation functional was parameterized using the generalized gradient approximation (GGA).[75] The lattice parameters and atomic positions were adopted from the experimental data in order to have a direct comparison. A 16 × 16 × 16 k-mesh was used to guarantee a good convergence. Due to the limited size of the supercell, a simplified model to implement the partial Y substitution was used by replacing 1, 2 or 3 La by Y. This resulted in $La_{0.875}Y_{0.125}TaO_2N$, $La_{0.75}Y_{0.25}TaO_2N$, and $La_{0.625}Y_{0.375}TaO_2N$ as representatives of $La_{0.9}Y_{0.1}TaO_2N$, $La_{0.75}Y_{0.25}TaO_2N$, and $La_{0.7}Y_{0.3}TaO_2N$, respectively. Virtual crystal approximation was applied to model the experimentally observed disordered mixture of O and N atoms in the oxynitrides. In order to understand the experimental SQUID measurements, fixed moment calculations are done with the resulting total energies with respect to the total magnetic moments of the unit cells shown in Fig. S9,

ESI.† The band structures for the supercells are unfolded into the Brillouin zone of the primitive cell (Fig. S14, ESI†), which allows us to make a direct comparison. The optical conductivities are evaluated based on the complex dielectric functions including both the intraband and interband contributions.

7.4.4. Characterization

Powder X-Ray Diffraction (PXRD) measurements were carried out on a Rigaku Smartlab powder X-ray diffractometer using Ni-filtered Cu-$K_{\alpha 1,2}$ radiation in order to examine the phase purity and crystal structure of the oxides and oxynitrides. High-resolution (HR) synchrotron radiation PXRD measurements of selected oxide and oxynitride samples were performed at the beamline ID22 of the European Synchrotron Radiation Facility (ESRF) in Grenoble, France. The diffraction data were analyzed by Rietveld refinements[76,77] using FullProf. 2k.[78]

A potential long-range order of O and N in the $La_{0.9}Y_{0.1}TaO_2N$ sample was investigated *via* high resolution neutron diffraction at ambient temperature on SPODI at the Research Neutron Source Heinz Maier-Leibnitz (FRM II) in Garching, Germany.[79] Approximately 200 mg of the sample were loaded in a standard vanadium cylinder with a 6 mm outer diameter. The measurement was carried out at a wavelength of λ = 1.54818(2) Å using a take-off angle of 155° of the (551) atomic plane of the Ge monochromator.

The cationic composition of the samples was studied by inductively coupled plasma emission spectroscopy (ICP-OES) on a Spectro Ciros CCD ICP-OES instrument. The anionic composition was determined by hot gas extraction (HGE) using an Eltra ONH-2000 analyzer. Each sample was measured at least three times.

In situ ammonolysis under flowing NH_3 (80 mL min^{-1} NH_3 + 8 mL min^{-1} Ar) was carried out *via* thermogravimetric analysis (TGA) on a Netzsch STA 449F3 Jupiter with a Perseus-coupled Bruker FTIR spectrometer (Alpha). The subsequent reoxidation of $La_{0.9}Y_{0.1}TaO_2N$ was done under synthetic air (50 mL min^{-1} syn. air + 20 mL min^{-1} Ar).

To determine the oxidation state of Ta in $La_{1-x}Y_xTaO_2N$ and Y-substituted n-LTO, X-ray photoelectron spectroscopy (XPS) was performed with a Thermo VG Theta Probe 300 XPS system (Thermo Fisher Scientific). The incident beam had a spot size of 400 μm and was monochromatic with micro-focused Al-K_α radiation. A carbon tape was used as the sample holder and a flood gun was used to avoid undesirable charging effects. A Shirley-type inelastic background was chosen for background subtraction. The XPS spectra were analyzed as described previously.[14]

The morphology of the produced oxides and oxynitrides was investigated *via* scanning electron microscopy (SEM) (ZEISS GeminiSEM 500, 5 kV) using an in-lens detector.

UV-visible diffuse reflectance spectroscopy (DRS) was performed with a Carry 5000 UV-VIS NIR spectrophotometer. The baseline was measured with $BaSO_4$ as the reference. The optical bandgap was estimated by using the Kubelka–Munk conversion[50] and applying the tangential method.[14,32]

Nitrogen sorption was applied to obtain the data to determine the specific surface areas of the materials. First, the samples were annealed at 393 K to remove adsorbed water. Adsorption and desorption isotherms were recorded at liquid nitrogen temperature with an Autosorb-1-MP (detection limit: S_{BET} > 1 m^2 g^{-1}) from Quantachrome Instruments. The specific surface areas were determined by the Brunauer–Emmett–Teller[80] (BET) method.

X-ray absorption near-edge structure (XANES) characterization was carried out at the Spanish beamline BM25A SpLine[81] at ESRF. The measurements were performed in transmission mode using three high precision ionization chambers and an ethanol-cooled (203 K) double Si(111) crystal monochromator with an energy resolution of $\Delta E/E$ = 1.4 × 10^{-4}. The samples were pelletized with

cellulose for transmission measurements. The concentration of the samples was calculated to obtain an absorption jump of $\Delta\mu_{tot} \approx 1$ at the Ta L_{III}-edge (9.881 keV). XANES data were normalized using the Athena software package.[82]

Magnetometer surveys were carried out with a commercial VSM MPMS3 Superconducting Quantum Interference Device (SQUID) from Quantum Design. This system allows both conventional DC and VSM-type measurements. The hysteresis loops were measured at 2 K while the field was switched from −4 T to 4 T. For zero field cooling purposes the magnet was quenched to minimize the residual magnetic field. Depending on the sample and measurement type the effective sensitivity was in the range of 10^{-8} to 10^{-9} emu.

Surface photovoltage spectroscopy (SPS) measurements were performed using a vibrating gold mesh Kelvin probe (3 mm diameter, Delta PHI Besocke) mounted 1 mm above the film samples. The samples were placed inside a home-built vacuum chamber ($p \approx 10^{-4}$ mbar with a Pfeiffer HiCube 80 Eco turbo pump station). Monochromatic radiation was provided by a 150 W Xe lamp using an Oriel Cornerstone 130 monochromator ($I_0 \approx 1$ mW cm^{-2}). It was not compensated for the variable light intensity of the Xe lamp. A signal drift in the spectra was corrected by subtracting a dark background from the raw data. All reported contact potential difference (CPD) values were corrected by the CPD value in the dark. Effective bandgaps were obtained from the major photovoltage signals of the spectra using the tangent method. Charge separation reversibility was examined with light on/off scans under 2.48 eV monochromatic illumination.

7.5. Author Contributions

C. B. developed and synthesized the oxide precursors and perovskite-type oxynitrides, and performed and analyzed *in situ* ammonolysis, PXRD, DRS and TGA. M. W. and A. W. contributed to the discussion of the analysis. A. D. and F. O. performed and interpreted the SPS results with input from C. B. and M. W. M. C. and M. W. measured together HR-PXRD, whereas the data were refined by C. B. C. B., M. W., S. Y., and M. C. further interpreted the resulting Rietveld refinements from HR-PXRD and ND. G. R. and C. B. interpreted together the XPS data. E. S. C. and C. B. elaborated collectively the XANES data measured by E. S. C. E. G. and C. B. measured and interpreted the SQUID data. H. Z. performed and analyzed the DFT calculations with input from C. B. and M. W. C. B. wrote the paper. A. W. provided the research topic and contributions to the conclusions.

7.6. Conflicts of interest

All authors declare no conflicts of interest. All authors approved the submission of the manuscript.

7.7. Acknowledgements

The authors thank Mr Peter Schützendübe, Mr Samir Hammoud (Max Planck Institute for Intelligent Systems, Stuttgart), Mrs Annette Fuchs, Prof. Dr Joachim Maier, and Prof. Dr Bettina Lotsch (Max Planck Institute for Solid State Research, Stuttgart) for their help with XPS, chemical analysis, nitrogen sorption, and DRS, respectively. We thank Dr Angelika Verziridis (Institute for Material Science, University of Stuttgart) for fruitful discussions and Antoine Masson Grehaigne for synthesizing m-$YTaO_4$ and fruitful discussions regarding $YTa(O,N)_3$. We thank Dr Anatoliy Senyshyn (Heinz Maier-Leibnitz Zentrum (MLZ), Garching) for fruitful discussions regarding neutron diffraction and measuring the ND data. The band unfolding was done with the help of M.Sc. Niloofar Hadaeghi. The authors acknowledge the financial support and granted radiation beam time of the European Synchrotron Radiation Facility, Grenoble, France and Heinz Maier-Leibnitz Zentrum (MLZ), Garching,

Germany. This work was supported by the Deutsche Forschungsgemeinschaft within the priority program SPP 1613 “Solar H_2” (WE 2803/7-1). Support for surface photovoltage spectroscopy measurements was provided by the U.S. Department of Energy, Office of Science, Office of Basic Energy Sciences, under Grant DOE-SC0015329.

7.8. References

1 G. Zhang, G. Liu, L. Wang and J. T. S. Irvine, *Chem. Soc. Rev.*, 2016, 45, 5951–5984.

2 S. G. Ebbinghaus, H. P. Abicht, R. Dronskowski, T. Müller, A. Reller and A. Weidenkaff, *Prog. Solid State Chem.*, 2009, **37**, 173–205.

3 X. Chen, S. Shen, L. Guo and S. S. Mao, *Chem. Rev.*, 2010, **110**, 6503–6570.

4 J. Seo, T. Hisatomi, M. Nakabayashi, N. Shibata, T. Minegishi, M. Katayama and K. Domen, *Adv. Energy Mater.*, 2018, **8**, 1800094.

5 Y. K. Gaudy, S. Dilger, S. Landsmann, U. Aschauer, S. Pokrant and S. Haussener, *J. Mater. Chem. A*, 2018, **6**, 17337–17352.

6 J. Seo, M. Nakabayashi, T. Hisatomi, N. Shibata, T. Minegishi, M. Katayama and K. Domen, *J. Mater. Chem. A*, 2019, **7**, 493–502.

7 X. Sun, F. Wu, G. Liu and X. Xu, *J. Mater. Chem. A*, 2018, **6**, 20760–20768.

8 S. Ninova and U. Aschauer, *J. Mater. Chem. A*, 2017, **5**, 11040–11046.

9 M. Kodera, H. Urabe, M. Katayama, T. Hisatomi, T. Minegishi and K. Domen, *J. Mater. Chem. A*, 2016, **4**, 7658–7664.

10 M. Hojamberdiev, E. Zahedi, E. Nurlaela, K. Kawashima, K. Yubuta, M. Nakayama, H. Wagata, T. Minegishi, K. Domen and K. Teshima, *J. Mater. Chem. A*, 2016, **4**, 12807–12817.

11 A. E. Maegli, E. H. Otal, T. Hisatomi, S. Yoon, C. M. Leroy, N. Schäuble, Y. Lu, M. Grätzel and A. Weidenkaff, *Energy Procedia*, 2011, **22**, 61–66.

12 M. Hojamberdiev, M. F. Bekheet, J. N. Hart, J. J. M. Vequizo, A. Yamakata, K. Yubuta, A. Gurlo, M. Hasegawa, K. Domen and K. Teshima, *Phys. Chem. Chem. Phys.*, 2017, **19**, 22210–22220.

13 R. Marchand, F. Pors and Y. Laurent, *Ann. Chim. Fr.*, 1991, **16**, 553–560.

14 C. Bubeck, M. Widenmeyer, G. Richter, M. Coduri, E. Goering, S. Yoon and A. Weidenkaff, *Commun. Chem.*, 2019, **2**, 134.

15 C. Pan, T. Takata, K. Kumamoto, S. S. Khine Ma, K. Ueda, T. Minegishi, M. Nakabayashi, T. Matsumoto, N. Shibata, Y. Ikuhara and K. Domen, *J. Mater. Chem. A*, 2016, **4**, 4544–4552.

16 H. Kato, K. Ueda, M. Kobayashi and M. Kakihana, *J. Mater. Chem. A*, 2015, **3**, 11824–11829.

17 S. Ninova and U. Aschauer, *J. Mater. Chem. A*, 2019, **7**, 2129–2134.

18 J. Zhou, C. Zhou, Z. Shi, Z. Xu, S. Yan and Z. Zou, *J. Mater. Chem. A*, 2018, **6**, 7706–7713.

19 Y. Liu, W. Wang, X. Xu, J. P. Marcel Veder and Z. Shao, *J. Mater. Chem. A*, 2019, **7**, 7280–7300.

20 K. Maeda, H. Terashima, K. Kase, M. Higashi, M. Tabata and K. Domen, *Bull. Chem. Soc. Jpn.*, 2008, **81**, 927–937.

21 K. Maeda, M. Higashi, D. Lu, R. Abe and K. Domen, *J. Am. Chem. Soc.*, 2010, **132**, 5858–5868.

22 M. Hojamberdiev, M. F. Bekheet, J. N. Hart, J. J. M. Vequizo, A. Yamakata, K. Yubuta, A. Gurlo, M. Hasegawa, K. Domen and K. Teshima, *Phys. Chem. Chem. Phys.*, 2017, **19**, 22210–22220.

23 M. Liu, W. You, Z. Lei, T. Takata, K. Domen and C. Li, *Chinese J. Catal.*, 2006, **27**, 556–558.

24 L. Zhang, Y. Song, J. Feng, T. Fang, Y. Zhong, Z. Li and Z. Zou, *Int. J. Hydrogen Energy*, 2014, **39**, 7697–7704.

25 S. K. Suram, S. W. Fackler, L. Zhou, A. T. N’Diaye, W. S. Drisdell, J. Yano and J. M. Gregoire, *ACS Comb. Sci.*,

2018, **20**, 26–34.

26 I. E. Castelli, J. M. García-Lastra, F. Hüser, K. S. Thygesen and K. W. Jacobsen, *New J. Phys.*, 2013, **15**, 105026.

27 I. E. Castelli, D. D. Landis, K. S. Thygesen, S. Dahl, I. Chorkendorff, T. F. Jaramillo and K. W. Jacobsen, *Energy Environ. Sci.*, 2012, **5**, 9034–9043.

28 I. E. Castelli, K. S. Thygesen and K. W. Jacobsen, *J. Mater. Chem. A*, 2015, **3**, 12343–12349.

29 R. Vadapoo, M. Ahart, M. Somayazulu, N. Holtgrewe, Y. Meng, Z. Konopkova, R. J. Hemley and R. E. Cohen, *Phys. Rev. B*, 2017, **95**, 1–5.

30 W. Si, Z. P. Tehrani, F. Haydous, N. Marzari, I. E. Castelli, D. Pergolesi and T. Lippert, *J. Phys. Chem. C*, 2019, **123**, 26211–26217.

31 M. Widenmeyer, C. Peng, A. Baki, W. Xie, R. Niewa and A. Weidenkaff, in *Solid State Sciences*, 2016, **54**, pp. 7–16.

32 W. Li, E. Ionescu, R. Riedel and A. Gurlo, *J. Mater. Chem. A*, 2013, **1**, 12239–12245.

33 K. S. Exner, *ChemElectroChem*, 2018, **5**, 3243–3248.

34 R. Parsons, *Trans. Faraday Soc.*, 1958, **54**, 1053–1063.

35 M. Pichler, J. Szlachetko, I. E. Castelli, N. Marzari, M. Döbeli, A. Wokaun, D. Pergolesi and T. Lippert, *ChemSusChem*, 2017, **10**, 2099–2106.

36 P. Maillard, F. Tessier, E. Orhan, F. Cheviré and R. Marchand, *Chem. Mater.*, 2005, **17**, 152–156.

37 H. Schilling, H. Wolff, R. Dronskowski and M. Lerch, *Zeitschrift fur Naturforsch. - Sect. B J. Chem. Sci.*, 2006, **61**, 660–664.

38 H. Wolff, H. Schilling, M. Lerch and R. Dronskowski, *J. Solid State Chem.*, 2006, **179**, 2265–2270.

39 P. Maillard, O. Merdrignac-Conanec and F. Tessier, *Mater. Res. Bull.*, 2008, **43**, 30–37.

40 M. Zhong, T. Hisatomi, Y. Sasaki, S. Suzuki, K. Teshima, M. Nakabayashi, N. Shibata, H. Nishiyama, M. Katayama, T. Yamada and K. Domen, *Angew. Chemie Int. Ed.*, 2017, **56**, 4739–4743.

41 J. Su, T. Minegishi, Y. Kageshima, H. Kobayashi, T. Hisatomi, T. Higashi, M. Katayama and K. Domen, *J. Phys. Chem. Lett.*, 2017, **8**, 5712–5717.

42 T. Hisatomi, J. Kubota and K. Domen, *Chem. Soc. Rev.*, 2014, **43**, 7520–7535.

43 L. Kronik and Y. Shapira, *Surf. Sci. Rep.*, 1999, **37**, 1–206.

44 X. Ma, X. Cui, Z. Zhao, M. A. Melo, E. J. Roberts and F. E. Osterloh, *J. Mater. Chem. A*, 2018, **6**, 5774–5781.

45 M. Rodríguez-Pérez, E. J. Canto-Aguilar, R. García-Rodríguez, A. T. De Denko, G. Oskam and F. E. Osterloh, *J. Phys. Chem. C*, 2018, **122**, 2582–2588.

46 M. A. Melo, Z. Wu, B. A. Nail, A. T. De Denko, A. F. Nogueira and F. E. Osterloh, *Nano Lett.*, 2018, **18**, 805–810.

47 Z. Wu, Z. Zhao, G. Cheung, R. M. Doughty, A. R. Ballestas-Barrientos, B. Hirmez, R. Han, T. Maschmeyer and F. E. Osterloh, *J. Electrochem. Soc.*, 2019, **166**, H3014–H3019.

48 S. H. Porter, Z. Huang and P. M. Woodward, *Cryst. Growth Des.*, 2014, **14**, 117–125.

49 P. Hartman and H. K. Chan, *Pharm. Res. An Off. J. Am. Assoc. Pharm. Sci.*, 1993, **10**, 1052–1058.

50 G. Kortüm, W. Braun and G. Herzog, *Angew. Chemie Int. Ed. English*, 1963, **2**, 333–341.

51 P. Thiel, S. Populoh, S. Yoon, G. Saucke, K. Rubenis and A. Weidenkaff, *J. Phys. Chem. C*, 2015, **119**, 21860–21867.

52 N. Vonrüti and U. Aschauer, *Phys. Rev. Mater.*, 2018, **2**, 105401.

53 R. F. Berger, C. J. Fennie and J. B. Neaton, *Phys. Rev. Lett.*, 2011, **107**, 1–5.

54 Z. C. Zhao, C. L. Yang, Q. T. Meng, M. S. Wang and X. G. Ma, *Appl. Phys. A Mater. Sci. Process.*, 2019, 125, 789.

55 D. Briggs and J. T. Grant, *Surface Analysis by Auger and X-ray Photoelectron Spectroscopy*, IM Publications, 2003.

56 C. Nordling, *Angew. Chemie*, 1972, **4**, 144–153.

57 G. S. Henderson, F. M. F. De Groot and B. J. A. Moulton, *Rev. Mineral. Geochemistry*, 2014, **78**, 75–138.

58 T. Siegrist, R. J. Cava and J. J. Krajewski, *Mater. Res. Bull.*, 1997, **32**, 881–887.

59 J. E. Penner-Hahn, *Encycl. Life Sci.*, 2005, 2–5.

60 A. O. Ibidunni, R. L. Masaitis, R. L. Opila, A. J. Davenport, H. S. Isaacs and J. A. Taylor, *Surf. Interface Anal.*, 1993, **20**, 559–564.

61 B. Poumellec, J. F. Marucco and E. Touzelin, *Phys. status solidi*, 1986, **137**, 519–531.

62 J. M. D. Coey, *Solid State Sci.*, 2005, **7**, 660–667.

63 Y. C. Chen, E. Goering, L. Jeurgens, Z. Wang, F. Phillipp, J. Baier, T. Tietze and G. Schütz, *Appl. Phys. Lett.*, 2013, **103**, 162405.

64 T. Tietze, P. Audehm, Y. C. Chen, G. Schütz, B. B. Straumal, S. G. Protasova, A. A. Mazilkin, P. B. Straumal, T. Prokscha, H. Luetkens, Z. Salman, A. Suter, B. Baretzky, K. Fink, W. Wenzel, D. Danilov and E. Goering, *Sci. Rep.*, 2015, **5**, 5 : 8871.

65 B. D. Cullity and C. D. Graham, *Introduction to magnetic materials*, John Wiley & Sons Inc., 2nd edn., 2008.

66 D. Tatar and B. Düzgün, *Pramana - J. Phys.*, 2012, **79**, 137–150.

67 J. Jia, A. Takaya, T. Yonezawa, K. Yamasaki, H. Nakazawa and Y. Shigesato, *J. Appl. Phys.*, 2019, **125**, 245303.

68 H. Liu, X. Shi, F. Xu, L. Zhang, W. Zhang, L. Chen, Q. Li, C. Uher, T. Day and G. Snyder Jeffrey, *Nat. Mater.*, 2012, **11**, 422–425.

69 T. L. Shelton, N. Harvey, J. Wang and F. E. Osterloh, *Appl. Catal. A Gen.*, 2016, **521**, 168–173.

70 T. Takata and K. Domen, *J. Phys. Chem. C*, 2009, **113**, 19386–19388.

71 M. Widenmeyer, T. Kohler, M. Samolis, A. T. D. Denko, X. Xiao, W. Xie, F. E. Osterloh and A. Weidenkaff, *Zeitschrift fur Phys. Chemie*, 2020, 1–23.

72 Y. Wang, S. Jin, G. Pan, Z. Li, L. Chen, G. Liu and X. Xu, *J. Mater. Chem. A*, 2019, **7**, 5702–5711.

73 K. Koepernik and H. Eschrig, *Phys. Rev. B - Condens. Matter Mater. Phys.*, 1999, **59**, 1743–1757.

74 Please also see http://www.fplo.de for the documentation of the code.

75 J. P. Perdew, K. Burke and M. Ernzerhof, *Phys. Rev. Lett.*, 1996, **77**, 3865–3868.

76 H. M. Rietveld, *Acta Crystallogr.*, 1967, **22**, 151–152.

77 H. M. Rietveld, *J. Appl. Crystallogr.*, 1969, **2**, 65–71.

78 J. Rodriguez-Carvajal, FullProf. 2k, version 5.30, 2012, ILL.

79 M. Hoelzel, A. Senyshyn and O. Dolotko, *J. large-scale Res. Facil. JLSRF*, 2015, **1**, 5.

80 S. Brunauer, P. H. Emmett and E. Teller, *J. Am. Chem. Soc.*, 1938, **60**, 309–319.

81 G. R. Castro, *J. Synchrotron Radiat.*, 1998, **5**, 657–660.

82 B. Ravel and M. Newville, *J. Synchrotron Radiat.*, 2005, **12**, 537–541.

7.9. Supplementary Information

7.9.1. Y-substituted, nanocrystalline lanthanum tantalum oxide (n-LTO)

After synthesis and calcination at 923 K the oxide precursors (10 mol% Y, 25 mol% Y, 30 mol% Y) were nanocrystalline (Fig. S1 a)) and white as reported for n-LTO[1].

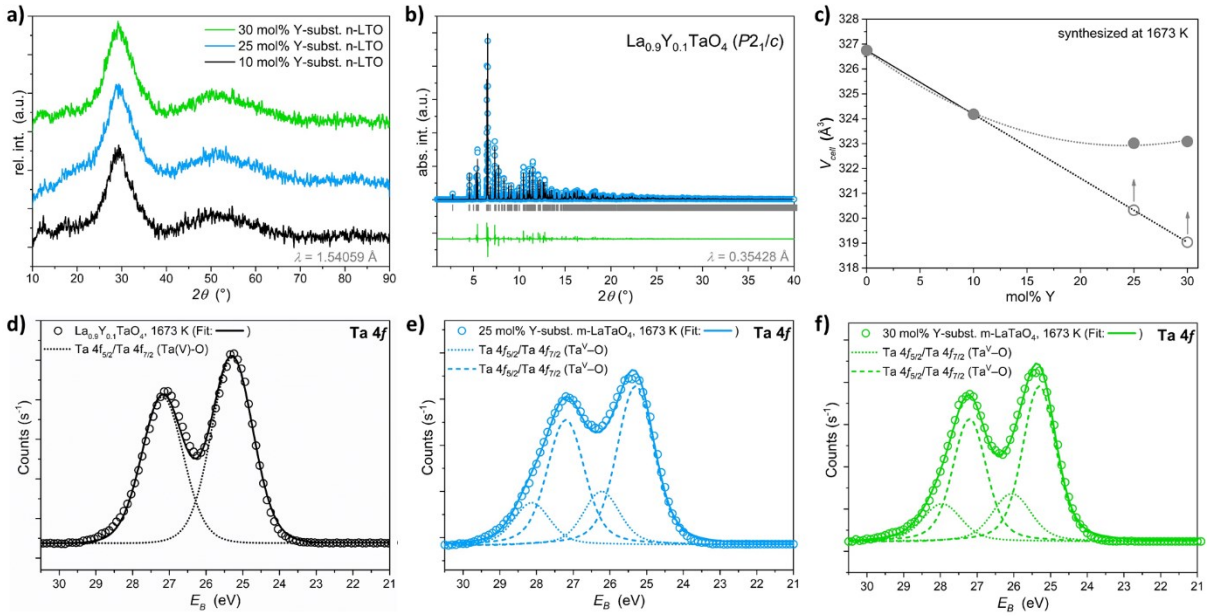

Fig. S1. a) PXRD patterns of Y-substituted nanocrystalline lanthanum tantalum oxide (n-LTO) (10 mol% Y, 25 mol% Y, 30 mol% Y) precursors. b) Rietveld refinements of the crystal structure of microcrystalline $La_{0.9}Y_{0.1}TaO_4$ in space group $P2_1/c$ from HR-PXRD data. c) Vegard's plot of the unit cell volumes of microcrystalline oxide precursors (10 mol% Y, 25 mol% Y, 30 mol% Y). The open circles represent the expected unit cell volume and the closed circles the determined unit cell volume. d)-f) XPS spectra of the Ta 4*f* region of Y-substituted microcrystalline $LaTaO_4$ (m-$LaTaO_4$) (10 mol% Y, 25 mol% Y, 30 mol% Y) samples treated at 1673 K. The solid line stands for the overall fit, the open circles represent the measurement data and the scattered lines are the fitting results of the Ta 4*f* orbitals.

The synthesized Y-substituted n-LTO powders had specific surface areas between 9 m^2/g and 14 m^2/g which were slightly larger than that of n-LTO[1]. The morphologies of Y-substituted n-LTO (10 mol% Y, 25 mol% Y, 30 mol% Y) were similar to each other and had very small primary particles in the nm-range (Fig. S2 a)-c)). In contrast to m-$LaTaO_4$[1] and heavily Y-substituted m-$LaTaO_4$ (25 mol% Y and 30 mol% Y), 10 mol% Y-substituted m-$LaTaO_4$ ($La_{0.9}Y_{0.1}TaO_4$, Fig. S1 b)) was reproducibly single-phase after crystallization and could be refined in the monoclinic space group $P2_1/c$ (Fig. S1 b)). Synthesis of the two other Y-substituted m-$LaTaO_4$ (25 mol% Y, 30 mol% Y) samples resulted in two polymorphs which could be refined in the space groups $Cmc2_1$ and $P2_1/c$. The refinements of the HR-PXRD patterns revealed even a third phase (Fig. S3 a) and b)) which, however, was not observed by the XPS spectra of the Ta 4*f* region (Fig. S1 d)-f)). The fact that the third phase was only detected by HR-PXRD in the bulk sample can be explained by the surface-sensitivity of the XPS method resulting from the small mean-free path (normally between 1 and 10 nm^2) of the photo-emitted electrons. The third phase was identified as $YTaO_4$ refined in the space group $P2/a$. The Vegard's plot shown in Figure S1 c) indicates a solubility limit of Y^{3+} in $LaTaO_4$ of approximately 10 mol% since the unit cell volumes of the samples with a nominal Y content of 25 mol% and 30 mol% did not differ much from that of the sample with 10 mol% Y. A similar solubility of Y has been previously observed in $Ca_{1-x}Y_xZrO_{3+0.5x}$.[3] Chemical analysis showed that the Y solubility of the oxynitrides $La_{1-x}Y_xTaO_2N$ (Fig. 2 a) exceeds

~10 mol% Y which was achieved for the 25 mol% and 30 mol% Y-substituted m-$La_{1-x}Y_xTaO_4$ (Tab. S2 a), b) and S3 a), b)). XPS measurements of the Ta 4*f* region of Y-substituted m-$LaTaO_4$ (10 mol% Y, 25 mol% Y, 30 mol% Y) were performed after treatment at 1673 K in order to have a Ta^{5+} reference. The XPS Ta 4*f* spectra of 25 mol% Y and 30 mol% Y were fitted with two binding states, while only one binding state was sufficient for $La_{0.9}Y_{0.1}TaO_4$ (Fig. S1 d)-f)). Hence, the presence of the two phases with space groups $Cmc2_1$ and $P2_1/c$ mentioned above was confirmed *via* the Ta 4*f* XPS data. The determined binding energies of the Ta $4f_{7/2}$ orbitals of all samples were in good agreement with already reported data of Ta(V)–O binding characters.[1,4,5] Since two binding states were sufficient to fit the data of the samples with Y contents of 25 mol% and 30 mol% despite the evidence of a third phase in the HR-PXRD patterns, the binding energy assignment was not entirely possible. The binding energies of the Ta $4f_{5/2}$ and the Ta $4f_{7/2}$ orbitals are listed in Table S4. Application of the Kubelka-Munk[6] function on the DRS measurement data revealed optical band gaps of E_G = 4.5 ± 0.1 eV for Y-substituted n-LTO (10 mol% Y, 25 mol% Y, 30 mol% Y) (Fig. S4). These were good in agreement with the optical band gap of n-LTO[1] and m-$LaTaO_4$[1].

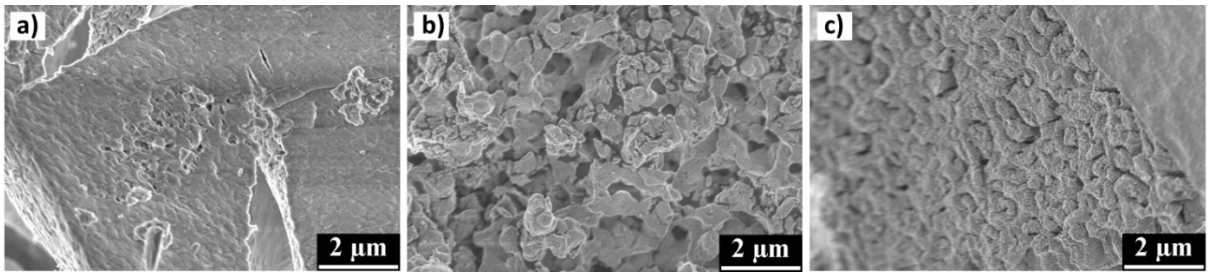

Fig. S2. SEM images of the white nanocrystalline Y-substituted n-LTO oxide precursors. a) 10 mol% Y. b) 25 mol% Y and c) 30 mol% Y.

Tab. S1. a) Unit cell parameters of m-$La_{0.9}Y_{0.1}TaO_4$.

Unit Cell Parameter	$La_{0.9}Y_{0.1}TaO_4$
***a* (Å)**	7.63033(8)
***b* (Å)**	5.55665(6)
***c* (Å)**	7.79671(8)
***β* (°)**	101.2852(6)
V_{cell} **(Å³)**	324.181(6)
Space group	$P2_1/c$
Phase fraction (wt.-%)	100
R_p **(%)**	11.2
R_{wp} **(%)**	14.9
χ^2	10.6
R_{Bragg} **(%)**	8.81

Tab. S1. b) Refined atom positions of m-$La_{0.9}Y_{0.1}TaO_4$ in space group $P2_1/c$ synthesized at 1673 K.

Atom	Wyck. Symb.	x	y	z	B_{iso} (Å^2)	sof.[a]
La	4*e*	0.34351(2)	0.7724(5)	0.09718(2)	1.013(4)	0.9[b]
Y	4*e*	0.34351(2)	0.7724(5)	0.09718(2)	1.013(4)	0.1[b]
Ta	4*e*	0.16824(1)	0.2652(3)	0.30151(2)	0.820(2)	1[b]
O(1)	4*e*	0.161(2)	0.153(2)	0.043(2)	1[b]	1[b]
O(2)	4*e*	0.062(2)	0.584(3)	0.216(2)	1[b]	1[b]
O(3)	4*e*	0.377(2)	0.468(3)	0.333(2)	1[b]	1[b]
O(4)	4*e*	0.343(2)	0.009(3)	0.359(2)	1[b]	1[b]

[a]site occupation factor, [b]fixed

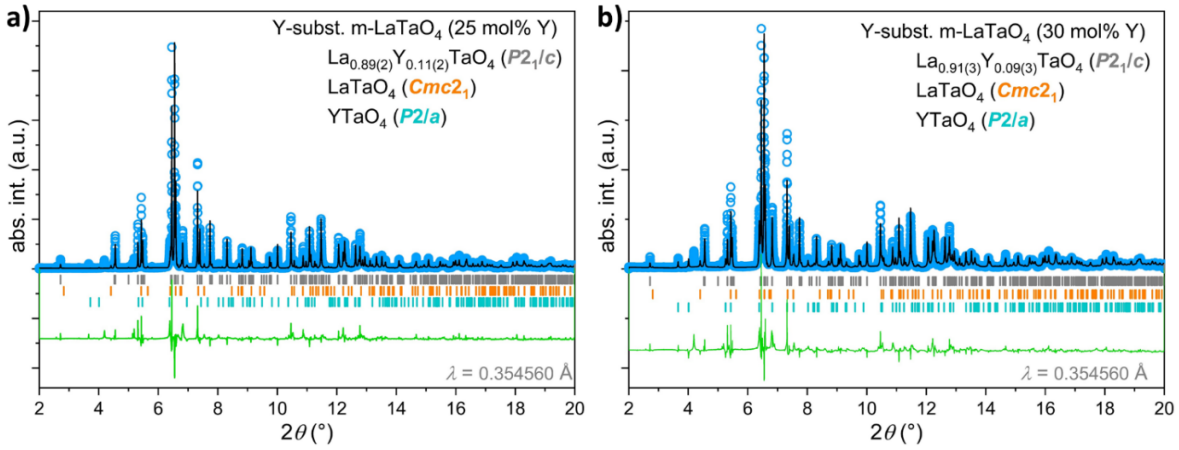

Fig. S3. Rietveld refinements of the HR-PXRD data of a) Y-substituted m-$LaTaO_4$ (25 mol% Y) and b) Y-substituted m-$LaTaO_4$ (30 mol% Y). The reflection positions of $LaTaO_4$ in the space group $Cmc2_1$ are marked in violet and those of $La_{1-x}Y_xTaO_4$ in the space group $P2_1/c$ in gray. The reflections of the third phase $YTaO_4$ in space group $P2/a$ are marked in blue.

Tab. S2. a) Unit cell parameters of both polymorphs of Y-substituted m-$LaTaO_4$ (25 mol% Y) and $YTaO_4$ synthesized at 1673 K (HR-PXRD data).

Unit Cell Parameter	$La_{0.89(2)}Y_{0.11(2)}TaO_4$	$LaTaO_4$	$YTaO_4$
***a* (Å)**	7.63354(2)	3.8792(5)	5.3534(2)
***b* (Å)**	5.55541(2)	14.3987(2)	5.4682(2)
***c* (Å)**	7.79508(2)	5.9953(7)	5.1089(2)
***β* (°)**	101.2300(2)	90	97.318(2)
V_{cell} **(Å^3)**	324.240(2)	334.87(7)	148.34(8)
Space group	$P2_1/c$	$Cmc2_1$	$P2/a$
Phase fraction (wt.-%)	90.12(1)	7.54(3)	2.34(2)
R_p **(%)**		19.5	
R_{wp} **(%)**		25.3	
χ^2		27.9	
R_{Bragg} **(%)**	16.6	42.5	66.0

Tab. S2. B) Refined atom positions of $La_{0.89(2)}Y_{0.11(2)}TaO_4$ in space group $P2_1/c$ in Y-substituted m-$LaTaO_4$ (25 mol% Y).

Atom	Wyck. Symb.	X	y	z	B_{iso} (Å^2)	sof.[a]
La	4*e*	0.3430(4)	0.7729(1)	0.0966(4)	1.030(1)	0.89(2)
Y	4*e*	0.3430(4)	0.7729(1)	0.0966(4)	1.030(1)	0.11(2)
Ta	4*e*	0.1652(3)	0.2635(1)	0.3042(3)	1.054(8)	1[c]
O(1)	4*e*	0.175[b]	0.157[b]	0.052[b]	2[c]	1[c]
O(2)	4*e*	0.052[b]	0.589[b]	0.207[b]	2[c]	1[c]
O(3)	4*e*	0.381[b]	0.485[b]	0.335[b]	2[c]	1[c]
O(4)	4*e*	0.334[b]	0.009[b]	0.381[b]	2[c]	1[c]

[a]site occupation factor, [b]adopted from Kurova *et al.*[7], [c]fixed

Tab. S2. c) Refined atom positions of $LaTaO_4$ in space group $Cmc2_1$ in Y-substituted m-$LaTaO_4$ (25 mol% Y).

Atom	Wyck. Symb.	x	y	Z	B_{iso} (Å^2)	sof.[a]
La	4*a*	0	0.1755(2)	0.3971(2)	1[c]	1[c]
Ta	4*a*	0	0.4129(1)	0.3266(2)	1[c]	1[c]
O(1)	4*a*	0	0.304[b]	0.408[b]	2[c]	1[c]
O(2)	4*a*	0	0.331[b]	0.871[b]	2[c]	1[c]
O(3	4*a*	0	0.470[b]	0.532[b]	2[c]	1[c]
O(4)	4*a*	0	0.915[b]	0.250[b]	2[c]	1[c]

[a]site occupation factor, [b]adopted from Titov *et al.*[8], [c]fixed

Tab. S2. d) Refined atom positions of $YTaO_4$ in space group $P2/a$ in Y-substituted m-$LaTaO_4$ (25 mol% Y).

Atom	Wyck. Symb.	x	y	z	B_{iso} (Å^2)	sof.[a]
Y	2*f*	¼	0.739(2)	0	1[c]	1[c]
Ta	2*e*	¼	0.207(9)	½	1[c]	1[c]
O(1)	4*g*	0.489[b]	0.434[b]	0.268[b]	2[c]	1[c]
O(2)	4*g*	0.102[b]	0.084[b]	0.252[b]	2[c]	1[c]

[a]site occupation factor, [b]adopted from Brixner *et al.*[9], [c]fixed

Tab. S3. a) Unit cell parameters of both polymorphs of Y-substituted m-$LaTaO_4$ (30 mol%) and $YTaO_4$ synthesized at 1673 K (HR-PXRD data).

Unit Cell Parameter	$La_{0.91(3)}Y_{0.09(3)}TaO_4$	$LaTaO_4$	$YTaO_4$
***a* (Å)**	7.6326(2)	3.8454(2)	5.4159(6)
***b* (Å)**	5.5559(2)	14.540(6)	5.5545(7)
***c* (Å)**	7.7950(3)	6.008(2)	5.0900(5)
***β* (°)**	101.245(2)	90	95.473(9)
V_{cell} **(Å^3)**	324.209(2)	335.9(3)	152.42(3)
Space group	$P2_1/c$	$Cmc2_1$	$P2/a$
Phase fraction (wt.-%)	79.29(8)	3.03(2)	17.68(4)
R_p **(%)**		17.6	
R_{wp} **(%)**		23.6	
χ^2		20.2	
R_{Bragg} **(%)**	13.4	38.2	33.1

Tab. S3. b) Refined atom positions of $La_{0.913(3)}Y_{0.09(3)}TaO_4$ in space group $P2_1/c$ in Y-substituted m-$LaTaO_4$ (30 mol% Y).

Atom	Wyck. Symb.	*x*	*y*	*z*	B_{iso} (Å^2)	sof.[a]
La	4*e*	0.3436(5)	0.7717(1)	0.0973(5)	1.651(2)	0.91(3)
Y	4*e*	0.3436(5)	0.7717(1)	0.0973(5)	1.651(2)	0.09(3)
Ta	4*e*	0.1663(4)	0.2621(1)	0.3038(4)	1.805(9)	1[c]
O(1)	4*e*	0.175[b]	0.157[b]	0.052[b]	2[c]	1[c]
O(2)	4*e*	0.052[b]	0.589[b]	0.207[b]	2[c]	1[c]
O(3)	4*e*	0.381[b]	0.485[b]	0.335[b]	2[c]	1[c]
O(4)	4*e*	0.334[b]	0.009[b]	0.381[b]	2[c]	1[c]

[a]site occupation factor, [b]adopted from Kurova *et al.*[7], [c]fixed

Tab. S3. c) Refined atom positions of $LaTaO_4$ in space group $Cmc2_1$ in Y-substituted m-$LaTaO_4$ (30 mol% Y).

Atom	Wyck. Symb.	*x*	*y*	*z*	B_{iso} (Å^2)	sof.[a]
La	4*a*	0	0.253(5)	0.170(6)	1[c]	1[c]
Ta	4*a*	0	0.447(3)	0.532(5)	1[c]	1[c]
O(1)	4*a*	0	0.304[b]	0.408[b]	2[c]	1[c]
O(2)	4*a*	0	0.331[b]	0.871[b]	2[c]	1[c]
O(3)	4*a*	0	0.470[b]	0.532[b]	2[c]	1[c]
O(4)	4*a*	0	0.915[b]	0.250[b]	2[c]	1[c]

[a]site occupation factor, [b]adopted from Titov *et al.*[8], [c]fixed

Tab. S3. D) Refined atom positions of $YtaO_4$ in space group *P2/a* in Y-substituted m-$LaTaO_4$ (30 mol% Y).

Atom	Wyck. Symb.	*X*	*y*	*z*	B_{iso} (Å^2)	sof.[a]
Y	2*f*	¼	0.734(4)	0	1[c]	1[c]
Ta	2*e*	¼	0.286(2)	½	1[c]	1[c]
O(1)	4*g*	0.489[b]	0.434[b]	0.268[b]	2[c]	1[c]
O(2)	4*g*	0.102[b]	0.084[b]	0.252[b]	2[c]	1[c]

[a]site occupation factor, [b]adopted from Brixner *et al.*[9], [c]fixed

Tab. S4. Binding energies of the Ta $4f_{5/2}$ and the respective Ta $4f_{7/2}$ orbitals of Y-substituted m-$LaTaO_4$ (10 mol% Y, 25 mol% Y, 30 mol% Y).

Compound	$E_{B.Ta\ 4f5/2}$ (eV)	$E_{B.Ta\ 4f7/2}$ (eV)
$La_{0.9}Y_{0.1}TaO_4$	27.2	25.3
Y-substituted m-$LaTaO_4$ (x_Y = 25 mol%)	28.0	26.1
	27.2	25.3
Y-substituted m-$LaTaO_4$ (x_Y = 30 mol%)	27.1	25.2
	28.1	26.2

7.9.2. DRS spectra of the oxide precursors Y-subst. n-LTO and nanocrystalline yttrium tantalum oxide (n-YTO)

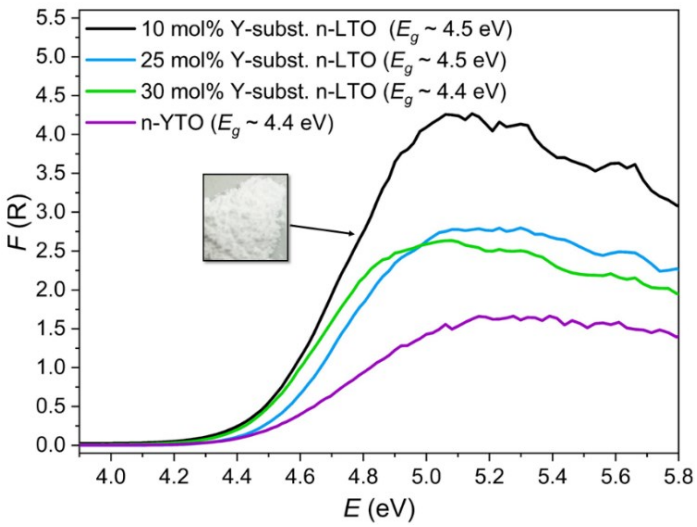

Fig. S4. Diffuse reflectance spectra - converted to a Kubelka-Munk[6] plot - of Y-substituted n-LTO (10 mol% Y, 25 mol% Y, 30 mol% Y) and n-YTO.

7.9.3. Oxynitrides $La_{1-x}Y_xTaO_2N$

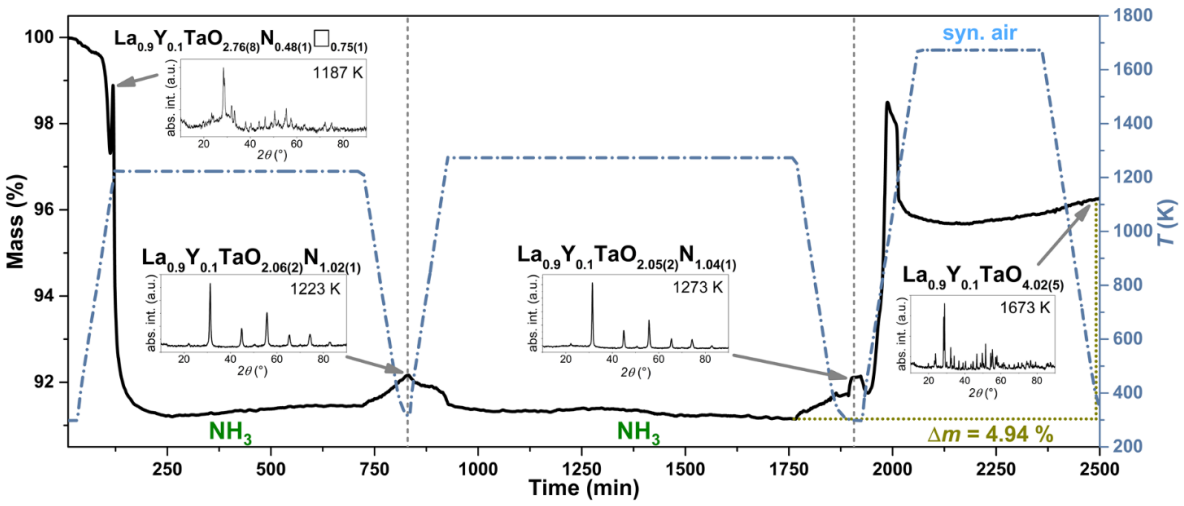

Fig. S5. TGA of *in situ* experiments of the ammonolysis of 10 mol% Y-substituted n-LTO (10 vol.% Ar in NH_3) and the subsequent reoxidation of $La_{0.9}Y_{0.1}TaO_2N$ with heating and cooling rates of 10 K/min. The displayed PXRD patterns and the anionic compositions were measured *ex situ* after specific termination experiments. The formation of the oxynitride is effected by means of the intermediate $La_{0.9}Y_{0.1}Ta^{IV}O_{2.76(8)}N_{0.48(1)}\square_{0.75(9)}$ (1187 K) suggesting a soft topotactic reaction[1] to $La_{0.9}Y_{0.1}Ta^{IV}O_2N$.

7.9.4. Crystal structure analysis of the intermediate $La_{0.9}Y_{0.1}TaO_{2.76(8)}N_{0.48(1)}\square_{0.75(9)}$

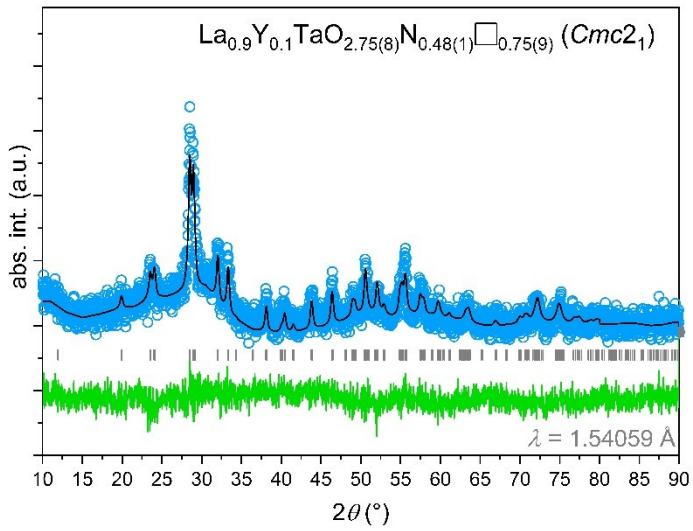

Fig. S6. Rietveld refinements of the crystal structure of $La_{0.9}Y_{0.1}TaO_{2.76(8)}N_{0.48(1)}\square_{0.75(9)}$ in space group type $Cmc2_1$.

Tab. S5. a) Unit cell parameters of $La_{0.9}Y_{0.1}TaO_{2.76(8)}N_{0.48(1)}\square_{0.75(9)}$ in space group type $Cmc2_1$.

Unit Cell Parameter	$La_{0.9}Y_{0.1}TaO_{2.76(8)}N_{0.48(1)}\square_{0.75(9)}$
$\boldsymbol{a}$ **(Å)**	3.9140(8)
$\boldsymbol{b}$ **(Å)**	14.806(4)
$\boldsymbol{c}$ **(Å)**	5.5897(2)
$\boldsymbol{V_{cell}}$ **(Å^3)**	323.94(2)
Space group	$Cmc2_1$
$\boldsymbol{R_p}$ **(%)**	7.29
$\boldsymbol{R_{wp}}$ **(%)**	9.16
$\boldsymbol{\chi^2}$	1.09
$\boldsymbol{R_{Bragg}}$ **(%)**	9.12

Tab. S5. b) Atom positions of $La_{0.9}Y_{0.1}TaO_{2.76(8)}N_{0.48(1)}\square_{0.75(9)}$ in space group type $Cmc2_1$.

Atom	Wyck. Symb.	x	y	z	B_{iso} (Å^2)	sof.[a]
La	4a	0	0.1713(1)	0.26(4)	2[b]	0.9[b]
Y	4a	0	0.1713(1)	0.26(4)	2[b]	0.1[b]
Ta	4a	0	0.4152(2)	0.29(4)	2[b]	1[b]
O(1)	4a	0	0.353(2)	0.36(5)	1[b]	1[b]
O(2)	4a	0	0.296(2)	1.00(6)	1[b]	1[b]
O(3)	4a	0	0.485(1)	0.66(5)	1[b]	1[b]
O(4)	4a	0	0.914(1)	0.250[b]	1[b]	1[b]

[a]site occupancy factor, [b]fixed

7.9.5. Crystal structure analysis of $La_{1-x}Y_xTaO_2N$

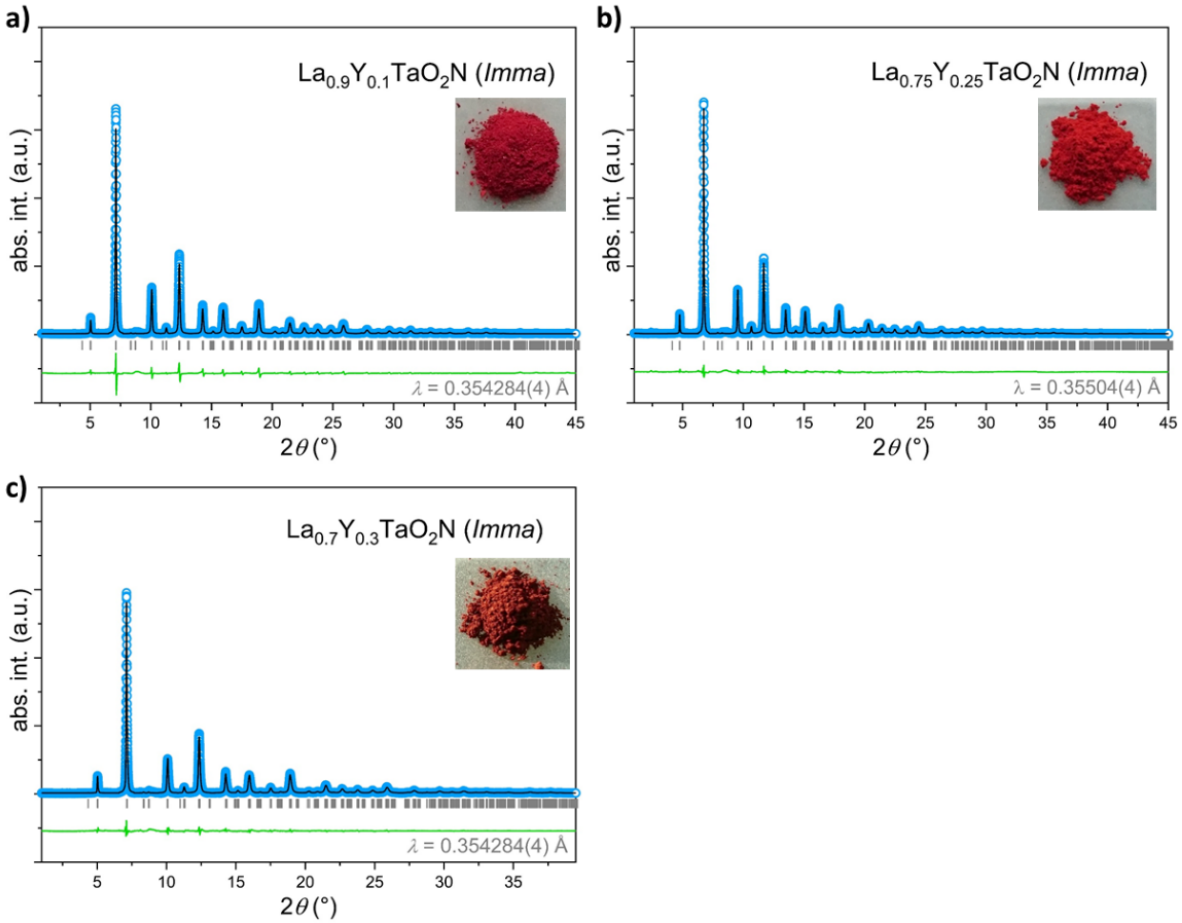

Fig. S7. a)-c) Rietveld refinements of the crystal structure of $La_{1-x}Y_xTaO_2N$ (x = 0.1, 0.25, 0.3) with the respective powder images.

Tab. S6. a) Unit cell parameters of $La_{1-x}Y_xTaO_2N$ (x = 0.1, 0.25, 0.3) from HR-PXRD data.

Unit Cell Parameter	$La_{0.9}Y_{0.1}TaO_2N$	$La_{0.75}Y_{0.25}TaO_2N$	$La_{0.7}Y_{0.3}TaO_2N$
***a* (Å)**	5.7093(2)	5.6993(5)	5.7044(2)
***b* (Å)**	8.0563(2)	8.0845(3)	8.0908(2)
***c* (Å)**	5.7322(2)	5.6901(6)	5.6709(2)
V_{cell} (Å^3)	263.66(1)	262.18(4)	261.73(2)
Space group	*Imma*	*Imma*	*Imma*
Phase fraction (wt.-%)	100	100	100
R_p (%)	5.56	6.17	7.71
R_{wp} (%)	9.47	9.60	11.4
χ^2	4.72	4.65	5.76
R_{Bragg} (%)	3.94	4.14	19.5

Tab. S6. b) Refined atom positions of $La_{0.9}Y_{0.1}TaO_2N$ from HR-PXRD data (space group: *Imma*).

Atom	Wyck. Symb.	*x*	*y*	*z*	B_{iso} (Å^2)	sof.[a]
La	4*e*	0	¼	0.5[c]	0.735(1)	0.9[d]
Y	4*e*	0	¼	0.5[c]	0.735(1)	0.1[d]
Ta	4*a*	0	0	0	0.332(1)	1[d]
O(1)	4*e*	0	¼	0.090(5)	2.645(2)[b]	⅔[d]
N(1)	4*e*	0	¼	0.090(5)	2.645(2)[b]	⅓[d]
O(2)	8*g*	¼	0.978(2)	¼	2.645(2)[b]	⅔[d]
N(2)	8*g*	¼	0.978(2)	¼	2.645(2)[b]	⅓[d]

[a]site occupancy factor, [b]constrained, [c]fixed according to Porter *et al.*[10], [d]fixed

Tab. S6. c) Refined atom positions of $La_{0.75}Y_{0.25}TaO_2N$ from HR-PXRD data (space group: *Imma*).

Atom	Wyck. Symb.	*x*	*y*	*z*	B_{iso} (Å^2)	sof.[a]
La	4*e*	0	¼	0.5[c]	0.986(1)	0.75[d]
Y	4*e*	0	¼	0.5[c]	0.986(1)	0.25[d]
Ta	4*a*	0	0	0	0.405(1)	1[d]
O(1)	4*e*	0	¼	0.083(7)	3.345(3)[b]	⅔[d]
N(1)	4*e*	0	¼	0.083(7)	3.345(3)[b]	⅓[d]
O(2)	8*g*	¼	0.970(3)	¼	3.345(3)[b]	⅔[d]
N(2)	8*g*	¼	0.970(3)	¼	3.345(3)[b]	⅓[d]

[a]site occupancy factor, [b]constrained, [c]fixed according to Porter *et al.*[10], [d]fixed

Tab. S6. d) Refined atom positions of $La_{0.7}Y_{0.3}TaO_2N$ from HR-PXRD data (space group: *Imma*).

Atom	Wyck. Symb.	*x*	*y*	*z*	B_{iso} (Å^2)	sof.[a]
La	4*e*	0	¼	0.5[c]	0.910(2)	0.7[d]
Y	4*e*	0	¼	0.5[c]	0.910(2)	0.3[d]
Ta	4*a*	0	0	0	0.364(1)	1[d]
O(1)	4*e*	0	¼	0.075(6)	3.473(4)[b]	⅔[d]
N(1)	4*e*	0	¼	0.075(6)	3.473(4)[b]	⅓[d]
O(2)	8*g*	¼	0.973(4)	¼	3.473(4)[b]	⅔[d]
N(2)	8*g*	¼	0.973(4)	¼	3.473(4)[b]	⅓[d]

[a]site occupancy factor, [b]constrained, [c]fixed according to Porter *et al.*[10], [d]fixed

7.9.6. Neutron diffraction

Since $LaTaON_2$[1,11,12] at room temperature was reported to be either orthorhombic (space group *Imma*) or monoclinic (*C*2/*m* or equivalent *I*2/*m*) and $LaTaO_2N$ only orthorhombic (*Imma*)[1], the ND data were refined by using both space group types. In accordance with the HR-PXRD results, refinements of the ND data (Fig. S8) were also most robust by using the *Imma* space group resulting in the lowest χ^2 value. Unfortunately, the limited ND data quality owing to the small sample size of only 200 mg (obtained after *ex situ* ammonolysis) and contributions from the sample container (vanadium can) did not allow precise determination of the anionic composition of $La_{0.9}Y_{0.1}TaO_2N$ by means of the occupancy factors combined with high B_{iso} values.

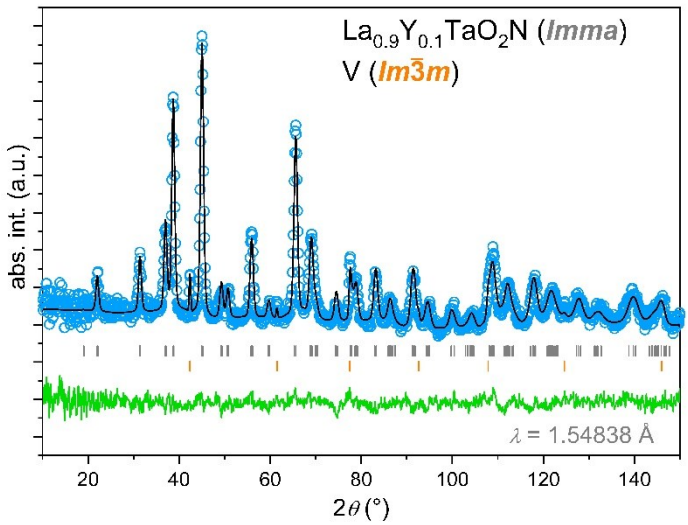

Fig. S8. Rietveld refinements of the ND data of $La_{0.9}Y_{0.1}TaO_2N$. The compound was synthesized under flowing ammonia at 1223 K for 10 h.

Tab. S7. a) Unit cell parameters of $La_{0.9}Y_{0.1}TaO_2N$ from ND data (space group: *Imma*).

Unit Cell Parameter	$La_{0.9}Y_{0.1}TaO_2N$		V
***a* (Å)**	5.716(2)		3.0303(7)
***b* (Å)**	8.059(3)		3.0303(7)
***c* (Å)**	5.740(3)		3.0303(7)
V_{cell} (Å^3)	264.41(2)		27.825(1)
Space group	*Imma*		*Im*$\bar{3}$*m*
Phase fraction (wt.-%)	45.92(2)		54.08(5)
R_p (%)		2.46	
R_{wp} (%)		3.21	
χ^2		4.94	
R_{Bragg} (%)	10.6		93.3

Tab. S7. b) Refined atom positions of $La_{0.9}Y_{0.1}TaO_2N$ from ND data (space group: *Imma*).

Atom	Wyck. Symb.	*x*	*y*	*z*	B_{iso} (Å^2)	sof.[a]
La	4*e*	0	¼	0.495(5)	2.6(2)	0.9[b]
Y	4*e*	0	¼	0.495(5)	2.6(2)	0.1[b]
Ta	4*a*	0	0	0	2.0(2)	1[b]
O(1)	4*e*	0	¼	0.076(2)	1.9(1)	⅔[b]
N(1)	4*e*	0	¼	0.076(2)	1.9(1)	⅓[b]
O(2)	8*g*	¼	0.964(1)	¼	1.9(1)	⅔[b]
N(2)	8*g*	¼	0.964(1)	¼	1.9(1)	⅓[b]

[a]site occupancy factor, [b]fixed

Tab. S7. c) Unit cell parameters of $La_{0.9}Y_{0.1}TaON_2$ as alternative structure model (space group: *Imma*).

Unit Cell Parameter	$La_{0.9}Y_{0.1}TaON_2$		V
***a* (Å)**	5.712(2)		3.0283(5)
***b* (Å)**	8.061(3)		3.0283(5)
***c* (Å)**	5.732(2)		3.0283(5)
V_{cell} (Å^3)	263.9(1)		27.771(8)
Space group	*Imma*		$Im\bar{3}m$
Phase fraction (wt.-%)	21(5)		79(27)
R_p (%)		2.30	
R_{wp} (%)		2.93	
χ^2		4.00	
R_{Bragg} (%)	10.7		44.0

Tab. S7. d) Refined atom positions from ND data using $La_{0.9}Y_{0.1}TaON_2$ as alternative structure model (space group: *Imma*).

Atom	Wyck. Symb.	*x*	*y*	*z*	B_{iso} (Å^2)	sof.[a]
La(1)	4*e*	0	¼	0.5[c]	1[b]	0.9[b]
Y(1)	4*e*	0	¼	0.5[c]	1[b]	0.1[b]
Ta(1)	4*a*	0	0	0	1[b]	1[b]
O(1)	4*e*	0	¼	0.076(2)	0.6(2)	0.55(9)
N(1)	4*e*	0	¼	0.076(2)	0.6(2)	0.45(9)
O(2)	8*g*	¼	0.9636(9)	¼	3.4(2)	0.05(7)
N(2)	8*g*	¼	0.9636(9)	¼	3.4(2)	0.95(7)

[a]site occupancy factor, [b]fixed, [c]fixed according to Porter *et al.*[10]

7.9.7. Bond length and angle analysis by Rietveld refinements

Tab. S8. a) Ta–*X*–Ta angles and average Ta-*X*-Ta angle of $La_{1-x}Y_xTaO_2N$ (x = 0, 0.1, 0.25, 0.3) *via* Rietveld refinements of the respective HR-PXRD data.

Compound	$LaTaO_2N$[1]	$La_{0.9}Y_{0.1}TaO_2N$	$La_{0.75}Y_{0.25}TaO_2N$	$La_{0.7}Y_{0.3}TaO_2N$
$\measuredangle_{Ta-X1-Ta}$ (°)	153.7(2)	151.3(3)	153.7(4)	149.6(2)
$\measuredangle_{Ta-X2-Ta}$ (°)	169.99(6)	169.98(6)	166.26(1)	165.33(8)
$\measuredangle_{average}$ (°)	161.85(8)	160.65(8)	160.0(5)	157.47(9)

Tab. S8. b). Distances in the $Ta(O,N)_6$ octahedron of $La_{1-x}Y_xTaO_2N$ (x = 0[1], 0.1, 0.25, 0.3) *via* Rietveld refinements of the respective HR-PXRD data.

Compound	$LaTaO_2N$[1]	$La_{0.9}Y_{0.1}TaO_2N$	$La_{0.75}Y_{0.25}TaO_2N$	$La_{0.7}Y_{0.3}TaO_2N$
$d_{Ta-(O,N)1}$ **(Å)**	2.0428(2)[1]	2.0420(2)	2.0260(1)	2.0263(1)
$d_{Ta-(O,N)2}$ **(Å)**	2.0428(2)[1]	2.0420(2)	2.0260(1)	2.0263(1)
$d_{Ta-(O,N)3}$ **(Å)**	2.0428(2)[1]	2.0420(2)	2.0260(1)	2.0263(1)
$d_{Ta-(O,N)4}$ **(Å)**	2.0428(2)[1]	2.0420(2)	2.0260(1)	2.0263(1)
$d_{Ta-(O,N)5}$ **(Å)**	2.0799(7)[1]	2.1113(7)	2.1263(5)	2.1664(6)
$d_{Ta-(O,N)6}$ **(Å)**	2.0799(7)[1]	2.1113(7)	2.1263(5)	2.1664(6)
$d_{Ta-(O,N),average}$ **(Å)**	2.0551(7)	2.0651(4)	2.0594(6)	2.0730(2)

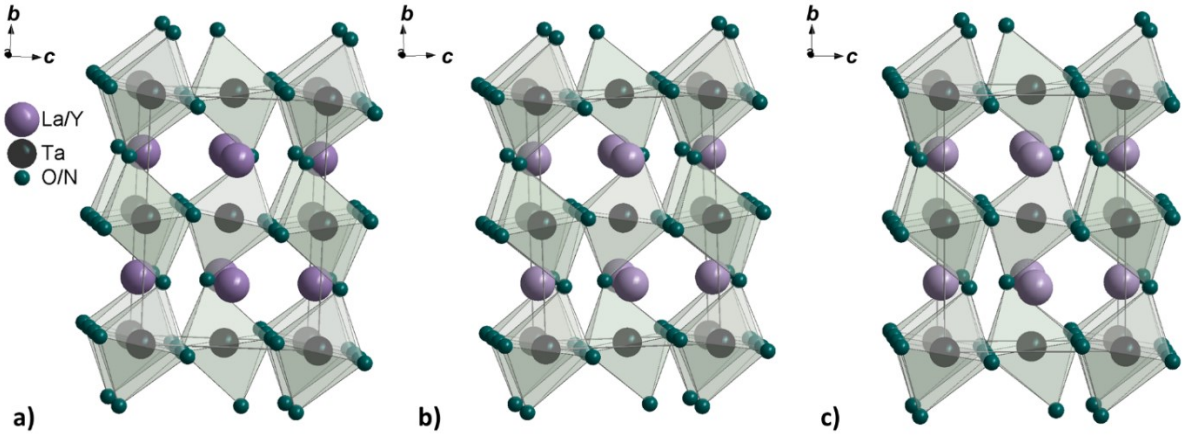

Fig. S9. Section of the crystal structure of a) $La_{0.9}Y_{0.1}TaO_2N$, b) $La_{0.75}Y_{0.25}TaO_2N$, and c) $La_{0.7}Y_{0.3}TaO_2N$ based on the results obtained *via* Rietveld refinements.

7.9.8. Determination of band edges

To determine the band edge positions of $La_{1-x}Y_xTa^{IV}O_2N$ Mott-Schottky-analyses were carried out. However, none of these experiments were successful, because either the particulate films were detached by the electrolyte from the substrate or the grain boundary resistance was exceeding the accessible range. Additionally, the experimental determination of the band edge positions is challenging due to the fact that the classical Mott-Schottky-analysis is often not straightforward for particle-based films of oxides or even oxynitrides.[13] Since experimental attempts to measure the band edge positions failed, an approach based on the absolute electronegativities of the constituent elements to calculate the band edge positions was used.[14] This was previously successfully applied to $CaTaO_2N$.[15] For $La_{1-x}Y_xTaO_2N$ ($x \leq 0.3$) and $LaTaON_2$ the calculated values for E_{CBM} and E_{VBM} are summarized in Table S9 together with those of $CaTaO_2N$ as calculated reference. In the latter case the calculated and the reported value agree very well. By comparing $LaTa^{V}ON_2$ and $LaTa^{IV}O_2N$ two things become obvious: i) interestingly the CBM position is nearly unaffected by the valence change from Ta^{5+} to Ta^{4+} and ii) in agreement with the lower nitrogen content the VBM of $La_{1-x}Y_xTaO_2N$ is shifted to a higher potential. Based on the data given in Tab. S9 none of the lanthanum containing materials would meet the requirements of overall solar water splitting because the potential of the VBM is lower than the redox potential of O_2/H_2O. In contrast, DFT calculations are showing a different situation for $LaTaON_2$, since there the potential of the VBM is much higher at about 1.8 V clearly exceeding the 1.23 V of water oxidation reaction. Consequently, the CBM position is also at much higher potential (even being slightly positive, ca. 0.1 V), hence, not suitable for water reduction reaction.[16] The calculated band edge positions for $CaTaO_2N$ are showing as well an offset towards a higher potential by about 0.5 V in comparison with the model using the absolute electronegativity.[15,16]

Tab. S9. Calculated band edge positions of $La_{1-x}Y_xTaO_2N$, $LaTaON_2$, and $CaTaO_2N$.

Material	E_{CBM} (V)	E_{VBM} (V)
$LaTaO_2N$	−1.20	0.70
$La_{0.9}Y_{0.1}TaO_2N$	−1.19	0.73
$La_{0.75}Y_{0.25}TaO_2N$	−1.17	0.79
$La_{0.7}Y_{0.3}TaO_2N$	−1.21	0.67
$LaTaON_2$	−1.28	0.52
$CaTaO_2N$	−0.94	1.49
$CaTaO_2N$[15]	−0.88	1.55
$CaTaO_2N$[16]	∼−0.40	∼1.90

So, to conclude it is still an open question if the band edge positions of $LaTa^{V}ON_2$ and $La_{1-x}Y_xTa^{IV}O_2N$ meet the requirements for overall solar water splitting because the obtained results deviate from each other depending on the applied method of determination. Keeping the observed offset of ca. 0.5 V in mind the materials might be suitable.

7.9.9. Crystal structure and optical bandgap analysis of Y–Ta–O and Y–Ta–O–N phases

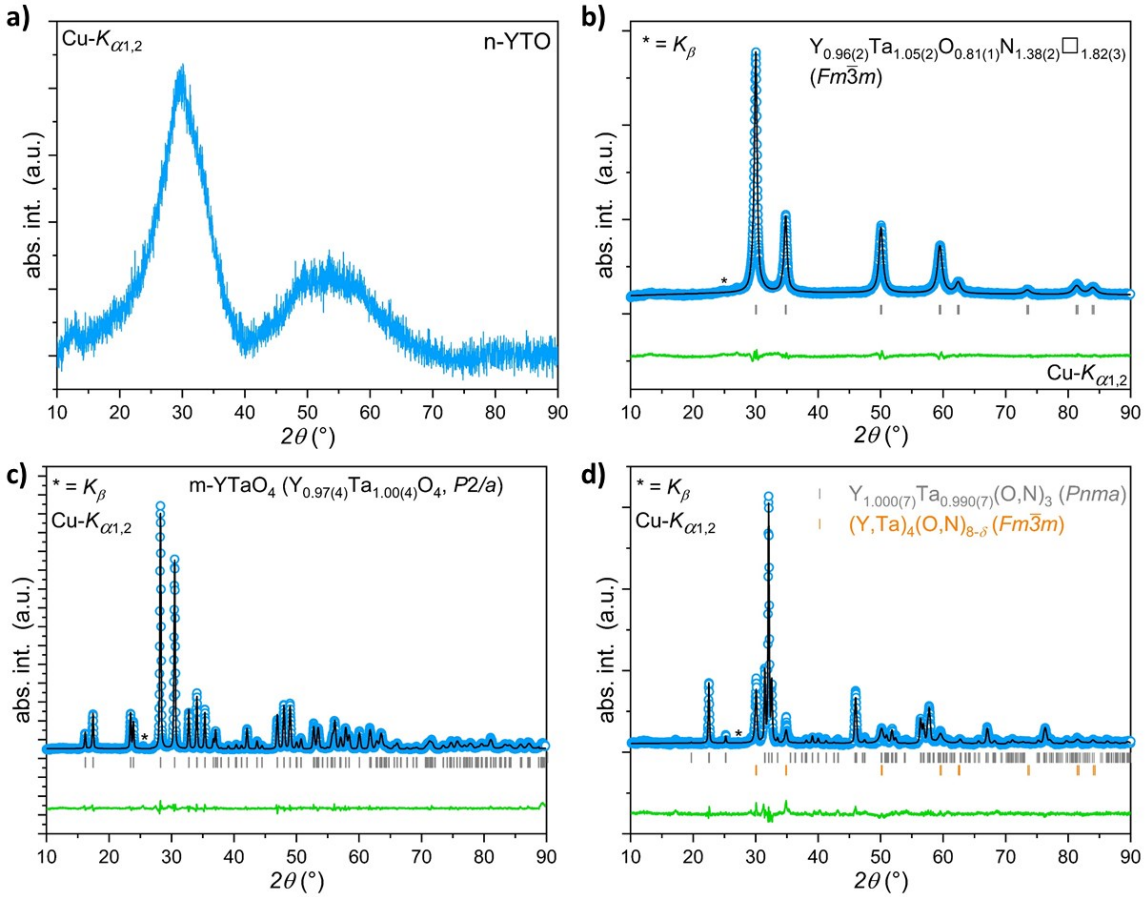

Fig. S10. a) Diffraction pattern of n-YTO. As expressed by the very large full width at half maximum (FWHM) of ca. 10° of the Bragg reflections n-YTO contains very small crystallites (nanocrystallites). b) Rietveld refinements of defect-fluorite-type phase. c) Rietveld refinements of m-$YTaO_4$ (synthesized at 1473 K) and d) Rietveld refinements of the mixture of perovskite-type phase and defect-fluorite-type phase ($YTa(O,N,\square)_4$) obtained after several *ex situ* ammonolysis cycles.

Tab. S10. a) Unit cell parameters of $Y_{0.96(2)}Ta_{1.05(2)}O_{0.81(1)}N_{1.38(2)}\square_{1.82(3)}$, $Y_{0.97(4)}Ta_{1.00(4)}O_4$, $Y_{1.000(7)}Ta_{0.990(7)}(O,N)_3$, and $YTa(O,N,\square)_4$ from PXRD data.

Unit Cell Parameter	$Y_{0.96(2)}Ta_{1.05(2)}O_{0.81(1)}N_{1.38(2)}\square_{1.82(3)}$	$Y_{0.97(4)}Ta_{1.00(4)}O_4$	$Y_{1.000(7)}Ta_{0.990(7)}(O,N)_3$	$YTa(O,N,\square)_4$
a (Å)	5.1536(2)	5.2942(5)	5.6851(4)	5.1464(4)
b (Å)	≡ a	5.4646(5)	7.8795(9)	≡ a
c (Å)	≡ a	5.1070(5)	5.4954(6)	≡ a
V_{cell} (Å^3)	136.88(7)	146.86(2)	246.17(4)	136.31(2)
Space group	$Fm\bar{3}m$	$P2/a$	$Pnma$	$Fm\bar{3}m$
Phase fraction (wt.-%)	100	100	82(2)	18(2)
R_p (%)	5.78	6.33	7.89	
R_{wp} (%)	7.18	8.1	10.3	
χ^2	1.74	1.98	3.57	
R_{Bragg} (%)	6.18	7.62	7.96	18.4

Tab. S10. b) Refined atom positions of $Y_{0.96(2)}Ta_{1.05(2)}O_{0.81(1)}N_{1.38(2)}\square_{1.82(3)}$ from PXRD data (space group: $Fm\bar{3}m$).

Atom	Wyck. Symb.	*x*	*y*	*z*	B_{iso} (Å^2)	sof.[a]
Y	4*a*	0	0	0	2[b]	0.5[c]
Ta	4*a*	0	0	0	2[b]	0.5[c]
O	8*c*	¼	¼	¼	1.5[b]	0.2025[d]
N	8*c*	¼	¼	¼	1.5[b]	0.34375[d]

[a]site occupancy factor, [b]fixed, [c]adopted from Rooksby *et al.*[17], [d]fixed according to HGE

Tab. S10. c) Refined atom positions of $Y_{0.97(4)}Ta_{1.00(4)}O_4$ (synthesized at 1473 K) from PXRD data (space group: $P2/a$).

Atom	Wyck. Symb.	*x*	*y*	*z*	B_{iso} (Å^2)	sof.[a]
Ta	2*f*	¼	0.3059(4)	½	3.12(2)	0.505(2)
Y	2*e*	¼	0.7672(6)	0	3.01(2)	0.491(2)
O(1)	4*g*	0.505(4)	0.438(2)	0.256(3)	3.290(7)	1[b]
O(2)	4*g*	0.091(3)	0.083(2)	0.248(3)	4.26(2)	1[b]

[a]site occupancy factor, [b]fixed

Tab. S10. d) Refined atom positions of $Y_{1.000(7)}Ta_{0.990(7)}(O,N)_3$ from PXRD data (space group: *Pnma*). Due to the unknown N content and the virtually equal atomic form factors of O^{2-} and N^{3-} the refinements were carried out only using O^{2-} as anion.

Atom	Wyck. Symb.	*x*	*y*	*z*	B_{iso} (Å^2)	sof.[a]
Y	4*c*	0.449(1)	¼	0.013(3)	3.3(2)	1.000(7)[b]
Ta	4*b*	0	0	0	2.1(1)	0.990(7)[b]
O(1)	4*c*	0.498(8)	¼	0.623(7)	1.5[c]	1[c]
O(2)	8*d*	0.136(4)	1.047(4)	0.279(6)	1.5[c]	1[c]

[a]site occupancy factor, [b]constrained, [c]fixed

Tab. S10. e) Refined atom positions of $YTa(O,N,\square)_4$ from PXRD data (space group: $Fm\bar{3}m$). Due to the unknown N content and the virtually equal atomic form factors of O^{2-} and N^{3-} the refinements were carried out only using O^{2-} as anion.

Atom	Wyck. Symb.	*x*	*y*	*z*	B_{iso} (Å^2)	sof.[a]
Y	4*a*	0	0	0	2[b]	0.5[c]
Ta	4*a*	0	0	0	2[b]	0.5[c]
O	8*c*	¼	¼	¼	12[b]	0.55[d]

[a]site occupancy factor, [b]fixed, [c]adopted from Rooksby *et al.*[17], [d]fixed according to composition of $YTa(O,N,\square)_4$ produced from n-YTO.

7.9.10. DRS spectra of yttrium tantalum oxynitride

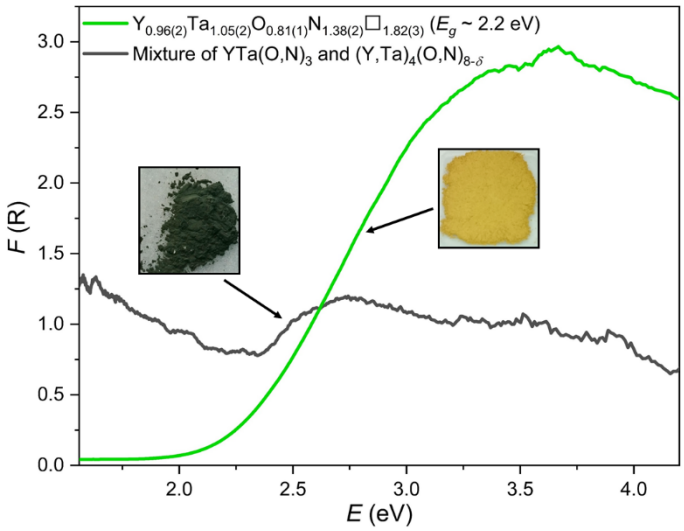

Fig. S11. Diffuse reflectance spectra - converted according to Kubelka-Munk[6] - of $Y_{0.96(2)}Ta_{1.05(2)}O_{0.81(1)}N_{1.38(2)}\square_{1.82(3)}$ and the mixture of $YTa(O,N)_3$ and $YTa(O,N,\square)_4$.

7.9.11. Composition of $La_{1-x}Y_xTaO_2N$ (x = 0.1, 0.25, 0.3), n-YTO, and defect-fluorite phase

Tab. S11. Weight fractions of the respective constituents of $La_{1-x}Y_xTaO_2N$ (x = 0.1, 0.25, 0.3), n-YTO, and $Y_{0.96(2)}Ta_{1.05(2)}O_{0.81(1)}N_{1.38(2)}\square_{1.82(3)}$ determined *via* ICP-OES and HGE.

Element	$La_{0.9}Y_{0.1}TaO_2N$	$La_{0.75}Y_{0.25}TaO_2N$	$La_{0.7}Y_{0.3}TaO_2N$	n-YTO	$Y_{0.96(2)}Ta_{1.05(2)}O_{0.81(1)}N_{1.38(2)}\square_{1.82(3)}$
La (wt.-%)	33.2 ± 0.4	28.2 ± 0.3	26.1 ± 0.4		
La	0.90(9)	0.76(6)	0.70(2)		
Y (wt.-%)	2.05 ± 0.08	5.03 ± 0.07	6.95 ± 0.08	26.4 ± 0.3	28.6 ± 0.3
Y	0.08(8)	0.21(4)	0.29(2)	1.00(4)	0.96(2)
Ta (wt.-%)	47.7 ± 0.5	48.9 ± 0.5	48.7 ± 0.5	54.2 ± 0.6	60.5 ± 0.7
Ta	1.00(3)	1.02(1)	1.00(6)	0.99(6)	1.05(2)
O (wt.-%)	8.74 ± 0.1	8.91 ± 0.1	8.89 ± 0.09	19.3 ± 0.2	4.12 ± 0.05
O	1.98(6)	1.96(6)	1.91(9)	4.04(4)	0.81(1)
N (wt.-%)	3.88 ± 0.04	3.91 ± 0.04	4.38 ± 0.05		6.16 ± 0.08
N	1.01(4)	1.03(4)	1.08(1)		1.38(2)

7.9.12. X-Ray photoelectron spectroscopy – survey spectra

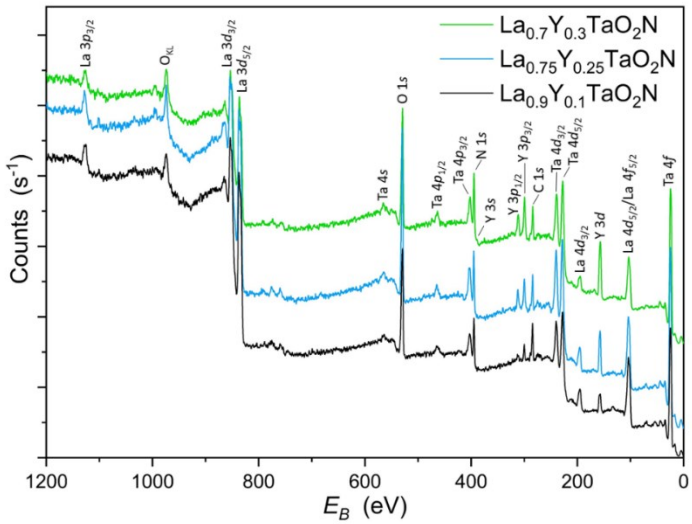

Fig. S12. XPS survey spectra of $La_{1-x}Y_xTaO_2N$ (x = 0.1, 0.25, 0.3).

7.9.13. Magnetic behavior

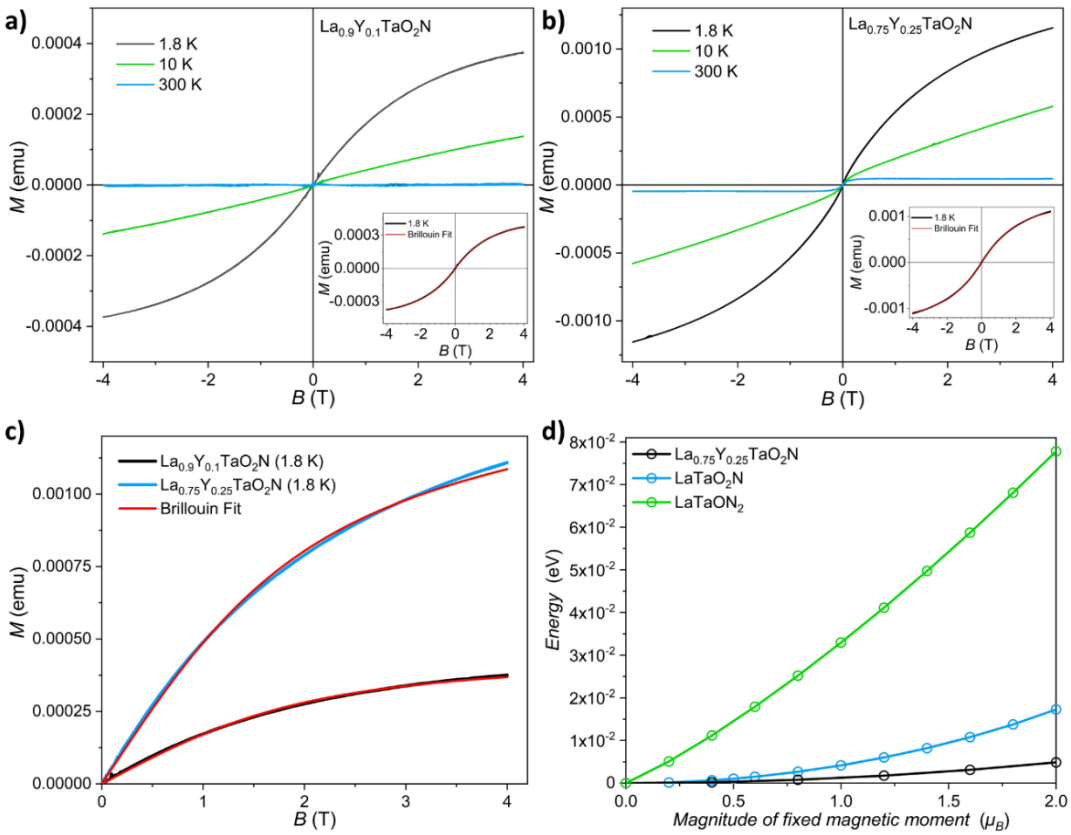

Fig. S13. Temperature dependent M vs. H plots of a) $La_{0.9}Y_{0.1}TaO_2N$ and b) $La_{0.75}Y_{0.25}TaO_2N$. No coercive fields are observed for both compounds pointing to a very tiny paramagnetic contribution at very low temperatures (1.8 K). The insets show the pure 1.8 K paramagnetic contribution, where the room temperature curves have been subtracted, to remove visible but small room temperature ferromagnetic behavior. c) Brillouin fits of $La_{0.9}Y_{0.1}TaO_2N$ and $La_{0.75}Y_{0.25}TaO_2N$. d) Total energies as a function of the magnetic moment μ_B for $LaTaON_2$, $LaTaO_2N$, and $La_{0.75}Y_{0.25}TaO_2N$.

7.9.14. Electronic band structure

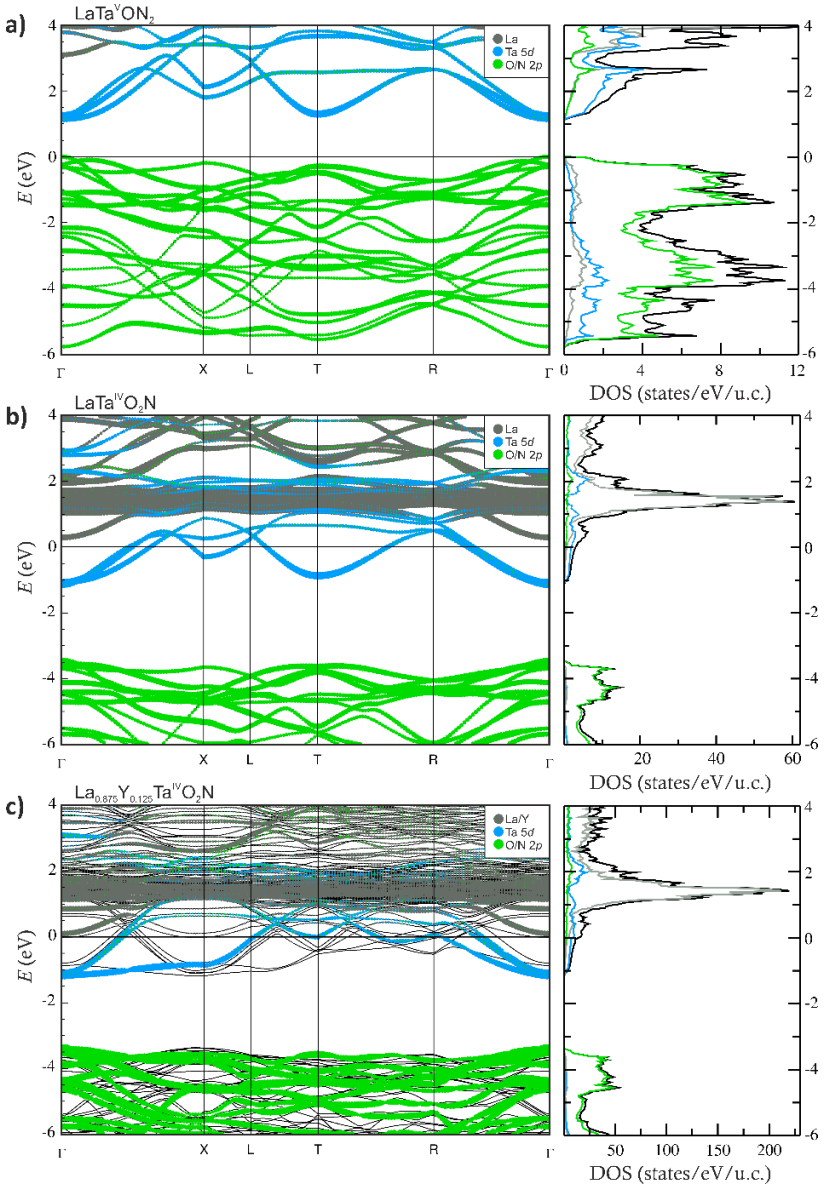

Fig. S14. Electronic band structure of a) $LaTaON_2$, b) $LaTaO_2N$ and c) $La_{0.875}Y_{0.125}TaO_2N$ showing the metallic nature of the Ta 5*d* levels of $La_{1-x}Y_xTaO_2N$ and the direct bandgap of $LaTaON_2$.

A change of the charge carrier excitation behavior between $LaTa^{V}ON_2$ and $La_{1-x}Y_xTa^{IV}O_2N$ is implied by the electronic band structures shown in Fig. S14. A classical semiconductor-like band structure is observed for $LaTaON_2$ (Fig. S14 b)) showing an electronic excitation from the valence band (VB) formed by O/N 2*p* states across the bandgap to the empty Ta 5*d* states in the conduction band (CB). The calculated bandgap is about 1.1 eV showing the typical underestimation of DFT calculations in comparison to the experimental optical bandgap of 1.8 eV.[1] For $La_{1-x}Y_xTaO_2N$ (Fig. S14 a) and c)) the assignment of VB and CB and transition of electrons during excitation is due to its metallic character not straightforward anymore because the highest occupied state is no longer located in the VB. Based on the determined optical bandgaps and the calculated electronic band structure of $La_{1-x}Y_xTaO_2N$ the excitation is not occurring from O/N 2*p* states (as in $LaTaON_2$) to the empty states in the CB. The calculated energetic difference is with ca. 2.5 eV (Γ-point) clearly larger than the experimental bandgap. Additionally, the fact that most DFT calculations underestimate bandgaps must be recalled. Therefore, an excitation from the partly occupied Ta 5d states to energetically higher empty levels seems to be responsible for the visible-light absorption. This transition shows a very similar offset

between calculated (ca. 1.4 eV) and experimental (1.88 eV – 1.96 eV) bandgap as observed for $LaTaON_2$. A similar behavior was previously described for the red metallic oxide photocatalyst $Sr_{1-x}NbO_3$.[18]

7.9.15. Surface photovoltage spectroscopy

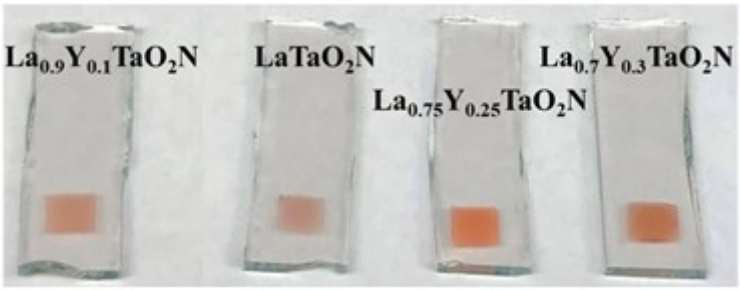

Fig. S15. $La_{1-x}Y_xTaO_2N$ (x = 0.1, 0.25, 0.3) films for SPS measurements.

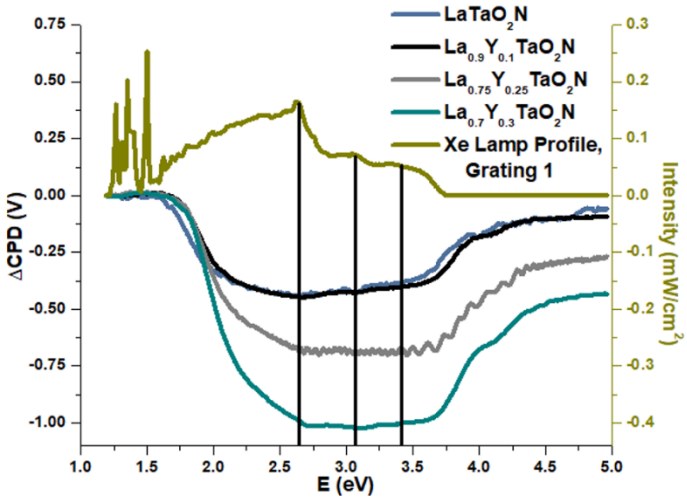

Fig. S16. SPS data for $La_{1-x}Y_xTaO_2N$ powder samples on FTO overlaid with the emission spectrum of the xenon lamp used for the measurements.

Tab. S12. Summary of SPS photo-onsets, estimated effective bandgaps, maximum photovoltage values, surface area by BET method, film thicknesses, and times for photovoltage formation and decay. Time constants τ_{on} and τ_{off} show the time required to reach 63.21% of the final photovoltage after turning the light on or off.

Material	Photo-onset (eV)	Effective $E_{G,eff}$ (eV)	Max ΔCPD (V)	S_{BET} (m^2/g)	Avg. Film Thickness (nm)	τ_{on} (s)	τ_{off} (s)
$LaTaO_2N$	1.58	1.65	-0.44	8.0	879 ± 167	21.91	89.46
$La_{0.9}Y_{0.1}TaO_2N$	1.68	1.74	-0.45	20.4	1315 ± 227	7.62	73.39
$La_{0.75}Y_{0.25}TaO_2N$	1.68	1.78	-0.69	21.1	1210 ± 190	10.65	205.96
$La_{0.7}Y_{0.3}TaO_2N$	1.64	1.78	-1.01	27.9	1526 ± 378	20.71	242.66

7.10. Supplementary References

1 C. Bubeck, M. Widenmeyer, G. Richter, M. Coduri, E. Goering, S. Yoon and A. Weidenkaff, *Commun. Chem.*, 2019, **2**, 134.

2 G. S. Henderson, F. M. F. De Groot and B. J. A. Moulton, *Rev. Mineral. Geochemistry*, 2014, **78**, 75–138.

3 M. Widenmeyer, C. Peng, A. Baki, W. Xie, R. Niewa and A. Weidenkaff, in *Solid State Sciences*, 2016, vol. 54, pp. 7–16.

4 C. M. Leroy, A. E. Maegli, K. Sivula, T. Hisatomi, N. Xanthopoulos, E. H. Otal, S. Yoon, A. Weidenkaff, R. Sanjines and M. Grätzel, *Chem. Commun.*, 2012, **48**, 820.

5 D. Logvinovich, J. Hejtmánek, K. Knížek, M. Maryško, N. Homazava, P. Tomeš, R. Aguiar, S. G. Ebbinghaus, A. Reller and A. Weidenkaff, *J. Appl. Phys.*, 2009, **105**, 023522.

6 G. Kortüm, W. Braun and G. Herzog, *Angew. Chemie Int. Ed. English*, 1963, **2**, 333–341.

7 T. A. Kurova and V. B. Aleksandrov, *Dokl. Akad. Nauk SSSR*, 1971, **201**, 1095–1098.

8 Y. O. Titov, A. M. Sich, V. Y. Markiv, N. M. Belyavina, A. O. Kapshuk and M. S. Slobodyanik, *Dopovidi Natsional'noi Akad. Nauk Ukr.*, 2003, **3**, 140–145.

9 L. H. Brixner and H. Y. Chen, *J. Electrochem. Soc.*, 1983, **130**, 2435–2443.

10 S. H. Porter, Z. Huang and P. M. Woodward, *Cryst. Growth Des.*, 2014, **14**, 117–125.

11 L. Clark, J. Oró-Solé, K. S. Knight, A. Fuertes and J. P. Attfield, *Chem. Mater.*, 2013, **25**, 5004–5011.

12 E. Günther, R. Hagenmayer and M. Jansen, *Z. Anorg. Allg. Chem.*, 2000, **626**, 1519–1525.

13 Laurence M. Peter, in *Photocatalysis: Fundamentals and Perspectives*, The Royal Society of Chemistry, 2016, pp. 1–28.

14 Y. Xu and M. A. A. Schoonen, *Am. Mineral.*, 2000, **85**, 543–556.

15 J. Xu, C. Pan, T. Takata and K. Domen, *Chem. Commun.*, 2015, **51**, 7191–7194.

16 I. E. Castelli, D. D. Landis, K. S. Thygesen, S. Dahl, I. Chorkendorff, T. F. Jaramillo and K. W. Jacobsen, *Energy Environ. Sci.*, 2012, **5**, 9034–9043.

17 H. P. Rooksby and E. A. D. White, *J. Am. Ceram. Soc.*, 1964, **47**, 94–96.

18 X. Xu, C. Randorn, P. Efstathiou and J. T. S. Irvine, *Nat. Mater.*, 2012, **11**, 595–598.

8. Observation of a possible diluted ferromagnetism above room temperature in cobalt-substituted $LaTa(O,N)_{3-\delta}$

Cora Bubeck, Eberhard Goering, Robert Lawitzki, Kathrin Küster, Wilfried Sigle, Marc Widenmeyer, Ulrich Starke, Clemens Ritter, Gabriel J. Cuello, Peter Nagel, Michael Merz, Stefan Schuppler, Gisela Schütz & Anke Weidenkaff

Abstract

Since 2000, the intensive effort in materials research to develop a diluted magnetic semiconductor exhibiting high-temperature (HT) ferromagnetism above room temperature was not successful. Here, the possible first bulk diluted HT-ferromagnetic non-metallic materials, based on the perovskite-type oxynitrides $LaTa_{1-x}Co_x(O,N)_{3-\delta}$ (x = 0.01, 0.03, 0.05) are realized. The Curie temperature of the synthesized powders exceeds 600 K and the sample magnetizations are large enough to be directly attracted by permanent magnets. Cobalt clusters as a possible source for the observed HT-ferromagnetism can be excluded, since all applied characterization methods verify phase purity. Applied conventional and element-specific magnetometry imply ferromagnetic intermediate spin (IS) Co^{3+} which is included in a ferromagnetic host matrix. This indicates a complex magnetic interplay between the existing crystal structure, the observed anionic vacancies, and the introduced cobalt ions. These results lay the foundation for the experimental investigation and design of further diluted HT-ferromagnetic semiconductors.

8.1. Introduction

Diluted magnetic semiconductors (DMS) such as ferromagnetic *p*-type $Ga_{1-x}Mn_xAs$ are very promising for applications in spintronics [1–4]. However, until now ferromagnetism at room temperature for DMS has not been observed. This desired property would open up big advances in developing multifunctional ferromagnetic devices for spintronics. In the year 2000 Dietl and co-workers predicted the possibility to obtain high-temperature (HT) ferromagnetism above room temperature *via* 3*d* transition metal doping in semiconductors and insulators (*e.g*. in ZnO or GaN) [1,2]. Dietl *et al*. expected that *p*-type materials containing a critical concentration of holes and magnetic ions leading to DMS should exhibit an even higher Curie temperature (T_C) than room temperature [1].

The stated prediction is very counterintuitive, because it is well-known that a strong prerequisite for room temperature ferromagnetism is a strong exchange interaction. This is not expected for large ionic distances between magnetic ions and/or holes existing in DMS [5]. Therefore – and despite many investigations during the last two decades – this is one of the most controversial research topics in materials science and condensed-matter physics [2,6].

Until now, it has been observed that homogeneously dissolved 3*d* transition metal ions in a non-magnetic semiconductor showed paramagnetism [7]. In other cases, secondary phases – such as simple metallic transition metal clusters – contributed to the ferromagnetic-like behavior [6,8]. In this context, new interesting magnetic phenomena such as the "d^0–magnetism" were found [9–11]. Even materials which were not doped with transition metals, such as pristine ZnO, revealed ferromagnetism [12]. The origin of this unexpected ferromagnetism is attributed to defect states, which are predominantly located at grain boundary sites [12–15]. Several other attempts to obtain HT-ferromagnetism above room temperature by 3*d* transition metal ion doping in non-magnetic semiconductors failed[2]. In particular, the attempt to realize HT-ferromagnetic thin films ended up in measuring magnetometer artefacts, contaminations, and ferromagnetic secondary phases [6]. Until now, the observed ferromagnetism in DMS was far below room temperature. Even for $Ga_{1-x}Mn_xAs$ or $Ge_{1-x}Mn_xTe$ the DMS ferromagnetic behavior is only observed below 200 K [2,16], therefore, a room temperature ferromagnetic DMS has not been realized.

To tailor many of the magnetic properties (*e.g*. magnetization, magnetocrystalline anisotropy, etc.) the doping by ions or substitution of ions in a materials' matrix is a powerful tool. Perovskite-type oxynitrides $AB(O,N)_3$ are normally considered to be suitable for visible light-driven applications or as cadmium-free inorganic pigments [17–20]. This is because they exhibit an extraordinary flexibility in *A*- and *B*-site substitution, with which the physical properties can be tuned [17,21]. We showed previously that $LaTa(O,N)_3$ has a clear non-magnetic semiconducting behavior with very small magnetic moments and diamagnetism at room temperature [17]. Therefore, it seems to be a promising non-magnetic matrix material for *B*-site substitution with tiny amounts of magnetic ions such as Co^{2+}.

Here, we show the realization of a HT-ferromagnetic bulk DMS by applying Co-substitution in $LaTa(O,N)_3$. We synthesized red perovskite-type oxynitrides $LaTa_{1-x}Co_x(O,N)_{3-\delta}$ (LTCON) with three different Co ion concentrations, namely 0.2 at% (x = 0.01), 0.6 at% (x = 0.03), and 1 at% (x = 0.05), which all exhibit ferromagnetism far above room temperature. By chemical analysis, advanced nanostructural characterization (*e.g*. state-of-the-art high-resolution transmission electron microscopy (HR-TEM)), and by synthesizing a reference sample containing a non-stoichiometric higher Co ion concentration (hereafter called Co-rich), we can rule out metallic (elemental) Co and Co-rich phases as the source for the observed HT-ferromagnetism. SQUID-based magnetometry and high-quality transmission (TR) mode X-ray magnetic circular dichroism (XMCD) proved significant non-metallic Co-related ferromagnetism and intermediate spin (IS) Co^{3+} down to 0.2 at% Co ions. The obtained single-phase HT-ferromagnetic LTCON powders have an optical bandgap E_G between 1.7 eV

and 1.9 eV and can be described as DMS because of the tiny Co ion concentrations and anionic vacancies inside.

8.2. Single-phase perovskite-type LTCON – Synthesizable or not?

The main question in many studies [2] is the solubility limit of ferromagnetic ions such as Co^{z+}, Fe^{z+}, or Ni^{z+} in the materials matrix. This is a crucial point, because if the majority of the Co ions are solved in the material the total magnetization (HT-ferromagnetism) cannot be related to the small remaining amounts of Co-rich secondary phases. Normally, materials containing such ions – especially oxynitrides – are difficult to synthesize [22]. Hence, an evaluation of the possibility for synthesis of LTCON by calculating the structural stability according to Li *et al.* [23] was done. According to the calculations the determined tolerance factor t [23] of LTCON is $0.934(5) \leq t \leq 0.936(9)$. Therefore, the samples should be synthesizable in the perovskite structure and should be single-phase. Additionally, Ta ions and Co ions exhibit similar effective ionic radii [24] making them suitable for a substitution with each other. Hence, by a careful evaluation of the synthesis parameters, single-phase LTCON samples with all three different Co ion concentrations should be possible.

Therefore, we used an appropriate synthesis protocol to produce LTCON: first, the bluish oxide precursors $LaTa_{1-x}Co_xO_{4-\delta}$ (LTCO) were prepared *via* a sol-gel-related method (Pechini method) (Fig. 1). Afterwards, the LTCO powders were ammonolyzed (heating under flowing NH_3 gas) in order to obtain LTCON. A more detailed chemical analysis of the LTCO precursors and formation of LTCON is described in the Supplemental Material Sec. I–II, Fig. S1–S12 and Tabs. S1–S4. After the synthesis of LTCON, we have chosen a series of complementary investigation techniques in order to give a complete picture of the single-phase nature of the materials and their ferromagnetic behavior. This is described in the following sections.

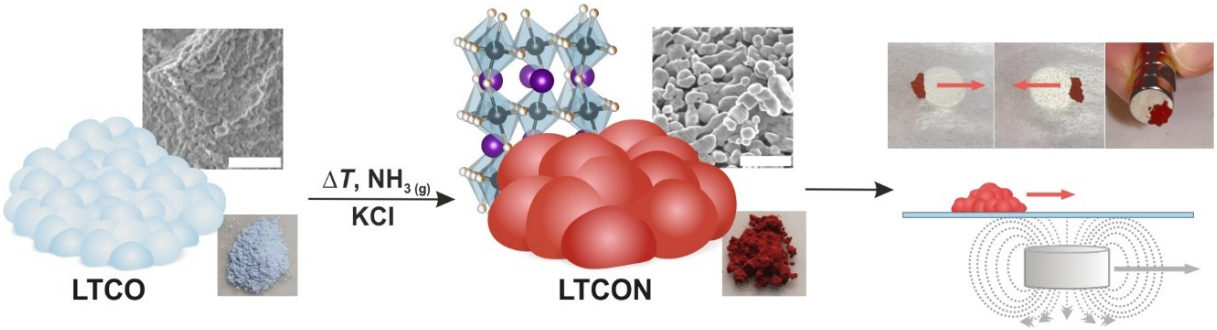

FIG. 1. Reaction path to LTCON. Reaction path from LTCO to LTCON, which can be attracted or moved by permanent magnets (Movie S1 and S2). Respective scanning electron microscopy (SEM) images (Scale bars: 500 nm) and sample photos are shown. In the depicted crystal structure, the purple ions represent La^{3+}. The Ta/Co ions (black/cyan) are 6-fold coordinated by N^{3-} and O^{2-} (white/orange) in an octahedral environment.

8.3. Structural and compositional investigations of LTCON

Scanning electron microscopy (SEM) shows that the synthesized LTCON particles exhibit an average size of 300 nm (Figs. 1, S1). However, high-resolution transmission electron microscopy (HR-TEM) reveal many smaller particles (average size 50 nm) which are agglomerated (Fig. 2a).

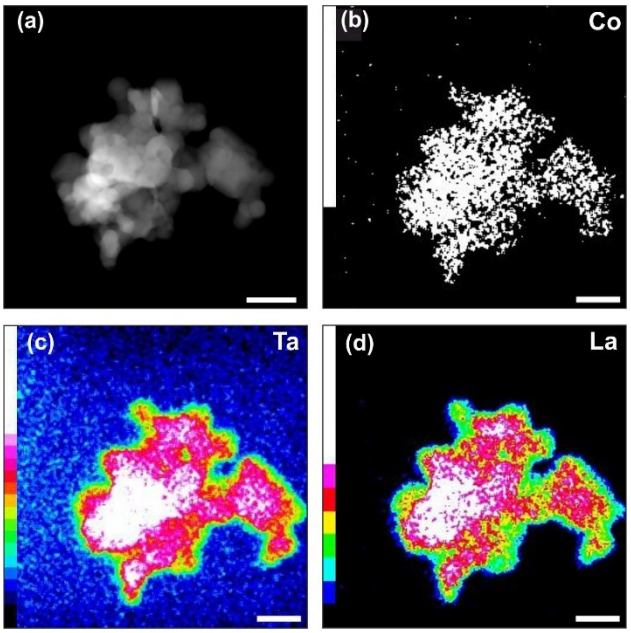

FIG. 2. HR-TEM investigations of LTCON-5. (a) Zoomed HAADF image of single-phase LTCON-5 nanoparticles and long-time measured EDX maps of (b) Co, (c) Ta, and (d) La. The different colors represent the concentration. By long-time measurements, the homogeneous distribution of the Co ions is obvious. Scale bars: 50 nm.

For imaging we used high-angle annular dark-field imaging (HAADF) and for further solubility investigations energy-dispersive X-ray spectroscopy (EDX). By conducting a long-time EDX measurement, the homogeneous distribution of all three elements (Ta, La, and Co) was verified. Especially, Co revealed a very homogeneous distribution in the material (Fig. 2b) without showing any sign of a secondary Co-rich phase in LTCON-5. For further information of the conducted electron microscopy experiments cf. Supplemental Material Sec. III.

The exact concentration of the cations (La, Ta, and Co ions) is investigated by inductively coupled plasma optical emission spectroscopy (ICP-OES) and reveals the expected compositions, which are implemented in Tab. S4. Furthermore, hot gas extraction (HGE) – determination of O and N contents – revealed anionic vacancies (δ) for LTCON. We will further discuss the importance of anionic vacancies in Sec. VII.

Crystal structure analysis (Powder X-Ray diffraction combined with Rietveld refinements) revealed the space group type *Imma* (Tabs. S5–S22) for all LTCON samples. This is a perovskite-type phase where the Ta/Co ions are coordinated in an octahedral environment by six anions. The same space group type is already reported for the non-magnetic perovskite-type oxynitrides $LaTaO_2N$ and $LaTaON_2$ [17]. Therefore, a change in the space group type is not expected, because we used very small concentrations of Co ions for *B*-site substitution in $LaTa(O,N)_3$ which should not affect the crystal structure by itself.

The colors of the LTCON powders range from red for $x = 0.01$ (LTCON-1) *via* dark red for $x = 0.03$ (LTCON-3) to a very dark red for $x = 0.05$ (LTCON-5) (Fig. 1 and Fig. S1). The obtained optical bandgap E_G of the oxynitrides determined by diffuse reflectance spectroscopy ($1.7\ \text{eV} \leq E_G \leq 1.9\ \text{eV}$) reflects the red color and points to a semiconductor (Fig. S8): metallic nanoparticles are typically black in color. Similar results in color and bandgap were obtained for pristine $LaTa(O,N)_3$ [17].

8.4. The importance of stoichiometry in LTCON

As stated above, secondary phases containing magnetic Co, Fe or Ni ions can produce HT-ferromagnetism. Therefore, the main question in many studies is the solubility limit of such ferromagnetic ions in the materials matrix [2]. In principle, possible ferromagnetic secondary phases in our samples could be either Co-rich particles or elemental Co clusters/particles.

In order to investigate if elemental Co as secondary phase is possible in our case, we deliberately produced one reference sample of LTCON-5 containing a non-stoichiometric amount of Co ions (Co^{z+} excess of 3.4 %)(cf. Supplemental Material Sec. III). In Figs. 3a–f, both samples – the stoichiometric and the Co-rich (non-stoichiometric) LTCON-5 – are presented and compared with each other.

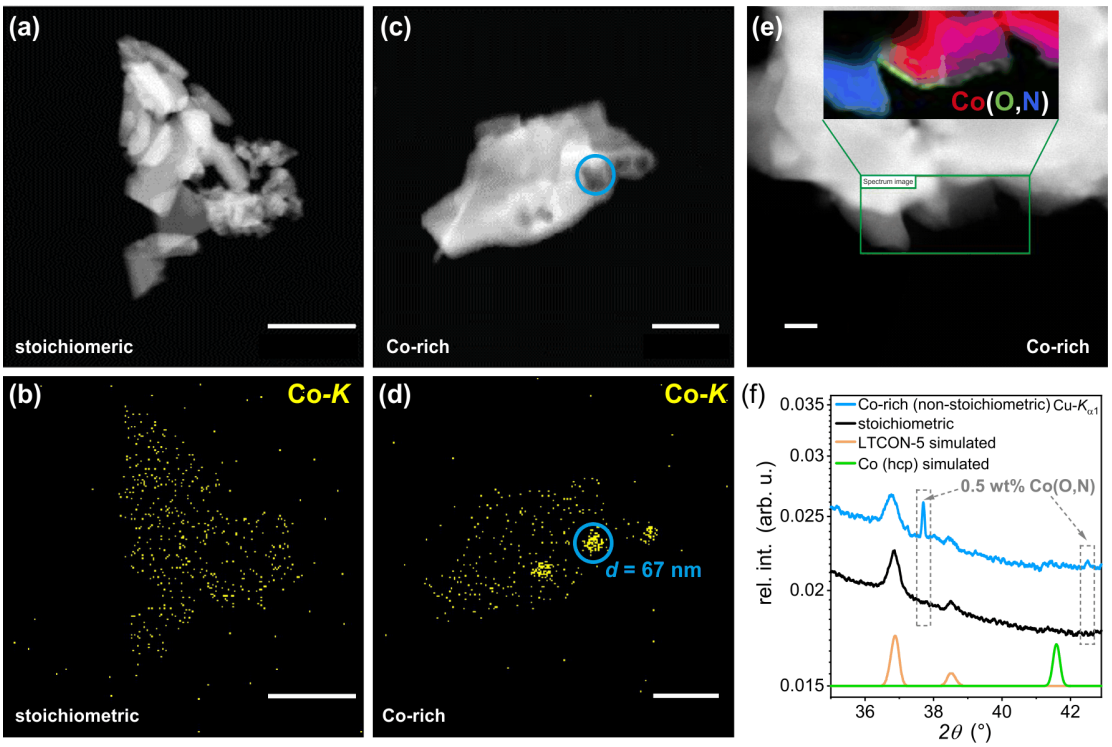

FIG. 3. HAADF/EDX and PXRD investigations of LTCON-5. (a)–(b) HAADF image (dark-field) and EDX map of single-phase (stoichiometric) LTCON-5 nanoparticles showing the homogeneous distribution of Co ions in the particles. Scale bars: 500 nm. (c) HAADF image of Co-rich LTCON-5 nanoparticles containing Co(O,N) nanoparticles. Scale bar: 250 nm. (d)–(e) EDX maps of Co-rich LTCON-5 nanoparticles containing Co(O,N) nanoparticles. Scale bars of (d): 250 nm and (e): 50 nm. In Fig. 3e, La and Ta are not measured. (f) PXRD data of the stoichiometric and Co-rich LTCON-5 samples.

We used HAADF, EDX, and powder X-ray diffraction (PXRD) for thorough characterization of both samples (Figs. 3a-f). The contrast variation of the nanoparticles observed by the HAADF imaging in Figs. 3a,c,e can be attributed to different crystal orientations of the particles proven by electron diffraction (Fig. S14). EDX allows the investigation of the homogeneous distribution of elements in a material. First, we investigated the non-stoichiometric sample: in combination with EDX, HAADF and PXRD only Co(O,N) nanoparticles with 0.5 wt% as a secondary phase exhibiting a diameter of 40 nm ≤ d ≤ 80 nm in the Co-rich LTCON-5 were found. Other elements such as La, Ta, O, and N, which were recorded, show a homogeneous distribution (Fig. S15 and Tab. S23). In Fig. 3f only PXRD reflections of the Co(O,N) phase in the Co-rich sample were found and no reflections of an elemental Co phase (Co-hcp or Co-fcc). This can be explained by the applied high temperatures and long ammonolysis

periods [25] which do not allow the formation of elemental (metallic) phases. Therefore, elemental Co in the Co-rich LTCON-5 can be excluded.

Instead, by using the exact stoichiometric amount of Co ions for the synthesis neither Co(O,N) particles nor elemental Co particles as secondary phases are found (Figs. 3b and f). Hence, the possibility to obtain Co-containing secondary phases in a stoichiometric weighed sample by using the applied synthesis procedure is very unlikely. This demonstrates that we synthesized single-phase LTCON powders where the Co ions are completely included in the materials matrix.

8.5. HT-ferromagnetism in single-phase perovskite-type LTCON

Next, we investigated the magnetic properties of LTCON-1, LTCON-3, and LTCON-5 *via* superconducting quantum interference device (SQUID) measurements (Figs. 4a–c).

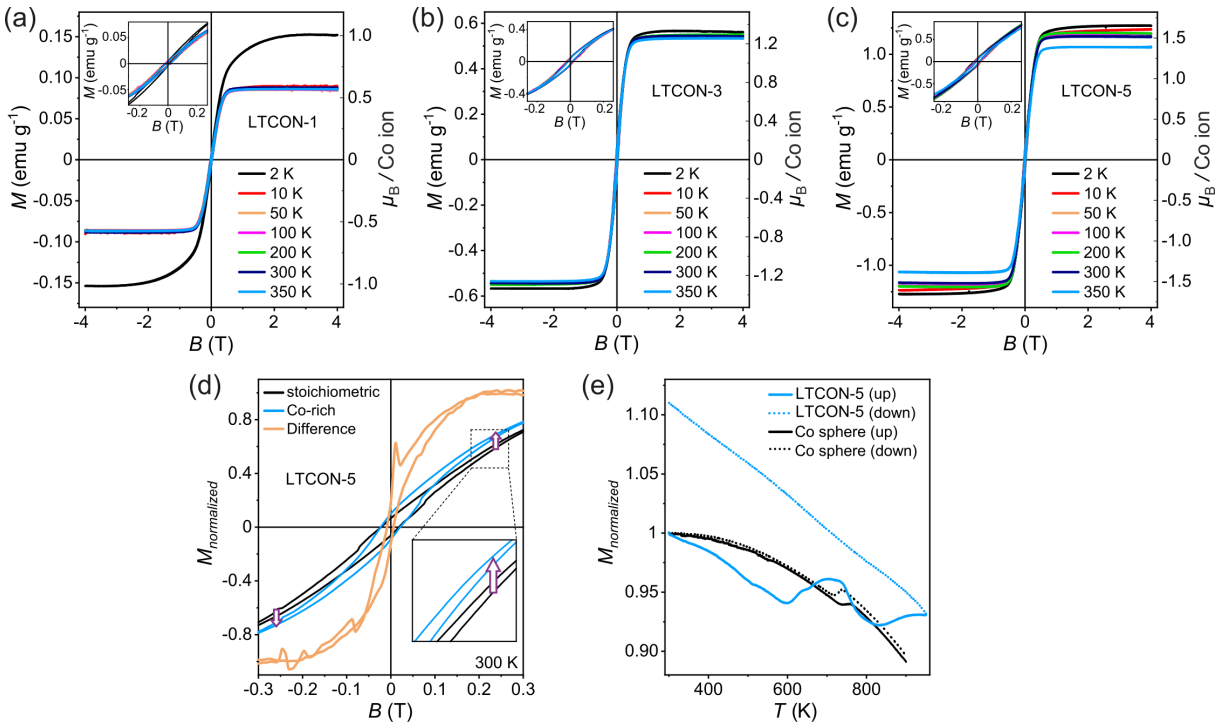

FIG. 4. Magnetic investigation of LTCON. (a)–(c) Magnetization curves of LTCON-1, LTCON-3, and LTCON-5. (d) Field-dependent magnetization curves at 300 K of the stoichiometric and Co-rich LTCON-5. The purple arrows indicate the almost constant difference between both. The difference has a much steeper slope at fields below 0.1 T. The difference signal could be related to the Co(O,N) particles identified in Fig. 3. For a better comparison, all curves were normalized. (e) Normalized magnetization versus temperature curves of single-phase LTCON-5 and a pure Co metal sphere.

At room temperature (300 K) a clear saturating behavior is observed, with 90 % of the saturation magnetization M_s at fields of about 0.3 T. The insets in Figs. 4a–c reveal a clear hysteretic behavior (hysteresis loops) with coercive fields (Tab. S24) indicating ferromagnetism. At 300 K, M_s increases with the amount of Co ions from LTCON-1 to LTCON-5 from 0.088 emu g^{-1} to 1.179 emu g^{-1} (Table I).

TABLE I. SQUID-based magnetic parameters at 300 K. The extracted magnetic parameters are the saturation magnetization (M_s), and the magnetic moment ($m_{\mathrm{Co\ ion}}$) per Co ion for each Co ion concentration (x).

Compound	x	M_s **(emu g^{-1})**	$m_{\mathrm{Co\ ion}}$ **(μ_B/Co ion)**
LTCON-1	0.01	0.088	0.60
LTCON-3	0.03	0.543	1.28
LTCON-5	0.05	1.179	1.53

In contrast to the observed clear HT-ferromagnetism of LTCON, the LTCO precursor exhibits just simple paramagnetism (Fig. S16) and pristine $LaTa(O,N)_3$ revealed at 300 K a diamagnetic behavior [17] in former studies. The processing of the raw SQUID data of LTCON is shown in Fig. S17. The observed strength of the ferromagnetic signal is orders of magnitude larger in contrast to former studies [6] (Supplemental Material Sec. IV), excluding measured SQUID artefacts and contaminants.

Additionally, all LTCON samples show an increase of a paramagnetic-like behavior with a similar absolute value at low temperatures. Because of the strong increase of the total sample magnetization with increasing Co ion concentration, the relative paramagnetic contribution is reduced for higher Co ion concentrations. This can be seen in the 2 K curves from LTCON-1 to LTCON-5 (Figs. 4a–c). The observed paramagnetism (Brillouin function shape) with respect to the ferromagnetism has a relative contribution of 60 % in LTCON-1. In comparison, for LTCON-5 the contribution difference is only 4 %. However, the absolute paramagnetic contribution is almost similar in strength for all three oxynitride samples.

In addition, a clear increase in the magnetic moment per Co ion is observed. If we attribute the whole sample magnetization completely to the given amount of Co ions, we can calculate a magnetic moment per Co ion. This is increasing from 0.6 μ_B/Co ion to 1.53 μ_B/Co ion. The observed unexpected high sample magnetizations lead to macroscopic attracting forces by conventional permanent magnets. Fig. 1 shows the mechanical movement of the whole LTCON-5 powder by permanent magnets (Movie S1 and S2). Of course, such magnetic force-related effects are always present for samples exhibiting the same magnetization. However – because the entire powder is moved – it demonstrates a homogeneous magnetic behavior combined with a homogeneous material composition.

In former reports undesired elemental transition metal clusters were responsible at least for some parts of the measured magnetization curves [8,26]. We already excluded particulate Co-rich secondary phases such as Co(O,N) and particulate elemental Co by chemical analysis. Now, we exclude elemental Co clusters by magnetic investigations because of their tiny size: small clusters of elemental Co would reveal a superparamagnetic behavior [27]. Therefore, we compared calculated magnetization curves of elemental Co clusters at different temperatures (10 K to 350 K) with the measured magnetization curve of LTCON-5 at 300 K (Fig. S18). The calculated magnetization curves for elemental Co clusters reveal a very strong temperature dependence indicating superparamagnetism (Supplemental Material Sec. V). Superparamagnetic materials also reveal a strong increase of the coercive fields at low temperatures, which remarkably decrease at room temperature [28,29]. Even larger elemental Co clusters [30] and elemental Co particles reveal observable temperature dependencies in saturation magnetization, shape, and coercive fields between 10 K and room temperature. All this cluster-like behavior is absolutely not observed for our samples (Figs. 4a–c): our obtained coercive fields and curve shapes are almost temperature-independent. Therefore, this by itself is a clear proof for the absence of superparamagnetic elemental Co clusters in LTCON.

Not only the absence of temperature dependence, also the relative high saturation field is an additional proof for the absence of Co clusters. LTCON contains a very low Co ion concentration. Therefore, the average distance of potential tiny elemental Co clusters would be quite large. In comparison to Li *et*

al. [29], the saturation field of Co clusters of 6 nm size with an elemental Co concentration of 43 ± 5 at% in the whole sample is at 0.15 T at room temperature. Since we have a Co ion concentration below 1 at%, we clearly can exclude dipole-dipole interactions between tiny Co clusters as a possible source for the wide hysteresis loops observed in LTCON.

Additionally, we compared the 300 K magnetization curves of the single-phase LTCON-5 and the Co-rich LTCON-5 (Fig. 4d). A clear difference is observed, that we attribute to the existing Co(O,N) nanoparticles in the Co-rich LTCON-5. We can estimate from the difference that the Co(O,N) particles have just a 7 % magnetic contribution to the total sample magnetization of the Co-rich sample. Furthermore, we performed SQUID measurements up to 950 K (Fig. 4e) in vacuum. The measurements show that the temperature dependence is quite different between LTCON-5 and elemental Co. The increase of the magnetization at 600 K indicates a partial decomposition by nitrogen loss and further vacancy formation rather than a complete decomposition of the material. It is worth to mention that this partial decomposition results in a 12 % increase in saturation magnetization, already indicating a correlation between ferromagnetism and vacancies. Since the T_C seems to be higher than the observed partial decomposition temperature of the material and the crystal structure is thermodynamically stable over the measured temperature range in vacuum (Supplemental Material Sec. VI, Fig. S19), the T_C cannot be determined with our SQUID system. In addition, the measured pure Co metal sphere shows the expected hysteretic hcp–fcc phase transition (local maximum), which is not visible in LTCON-5.

In order to identify possible different magnetic contributions of the Co ions to the sample magnetizations, we performed X-ray absorption spectroscopy (XAS) / XMCD at the Co-$L_{2,3}$ edges (Fig. 5). In Figs. 5a–c the bulk-sensitive transmission (TR) mode spectra of LTCON-1, LTCON-3, and LTCON-5 are presented. The measurements were performed at 300 K or at 77 K for LTCON-1. The 77 K spectrum of LTCON-1 is presented because of a more detailed peak structure originating from reduced Franck-Condon broadening [31]. By measuring LTCON-1 at 300 K (Fig 5d) the spectral shape resembles LTCON-3 and LTCON-5 at 300 K. In Figs. 5a-c, all three TR spectra reveal a significant XMCD signal and show similar multiplet-like peak structures giving the proof of oxidized Co species such as Co^{3+}/Co^{2+} [32–34]. For other perovskite-type Co-containing oxides with Co^{3+} or Co^{2+} in octahedral coordination (*e.g*. $LaCoO_3$) also Co-$L_{2,3}$ edge spectra with very similar spectral shape were observed [32,35,36].

By comparing the TR spectra of LTCON with a Co metal reference sample (Fig. 5d), possible existing elemental (metallic) Co cluster and/or Co particles as the origin of the observed HT-ferromagnetism can be excluded, finally: The reference Co metal TR spectra are measured with the same measurement parameters (*e.g*. exactly the same energy resolution) at the same beamtime. This allows a direct and precise comparison of energy shifts and line shapes between all measured samples. All LTCON XAS spectra and especially LTCON-5 show a clear non-metallic broad multiplet-like peak structure with a distinct shoulder before and after the main peak. This is very different to the shape of the Co metal spectrum. More important is the fact that the obtained XMCD signal *e.g*. of LTCON-5 is much broader in shape and significantly shifted to lower photon energies compared to the Co metal XMCD spectrum (Fig. 5e). If we assume that the Co ions in LTCON-5 would be partially segregated to a secondary metallic phase like Co clusters or particles, and this phase would be only related to the observed ferromagnetism, one would expect almost exactly the same XMCD signal in position, shape, and width as the XMCD signal determined from the reference Co spectrum. This is not the case. Hence, the shape of the measured TR spectra of LTCON and the different XMCD signal to the XMCD signal of Co metal are directly proving the intrinsic ferromagnetism of LTCON. If we now assume that the solubility limit of Co would be below 5% at the Ta-site, the spectral shape should be quite different between LTCON-1 and LTCON-5, because the relative amount of Co metal-like spectra must increase for LTCON-5. However, all spectra look identically, proving that the solubility is higher.

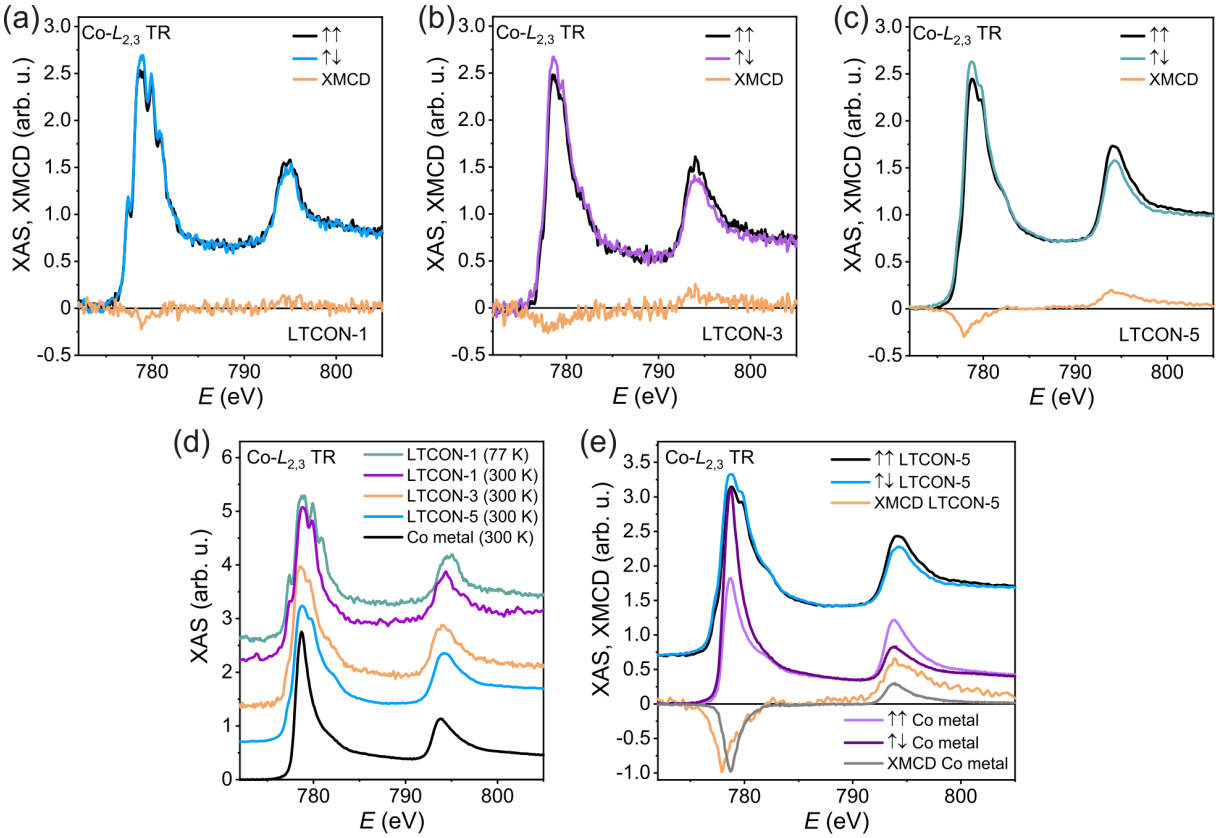

FIG. 5. XAS/XMCD measurements of LTCON. (a) TR spectrum of LTCON-1 measured at 77 K. (b) TR spectrum of LTCON-3 measured at 300 K. (c) Corresponding XAS/XMCD TR mode for LTCON-5 measured at 300 K. (d) Non-magnetic TR-mode XAS spectra of LTCON-1, LTCON-3, LTCON-5, and a pure metal Co TR spectrum measured at 300 K. In addition, a low temperature (77 K) TR spectrum of LTCON-1 containing more spectral details is presented. (e) TR-mode XMCD/XAS spectra of LTCON-5 and the Co metal reference sample. The XMCD signals were both scaled up to 1 in order to better compare the shape of both.

By applying sum rules [37,38] on the TR spectrum of LTCON-5 with the "upper limit" (see below) of holes of $n_H = 4$ (Co^{3+}), a spin moment of 1.14 ± 0.06 μ_B/Co^{3+} and a vanishing orbital moment of –0.01 ± 0.01 μ_B/Co^{3+} for LTCON-5 can be calculated. For LTCON-1 and LTCON-3, the determined moments are listed in Table II.

TABLE II. Orbital moments and spin moments of LTCON. The moments were determined *via* the measured XMCD/XAS spectra.

Compound	***x***	$m_{orb.}(\mu_B/Co^{3+})$	m_{spin} (μ_B/Co^{3+})
LTCON-1	0.01	–0.001 ± 0.01	0.44 ± 0.02
LTCON-3	0.03	–0.002 ± 0.01	1.0 ± 0.05
LTCON-5	0.05	–0.01 ± 0.01	1.14 ± 0.06

Additionally, by applying sum rules on the reference Co metal spectrum, a spin moment of $m_s = 1.64 \pm 0.08$ μ_B/Co^0 and an orbital moment of $m_l = 0.16 \pm 0.008$ μ_B/Co^0 are determined. These values are perfectly in agreement with the moments observed in well-known literature such as Chen *et al.* [39] and prove the accuracy of the determined sum rule results for LTCON in Table II. The XMCD-based magnetic moments for all LTCON powders are 25 % below the SQUID-based magnetic moments per Co ion. The measured TR spectra point to IS-Co^{3+} consistent to the obtained 25 % reduced magnetic

moments in comparison to the SQUID results [36]. However, other oxidation state contributions such as Co^{2+} cannot be excluded. Therefore, n_H (*e.g*. by using $n_H = 3$ for Co^{2+}) will be below 4 on average for all Co ions and, hence, the sum rule results further decrease. Because of the observed difference to the SQUID-based values, the obtained XMCD results proof that besides the ferromagnetic Co ions in LTCON the host matrix has to be magnetically polarized. This can also explain the ferromagnetic long-range ordering which is observed in LTCON.

If we still would try to attribute the sample magnetizations to a non-observed secondary phase, by questioning the observed spectral shapes and the energy shifts between Co metal and LTCON XMCD spectra, the total magnetization must then be related to this secondary phase. As we have demonstrated above for the non-stoichiometric sample we can easily observe a secondary phase with a Co^{z+} excess of 3.4 %. Thus, we can start a thought experiment: We imagine a two-phase sample with 10 % from a ferromagnetic Co-containing phase and 90 % from a non-ferromagnetic LTCON phase (Tab. S27). In this case the Co magnetic moment would belong completely to the ferromagnetic secondary phase. If we now take the result of the Co magnetic moment for the whole LTCON-5 sample ($1.14 \pm 0.06\ \mu_B/Co^{3+}$) we have to multiply by 10 the magnetic moment of Co^{3+} to get the magnetic moment for just 10 % of a ferromagnetic Co-containing secondary phase because of linear correlation. This means a Co spin moment of $11.4\ \mu_B/Co^{3+}$ would be present in the 10 % ferromagnetic secondary phase, whereas $0\ \mu_B/Co^{3+}$ would be in the 90 % of non-magnetic LTCON-5. The result of $11.4\ \mu_B/Co^{3+}$ is not possible.

To conclude, by having a close look at all results, even if a very small Co metal-like phase would be present it cannot explain the existing XAS/XMCD results and electron microscopy studies. All results tend to an intrinsic ferromagnetism of LTCON originating from diluted Co ions in the material.

8.6. Comparison to a similar system

For comparison we synthesized a similar system, namely $LaTa_{0.95}Ni_{0.05}(O,N)_{3-\delta}$ (LTNON). The Ni-based material exhibited the same space group type (*Imma*) and red color as LTCON (Supplemental Material Sec. VII, Fig. S20 and Tabs. S25, S26). However, by applying crystal structure analysis we found a very low solubility limit for Ni ions in the material (≤ 0.6 at%) revealing secondary phases such as Ni_3N, also easily observable as Ni-rich regions in the EDX measurement (Fig. S21). Additionally, the not-single-phase LTNON exhibited a small ferromagnetic contribution in combination with a large temperature-dependent paramagnetic contribution (Fig. S22) underlining the results that Ni^{z+} was not completely included into the crystal matrix (secondary phase visible). Since the chemical behavior of Ni^{z+} differs from that of Co^{z+} we want to emphasize that every other ion exhibits chemically different behaviors to Co^{z+} leading to different compositions and solubility limits. Therefore, our conclusion is that Co^{z+} is currently the only ion to get our observed results.

Hence, we demonstrated that it requires a careful evaluation of the synthesis parameters such as cationic stoichiometry and the choice of the right magnetic ion (Co^{z+}) for the synthesis to obtain a ferromagnetic behavior above RT in a DMS material.

8.7. Discussion of the HT-ferromagnetism in LTCON

As the presence of HT-ferromagnetism in LTCON is highly unexpected we try to provide a preliminary discussion of this phenomenon in comparison to the previous explanations given for the room temperature ferromagnetism found in pristine ZnO. For this compound, surface-related vacancies were identified to explain ferromagnetic coupling and the magnetic volume fraction was shown to be related to the amount of non-stoichiometric grain boundaries [12,14,15]. This is also consistent to recent studies on highly defective 2D ZnO nanosheets [40]. Since LTCON contains a significant amount of anion vacancies (Tab. S4), one could suggest that the effect observed in LTCON even in the bulk could be similar to the vacancy dominated ferromagnetic foam as discussed in other d^0 ferromagnetic materials [12,14,15]. Additionally, the introduced nitrogen ion can play a significant role by varying the ionic and covalent character of the *B*–*X* bonding [22], which might support the vacancy introduced changes in the electronic structure. Considering this, the mechanism of the observed HT-ferromagnetism in LTCON seems to be more complicated than that of defect-ridden ZnO.

The magnetization increases by a factor of about 13, whereas the Co ion concentration is increased by a factor of 5 (Table I and II): this is directly related to the XMCD-based change in Co^{3+} magnetic moments. This suggests that the Co ion is also mediating ferromagnetism and demonstrates a clear key ingredient. Since the calculated magnetic moments per Co ion determined from the XMCD measurements are at least 25 % lower than the by SQUID-determined values, we conclude that all of the existing Co ions are not sufficient to explain the observed magnetic behavior. This again supports the presence of a bulk-like ferromagnetism, whereas besides the Co ions extra magnetic moments must exist.

One also might think about a thread-like 3D single Co ion percolation network. If this network would be present, due to statistical Ta-site occupation a significant fraction of Co ions should not contribute to the percolation network, and a larger fraction of paramagnetic ions should exist in the bulk, which is also not observed in LTCON.

Hence, after two decades of intensive research in the magnetism community, our study demonstrates the realization of a HT-ferromagnetic DMS by partially substituting Ta with Co ions in a $LaTa(O,N)_3$ matrix. This highly reproducible result lays the foundation for a new research field investigating and developing same or similar DMS systems. Furthermore, it can resurrect the general research field of DMS, which had fallen out of favor over the last few years due to the lack of success. We expect that future investigations will focus on discovering new material matrices, which exhibit room temperature DMS, and understanding the underlying origin of the dilute ferromagnetic ordering.

8.8. Acknowledgements

The authors thank Mr. Samir Hammoud for HGE and ICP-OES measurements, Dr. Sebastian Bette, Mrs. Christine Stefani, Prof. Dr. Robert Dinnebier for PXRD (D8 Bruker) measurements, Mrs. Annette Fuchs and Prof. Dr. Joachim Maier for nitrogen sorption, Dr. Maximilian Hackner and Prof. Dr. Joachim Spatz for providing the glovebox for synthesis. For fruitful discussions and proof reading we acknowledge Dr. Max T. Birch. Thanks goes to Dipl.-Ing. Claudia Fasel and Dr. Rotraut Merkle for TGA-MS measurements and Dr. Sven Fecher and Dr. Songhak Yoon for fruitful discussions. The authors acknowledge the financial support of the Institut Laue Langevin, Grenoble, France and the reactor beamtime. We thank the synchrotron light source KARA and the KNMF, both Karlsruhe, Germany, for the provision of beamtime. C.B., M.W., and A.W. thank the German Research Foundation for financial support within the priority program SPP 1613 “Solar H_2” (WE 2803/7-1).

8.9. Appendix

8.9.1. Methods

8.9.1.1. Synthesis of LTCO

The oxides were prepared *via* a Pechini method which is based on the one already reported for n-LTO [17]. First, $TaCl_5$ (Alfa Aesar, 99.99 %) and $Co(NO_3)_2{\cdot}6H_2O$ (Merck, EMSURE®) were loaded in an exact stoichiometric amount into a Schlenk flask under argon and 50 mL of dried methanol was added. The amount of substance of the *B*-site cations Ta and Co was calculated to be 0.01 mol in total. For the Co-rich sample an additional amount (4 %) of $Co(NO_3)_2{\cdot}6H_2O$ was added. Afterwards, 0.03 mol water-free citric acid (Sigma Aldrich, ≥ 99.0 %) for all samples was added. 0.01 mol $La(NO_3)_3{\cdot}6H_2O$ (Sigma Aldrich, 99.99 %) was weighed into a second Schlenk flask and citric acid was added in the same molar ratio as for the *B*-site cations. The mixture was dissolved in 10 mL of dried methanol and the solutions of both Schlenk flasks were combined in one Schlenk flask and stirred under reflux for 2 h at 353 K with addition of a 15-fold molar excess of ethylene glycol (Merck, EMPLURA®). The dispersion was transferred to a crystallizing dish and heated for 10 h at 393 K followed by a thermal treatment at 573 K for 5 h as reported before [17]. The resulting black xerogel was calcined in an alumina crucible for 16 h at 923 K to obtain the nanocrystalline $LaTa_{1-x}Co_xO_{4-\delta}$ (LTCO) with x = 0.01 (LTCO-1), x = 0.03 (LTCO-3), x = 0.05 (LTCO-5).

8.9.1.2. Synthesis of LTCON

The synthesis of $LaTa_{1-x}Co_x(O,N)_{3-\delta}$ (LTCON) with x = 0.01 (LTCON-1), x = 0.03 (LTCON-3), x = 0.05 (LTCON-5) is described in the following: 350 mg of LTCO was loaded into an alumina boat and placed into a conventional thermal gas flow ammonolysis setup. Ammonolysis was carried out for 10 h at 1,223 K with two subsequent ammonolysis cycles for 14 h at 1,273 K and KCl flux addition (1:1 weight ratio). The applied ammonia flow for all cycles was 300 mL·min^{-1} NH_3 (Westfalen AG, > 99.98 %). The same conditions were used to prepare the Co-rich LTCON-5 sample.

8.9.2. Sample Characterization

8.9.2.1. Crystal Structure

Powder X-ray diffraction (PXRD) measurements at room temperature were carried out on a Bruker D8-Advance powder X-ray diffractometer using Cu-K_{α_1} radiation (Ge(111) monochromator), Bragg Brentano geometry, and a Lynx-Eye detector. Additionally, a Rigaku Smartlab powder X-ray diffractometer (Cu-$K\alpha_{1,2}$) was used. The continuous scans covered an angular range of 5° ≤ 2θ ≤ 90° with an angular step interval of 0.007°. The collected diffraction data were evaluated *via* Rietveld refinements using *FullProf.* 2k [41–43]. Pseudo-Voigt functions were selected to describe the reflection profile and the background was linearly interpolated between a set of background points with refinable heights.

8.9.2.2. Chemical Composition

The chemical composition of the produced samples was investigated *via* inductively coupled plasma optical emission spectroscopy (ICP-OES) using a Spectro Ciros CCD ICP-OES instrument for cations and hot gas extraction technique (HGE) using an Eltra ONH-2000 analyzer for the anions.

8.9.2.3. In Situ Experiments - Formation

In situ ammonolysis [17] was performed by thermogravimetric analysis (TGA) using a Netzsch STA 449 F3 Jupiter. The measurements were carried out under flowing NH_3 (80 mL·min^{-1} NH_3 + 8 mL·min^{-1} Ar) with a heating rate of 10 K·min^{-1} up to 1,273 K.

8.9.2.4. X-Ray Photoelectron Spectroscopy

X-ray photoelectron spectroscopy (XPS) was carried out using a Kratos Axis Ultra system with a monochromatized Al- K_a source (1,486.6 eV) holding a base pressure in the lower 10^{-10} mbar range. The powders were fixed on an indium foil and a flood gun was used in order to avoid charging effects. The binding energy was calibrated by setting the C 1*s* of adventitious carbon to 284.5 eV [44] with respect to the Fermi level. Analysis of the XPS data was performed with Casa XPS software. The energy separation and peak area of the Ta $4f_{7/2}$ and Ta $4f_{5/2}$ orbitals were constrained according to literature [44]. The low signal to noise ratio together with a non-flat background did not allow for any reasonable fitting of the Co 2*p* region.

8.9.2.5. Electron Microscopy Investigations

The particle morphology of the produced LTCON and LTCO was analyzed *via* scanning electron microscopy (SEM) (ZEISS GeminiSEM 500, 2 kV) and the in-lens detector was used for imaging. For energy-dispersive X-ray spectroscopy (EDX) a window-containing XFlash® 6|60 (Bruker) detector was used. The accelerating voltage for EDX measurements was 15 kV.

For transmission electron microscopy (TEM) investigations the particles of LTCON were dispersed in ethanol and drop-cast on a Cu grid covered with an amorphous carbon foil and with a mesh size of 200 µm provided by Plano. Small accumulations of oxynitride and oxide particles, respectively, were investigated on a Philips CM-200 FEG TEM operated at 200 kV, applying bright- and dark-field imaging. In order to verify the space group determined by Rietveld refinements of the PXRD and neutron diffraction (ND) data, selected-area diffraction patterns were recorded. The recorded polycrystalline diffraction patterns were analyzed by using the JEMS software package [45]. Colored grain orientation maps were constructed by the overlay of five dark-field images recorded with varying beam tilt. The composition and homogeneity of selected particles were analyzed with an EDX system from EDAX. Elemental mappings were collected with a probe size of 3 nm, a step size of ~2 nm, and a dwell time of 15 ms per pixel. The objective polepiece of the device contains only iron.

High-resolution transmission electron microscopy (HR-TEM) was performed by using the state-of-the-art JEOL ARM200F TEM coupled with an EDX system from JEOL (plus Bruker) at the "Stuttgart Center for Electron Microscopy (StEM)" in Stuttgart. The microscope was operated at 200 kV. The LTCON-5 particles were prepared as described above for the Philips CM-200 FEG TEM. To discriminate the measured cobalt concentration from the cobalt in the polepiece, Co-free $LaTaON_2$ (synthesized after ref. [17]) was measured as reference.

8.9.2.6. Diffuse Reflectance Spectroscopy

UV-visible diffuse reflectance spectra (DRS) were recorded by using a Carry 5000 UV–VIS NIR spectrophotometer. The spectra were measured in the range of 200 nm to 800 nm and the Kubelka-Munk [46] conversion was applied to the recorded reflectance spectra. The optical bandgaps were estimated by extrapolating the onset of absorption to the abscissa.

8.9.2.7. SQUID

Magnetometer surveys were carried out with a commercial VSM MPMS3 superconducting quantum interference device (SQUID) from Quantum Design. This system allows both conventional DC and VSM-type measurements. The temperature ranged from 1.8 K up to 350 K (oven option: T < 1,000 K, p < 150 mTorr), while the field was switched up to 4 T. For zero field cooling purposes the magnet was quenched to minimize the residual magnetic field. Depending on the sample and the measurement type the effective sensitivity is in the range of 10^{-8} – 10^{-9} emu. The pressed powder anisotropy measurements for in- and out-of-plane measurements were performed with a Quantum Design MPMS 7 system, because the detection system is less sensitive for variations in the filling factor, providing

better precision and comparability for anisotropic sample geometries. The weight of the measured pure Co metal sphere was 4.3 mg. The diamagnetic background originating from the sample holder was subtracted from a finite linear slope determined from the negative slope of the raw SQUID data (Fig. S17). Since perovskite-type oxynitride powders exhibit a very bad sinter ability (therefore high grain-boundary resistivity) and the particles are in the nm-range, carrier-mediated magnetic measurements were not performed.

8.9.2.8. XAS / XMCD

X-ray magnetic circular dichroism (XMCD) and X-ray absorption spectroscopy (XAS) experiments were performed at the synchrotron ANKA/KARA at KIT, Karlsruhe, in order to measure local atomic magnetic moments. All XMCD and XAS spectra were recorded at the WERA beamline with an energy resolution of about $\Delta E/E = 2 \cdot 10^{-4}$. At the Co–$L_{2,3}$ edge the degree of circular polarization was 82 %, which was used for sum rule corrections. We have used our own superconducting magnet end station providing ultra-fast field switching with ramping rates up to 1.5 $T \cdot s^{-1}$. All spectra were measured in an applied magnetic field up to 4 T. Each XMCD spectrum was measured as a function of energy with fixed light helicity and field. The energy was swiped uniformly with a rate (monochromator speed) of 0.2 $eV \cdot s^{-1}$ measured for each spectrum while simultaneously reading out the transmission data (TR) and incident X-ray (Au grid for I_0) current with about one data point every 0.03 eV. In order to get the XMCD data the circular light helicity was chosen (R = right, L = left), then two measurements were performed with reversed magnetic field (N = north; S = south). The sequence for a single full step run was RN→RS→LN→LS→LN→LS→RN→RS. This sequence minimized the effects of drift and further possible systematic errors. For better statistics, final spectra were averaged over consecutive spectra (in both helicities). TR and I_0 were measured using Keithley 6517A electrometers. The ramping rate (0.2 $eV \cdot s^{-1}$) was carefully chosen that no observable energy broadening could be detected. Each single XAS spectrum took about 3-5 minutes. No noticeable energy drift was observed between consecutive single spectra. Non-magnetic XAS spectra were obtained by averaging the magnetic XAS spectra for parallel and antiparallel aligned light helicity vs. magnetization direction. For the XMCD measurements, the sample powders (35 mg) were dispersed in 150 µL of ethanol (≥99.5 %, Ph. Eur.) and 50 µL of a terpineol (Aldrich, water-free) / ethyl cellulose (#46070, Fluka) / ethyl cellulose (#46080, Fluka) / ethanol (≥99.5 %, Ph. Eur.) mixture. The mixtures ("glue") were prepared as follows: first, a 10 wt% solution in ethanol (≥99.5 %, Ph. Eur.) of both ethyl cellulose batches was prepared. Afterwards, both 10 wt% ethyl cellulose solutions (#46070, and #46080), terpineol, and ethanol were mixed together in a 2.2 : 2.8 : 2.1 : 1.5 weight ratio. The dispersion of particles, ethanol, and "glue" was drop-casted on a 5 × 5 mm "SiN" membrane (thickness of 100 nm) which was sputtered with a 5 nm Cr thin film for better adhesion and electrical conductivity. As a detector for the transmitted light an almost magnetic field-independent Hamamatsu GaAsP diode (G1116 type) was used.

8.9.2.9. Neutron Diffraction

Neutron diffraction was carried out on the high-resolution D2B diffractometer (λ = 1.59417(2) Å) of the Institut Laue Langevin (ILL). The diffractograms of LTCON were recorded at 10 K and 300 K. The ND data (DOI: 10.5291/ILL-DATA.EASY-471, 10.5291/ILL-DATA.EASY-472, 10.5291/ILL-DATA.6-06-482) was refined using the *FullProf* 2k [43] and a pseudo-Voigt function was chosen to generate the line shape of the reflections. No magnetic refinements of the data were possible as due to the low amount of Co present in the samples (Ta was assumed to be non-magnetic) any magnetic contribution to the scattering falls short of the detection limit of neutrons.

8.9.2.10. Nitrogen Sorption

In order to investigate the specific surface area of the oxide precursors nitrogen sorption was carried out using an Autosorb-1-MP (Detection limit: $S_{BET} > 1\ m^2 \cdot g^{-1}$) from Quantachrome Instruments. First, the samples were annealed at 393 K in order to remove adsorbed water. Adsorption and desorption

isotherms were collected at 77 K. To determine the specific surface area the Brunauer-Emmett-Teller [47] (BET) method was used.

8.9.2.11. TGA-MS

To determine possible adsorbed water and organic residues on the oxide precursors surface TGA coupled with mass spectrometry (MS) was carried out on a Netzsch STA 449 C Jupiter coupled with a QMS 403C Aeolos® mass spectrometer. The oxide was heated to 1,473 K at a rate of 5 $K \cdot min^{-1}$ under synthetic air and then cooled to room temperature.

8.10. References

[1] T. Dietl, H. Ohno, F. Matsukura, J. Cibert, and D. Ferrand, *Zener Model Description of Ferromagnetism in Zinc-Blende Magnetic Semiconductors*, Science (80-.). **287**, 1019 (2000).

[2] T. Dietl, *A Ten-Year Perspective on Dilute Magnetic Semiconductors and Oxides*, Nat. Mater. **9**, 965 (2010).

[3] I. Žutić, J. Fabian, and S. Das Sarma, *Spintronics: Fundamentals and Applications*, Rev. Mod. Phys. **76**, 323 (2004).

[4] D. D. Awschalom and M. E. Flatté, *Challenges for Semiconductor Spintronics*, Nat. Phys. **3**, 153 (2007).

[5] H. Ohno, *Making Nonmagnetic Semiconductors Ferromagnetic*, Science (80-.). **281**, 951 (1998).

[6] L. M. C. Pereira, *Experimentally Evaluating the Origin of Dilute Magnetism in Nanomaterials*, J. Phys. D. Appl. Phys. **50**, 393002 (2017).

[7] M. Gacic, G. Jakob, C. Herbort, H. Adrian, T. Tietze, S. Brück, and E. Goering, *Magnetism of Co-Doped ZnO Thin Films*, Phys. Rev. B - Condens. Matter Mater. Phys. **75**, 205206 (2007).

[8] A. Ney, A. Kováacs, V. Ney, S. Ye, K. Ollefs, T. Kammermeier, F. Wilhelm, A. Rogalev, and R. E. Dunin-Borkowski, *Structural, Chemical and Magnetic Properties of Secondary Phases in Co-Doped ZnO*, New J. Phys. **13**, 103001 (2011).

[9] M. Venkatesan, C. B. Fitzgerald, and J. M. D. Coey, *Unexpected Magnetism in a Dielectric Oxide*, Nature **430**, 630 (2004).

[10] J. M. D. Coey, D^0 *Ferromagnetism*, Solid State Sci. **7**, 660 (2005).

[11] J. M. D. Coey, M. Venkatesan, and C. B. Fitzgerald, *Donor Impurity Band Exchange in Dilute Ferromagnetic Oxides*, Nat. Mater. **4**, 173 (2005).

[12] B. B. Straumal, A. A. Mazilkin, S. G. Protasova, A. A. Myatiev, P. B. Straumal, G. Schütz, P. A. Van Aken, E. Goering, and B. Baretzky, *Magnetization Study of Nanograined Pure and Mn-Doped ZnO Films: Formation of a Ferromagnetic Grain-Boundary Foam*, Phys. Rev. B - Condens. Matter Mater. Phys. **79**, 205206 (2009).

[13] J. M. D. Coey, P. Stamenov, R. D. Gunning, M. Venkatesan, and K. Paul, *Ferromagnetism in Defect-Ridden Oxides and Related Materials*, New J. Phys. **12**, 053025 (2010).

[14] T. Tietze et al., *Interfacial Dominated Ferromagnetism in Nanograined ZnO: A MSR and DFT Study*, Sci. Rep. **5 : 8871**, (2015).

[15] Y. C. Chen, E. Goering, L. Jeurgens, Z. Wang, F. Phillipp, J. Baier, T. Tietze, and G. Schütz, *Unexpected Room-Temperature Ferromagnetism in Bulk ZnO*, Appl. Phys. Lett. **103**, 162405 (2013).

[16] Y. Fukuma, H. Asada, S. Miyawaki, T. Koyanagi, S. Senba, K. Goto, and H. Sato, *Carrier-Induced Ferromagnetism in* $Ge_{0.92}Mn_{0.08}Te$ *Epilayers with a Curie Temperature up to 190 K*, Appl. Phys. Lett. **93**, 252502 (2008).

[17] C. Bubeck, M. Widenmeyer, G. Richter, M. Coduri, E. Goering, S. Yoon, and A. Weidenkaff, *Tailoring of an Unusual Oxidation State in a Lanthanum Tantalum(IV) Oxynitride via Precursor Microstructure Design*, Commun. Chem. **2**, 134 (2019).

[18] M. Yang, J. Oró-Solée, J. A. Rodgers, A. B. Jorge, A. Fuertes, and J. P. Attfield, *Anion Order in Perovskite Oxynitrides*, Nat. Chem. **3**, 47 (2011).

[19] A. E. Maegli, S. Pokrant, T. Hisatomi, M. Trottmann, K. Domen, and A. Weidenkaff, *Enhancement of Photocatalytic Water Oxidation by the Morphological Control of* $LaTiO_2N$ *and Cobalt Oxide Catalysts*, J. Phys. Chem. C **118**, 16344 (2014).

[20] M. Jansen and H. P. Letschert, *Inorganic Yellow-Red Pigments without Toxic Metals*, Nature **404**, 980 (2000).

[21] C. Bubeck et al., *Bandgap-Adjustment and Enhanced Surface Photovoltage in Y-Substituted* $LaTa^{IV}O_2N$, J. Mater. Chem. A **8**, 11837 (2020).

[22] S. Mo, Y. Kurauchi, T. Katayama, Y. Hirose, and T. Hasegawa, *Theoretical Investigation of the Role of the Nitride Ion in the Magnetism of Oxynitride* $MnTaO_2N$, J. Phys. Chem. C **123**, 25379 (2019).

[23] W. Li, E. Ionescu, R. Riedel, and A. Gurlo, *Can We Predict the Formability of Perovskite Oxynitrides from Tolerance and Octahedral Factors?*, J. Mater. Chem. A **1**, 12239 (2013).

[24] R. D. Shannon, *Revised Effective Ionic Radii and Systematic Studies of Interatomic Distances in Halides and Chaleogenides*, Acta Crystallogr. Sect. A **32**, 751 (1976).

[25] P. Adamski, D. Moszyński, A. Komorowska, M. Nadziejko, A. Sarnecki, and A. Albrecht, *Ammonolysis of Cobalt Molybdenum Oxides - In Situ XRD Study*, Inorg. Chem. **57**, 9844 (2018).

[26] J. H. Park, M. G. Kim, H. M. Jang, S. Ryu, and Y. M. Kim, *Co-Metal Clustering as the Origin of Ferromagnetism in Co-Doped ZnO Thin Films*, Appl. Phys. Lett. **84**, 1338 (2004).

[27] S. Zhou, K. Potzger, J. Von Borany, R. Grötzschel, W. Skorupa, M. Helm, and J. Fassbender, *Crystallographically Oriented Co and Ni Nanocrystals inside ZnO Formed by Ion Implantation and Postannealing*, Phys. Rev. B - Condens. Matter Mater. Phys. **77**, 035209 (2008).

[28] S. R. Shinde, S. B. Ogale, J. S. Higgins, H. Zheng, A. J. Millis, V. N. Kulkarni, R. Ramesh, R. L. Greene, and T. Venkatesan, *Co-Occurrence of Superparamagnetism and Anomalous Hall Effect in Highly Reduced Cobalt-Doped Rutile $TiO_{2-\delta}$ Films*, Phys. Rev. Lett. **92**, 166601 (2004).

[29] D. Y. Li et al., *Anisotropic Magnetism and Spin-Dependent Transport in Co Nanoparticle Embedded ZnO Thin Films*, J. Appl. Phys. **114**, 033909 (2013).

[30] J. P. Chen, C. M. Sorensen, K. J. Klabunde, and G. C. Hadjipanayis, *Enhanced Magnetization of Nanoscale Colloidal Cobalt Particles*, Phys. Rev. B **51**, 527 (1995).

[31] C.-O. Almbladh and L. Hedin, *Beyond the One-Electron Model. Many-Body Effects in Atoms, Molecules, and Solids*, in *Handbook of Synchrotron Radiation*, edited by E.-E. Koch, 1b ed. (North-Holland, 1983), pp. 607–904.

[32] F. M. F. de Groot, J. C. Fuggle, B. T. Thole, and G. A. Sawatzky, *2*p *X-Ray Absorption of 3*d *Transition-Metal Compounds: An Atomic Multiplet Description Including the Crystal Field*, Phys. Rev. B **42**, 5459 (1990).

[33] G. Van Der Laan and I. W. Kirkman, *The 2*p *Absorption Spectra of 3*d *Transition Metal Compounds in Tetrahedral and Octahedral Symmetry*, J. Phys. Condens. Matter **4**, 4189 (1992).

[34] K. Rode et al., *Magnetism of (Zn,Co)O Thin Films Probed by X-Ray Absorption Spectroscopies*, Appl. Phys. Lett. **92**, 012509 (2008).

[35] M. W. Haverkort et al., *Spin State Transition in $LaCoO_3$ Studied Using Soft X-Ray Absorption Spectroscopy and Magnetic Circular Dichroism*, Phys. Rev. Lett. **97**, 176405 (2006).

[36] M. Merz, P. Nagel, C. Pinta, A. Samartsev, H. V. Löhneysen, M. Wissinger, S. Uebe, A. Assmann, D. Fuchs, and S. Schuppler, *X-Ray Absorption and Magnetic Circular Dichroism of $LaCoO_3$, $La_{0.7}Ce_{0.3}CoO_3$, and $La_{0.7}Sr_{0.3}CoO_3$ Films: Evidence for Cobalt-Valence-Dependent Magnetism*, Phys. Rev. B - Condens. Matter Mater. Phys. **82**, 174416 (2010).

[37] B. T. Thole, P. Carra, F. Sette, and G. Van Der Laan, *X-Ray Circular Dichroism as a Probe of Orbital Magnetization*, Phys. Rev. Lett. **68**, 1943 (1992).

[38] P. Carra, B. T. Thole, M. Altarelli, and X. Wang, *X-Ray Circular Dichroism and Local Magnetic Fields*, Phys. Rev. Lett. **70**, 694 (1993).

[39] C. T. Chen, Y. U. Idzerda, H. J. Lin, N. V. Smith, G. Meigs, E. Chaban, G. H. Ho, E. Pellegrin, and F. Sette, *Experimental Confirmation of the X-Ray Magnetic Circular Dichroism Sum Rules for Iron and Cobalt*, Phys. Rev. Lett. **75**, 152 (1995).

[40] X. Yin, Y. Wang, R. Jacobs, Y. Shi, I. Szlufarska, D. Morgan, and X. Wang, *Massive Vacancy Concentration Yields Strong Room-Temperature Ferromagnetism in Two-Dimensional ZnO*, Nano Lett. **19**, 7085 (2019).

[41] H. M. Rietveld, *Line Profiles of Neutron Powder-Diffraction Peaks for Structure Refinement*, Acta Crystallogr. **22**, 151 (1967).

[42] H. M. Rietveld, *A Profile Refinement Method for Nuclear and Magnetic Structures*, J. Appl. Crystallogr. **2**, 65 (1969).

[43] J. Rodriguez-Carvajal, *FullProf. 2k, Version 5.30, 2012, ILL*, (unpublished).

[44] F. Moulder, W. F. Stickle, P. E. Sobol, and K. D. Bomben, *Handbook of X-Ray Photoelectron Spectroscopy* (Perkin-Elmer Corporation, 1992).

[45] P. Stadelmann, *Image Analysis and Simulation Software in Transmission Electron Microscopy*, Microsc. Microanal. **9**, 60 (2003).

[46] G. Kortüm, W. Braun, and G. Herzog, *Principles and Techniques of Diffuse-Reflectance Spectroscopy*, Angew. Chemie Int. Ed. English **2**, 333 (1963).

[47] S. Brunauer, P. H. Emmett, and E. Teller, *Adsorption of Gases in Multimolecular Layers*, J. Am. Chem. Soc. **60**, 309 (1938).

8.11. Supplemental Material

Supplemental Material – Discussion

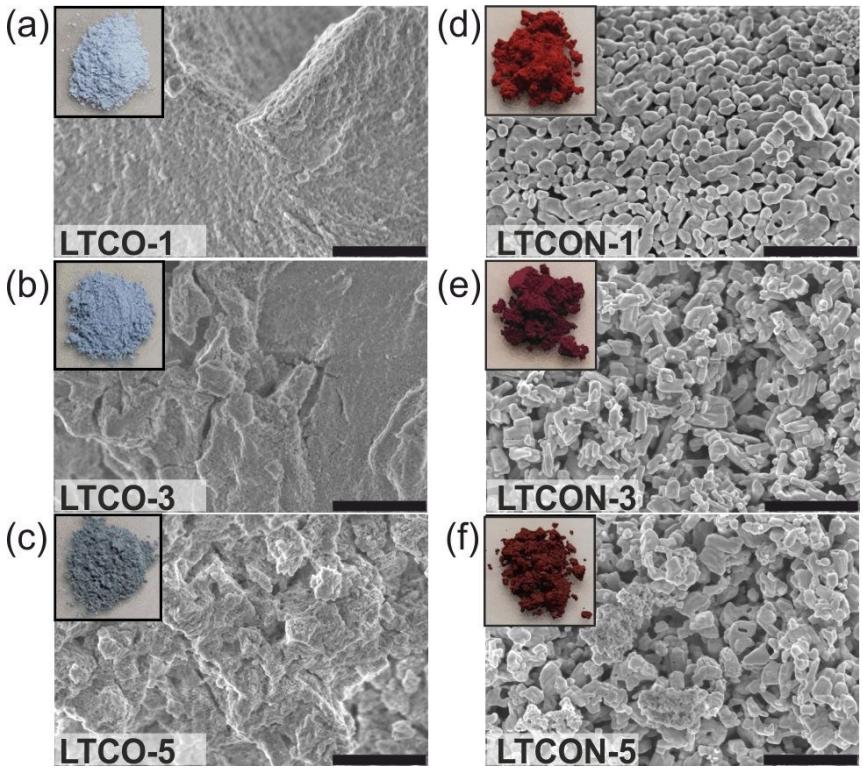

Fig. S1. SEM images, and sample photos of the oxides and oxynitrides. Respective SEM images of (a)–(c) all LTCO and (d)–(f) all LTCON powders showing primary particles in the nm-range with the respective sample photos showing the colored powders. Scale bars: 1 µm.

8.11.1. Supplemental Material Sec. I: Chemical analysis of LTCO

Powder X-ray diffraction (PXRD) reveals nanocrystalline oxide precursors for all three Co ion concentrations (Fig. S2). Similar PXRD patterns were already obtained for the synthesized and used nanocrystalline oxide precursors in ref. [1]. Because of the nanocrystallinity of the oxides, the determination of phase purity was not possible by PXRD. Therefore, the oxides were investigated by transmission electron microscopy (TEM) and energy-dispersive X-ray spectroscopy (EDX) (Fig. S3). The obtained TEM images show tiny primary particles in the nm-range, which were agglomerated to porous secondary particles pointing to the nanocrystallinity of the powders. By recording selected area electron diffraction (SAED) patterns no rings were visible. The recorded EDX maps reveal for all three Co ion concentrations a homogeneous distribution of Co and Ta and give no hint for secondary phases. The resolution was 10 nm per single Co photon count. Hence, we assume because of the EDX and SAED results the oxides to be phase pure.

To determine the anionic and cationic compositions of the single-phase oxides hot-gas extraction (HGE) (Tab. S1) and inductively coupled plasma optical emission spectroscopy (ICP-OES) were used, respectively. The lower obtained oxygen weight fractions for the oxides in comparison to the expected ones with a ratio of La:(Ta,Co):O = 1:1:4 (x = 0.01: 16.73 wt% O, x = 0.03: 16.83 wt% O, x = 0.05: 17.31 wt% O) were pointing to oxygen vacancies in the samples (Tab. S1). The expected oxygen weight fractions for the oxides were derived from the very similar assumed ratio for n-LTO (nanocrystalline "$LaTaO_4$") which was obtained at the same temperature with the same synthesis method. [1] By calcinating LTCO-1 ($LaTa_{0.99}Co_{0.01}O_{3.99(6)}$) at 1273 K to form crystalline LTCO-1 HGE measurements

revealed a composition of $LaTa_{0.99}Co_{0.01}O_{3.93(9)}$. The found amount of oxygen vacancies in crystalline LTCO-1 (c-$LaTa_{0.99}Co_{0.01}O_{3.93(9)}$) seems plausible from the fact that Co as *B*-site cation has a lower valence state than Ta which has normally 5+ [1] resulting in a higher concentration of anionic vacancies because of charge compensation. In order to verify the phase purity of crystalline LTCO-1 a PXRD pattern was recorded (Fig. S4). The recorded pattern was refined in the space group type $Cmc2_1$ revealing a single-phase oxide because no additional reflections were observed (Tabs. S2–S3).

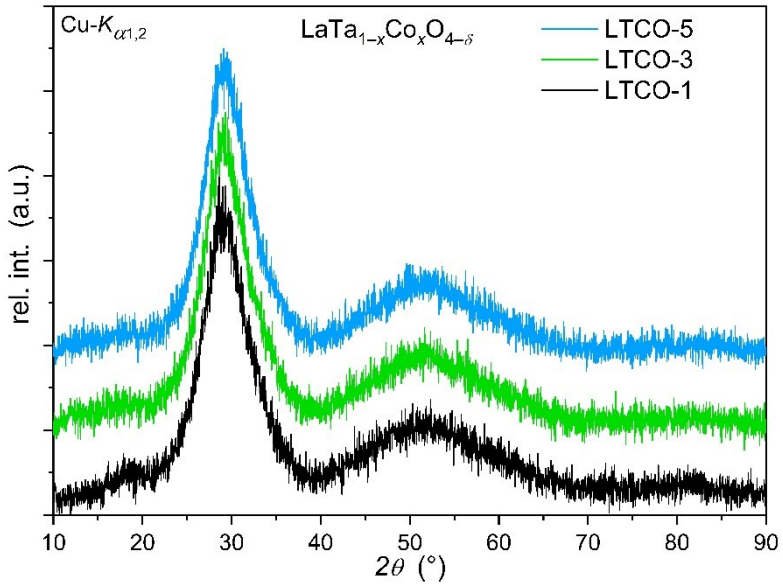

Fig. S2. Powder X-ray diffraction (PXRD) patterns of nanocrystalline LTCO. The patterns show nanocrystalline, nearly amorphous $LaTa_{1-x}Co_xO_{4-\delta}$ (LTCO) obtained after the used soft chemistry procedure. The anionic compositions were determined by HGE (Tab. S1).

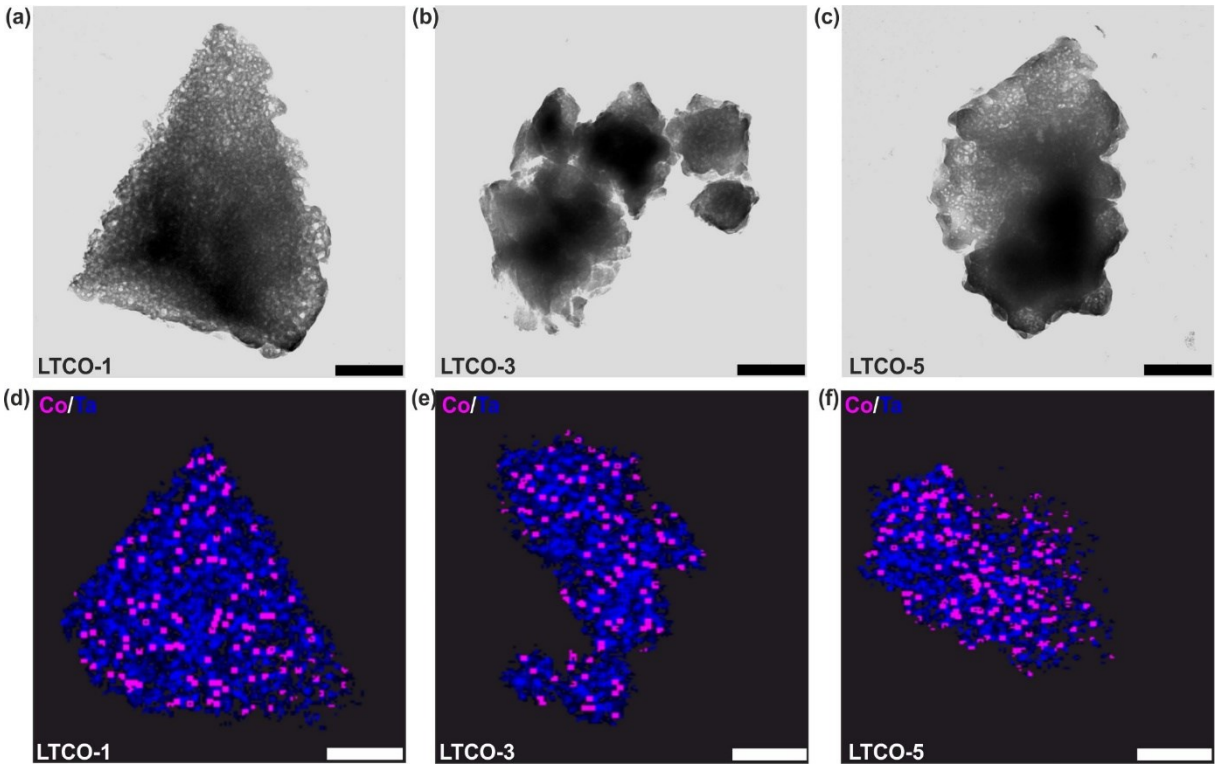

Fig. S3. TEM images and EDX mappings of LTCO. (a)–(c) TEM images of particles of the oxides and (d)–(f) EDX maps of the LTCO powders showing the homogeneous distribution of Co (pink) and Ta (blue) in the particles. The pixels were averaged with 3 x 3 pixels showing a pixel size of d = 10 nm. This means that one Co ion is present in a region of 10 x 10 nm^2 because of the low number of single counts. Scale bars of all images: 100 nm.

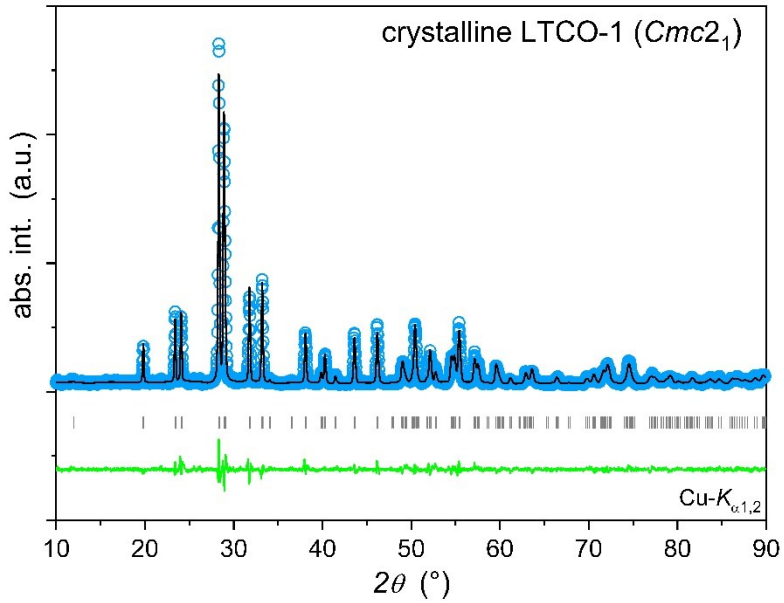

Fig. S4. Rietveld refinements of crystalline LTCO-1. The refinements reveal space group type $Cmc2_1$ for crystalline LTCO-1 (c-$LaTa_{0.99}Co_{0.01}O_{3.93(9)}$).

Tab. S1. Compositions of the oxide precursors. Oxygen content of LTCO and crystalline LTCO-1 (calcined at 1273 K) determined by hot gas extraction (HGE).

Compound	w ($O_{expected}$) (wt%)	w(O) (wt%)	O
LTCO-1	16.73	16.7 ± 0.3	3.99(6)
LTCO-3	16.83	16.7 ± 0.3	3.97(1)
LTCO-5	16.94	16.6 ± 0.4	3.91(9)
crystalline LTCO-1	16.73	16.5 ± 0.3	3.93(9)

Tab. S2. Unit cell parameters of crystalline LTCO-1 (c-$LaTa_{0.99}Co_{0.01}O_{3.93(9)}$). They were determined by Rietveld refinements.

Unit Cell Parameter	crystalline LTCO-1
Space group type	$Cmc2_1$
a (Å)	3.9304(4)
b (Å)	14.7690(1)
c (Å)	5.6286(5)
V_{cell} (Å^3)	326.73(5)
ρ (g·cm^{-3})	7.785
Phase fraction (wt%)	100
R_p (%)	7.45
R_{wp} (%)	9.50
χ^2	2.26
R_{Bragg} (%)	4.51

Tab. S3. Refined atom positions of crystalline LTCO-1 (c-$LaTa_{0.99}Co_{0.01}O_{3.93(9)}$). The determined space group type is $Cmc2_1$.

Atom	Wyck. Symb.	x	y	z	B_{iso} (Å^2)	sof[1]
La	4a	0	0.1699(2)	0.01956[2]	1.6(8)	1[2]
Ta	4a	0	0.4146(2)	0.05882[2]	2.1(4)	0.99[2]
Co	4a	0	0.4146(2)	0.05882[2]	2.1(4)	0.01[2]
O(1)	4a	0	0.281(2)	0.25982[2]	0.5[2]	1[2]
O(2)	4a	0	0.350(2)	0.81404[2]	0.5[2]	1[2]
O(3)	4a	0	0.513(3)	0.40898[2]	0.5[2]	1[2]
O(4)	4a	0	0.888(2)	0.13644[2]	0.5[2]	1[2]

[1]site occupancy factor, [2]fixed

8.11.2. Supplemental Material Sec. II: Chemical analysis and formation of LTCON

The cationic and anionic compositions of the oxynitrides were determined by HGE and ICP-OES (Tab. S4). The results revealed anionic vacancies for all three Co ion concentrations and, hence, were leading to the following anionic compositions: $LaTa_{0.99}Co_{0.01}O_{0.96(3)}N_{1.98(2)}\square_{0.05(5)}$ (LTCON-1), $LaTa_{0.97}Co_{0.03}O_{0.99(1)}N_{1.97(3)}\square_{0.03(4)}$ (LTCON-3), $LaTa_{0.95}Co_{0.05}O_{1.12(6)}N_{1.84(1)}\square_{0.03(3)}$ (LTCON-5). The square (□) represents the vacancies.

The crystal structures of the obtained oxynitrides were proven by neutron diffraction (ND) and powder X-ray diffraction (PXRD). Rietveld refinements of the PXRD and ND data reveal the space group type *Imma* for all oxynitrides (Figs. S5–S6, and Supplementary Tables 4–22) which was already observed for the perovskite-type oxynitrides $LaTaON_2$ and $LaTaO_2N$. [1] The contributions of the vanadium can (V) and cryo furnace (CF) (at 10 K) were considered in the refinements of the ND data at 10 K and 300 K since, small sample amounts of ca. 600 mg were used for measurements. Due to the small Co ion concentrations in the samples' magnetic contributions in the ND data was neither found at 10 K nor at 300 K.

To investigate the oxidation states of Ta in LTCON X-ray photoelectron spectroscopy (XPS) measurements were carried out and revealed two binding characters: Ta^{III}–(O,N) and Ta^{V}–(O,N) (Fig. S7). The XPS investigation and determination of the binding characters of the oxynitrides was done according to ref. [1]. The value of the binding energy $E_{B,Ta4f7/2}$ = 23.7 eV which refers to Ta^{III}–(O,N) according to the applied point charge model [1,2] was also found during *in situ* ammonolysis of n-LTO [1]. XPS is a very surface-sensitive method because of the very small mean free paths of the electrons [3]. Therefore, the concentrations of the Ta oxidation states reflects the first few nanometers and, hence, not the whole sample. [1] Consequently, Ta^{3+} is just present at the surface whereas Ta^{5+} is the main oxidation state. This was already observed for $LaTa^{V}ON_2$ [1]. The chemical environment of Ta in LTCON was supposed to be similar to $LaTa(O,N)_3$ [1]. This can be better understood by thinking about the potential Co ion concentration per unit cell in LTCON. For example, in one unit cell of LTCON-5 (formula unit *FU* = 4) just 0.2 Co ions on average are present leading to a similar chemical environment of Ta ions in LTCON-5 as in $LaTa(O,N)_3$. The determined Ta oxidation states indicated to oxidized Co including several possible oxidation states such as Co^{2+} and Co^{3+}. In order to get an additional information about the oxidation state of the Co ions in the samples we performed XPS measurements. However, the amount of Co ions (≤ 1 at%) is too low for detection. XPS is a very surface-sensitive method, and hence, the amount of possible detected Co ions is even lower. Therefore, additional information of the Co oxidation states in the samples cannot be obtained. Therefore, the only indication of the Co oxidation states can be obtained by X-ray absorption spectroscopy (XAS), where *e.g*. Co^{2+} and Co^{3+} with similar spectral shape as reported in ref. [4] can be found.

For LTCON-1 the red color is very similar to the previously reported color of $LaTaO_2N$ [1] indicating a low optically active defect concentration [1]. However, diffuse reflectance spectroscopy (DRS) measurements reveal an increasing reflectance (*R*) beyond the optical bandgap to higher wavelengths by increasing Co ion concentration (Fig. S8a). The optical bandgaps of LTCON were determined by applying the tangent method on the to Kubelka-Munk [5] plots converted curves as for $LaTa(O,N)_3$ [1] (Fig. S8b). The values of the optical bandgaps are: 1.9 eV (LTCON-1), 1.8 eV (LTCON-3), and 1.7 eV (LTCON-5). The measured DRS revealed the characteristic shape and behavior of a typical pure semiconductor absorption edge, for example in ZnO [6,7] or TiO_2 [8], while the spectra of metallic precipitates are quite different, even for very small metal bulk contributions [9,10].

The formation of LTCON was exemplarily investigated by *in situ* ammonolysis of LTCO-1 (Fig. S9a). From 298 K to 738 K a first mass change of –0.5 % can be derived from the desorption of organic residues and adsorbed water from the sample which was reported before for *in situ* ammonolysis of nanocrystalline lanthanum tantalum oxide (n-LTO) [1]. To confirm this, a thermogravimetric analysis coupled with mass spectrometry (TGA-MS) (Fig. S10) in synthetic air was carried out and revealed besides the measured mass change (–0.5 %) weak MS signals for m/z = 17 (OH^+), 18 (H_2O^+), 44 (CO_2^+). At T > 1120 K a second mass change of –3 % was observed caused by a further release of CO_2 (m/z =

12 (C^+), 22 (CO_2^{2+}), 44 (CO_2^+), 45 ($^{13}CO_2^+$)) and some NO_2 (m/z = 46 (NO_2^+)) remaining from the used nitrate starting materials. This confirms the before stated assumption. Since during *in situ* ammonolysis ammonia as reducing atmosphere was present, a further formation of oxygen vacancies in LTCO-1 can take place besides the release of H_2O, CO_2, and nitrous gases. The formation of oxygen vacancies during ammonolysis of oxide precursors was already observed for $LaTaO_4$ [1]. According to ref. [1] the following negative mass change, which occurs at 878 K (–1.6 %) in the sample is the starting point of nitrogen incorporation. Our LTCO-1 precursor already contains oxygen vacancies like the termination product of microcrystalline $LaTaO_4$ during *in situ* ammonolysis before nitrogen incorporation [1]. Additionally, it has a similar microstructure as the reported n-LTO [1] – tiny particle size of several nm, nanocrystalline, high specific surface area (S_{BET}) of 31.3 m^2/g. Therefore, we assume a product between $LaTaON_2$ [1] (obtained from $LaTaO_4$) and $LaTaO_2N$ [1] (obtained from n-LTO). This can also be verified by the "intermediate" reaction progression of LTCON in Fig. S11 (inset). After 10 h at 1223 K an overall negative mass change of –5.0 % was achieved. This is smaller than calculated for a full conversion to the expected product $LaTa_{0.99}Co_{0.01}ON_2$ (expected mass change: $\Delta m_{calc.}$ = –5.2 %) meaning the conversion was not completed after the first cycle. During cooling as for n-LTO [1] an absorption and desorption of gaseous species was observed. In order to identify the received product after the first ammonolysis cycles the formation of LTCON-1 and LTCON-3 were investigated by *ex situ* ammonolysis. After the first *ex situ* ammonolysis cycle at 1223 K / 10 h both products of LTCON-1 and LTCON-3 in comparison to the products of n-LTO and m-$LaTaO_4$ ($LaTaO_2N$ and $LaTaON_2$) [1] and in agreement with the observed progression of the *in situ* ammonolysis of LTCO-1 are not phase pure (Figs. S9b,c). Instead, a secondary phase in both compounds (shoulders at the reflections for LTCON-1 and a clear crystalline secondary phase for LTCON-3) was observed. The secondary phase for LTCON-3 shows a similar pattern as the crystalline LTCO-1 in Fig. S4, which can be one factor for the intermediate reaction progression. Additionally, the continuing mass decrease observed during the first (–5 %) and second cycle (–1.4 %) of *in situ* ammonolysis along with the total mass change of –6.4 % confirms the formation of a perovskite-type phase, keeping in mind the observed release of organic residues. The obtained reaction behavior of Co-substituted samples clearly deviated from the reported behavior of n-LTO [1]. On the one hand, a crystalline oxide precursor ($LaTaO_4$) with particles in the µm-range and low specific surface area (S_{BET}) leads to the O : N ratio of 1 : 2. On the other hand, a nanocrystalline oxide precursor (n-LTO) with particles in the nm-range and higher S_{BET} leads to O : N = 2 : 1 [1]. In our case, we obtained "$LaTa_{1-x}Co_xON_2$" as a product in-between containing particles with a size in the nm-range instead of µm-range but the absence of Ta^{4+}. We assume, that the oxygen vacancies present in our oxide LTCO precursors are the driving force for this. Also, the present Co ions can support the enhanced vacancy formation. In that case, the already present anionic vacancies can force an enhanced vacancy formation and nitrogen incorporation leading to a higher nitrogen content and with it to a ratio of O : N = 1 : 2. Additionally, the present oxygen vacancies can hamper the Ta reduction since by X-ray photoelectron spectroscopy (XPS) measurements a Ta^{III}–(O,N) and a Ta^{V}–(O,N) binding character (instead of a Ta^{IV}–(O,N) binding character) was determined for all three oxynitrides (Fig. S7). This can be understood by the higher nitrogen content forcing the Ta to stay in the 5+ state for charge compensation. Therefore, we can add besides the recent reported microstructure of the oxide precursor [1] the presence of oxygen vacancies in the oxide precursor as parameter to tailor the oxidation state of *B*-site cations in oxynitride phases.

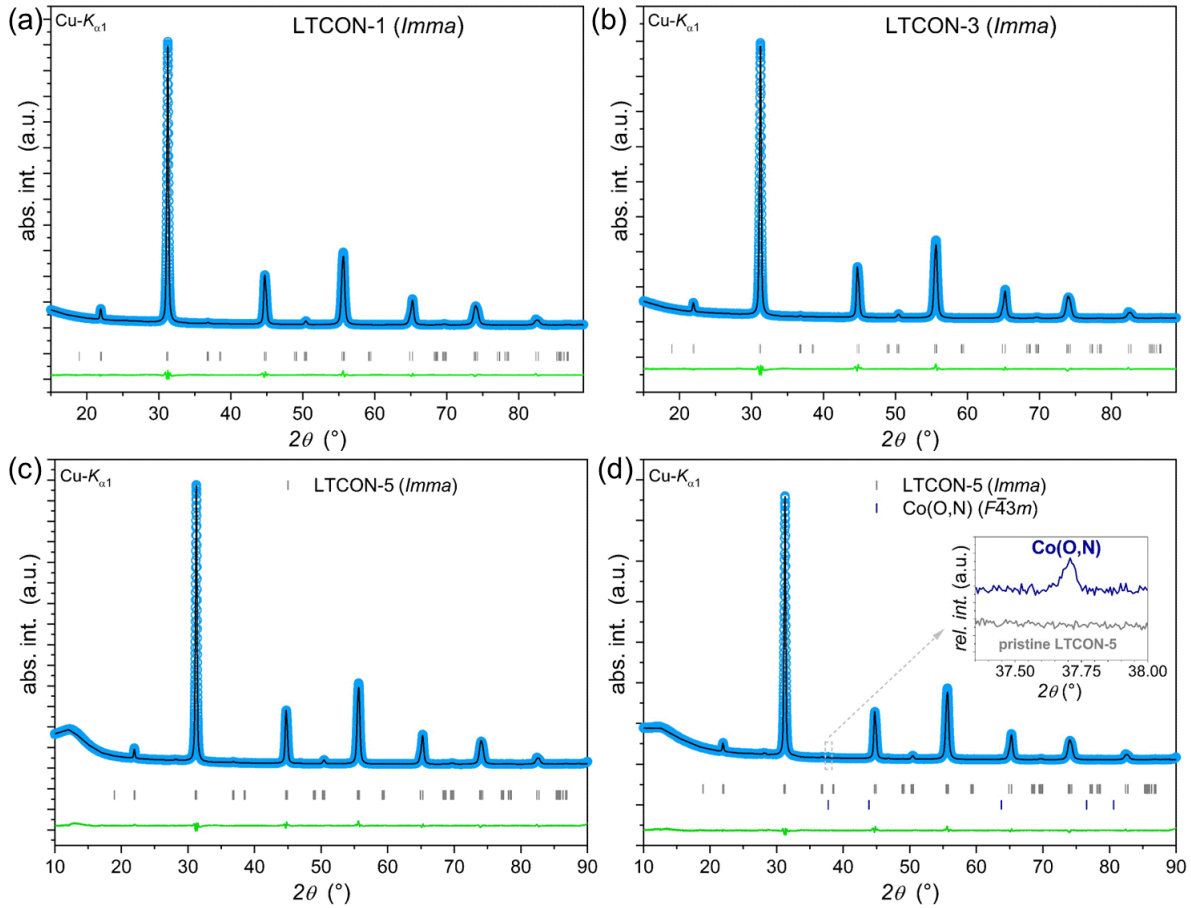

Fig. S5. Rietveld refinements of the PXRD data of the oxynitrides. (a)–(c) Rietveld refinements of PXRD data of single-phase LTCON-1, LTCON-3, and LTCON-5 at 300 K in space group type *Imma*. (d) Rietveld refinements of LTCON-5 containing Co(O,N) as secondary phase.

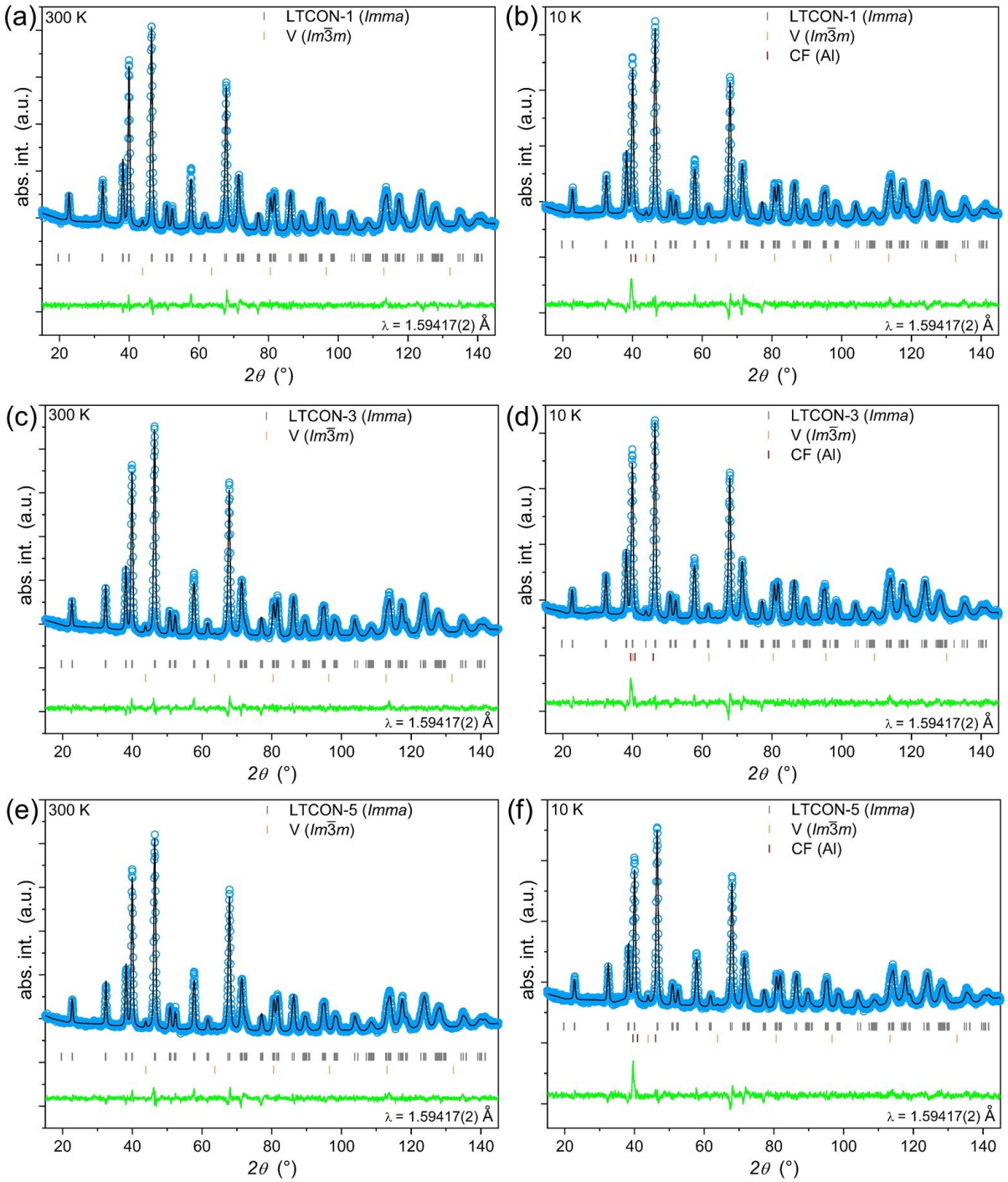

Fig. S6. Rietveld refinements of the ND data of LTCON. Rietveld refinements of ND data of (a) LTCON-1 at 300 K in space group type *Imma*. (b) LTCON-1 at 10 K in space group type *Imma*. (c) LTCON-3 at 300 K in space group type *Imma*. (d) LTCON-3 at 10 K in space group type *Imma*. (e) LTCON-5 at 300 K in space group type *Imma*. (f) LTCON-5 at 10 K in space group type *Imma*. CF refers to the scattering contribution of the cryo furnace.

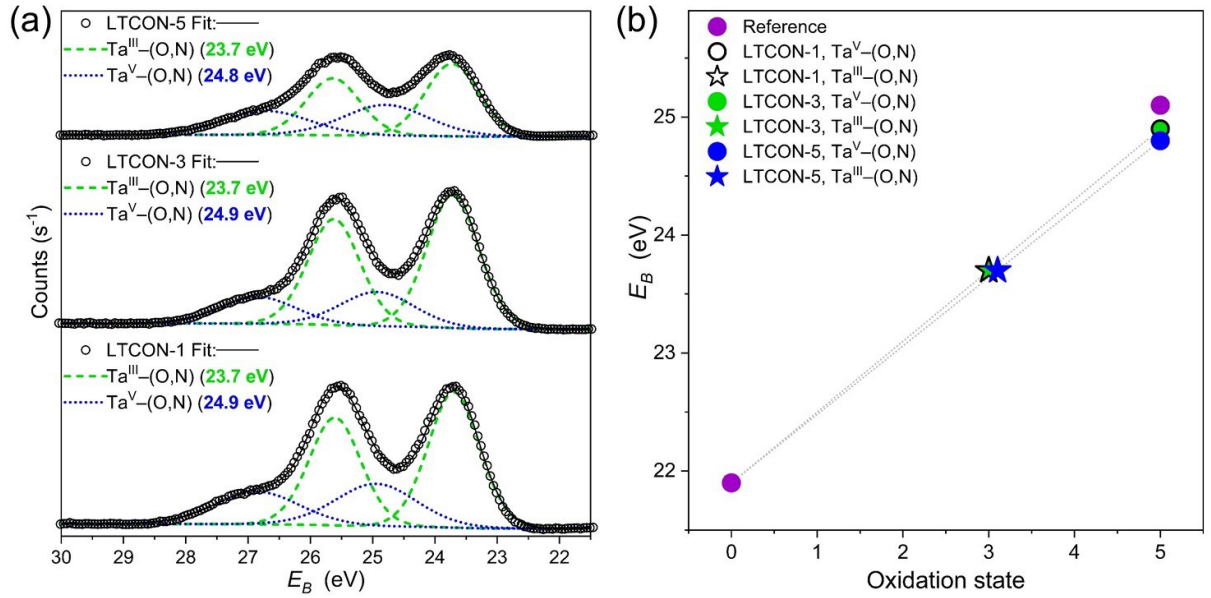

Fig. S7. XPS measurements of the Ta 4*f* regions of the oxynitrides. (a) Ta 4*f* spectra of LTCON and (b) the applied point charge model [1,2]. The binding energy of the Ta^{5+} reference as reported in ref. [1] was used.

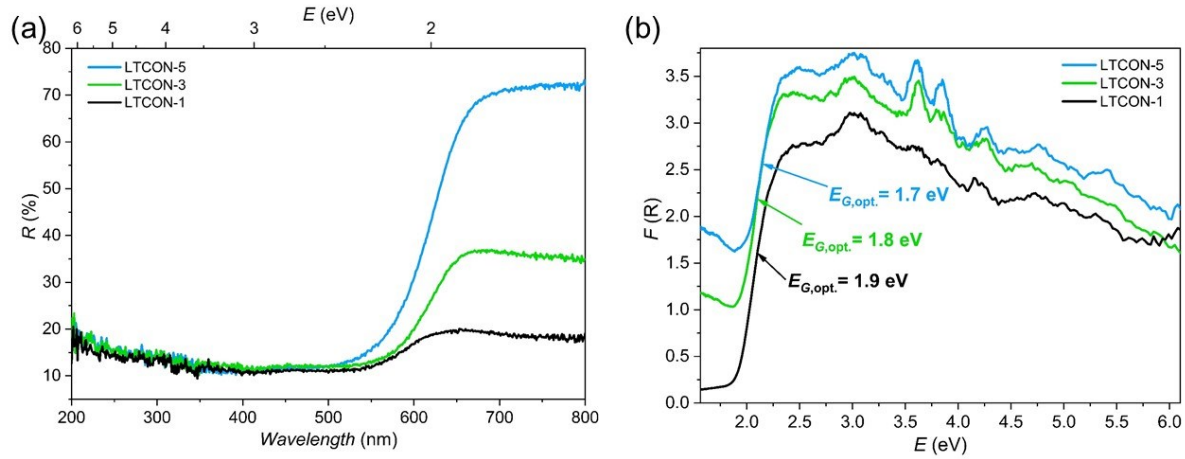

Fig. S8. DRS measurements of LTCON. (a) Measured reflectance spectra of LTCON and (b) Kubelka-Munk converted curves of the measured reflectance spectra for LTCON.

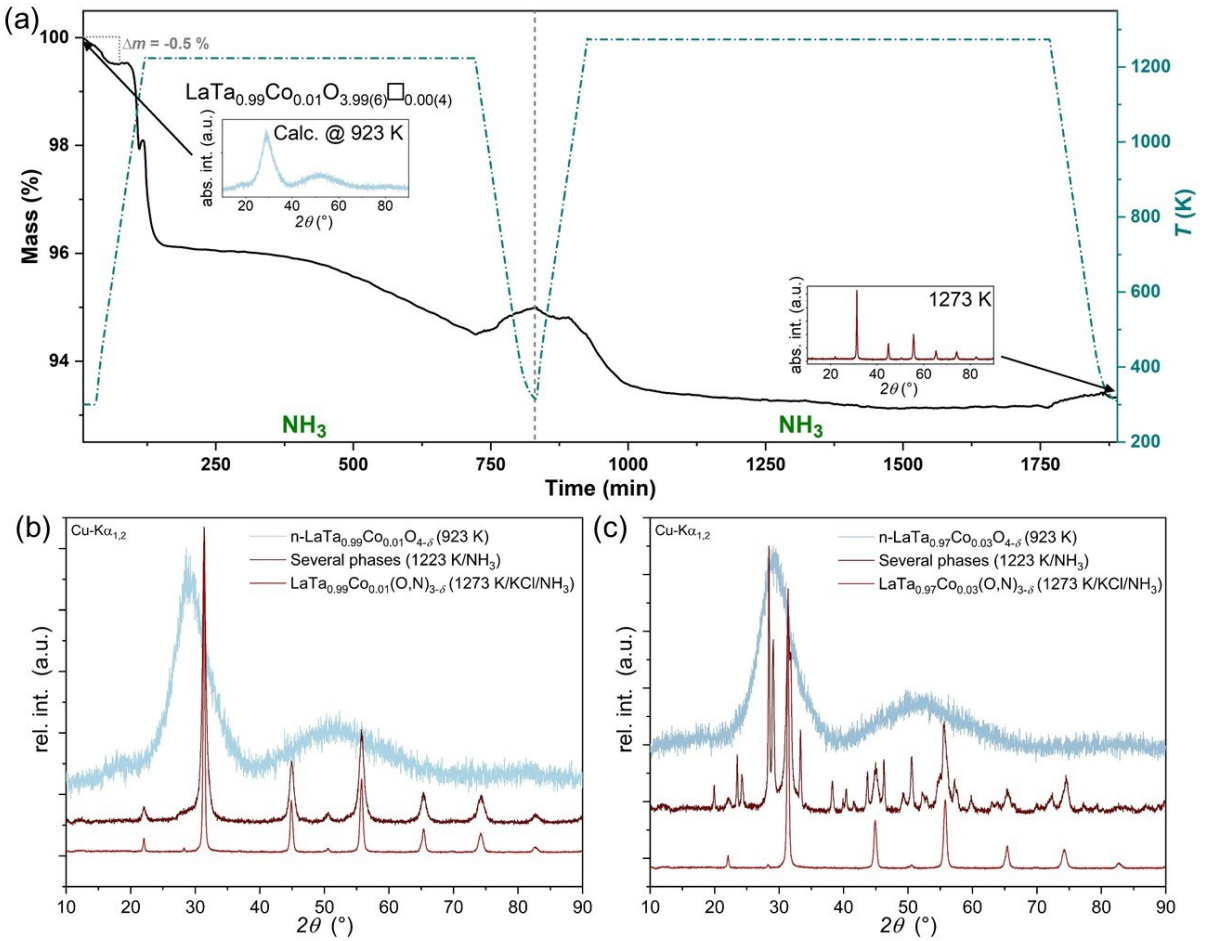

Fig. S9. *In situ* ammonolysis investigations *via* thermogravimetric analysis (TGA). (a) *In situ* ammonolysis of LTCO-1. For a better visibility of the oxygen vacancies the compound LTCO-1 is written in the figure as $LaTa_{0.99}Co_{0.01}O_{3.99(6)}\square_{0.00(4)}$. The square (□) represents the vacancies. The reaction steps observed by performing *in situ* ammonolysis (10 vol% Ar in NH_3) were similar to that of $LaTaO_2N$ [1]. However, one difference is observed for LTCO-1: After the first cycle the obtained oxynitride is according to PXRD not phase pure. The curve colors are reflecting the colors of the samples. (b)–(c) Powder diffraction patterns of the products of LTCON from the *ex situ* ammonolysis of the oxides (blue) to the oxynitrides.

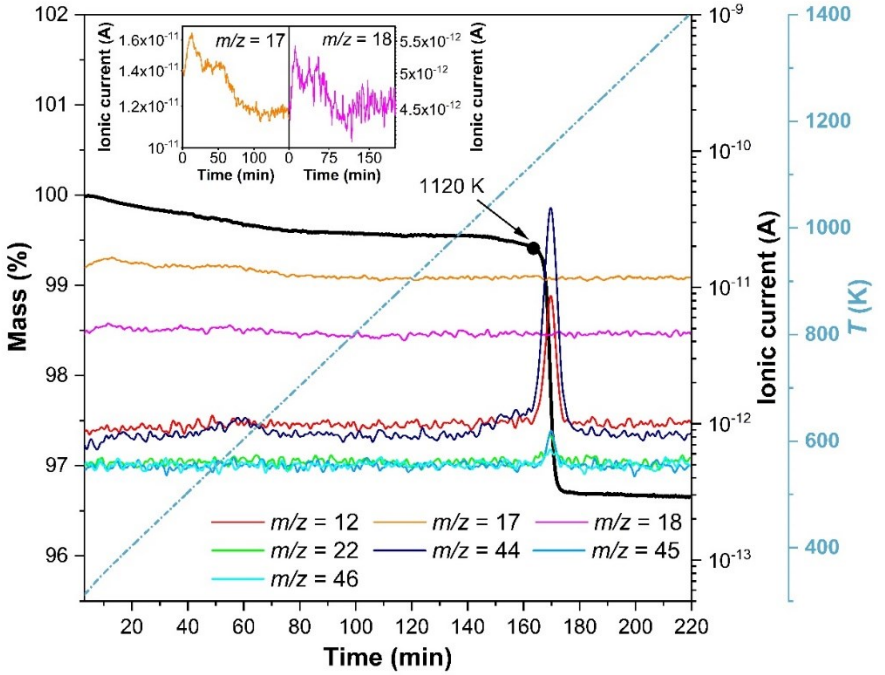

Fig. S10. Thermogravimetric analysis coupled with mass spectrometry (TGA-MS). TGA-MS experiment of LTCO-1 in synthetic air revealing adsorbed water and CO_2 pointing to organic residues on the sample's surface (5 K min^{-1}).

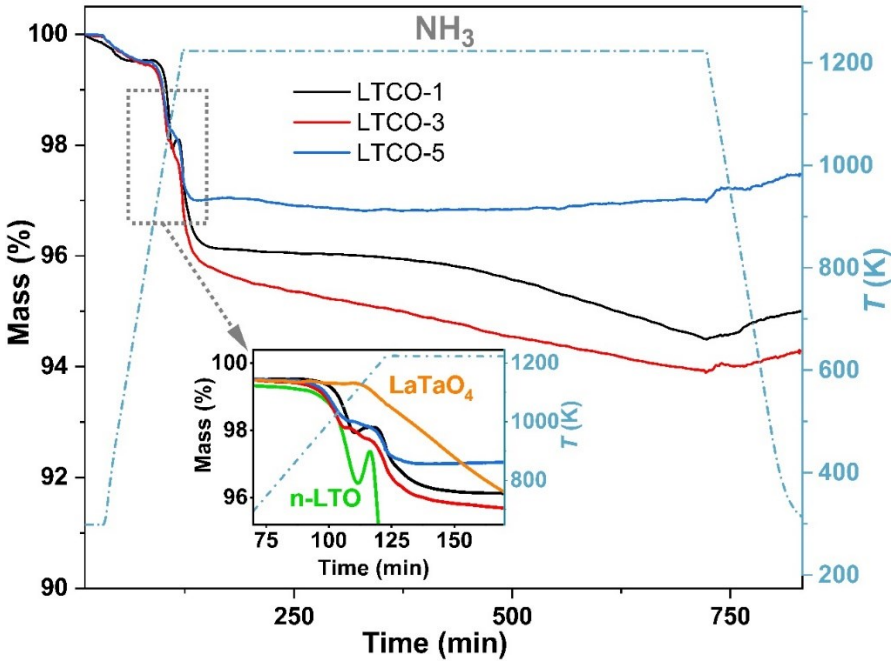

Fig. S11. *In situ* ammonolysis of the oxides. *In situ* ammonolysis (10 vol% Ar in NH_3) of LTCO. The reaction steps are similar to those of $LaTa^{IV}O_2N$ [1] on the first view. However, some differences were observed by the use of LTCO: The present oxygen vacancies lead to a continuous flattening of the local maximum between 1050 K and 1223 K (inset) and to an anionic ratio of nearly O : N = 1:2 in LTCON. The obtained curve progressions (black (LTCO-1), red (LTCO-3), and blue (LTCO-5)) lay in between the curve progressions of the unsubstituted nanocrystalline lanthanum tantalum oxide n-LTO (green) and microcrystalline $LaTaO_4$ (orange). The shown reference samples n-LTO and $LaTaO_4$ were synthesized according to ref. [1]. The dashed line represents the temperature.

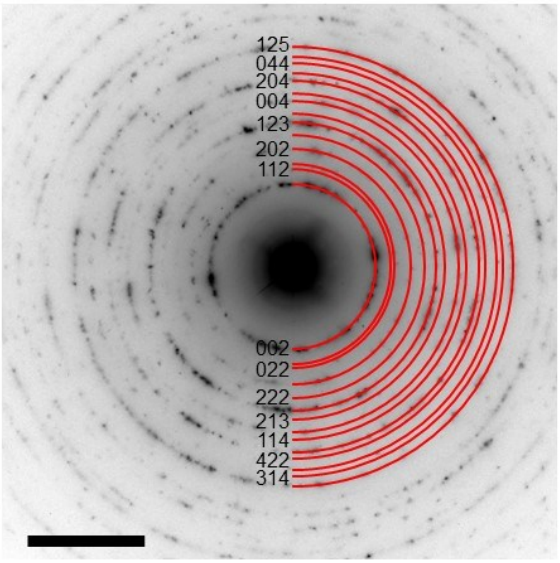

Fig. S12. Selected-area diffraction pattern of LTCON-5. Selected-area electron diffraction pattern and the ring annotations according to the *Imma* space group. Scale bar: 5 nm^{-1}.

Tab. S4. Compositions of LTCON after the third ammonolysis cycle. The compositions were determined by inductively coupled plasma optical emission spectroscopy (ICP-OES) and hot gas extraction (HGE).

Compound	La[1]	Ta[1]	Co[1]	O[2]	N[2]	□[3]
LTCON-1 (wt%)	39.3 ± 0.4	48.8 ± 0.5	0.20 ± 0.01	4.3 ± 0.1	7.65 ± 0.09	
LTCON-1	1.04 ± 0.01	0.98 ± 0.01	0.012 ± 0.007	0.96 ± 0.03	1.98 ± 0.02	0.05(5)
LTCON-3 (wt%)	39 ± 0.4	47.9 ± 0.5	0.47 ± 0.03	4.38 ± 0.05	7.7 ± 0.1	
LTCON-3	1.03 ± 0.02	0.96 ± 0.01	0.029 ± 0.002	0.99 ± 0.01	1.97 ± 0.03	0.03(4)
LTCON-5 (wt%)	39.4 ± 0.4	47.5 ± 0.5	0.80 ± 0.02	5.03 ± 0.06	7.21 ± 0.08	
LTCON-5	1.01 ± 0.01	0.94 ± 0.01	0.049 ± 0.001	1.13 ± 0.05	1.84 ± 0.02	0.03(3)

[1] ICP-OES, [2] HGE, [3] Calculated vacancies obtained from HGE measurements

Tab. S5. Unit cell parameters of the oxynitrides. Unit cell parameters of single phase LTCON-1, LTCON-3, and LTCON-5 at 300 K from refinements of the PXRD data.

Unit Cell Parameter	LTCON-1	LTCON-3	LTCON-5
Space group type	*Imma*	*Imma*	*Imma*
a (Å)	5.7145(5)	5.7147(2)	5.7140(1)
b (Å)	8.0642(3)	8.0647(1)	8.0665(4)
c (Å)	5.7442(7)	5.7447(4)	5.7423(3)
V_{cell} ($Å^3$)	264.71(6)	264.76(1)	264.67(8)
ρ ($g \cdot cm^{-3}$)	9.106	9.033	8.973
Phase fraction (wt%)	100	100	100
R_p (%)	2.30	2.29	2.12
R_{wp} (%)	3.13	3.17	2.94
χ^2	5.65	4.96	7.17
R_{Bragg} (%)	1.06	2.40	1.48

Tab. S6. Refined atom positions of LTCON. The space group type *Imma* was determined by refinements of the PXRD data.

Compound	Atom	Wyck. Symb.	*x*	*y*	*z*	B_{iso} (Å^2)	sof[1]
	La	4*e*	0	¼	0.5[4]	1.74(1)	1[2]
	Ta	4*a*	0	0	0	1.49(7)	0.99[2]
	Co	4*a*	0	0	0	1.49(7)	0.01[2]
LTCON-1	O(1)	4*e*	0	¼	0.1021(2)	0.5[2]	0.32564[3]
	N(1)	4*e*	0	¼	0.1021(2)	0.5[2]	0.68179[3]
	O(2)	8*g*	¼	0.9659(7)	¼	0.5[2]	0.32564[3]
	N(2)	8*g*	¼	0.9659(7)	¼	0.5[2]	0.68179[3]
	La	4*e*	0	¼	0.5[4]	1.13(8)	1[2]
	Ta	4*a*	0	0	0	0.71(8)	0.97[2]
	Co	4*a*	0	0	0	0.71(8)	0.03[2]
LTCON-3	O(1)	4*e*	0	¼	0.0952(2)	0.5[2]	0.33920[3]
	N(1)	4*e*	0	¼	0.0952(2)	0.5[2]	0.65661[3]
	O(2)	8*g*	¼	0.9659(8)	¼	0.5[2]	0.33920[3]
	N(2)	8*g*	¼	0.9659(8)	¼	0.5[2]	0.65661[3]
	La	4*e*	0	¼	0.5[4]	1.30(6)	1[2]
	Ta	4*a*	0	0	0	0.75(2)	0.95[2]
	Co	4*a*	0	0	0	0.75(2)	0.05[2]
LTCON-5	O(1)	4*e*	0	¼	0.0962(2)	0.5[2]	0.37524[3]
	N(1)	4*e*	0	¼	0.0962(2)	0.5[2]	0.61380[3]
	O(2)	8*g*	¼	0.9682(8)	¼	0.5[2]	0.37524[3]
	N(2)	8*g*	¼	0.9682(8)	¼	0.5[2]	0.61380[3]

[1]site occupancy factor, [2]fixed, [3]fixed according to HGE results, [4]fixed according to Porter *et al*. [11]

Tab. S7. Distances in the $[(Ta,Co)(O,N)_6]^{z-}$ octahedra of LTCON. They were determined *via* Rietveld refinements of the respective PXRD data.

Compound	LTCON-1	LTCON-3	LTCON-5
$d_{(Ta,Co)-(O,N)1}$ (Å)	2.047(2)	2.040(3)	2.0414(8)
$d_{(Ta,Co)-(O,N)2}$ (Å)	2.047(2)	2.040(3)	2.0414(8)
$d_{(Ta,Co)-(O,N)3}$ (Å)	2.047(2)	2.040(3)	2.0414(8)
$d_{(Ta,Co)-(O,N)4}$ (Å)	2.047(2)	2.040(3)	2.0414(8)
$d_{(Ta,Co)-(O,N)5}$ (Å)	2.057(3)	2.076(8)	2.091(2)
$d_{(Ta,Co)-(O,N)6}$ (Å)	2.057(3)	2.076(8)	2.091(2)
$d_{(Ta,Co)-(O,N),average}$ (Å)	2.050(6)	2.052(5)	2.058(1)

Tab. S8. Angles in the $[(Ta,Co)(O,N)_6]^{z-}$ octahedra of LTCON. They were determined *via* Rietveld refinements of the respective PXRD data.

Compound	LTCON-1	LTCON-3	LTCON-5
$\measuredangle_{(Ta,Co)-X(1)-(Ta,Co)}$ (°)	156.81(1)	151.8(3)	149.36(9)
$\measuredangle_{(Ta,Co)-X(2)-(Ta,Co)}$ (°)	163.11(6)	165.49(1)	165.56(3)
$\measuredangle_{average}$ (°)	159.96(4)	158.7(2)	157.4(7)

Tab. S9. Unit cell parameters of LTCON-5 containing Co(O,N). Unit cell parameters of $LaTa_{0.95}Co_{0.05}(O,N)_{3-\delta}$ and Co(O,N) at 300 K from refinements of the PXRD data.

Unit Cell Parameter	LTCON-5		Co(O,N)
Space group type	*Imma*		$F\bar{4}3m$
a (Å)	5.7137(6)		4.12478[1]
b (Å)	8.0625(6)		
c (Å)	5.7433(9)		
V_{cell} (Å^3)	264.58(4)		70.1784
ρ (g·cm^{-3})	8.976		6.998
Phase fraction (wt%)	99.4(8)		0.5(2)
R_p (%)		2.15	
R_{wp} (%)		3.85	
χ^2		3.70	
R_{Bragg} (%)	2.33		16.5

[1]fixed

Tab. S10. Atom positions of Co(O,N). The space group type $F\bar{4}3m$ was determined by refinements of the PXRD data. The atom positions were taken from Suzuki *et al*. [12], whereas the concentrations of Co, N, and O were determined by EDX.

Atom	Wyck. Symb.	x	y	z	B_{iso} (Å^2)	sof[1]
Co	4*a*	0	0	0	1[2]	1[2]
O	4*c*	¼	¼	¼	0.5[2]	0.5[2]
N	4*c*	¼	¼	¼	0.5[2]	0.5[2]

[1]site occupancy factor, [2]fixed

Tab. S11. Unit cell parameters of single-phase LTCON-1 (from ND data). The V originates from the sample container.

Temperature	Unit Cell Parameter	LTCON-1		V
	Space group type	*Imma*		$Im\bar{3}m$
	a (Å)	5.7112(4)		3.0218(1)
	b (Å)	8.0574(5)		3.0218(1)
	c (Å)	5.7458(4)		3.0218(1)
	V_{cell} (Å^3)	264.41(3)		27.594(2)
300 K	ρ (g·cm^{-3})	9.117		6.132
	Phase fraction (wt%)	24.66(2)		75.34(8)
	R_p (%)		2.87	
	R_{wp} (%)		3.65	
	χ^2		1.31	
	R_{Bragg} (%)	3.07		8.23
	Space group type	*Imma*		$Im\bar{3}m$
	a (Å)	5.7019(4)		3.014(3)
	b (Å)	8.0471(6)		3.014(3)
	c (Å)	5.7394(5)		3.014(3)
	V_{cell} (Å^3)	263.35(3)		27.39(3)
10 K	ρ (g·cm^{-3})	9.154		6.178
	Phase fraction (wt%)	26.76(3)		73.24(1)
	R_p (%)		3.24	
	R_{wp} (%)		4.37	
	χ^2		1.65	
	R_{Bragg} (%)	4.16		10.1

Tab. S12. Refined atom positions of LTCON-1 obtained from ND data. The space group type *Imma* was determined by refinements of the ND data.

Temperature	Atom	Wyck. Symb.	x	y	z	B_{iso} (Å^2)	sof[1]
	La	4*e*	0	¼	0.5[4]	0.6[2]	1[2]
	Ta	4*a*	0	0	0	0.3[2]	0.99[2]
	Co	4*a*	0	0	0	0.3[2]	0.01[2]
300 K	O(1)	4*e*	0	¼	0.0686(4)	0.771(6)	0.32564[3]
	N(1)	4*e*	0	¼	0.0686(4)	0.771(6)	0.68179[3]
	O(2)	8*g*	¼	0.9633(5)	¼	1.595(4)	0.32564[3]
	N(2)	8*g*	¼	0.9633(5)	¼	1.595(4)	0.68179[3]
	La	4*e*	0	¼	0.5[4]	0.6[2]	1[2]
	Ta	4*a*	0	0	0	0.3[2]	0.99[2]
	Co	4*a*	0	0	0	0.3[2]	0.01[2]
10 K	O(1)	4*e*	0	¼	0.0691(6)	0.873(8)	0.32564[3]
	N(1)	4*e*	0	¼	0.0691(6)	0.873(8)	0.68179[3]
	O(2)	8*g*	¼	0.9622(3)	¼	1.595(5)	0.32564[3]
	N(2)	8*g*	¼	0.9622(3)	¼	1.595(5)	0.68179[3]

[1]site occupancy factor, [2]fixed, [3]fixed according to HGE results, [4]fixed according to Porter *et al*. [11]

Tab. S13. Distances in the $[(Ta,Co)(O,N)_6]^{z-}$ octahedron of LTCON-1. They were determined *via* Rietveld refinements of the respective ND data.

Compound	LTCON-1 (300 K)	LTCON-1 (10 K)
$d_{(Ta,Co)-(O,N)1}$ (Å)	2.0468(3)	2.0453(4)
$d_{(Ta,Co)-(O,N)2}$ (Å)	2.0468(3)	2.0453(4)
$d_{(Ta,Co)-(O,N)3}$ (Å)	2.0468(3)	2.0453(4)
$d_{(Ta,Co)-(O,N)4}$ (Å)	2.0468(3)	2.0453(4)
$d_{(Ta,Co)-(O,N)5}$ (Å)	2.0526(6)	2.0505(7)
$d_{(Ta,Co)-(O,N)6}$ (Å)	2.0526(6)	2.0505(7)
$d_{(Ta,Co)-(O,N),average}$ (Å)	2.0487(5)	2.0470(8)

Tab. S14. Angles in the $[(Ta,Co)(O,N)_6]^{z-}$ octahedron of LTCON-1. They were determined *via* Rietveld refinements of the respective ND data.

Compound	LTCON-1 (300 K)	LTCON-1 (10 K)
$\measuredangle_{(Ta,Co)-X(1)-(Ta,Co)}$ (°)	157.86(3)	157.70(3)
$\measuredangle_{(Ta,Co)-X(2)-(Ta,Co)}$ (°)	163.39(2)	162.89(4)
$\measuredangle_{average}$ (°)	160.62(7)	160.29(8)

Tab. S15. Unit cell parameters of single-phase LTCON-3 (from ND data). The V originates from the sample container.

Temperature	Unit Cell Parameter	LTCON-3	V
300 K	Space group type	*Imma*	$Im\bar{3}m$
	a (Å)	5.7134(4)	3.026(1)
	b (Å)	8.0609(5)	3.026(1)
	c (Å)	5.7484(4)	3.026(1)
	V_{cell} (Å^3)	264.74(3)	27.71(2)
	ρ (g·cm^{-3})	9.034	6.106
	Phase fraction (wt%)	25.05(2)	74.95(8)
	R_p (%)	2.81	
	R_{wp} (%)	3.57	
	χ^2	1.27	
	R_{Bragg} (%)	2.80	10.9
10 K	Space group type	*Imma*	$Im\bar{3}m$
	a (Å)	5.7057(5)	3.020(2)
	b (Å)	8.0519(7)	3.020(2)
	c (Å)	5.7409(5)	3.020(2)
	V_{cell} (Å^3)	263.75(4)	27.53(3)
	ρ (g·cm^{-3})	9.007	6.143
	Phase fraction (wt%)	25.03(2)	74.97(1)
	R_p (%)	3.21	
	R_{wp} (%)	4.33	
	χ^2	1.58	
	R_{Bragg} (%)	3.37	8.11

Tab. S16. Refined atom positions of LTCON-3 obtained from ND data. The space group type *Imma* is determined by refinements of the ND data.

Temperature	Atom	Wyck. Symb.	*x*	*y*	*z*	B_{iso} (Å^2)	sof[1]
	La	4*e*	0	¼	0.5[4]	0.6[2]	1[2]
	Ta	4*a*	0	0	0	0.3[2]	0.97[2]
	Co	4*a*	0	0	0	0.3[2]	0.03[2]
300 K	O(1)	4*e*	0	¼	0.0690(4)	0.613(6)	0.33920[3]
	N(1)	4*e*	0	¼	0.0690(4)	0.613(6)	0.65661[3]
	O(2)	8*g*	¼	0.9637(2)	¼	1.670(4)	0.33920[3]
	N(2)	8*g*	¼	0.9637(2)	¼	1.670(4)	0.65661[3]
	La	4*e*	0	¼	0.5[4]	0.6[2]	1[2]
	Ta	4*a*	0	0	0	0.3[2]	0.97[2]
	Co	4*a*	0	0	0	0.3[2]	0.03[2]
10 K	O(1)	4*e*	0	¼	0.0703(5)	0.570(7)	0.33920[3]
	N(1)	4*e*	0	¼	0.0703(5)	0.570(7)	0.65661[3]
	O(2)	8*g*	¼	0.9626(3)	¼	1.738(6)	0.33920[3]
	N(2)	8*g*	¼	0.9626(3)	¼	1.738(6)	0.65661[3]

[1]site occupancy factor, [2]fixed, [3]fixed according to HGE results, [4]fixed according to Porter *et al*. [11]

Tab. S17. Distances in the $[(Ta,Co)(O,N)_6]^{z-}$ octahedron of LTCON-3. They were determined *via* Rietveld refinements of the respective ND data.

Compound	LTCON-3 (300 K)	LTCON-3 (10 K)
$d_{(Ta,Co)-(O,N)1}$ (Å)	2.0472(3)	2.0458(4)
$d_{(Ta,Co)-(O,N)2}$ (Å)	2.0472(3)	2.0458(4)
$d_{(Ta,Co)-(O,N)3}$ (Å)	2.0472(3)	2.0458(4)
$d_{(Ta,Co)-(O,N)4}$ (Å)	2.0472(3)	2.0458(4)
$d_{(Ta,Co)-(O,N)5}$ (Å)	2.0539(5)	2.0530(6)
$d_{(Ta,Co)-(O,N)6}$ (Å)	2.0539(5)	2.0530(6)
$d_{(Ta,Co)-(O,N),average}$ (Å)	2.0494(7)	2.0482(5)

Tab. S18. Angles in the $[(Ta,Co)(O,N)_6]^{z-}$ octahedron of LTCON-3. They were determined *via* Rietveld refinements of the respective ND data.

Compound	LTCON-3 (300 K)	LTCON-3 (10 K)
$\measuredangle_{(Ta,Co)-X(1)-(Ta,Co)}$ (°)	157.73(2)	157.33(3)
$\measuredangle_{(Ta,Co)-X(2)-(Ta,Co)}$ (°)	163.57(2)	163.07(2)
$\measuredangle_{average}$ (°)	160.65(2)	160.20(3)

Tab. S19. Unit cell parameters of single-phase LTCON-5 (from ND data). The V originates from the sample container.

Temperature	Unit Cell Parameter	LTCON-5		V
	Space group type	*Imma*		$Im\bar{3}m$
	a (Å)	5.7108(3)		3.022(1)
	b (Å)	8.0565(5)		3.022(1)
	c (Å)	5.7465(4)		3.022(1)
	V_{cell} (Å^3)	264.39(3)		27.58(3)
300 K	ρ (g·cm^{-3})	8.988		6.133
	Phase fraction (wt%)	25.45(2)		74.55(8)
	R_p (%)		2.89	
	R_{wp} (%)		3.74	
	χ^2		1.36	
	R_{Bragg} (%)	3.04		10.6
	Space group type	*Imma*		$Im\bar{3}m$
	a (Å)	5.7017(5)		3.017(3)
	b (Å)	8.0460(7)		3.017(3)
	c (Å)	5.7390(6)		3.017(3)
	V_{cell} (Å^3)	263.28(4)		27.45(5)
10 K	ρ (g·cm^{-3})	9.027		6.167
	Phase fraction (wt%)	33.2(7)		66.7(3)
	R_p (%)		3.90	
	R_{wp} (%)		5.38	
	χ^2		2.15	
	R_{Bragg} (%)	9.55		24.2

Tab. S20. Refined atom positions of LTCON-5 obtained from ND data. The space group type *Imma* is determined by refinements of the ND data.

Temperature	Atom	Wyck. Symb.	x	y	z	B_{iso} (Å^2)	sof[1]
	La	4*e*	0	¼	0.5[4]	0.6[2]	1[2]
	Ta	4*a*	0	0	0	0.3[2]	0.95[2]
	Co	4*a*	0	0	0	0.3[2]	0.05[2]
300 K	O(1)	4*e*	0	¼	0.0705(5)	0.539(6)	0.37524[3]
	N(1)	4*e*	0	¼	0.0705(5)	0.539(6)	0.61380[3]
	O(2)	8*g*	¼	0.9633(2)	¼	1.451(5)	0.37524[3]
	N(2)	8*g*	¼	0.9633(2)	¼	1.451(5)	0.61380[3]
	La	4*e*	0	¼	0.5[4]	0.6[2]	1[2]
	Ta	4*a*	0	0	0	0.3[2]	0.95[2]
	Co	4*a*	0	0	0	0.3[2]	0.05[2]
10 K	O(1)	4*e*	0	¼	0.0696(8)	1.044(9)	0.37524[3]
	N(1)	4*e*	0	¼	0.0696(8)	1.044(9)	0.61380[3]
	O(2)	8*g*	¼	0.9620(4)	¼	1.688(7)	0.37524[3]
	N(2)	8*g*	¼	0.9620(4)	¼	1.688(7)	0.61380[3]

[1]site occupancy factor, [2]fixed, [3]fixed according to HGE results, [4]fixed according to Porter *et al*. [11]

Tab. S21. Distances in the $[(Ta,Co)(O,N)_6]^{z-}$ octahedron of LTCON-5. They were determined *via* Rietveld refinements of the respective ND data.

Compound	LTCON-5 (300 K)	LTCON-5 (10 K)
$d_{(Ta,Co)-(O,N)1}$ (Å)	2.0469(2)	2.0455(5)
$d_{(Ta,Co)-(O,N)2}$ (Å)	2.0469(2)	2.0455(5)
$d_{(Ta,Co)-(O,N)3}$ (Å)	2.0469(2)	2.0455(5)
$d_{(Ta,Co)-(O,N)4}$ (Å)	2.0469(2)	2.0455(5)
$d_{(Ta,Co)-(O,N)5}$ (Å)	2.0545(6)	2.0509(8)
$d_{(Ta,Co)-(O,N)6}$ (Å)	2.0545(6)	2.0509(8)
$d_{(Ta,Co)-(O,N),average}$ (Å)	2.0494(7)	2.0473(6)

Tab. S22. Angles in the $[(Ta,Co)(O,N)_6]^{z-}$ octahedron of LTCON-5. They were determined *via* Rietveld refinements of the respective ND data.

Compound	LTCON-5 (300 K)	LTCON-5 (10 K)
$\measuredangle_{(Ta,Co)-X1-(Ta,Co)}$ (°)	157.25(3)	157.54(4)
$\measuredangle_{(Ta,Co)-X2-(Ta,Co)}$ (°)	163.38(9)	162.71(3)
$\measuredangle_{average}$ (°)	160.32(6)	160.12(9)

8.11.3. Supplemental Material Sec. III: Critical assessment of the Co ion concentration

We found that parameters such as the exact stoichiometric weighed ratio of the cations, and the amount of weighed oxide precursors prior to ammonolysis are crucial to get single-phase oxynitrides. By weighing 350 mg of LTCO containing the exact cationic stoichiometric amount single phase LTCON can be synthesized. The homogeneous distribution of the Co ions can be seen *via* transmission electron microscopy (TEM) and scanning electron microscopy (SEM) studies (Figs. S13–S15). In contrast, by weighing 350 mg of LTCO-5 with a slightly higher Co concentration (x = 0.0517), Co-rich nanoparticles with a diameter of 40 nm < d < 80 nm (HR-TEM investigations, Figs. 2 and 3) can be obtained. This is because of the non-stoichiometric weighed amount of the cations in the samples (too much Co in comparison to La and Ta). The composition of the Co-rich nanoparticles determined by EDX is Co(O,N) (Co : O : N = 50 at% : 25 at% : 25 at%). A phase with a similar composition ($CoO_{0.74}N_{0.24}$) was already synthesized elsewhere [13].

Both observations – single-phase oxynitrides and an oxynitride containing a Co-rich phase – were investigated further by scanning electron microscopy (SEM), transmission electron microscopy (TEM), and high-resolution transmission electron microscopy (HR-TEM) (Figs. 2, 3 and Figs. S13–S15). All three techniques were coupled with energy-dispersive X-ray spectroscopy (EDX). Because objective polepieces can contain cobalt a false Co concentration in the particles can be detected. Therefore, two different TEM devices – JEOL ARM200F and a Philips CM-200 FEG – were selected. The latter device contains a pure iron polepiece, whereas the polepiece of the JEOL ARM200F contains Co. By measuring a Co-free reference sample ($LaTaON_2$), using the JEOL ARM200F, the Co : Fe ratio was determined to Co : Fe = 0.7 (Tab. S23). This factor was used to discriminate the Co in the specimen from the Co in the polepiece using Supplementary Equation 1:

$$\frac{I_{Co}}{I_{Fe}} = \frac{I_{\text{Co, polepiece}} + I_{\text{Co, sample}}}{I_{\text{Fe, polepiece}}} = \frac{I_{\text{Co, polepiece}}}{I_{\text{Fe, polepiece}}} + \frac{I_{\text{Co, sample}}}{I_{\text{Fe, polepiece}}} = \frac{I_{\text{Co, sample}}}{I_{\text{Fe, polepiece}}} + 0.7 \qquad (1)$$

This ratio is considered by determining the Co ion concentration in the Co-containing LTCON samples. The obtained results of the Co ion concentrations are fitting well with the expected values (Tab. S23)

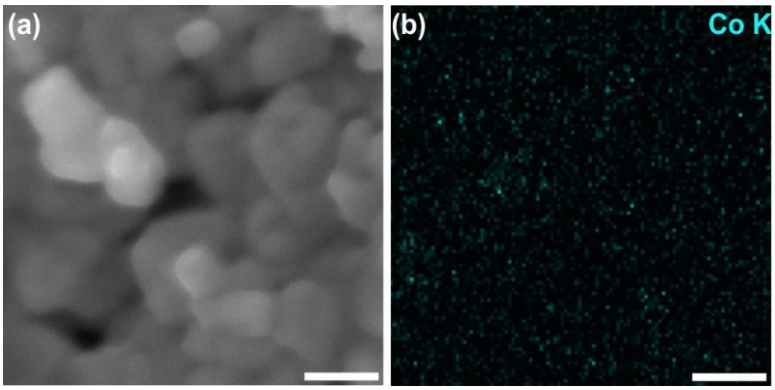

Fig. S13. SEM image and Co-*K* EDX map of LTCON-5 particles. (a) SEM image and (b) EDX map of agglomerated LTCON-5 nanoparticles showing the homogeneous distribution of Co ions in the particles. Scale bars: 200 nm.

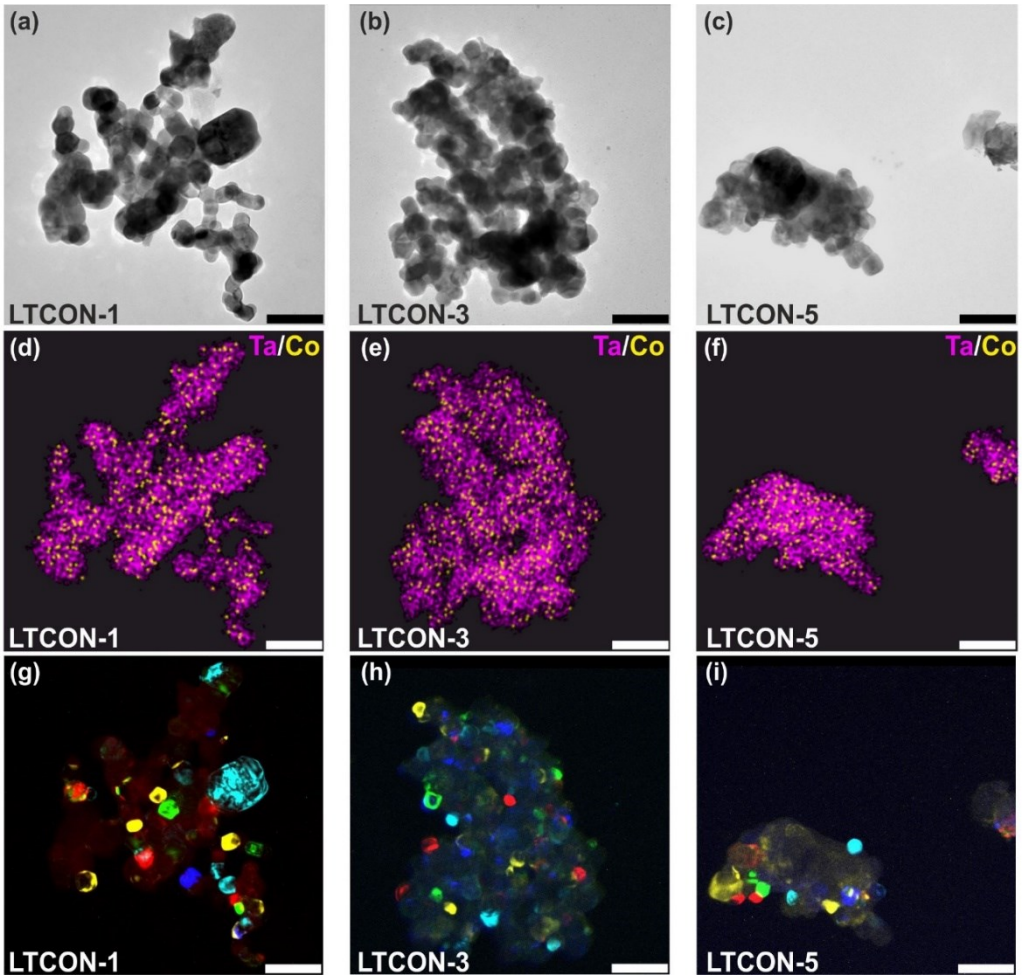

Fig. S14. TEM investigation of LTCON. (a)–(c) TEM images of particles of LTCON-1, LTCON-3, and LTCON-5 and (d)–(f) EDX maps of LTCON-1, LTCON-3, and LTCON-5 showing the homogeneous distribution of Co (yellow) and Ta (pink) in the particles. Elemental Co clusters or Co-rich secondary particles with a size larger than d = 4 nm can be excluded because of the pixel size. (g)–(i) The dark-field TEM images show in different colors the different crystal orientations of the particles. All scale bars: 100 nm.

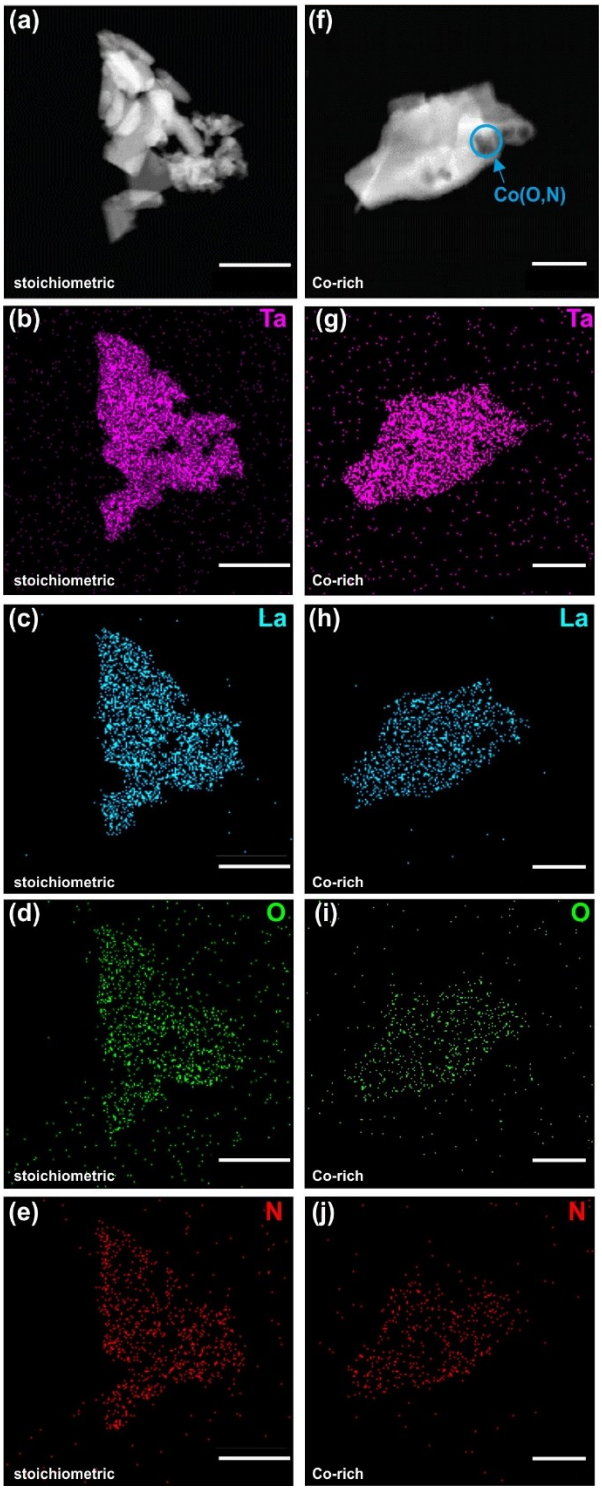

Fig. S15. HAADF/EDX investigation of LTCON-5. (a)–(e) Respective high-angle annular dark-field (HAADF) image and EDX maps of Ta, La, O, and N of single-phase (stoichiometric) LTCON-5 nanoparticles showing the homogeneous distribution of the elements. Scale bars: 500 nm. (f)–(j) Respective HAADF image and EDX maps of Ta, La, O, and N of LTCON-5 nanoparticles containing Co(O,N) nanoparticles showing the homogeneous distribution of Ta, La, O, and N. Scale bars: 250 nm.

Tab. S23. Measured Co and Fe intensities and determination of the Co concentration. The determination of the Co concentration is determined as described in the supplementary text for the HR-TEM JEOL microscope with a Co/Fe polepiece (cf. Supplementary Equation 1). Different lines represent measurements performed at different particles. The intensities are given in netcounts.

Sample	Co (counts)	Fe (counts)	Co : Fe	Co : Fe (corrected)	c_{Co} (at%)	$c_{Co,corrected}$ (at%)	$c_{Co,\ expected}$ (at%)	$c_{Co,\ determined}$ (at%)
LTCON-3	3468	1780	1.95	1.25	0.76	0.53	0.6	0.55
	3121	1362	2.29	1.59	0.9	0.63		
	6023	1914	3.15	2.45	0.78	0.54		
	21921	7037	3.12	2.42	0.82	0.57		
	6963	2598	2.68	1.98	0.69	0.48		
LTCON-5	1289	1570	0.82	0.12	1.26	0.88	1	0.83
	1547	1428	1.08	0.38	1.48	1.03		
	1332	629	2.12	1.42	1.19	0.83		
	1508	607	2.48	1.79	1.24	0.87		
	6864	2872	2.39	1.69	1.1	0.77		
	2368	961	2.46	1.77	1.29	0.90		
	2047	720	2.84	2.14	1.12	0.78		
$LaTaON_2$	2054	2756	0.7				0	0
	1790	2177						
	1483	1941						
	131	283						

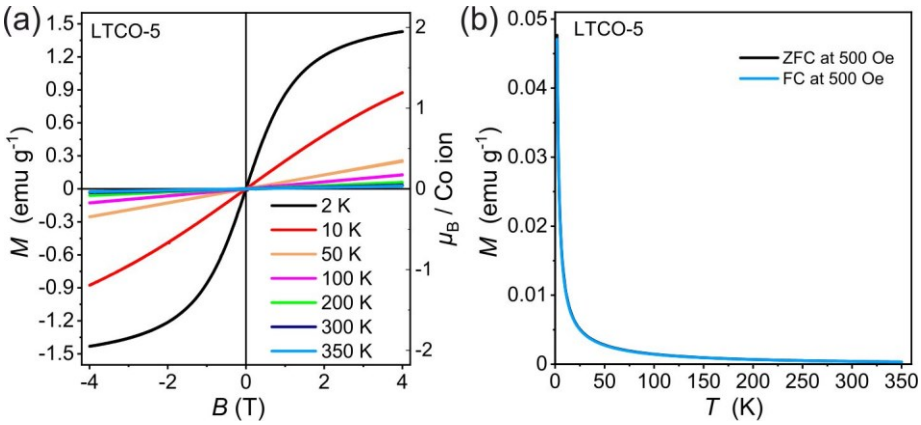

Fig. S16. SQUID-based magnetic measurements of LTCO-5. (a) Field-dependent magnetic measurement of LTCO-5. (b) Temperature-dependent magnetic measurement of LTCO-5. Both measurements reveal for the precursors simple paramagnetism over the entire measurement range.

8.11.4. Supplemental Material Sec. IV: Comparison between raw and processed SQUID data

In comparison to many earlier studies [14], in particular on Co-doped ZnO, the observed SQUID signal for LTCON is not dominated by a large diamagnetic background and a small ferromagnetic-like superimposed signal. For demonstration, we present in Fig. S17 a direct comparison between the raw (measured) and processed SQUID data of all LTCON samples. It is obvious that the relative amount of diamagnetic background increases with decreasing Co ion concentrations. Since for LTCON-3 (0.6 at% Co) almost no diamagnetism is present, the diamagnetic background for LTCON-1 (0.2 at% Co) is more prominent because of the lower Co ion concentration and with it the smaller ferromagnetic contribution. Nevertheless, in contrast to many other studies published on diluted magnetic semiconductors (DMS) (see referenced in the main text) the ferromagnetic contribution is quite large with 3–5 orders of magnitude above the detection limit of the SQUID device.

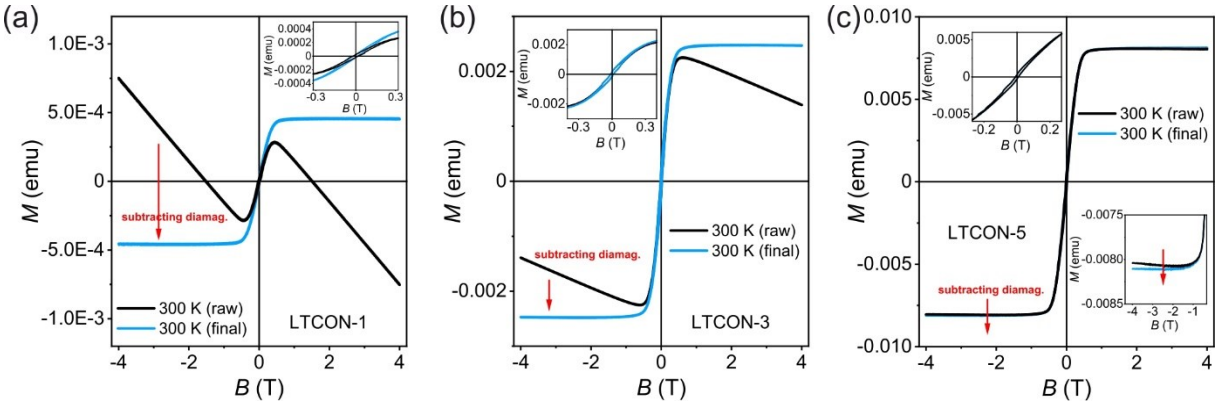

Fig. S17. Raw and diamagnetic background-corrected SQUID data of LTCON. (a)–(c) SQUID data (raw and processed) for all Co ion concentrations. The diamagnetic background was determined as the negative slope of the raw data.

8.11.5. Supplemental Material Sec. V: Exclusion of elemental Co clusters and secondary Co-rich phases

To compare the effect of Co-rich nanoparticles in LTCON-5 and single-phase LTCON-5 SQUID-based magnetometry was applied (Fig. 4d). This was done in order to identify possible Co-rich phases and to further proof if the high-temperature ferromagnetism is truly originating from LTCON. In Fig. 4d, normalized 300 K magnetization curves of the stoichiometric and the Co-rich (non-stoichiometric) samples are presented. In Fig. 4d both curves look quite similar in shape. By magnifying the low-field region - as shown in Fig. 4d - a small difference is observable where the Co-rich sample reveals an additional contribution, with a higher initial slope, as indicated by the blue curve. The purple arrows indicate a difference of about 7 % of the saturation value. By plotting the difference between both samples and normalize their saturation to unity, the additional phase as shown in by the orange curve can be identified. This contribution has a much higher slope compared to the main curves, which we interpret as a part of Co(O,N). Nevertheless, it is obvious that even for the Co-rich sample the dominating part is related to the main-phase magnetism, also consistent to our very rough bulk estimates as discussed above. Those larger nanoparticles reveal a much steeper hysteresis curve at 300 K as expected.

In Fig. S18a) calculated superparamagnetic Langevin-Function curves for an approximate 4 nm sized elemental Co cluster together with the measured room temperature (300 K) $M(H)$ curve of the LTCON-5 are presented (open circles). 3047 Co atoms per 4 nm cluster were assumed. We have chosen the size of 4 nm, because the 300 K behavior is most similar to our experimental results and the lowest resolution which was used for TEM experiments (Fig. S14) was 4 nm. As no temperature-dependent

significant shape variations were observed for LTCON-5, only the 300 K magnetization curve (Fig. 4c) was used for comparison. The shape of the measured 300 K $M(H)$ curve of LTCON-5 is by any means not consistent with all of the calculated temperature-dependent Langevin-functions [15]. In contradiction to the superparamagnetic model, the LTCON samples do not reveal any significant shape variations from 2 K up to 350 K. For example, Co-hcp as secondary phase in Co-doped ZnO shows these shape variations [14,16]. Therefore, the presence of superparamagnetic clusters made of any ferromagnetic material can be excluded as an explanation to our high-temperature ferromagnetism above room temperature. Especially, smaller clusters reveal an even stronger temperature dependence [17]. This can be seen nicely in Fig. S18b, where the size-dependence is presented at 300 K. Again, no simulated curve shape is consistent with our experimental data. The only roughly matching 300 K curve is related to simulated superparamagnetic elemental Co clusters with d = 4 nm. Therefore, much steeper curves should be visible at lower temperatures. To get an almost temperature-independent behavior in the range of 0.1 T ≤ B ≤ 1.0 T, considerably larger (*e.g.* d = 20 nm) elemental Co particles have to be present. However, the initial slope of those single-domain nanoparticles has to be very steep as it is shown in Fig. S18b in this case [18–20]. For a magnetization behavior as observed in our case, almost bulk-like, or multi-domain behavior is mandatory, where demagnetizing fields help to provide less steep susceptibilities. In the case of Co metal the single domain size of perfectly spherical elemental Co particles is at least 50 nm, and it is strongly increasing for even slight variations of the spherical shape [21,22]. To obtain similar hysteresis curves as measured for our samples, elemental Co particles in the range of 80-200 nm or larger agglomerates of small Co particles are necessary. In contrast, no hints of small and large ferromagnetic Co clusters were observed in the high-resolution transmission electron microscopy (HR-TEM) investigations (Figs. 3a – e, Figs. S13–15). In addition, due to the small Co ion concentration, dipole–dipole interactions between possible present elemental Co particles are too small to explain the hysteretic behavior as observed for LTCON. Even for more than one order of magnitude higher Co ion concentration, it was not observed experimentally [19]. The combination of measured almost temperature-independent $M(H)$ curves, the calculated Langevin-plots, and the performed (HR-)TEM studies clearly exclude superparamagnetic Co clusters and large multi-domain elemental Co particles as a possible source for the HT-ferromagnetism in LTCON.

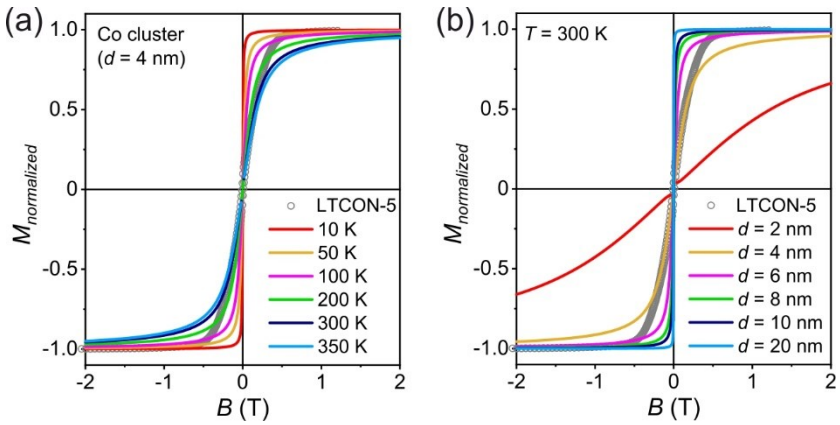

Fig. S18. Temperature- and size-dependent calculated $M(H)$ curves. The smallest size for possible Co clusters in the oxynitride samples is according to TEM/EDX investigations d = 4 nm. (a) The calculated curves of the 4 nm Co clusters were compared with the measured room temperature $M(H)$ curve at 300 K of LTCON-5. The curve shapes of the Co cluster 4 nm magnetization curves at different temperatures in comparison to those of LTCON-5 are totally different. (b) Similar comparison of the measured 300 K $M(H)$ curve at 300 K of LTCON-5 (open circles) with elemental Co cluster calculations for different cluster diameters.

Tab. S24. Determined coercive fields H_c of LTCON. The specific Co ion concentrations x are listed additionally.

Compound	x	H_c (Oe)
LTCON-1	0.01	188 (10 K)
		144 (300 K)
LTCON-3	0.03	243 (10 K)
		183 (300 K)
LTCON-5	0.05	245 (10 K)
		148 (300 K)

8.11.6. Supplemental Material Sec. VI: Miscellaneous

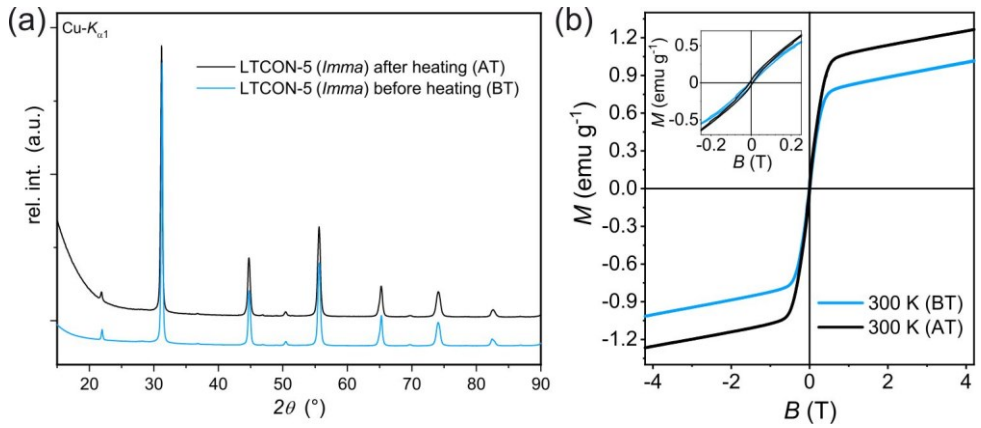

Fig. S19. Further high-temperature investigations of LTCON-5. (a) Complete diffractograms of LTCON-5 before the heating step (BT) and after the heating step (AT) in the SQUID furnace. (b) Hysteresis curves of LTCON-5 before the furnace measurement (BT) and afterwards (AT).

8.11.7. Supplemental Material Sec. VII: LTNON

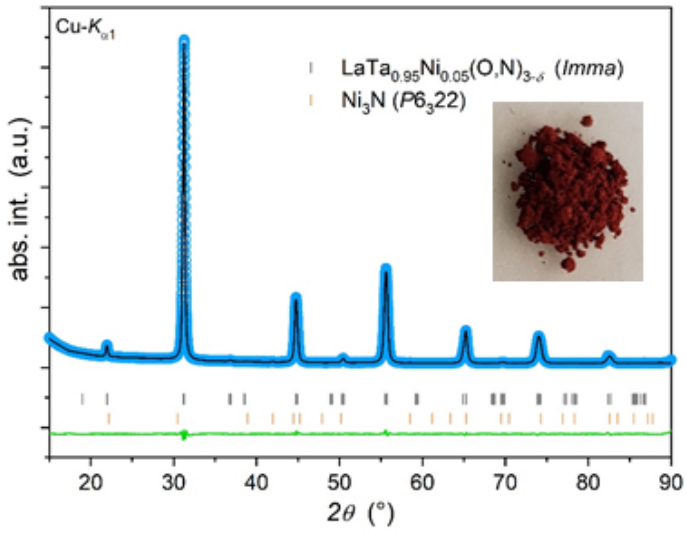

Fig. S20. Rietveld refinements of the PXRD data of LTNON. Secondary phase is Ni_3N. LTNON shows the same color as LTCON (see Foto).

Tab. S25. Unit cell parameters of LTNON (from PXRD data).

x_{Ni} (mol)	0.0498 ($x_{Ni, expected}$ = 0.05)	
Unit Cell Parameter	$LaTa_{1-x}Ni_x(O,N)_{3-\delta}$	Ni_3N
Space group type	*Imma*	$P6_322$
a (Å)	5.7157(1)	4.6271(7)
b (Å)	8.0689(8)	4.6271(7)
c (Å)	5.7422(5)	4.3079(1)
γ (°)	90	120
V_{cell} (Å^3)	264.83(2)	79.87(3)
ρ (g/cm^3)	8.983	7.904
Phase fraction (wt.-%)	98.1(5)	1.8(5)
R_p (%)	1.92	
R_{wp} (%)	2.59	
χ^2	5.53	
R_{Bragg} (%)	1.20	8.89

Tab. S26. Refined atom positions of crystalline LTNON which revealed the maximum solubility of Ni in LTNON with x = 0.023(2) ((≤ 0.6 at% Ni). Therefore, the real composition is determined as: $LaTa_{0.977(2)}Ni_{0.023(2)}(O,N)_3$.

Atom	Wyck. Symb.	x	y	z	B_{iso} (Å^2)	sof[1]
La	4*e*	0	¼	0.5[4]	1.3(6)	1[2]
Ta	4*a*	0	0	0	1.1(9)	0.977(2)
Ni	4*a*	0	0	0	1.1(9)	0.023(2)
O(1)	4*e*	0	¼	0.1071(2)	0.5[2]	0.402[3]
N(1)	4*e*	0	¼	0.1071(2)	0.5[2]	0.597[3]
O(2)	8*g*	¼	0.9698(7)	¼	0.5[2]	0.402[3]
N(2)	8*g*	¼	0.9698(7)	¼	0.5[2]	0.597[3]

[1]site occupancy factor, [2]fixed, [3]fixed according to HGE results, [4]fixed according to Porter *et al*. [11]

Tab. S27. Thought experiment. It shows the plausibility of the XMCD results for a 100 % ferromagnetic LTCON-5 sample.

Origin	**Percent of phase**	m_{spin} (μ_B/Co^{3+})
XMCD result	100 % ferromagnetic LTCON-5	**1.14 ± 0.06**
Thought experiment	90 % non-magnetic LTCON-5	**0**
Thought experiment	10 % ferromagnetic Co-containing phase	10 · 1.14 ~ **11.4**
Thought experiment	90 % non-magnetic LTCON-5 + 10 % ferromagnetic Co-containing phase	0.9 · 0 + 0.1 · 11.4 = **1.14**

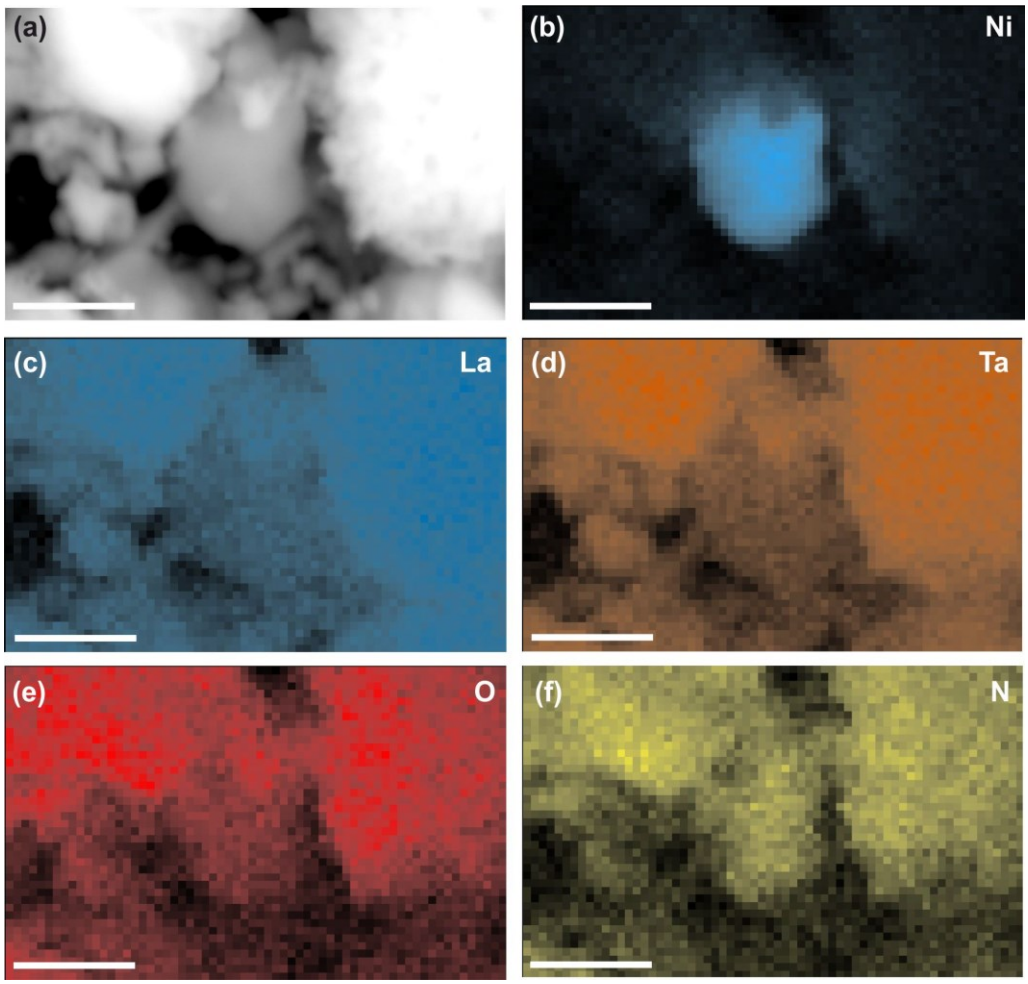

Fig. S21. SEM/EDX measurements of LTNON. (a) SEM image of LTNON and (b)–(f) the respective EDX measurements of Ni, La, Ta, O, and N. Scale bar: 500 nm

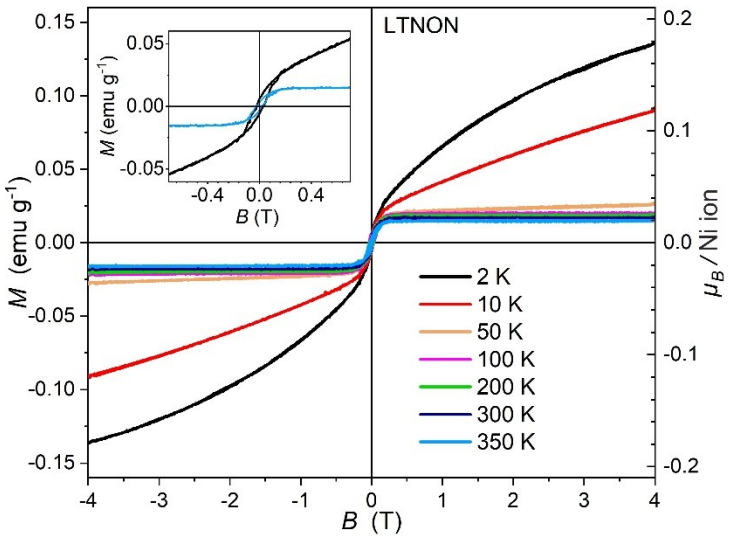

Fig. S22. SQUID-based magnetic measurements of LTNON.

8.12. Supplementary References

[1] C. Bubeck, M. Widenmeyer, G. Richter, M. Coduri, E. Goering, S. Yoon, and A. Weidenkaff, *Tailoring of an Unusual Oxidation State in a Lanthanum Tantalum(IV) Oxynitride via Precursor Microstructure Design*, Commun. Chem. **2**, 134 (2019).

[2] C. Nordling, *ESCA: Elektronen-Spektroskopie Für Chemische Analyse*, Angew. Chemie **84**, 144 (1972).

[3] G. S. Henderson, F. M. F. De Groot, and B. J. A. Moulton, *X-Ray Absorption near-Edge Structure (XANES) Spectroscopy*, Rev. Mineral. Geochemistry **78**, 75 (2014).

[4] F. M. F. de Groot, J. C. Fuggle, B. T. Thole, and G. A. Sawatzky, *2*p *X-Ray Absorption of 3*d *Transition-Metal Compounds: An Atomic Multiplet Description Including the Crystal Field*, Phys. Rev. B **42**, 5459 (1990).

[5] G. Kortüm, W. Braun, and G. Herzog, *Principles and Techniques of Diffuse-Reflectance Spectroscopy*, Angew. Chemie Int. Ed. English **2**, 333 (1963).

[6] M. R. Parra and F. Z. Haque, *Aqueous Chemical Route Synthesis and the Effect of Calcination Temperature on the Structural and Optical Properties of ZnO Nanoparticles*, J. Mater. Res. Technol. **3**, 363 (2014).

[7] C. Aydn, M. S. Abd El-Sadek, K. Zheng, I. S. Yahia, and F. Yakuphanoglu, *Synthesis, Diffused Reflectance and Electrical Properties of Nanocrystalline Fe-Doped ZnO via Sol-Gel Calcination Technique*, Opt. Laser Technol. **48**, 447 (2013).

[8] V. N. Kuznetsov, N. I. Glazkova, R. V. Mikhaylov, A. A. Murashkina, and N. Serpone, *Advanced Diffuse Reflectance Spectroscopy for Studies of Photochromic/Photoactive Solids*, J. Phys. Condens. Matter **31**, 424001 (2019).

[9] D. K. Bhui, H. Bar, P. Sarkar, G. P. Sahoo, S. P. De, and A. Misra, *Synthesis and UV-Vis Spectroscopic Study of Silver Nanoparticles in Aqueous SDS Solution*, J. Mol. Liq. **145**, 33 (2009).

[10] S. S. Sartiman, N. F. Djaja, and R. Saleh, *Chromium-Doped ZnO Nanoparticles Synthesized by Co-Precipitation: Chromium Effects*, Mater. Sci. Appl. **4**, 528 (2013).

[11] S. H. Porter, Z. Huang, and P. M. Woodward, *Study of Anion Order/Disorder in $RTaN_2O$ (R = La, Ce, Pr) Perovskite Nitride Oxides*, Cryst. Growth Des. **14**, 117 (2014).

[12] K. Suzuki, T. Kaneko, H. Yoshida, H. Morita, and H. Fujimori, *Crystal Structure and Magnetic Properties of the Compound CoN*, J. Alloys Compd. **224**, 232 (1995).

[13] M. Widenmeyer, L. Shlyk, N. Becker, R. Dronskowski, E. Meissner, and R. Niewa, *Synthesis of Metastable Co_4N, Co_3N, Co_2N, and $CoO_{0.74}N_{0.24}$ from a Single Azide Precursor and Intermediates in $CoBr_2$ Ammonolysis*, Eur. J. Inorg. Chem. **2016**, 4792 (2016).

[14] L. M. C. Pereira, *Experimentally Evaluating the Origin of Dilute Magnetism in Nanomaterials*, J. Phys. D. Appl. Phys. **50**, 393002 (2017).

[15] B. D. Cullity and C. D. Graham, *Introduction to Magnetic Materials*, 2nd ed. (John Wiley & Sons Inc., 2008).

[16] D. P. Norton et al., *Ferromagnetism in Cobalt-Implanted ZnO*, Appl. Phys. Lett. **83**, 5488 (2003).

[17] S. Zhou, K. Potzger, J. Von Borany, R. Grötzschel, W. Skorupa, M. Helm, and J. Fassbender, *Crystallographically Oriented Co and Ni Nanocrystals inside ZnO Formed by Ion Implantation and Postannealing*, Phys. Rev. B - Condens. Matter Mater. Phys. **77**, 035209 (2008).

[18] S. R. Shinde, S. B. Ogale, J. S. Higgins, H. Zheng, A. J. Millis, V. N. Kulkarni, R. Ramesh, R. L. Greene, and T. Venkatesan, *Co-Occurrence of Superparamagnetism and Anomalous Hall Effect in Highly Reduced Cobalt-Doped Rutile $TiO_{2-\delta}$ Films*, Phys. Rev. Lett. **92**, 166601 (2004).

[19] D. Y. Li et al., *Anisotropic Magnetism and Spin-Dependent Transport in Co Nanoparticle Embedded ZnO Thin Films*, J. Appl. Phys. **114**, 033909 (2013).

[20] M. Naeem, S. K. Hasanain, M. Kobayashi, Y. Ishida, A. Fujimori, S. Buzby, and S. I. Shah, *Effect of Reducing Atmosphere on the Magnetism of $Zn_{1-x}Co_xO$ (0≤x≤0.10) Nanoparticles*, Nanotechnology **17**, 2675 (2006).

[21] E. Seynaeve, G. Rens, A. V. Volodin, K. Temst, C. Van Haesendonck, and Y. Bruynseraede, *Transition from a Single-Domain to a Multidomain State in Mesoscopic Ferromagnetic Co Structures*, J. Appl. Phys. **89**, 531 (2001).

[22] A. Aharoni, *Elongated Single-Domain Ferromagnetic Particles*, J. Appl. Phys. **63**, 5879 (1988).

9. High flux and CO_2-resistance of $La_{0.6}Ca_{0.4}Co_{1-x}Fe_xO_{3-\delta}$ oxygen-transporting membranes

https://doi.org/10.1016/j.memsci.2019.05.007

Guoxing Chen, Wenmei Liu, Marc Widenmeyer, Pingjun Ying, Maofeng Dou, Wenjie Xie, Cora Bubeck, Ling Wang, Maria Fyta, Armin Feldhoff, Anke Weidenkaff

Abstract

Most of the currently used perovskite-based oxygen-transporting membranes have insufficient resistance towards CO_2 and high material costs that potentially limit their commercial applications. In the present work, a highly CO_2-tolerant oxygen permeation membrane based on $La_{0.6}Ca_{0.4}Co_{1-x}Fe_xO_{3-\delta}$ (x =0, 0.3, 0.5, 0.7, 1) was designed and prepared by a scalable reverse co-precipitation method. The oxygen permeation flux through the dense membranes was evaluated and found to be highly dependent on the Co/Fe ratio. $La_{0.6}Ca_{0.4}Co_{0.3}Fe_{0.7}O_{3-\delta}$ possessed the highest permeation flux among the investigated samples, achieving 0.76 ml min^{-1} cm^{-2} under an Air/He gradient and 0.5 ml min^{-1} cm^{-2} under an Air/CO_2 gradient at 1173 K for a 1 mm thick membrane. A combination study of first principles calculations and experimental measurements was conducted to advance the understanding of Co/Fe ratio effects on the oxygen migration behavior in $La_{0.6}Ca_{0.4}Co_{1-x}Fe_xO_{3-\delta}$. The observed oxygen permeability is three times higher than that reported in literature under similar conditions. The presented results demonstrate that this highly CO_2-tolerant membrane is a promising candidate for high temperature oxygen separation applications.

9.1. Introduction

Carbon capture and utilization (CCU) is one of the most promising solutions to limit the amount of CO_2 emissions to the atmosphere. Different techniques for the conversion of CO_2 into value-added chemical compounds or fuels activated by heat or electricity have been developed and studied, namely thermolysis, photocatalysis, plasma, and electrochemical methods [1–9]. As the first step of the recycling process, CO_2 molecules are captured either from industrial or conventional power plant exhaust gases via oxy-fuel combustion capture. Mixed ionic electronic conducting (MIEC) membranes have been attracting great attention because of their high selectivity towards oxygen at high temperature, which can be used to produce cost effective oxygen from air for oxy-fuel combustion. Regarding the constant presence of CO_2 in these processes, high oxygen permeability and excellent structural stability are among the fundamental requirements for a successful oxygen-transporting membrane material.

Different MIEC ceramic membrane materials were developed and evaluated for their CO_2-stability including single-phase perovskite-type oxide materials and dual-phase membrane materials [10–59]. The state-of-the-art oxygen transport materials are mainly single-phase perovskite oxide materials containing Ba and/or Sr on the *A*-site possessing high oxygen permeation fluxes because of the large ionic radii and hence larger free volume of oxygen vacancies. Unfortunately, these perovskite-type materials suffer from irreversible performance losses in the presence of reactive (acidic) gases (such as CO_2 and SO_2) [11–14]. The oxygen permeation fluxes of these membranes normally reach 1 ml min^{-1} cm^{-2} at around 1173 K and can even exceed 10 ml min^{-1} cm^{-2} at higher temperatures [13,14]. However, as little as 300 ppm of CO_2, less than the content in air, is sufficient to stop the oxygen permeation flux due to a membrane decomposition into carbonates and binary metal membranes was improved by the use of dual-phase materials with good structural stability and stable oxygen permeation flux [25–36,58,59], such as $Pr_{0.6}Sr_{0.4}FeO_{3-\delta}$ – $Ce_{0.9}Pr_{0.1}O_{2-\delta}$, $NiFe_2O_4$ – $Ce_{0.8}Tb_{0.2}O_{2-\delta}$, $Ce_{0.8}Gd_{0.2}O_{2-\delta}$ – $Ba_{0.95}La_{0.05}Fe_{1-x}Nb_xO_{3-\delta}$, $Ce_{0.9}Gd_{0.1}O_{2-\delta}$ – $Ba_{0.5}Sr_{0.5}Co_{0.8}Fe_{0.2}O_{3-\delta}$, or $Ce_{0.8}Sm_{0.2}O_{2-\delta}$ – $La_{0.9}Sr_{0.1}FeO_{3-\delta}$. Unfortunately, the oxygen permeation is still far away from the general requirements (1 ml min^{-1} cm^{-2}) of a low cost application. Other drawbacks are the use of expensive raw materials and complex phase compositions.

Developing Ba-free MIEC membranes is another more promising way to improve the CO_2 resistance [37–54,56]. The relatively small ionic radius of 135 pm of the Ca^{2+} cation, as compared with Ba^{2+} (r = 160 pm) and Sr^{2+} (r = 144 pm) cations [60], leads to a promising candidate. The smaller ionic radius leads to a decline of the crystal lattice energy of the corresponding carbonate and can be considered a reason for the lower stability of $CaCO_3$, which is confirmed by the Ellingham diagram [51]. Ca-containing perovskites have already shown to be promising candidates for electrode materials [61,62], while they gained less attention as MIEC materials [50–54]. *Teraoka* et al. reported a very high oxygen permeation flux (1.8 ml min^{-1} cm^{-2} at 1143 K in an air/He gradient) through a $La_{0.6}Ca_{0.4}Co_{0.8}Fe_{0.2}O_{3-\delta}$ membrane (1.5 mm in thickness) already in 1988 [50], while the best results of this earlier work have not been reproduced yet. Recently, *Efimov* et al. investigated $La_{1-x}Ca_xFeO_{3-\delta}$ (x = 0.4–0.6) and $La_{1-x}Ca_xCo_{0.8}Fe_{0.2}O_{3-\delta}$ (x = 0.4–0.6) perovskite systems with respect to their oxygen ion conducting properties and their chemical stability [51]. It was shown that only the first members of the these systems with x = 0.4 were almost single-phase perovskites, while a higher Ca content caused the formation of significant amounts of additional phases such as $CaFe_2O_5$, $Ca_3Co_{2-z}Fe_zO_6$, and Co_3O_4. The bulk $La_{0.6}Ca_{0.4}Co_{0.8}Fe_{0.2}O_{3-\delta}$ membrane exhibited an oxygen permeation flux of 0.43 ml min^{-1} cm^{-2} and a high stability in CO_2. *Stevenson* et al. and *Diethelm* et al. also found these secondary phases for the $La_{0.4}Ca_{0.6}Co_{1-x}Fe_xO_{3-\delta}$ material with introducing more Ca^{2+} [52,53]. The measured oxygen permeation fluxes (0.03–0.09 ml min^{-1} cm^{-2}) were much lower. The formation of impurity phases during preparation and operation of perovskite membranes may be one reason for the lacking interest in Ca-containing materials. Co and Fe are mostly chosen as *B*-site cations, while ferrates generally reveal a

better tolerance towards CO_2 [57]. In most studies, Co/Fe ratios of either 4 or ¼ and an EDTA-citrate sol-gel method are applied. Systematic studies of different Co/Fe ratios and other preparation methods have received less attention.

In this work, $La_{0.6}Ca_{0.4}Co_{1-x}Fe_xO_{3-\delta}$ (x = 0, 0.3, 0.5, 0.7, 1) powders and pellets were prepared as novel materials using a reverse coprecipitation method for CO_2-tolerant oxygen permeation membranes. The influence of different Co/Fe ratios on the crystal structure, CO_2 adsorption ability, morphology, oxygen permeability, electrical conductivity, structural stability as well as their relationship are studied. In addition, first principles calculations were used to investigate the effect of different Co/Fe ratios on the formation energy of oxygen vacancies and oxygen migration behavior.

9.2. Experimental section

9.2.1. Preparation of LCCF powder and membrane

Perovskite-type $La_{0.6}Ca_{0.4}Co_{1-x}Fe_xO_{3-\delta}$ (x = 0, 0.3, 0.5, 0.7, 1) powders were synthesized by a reverse co-precipitation method. $La(NO_3)_3{\cdot}6H_2O$ (Alfa Aesar, 99.9%), $Ca(NO_3)_2{\cdot}4H_2O$ (SIGMA-ALDRICH, > 99%), $Co(NO_3)_2{\cdot}6H_2O$ (SIGMA-ALDRICH, > 98%), and Fe $(NO_3)_3{\cdot}9H_2O$ (SIGMA-ALDRICH, > 98%) were used as sources of La, Ca, Co, and Fe, respectively. A mixed solution of weighed quantities of metal nitrates were added to a solution of ammonium carbonate at a rate of 3–4 ml min^{-1} under vigorous stirring at 343 K. The pH value was adjusted to 8.5–9 with ammonium carbonate (Alfa Aesar, $(NH_4)_2CO_3$, 30.0% NH_3) to produce a precipitate suspension. The precipitates were aged at 343 K for 1 h under stirring and then filtered and washed with hot demineralized water several times to remove excess ions, followed by drying at 383 K for 12 h. The dried material was crushed and calcined in air at 1273 K for 5 h yielding the final $La_{0.6}Ca_{0.4}Co_{1-x}Fe_xO_{3-\delta}$ powders. The powders were uniaxially pressed into disc-shaped membranes in a stainless steel mold (16 mm diameter) with a force of approximately 30 kN. These green disc-shaped membranes (~1 mm in thickness) were sintered in a muffle furnace at 1323 K for 20 h under stagnant air at a heating/cooling rate of 3 K min^{-1}. The sintered membranes/pellets had a relative density of around 90%, measured by the Archimedes' liquid displacement technique using demineralized water as medium.

9.2.2. Characterization of materials

Powder X-ray diffraction (PXRD) data of all samples before and after oxygen permeation tests were collected with a Rigaku Smartlab X-ray diffractometer using Cu-$K\alpha_{1,2}$ radiation. Cu-K_β radiation was suppressed using a thin nickel foil with approximately 90% efficiency. The diffraction patterns were recorded from 10° to 80° (2 theta) by continuous scanning at a scanning rate of 1°/min. Electrical resistivity and thermopower were measured by a ZEM-3 (ULVAC-RIKO®) in helium atmosphere from 323 K to 1023 K. The measurement uncertainty of both the electrical conductivity and the thermopower is ± 7%. Thermogravimetric analysis (TGA) was carried out with a NETZSCH STA 409C. Around 30 mg powdery sample was heated in an alumina crucible in pure CO_2 atmosphere at a flow rate of 50 ml min^{-1} and a heating rate of 10 K min^{-1} from room temperature to 1473 K. TGA in Ar at a flow rate of 50 mL min^{-1} and a heating rate of 10 K min^{-1} from room temperature to 1473 K was carried out on a NETZSCH STA 449. Surface morphology of the samples was examined by a Zeiss Gemini 500 scanning electron microscope (SEM) equipped with a Bruker XFlash 6|60 EDXS system at an acceleration voltage of 10.0 kV.

9.2.3. Measurements of oxygen permeation

The oxygen permeation was measured with a self-made high-temperature permeation cell. The membrane was tightly attached with CERAMABOND M-835 (T-E-Klebetechnik) to an aluminum oxide tube (16 mm). Another quartz glass tube (24 mm) served as the air side of the permeator. A more detailed description of the oxygen permeation set-up can be found elsewhere [63]. Synthetic air was fed at a rate of 150 ml min^{-1} to the feed side; He or CO_2 (29.0 ml min^{-1}) and Ne (1.0 ml min^{-1}) gases were fed to the sweep side. The temperature was 1023 K when changing the sweep gas from He to CO_2 prior to the oxygen permeation measurements. The effluents were analyzed by gas chromatography on an Agilent 6890 instrument equipped with a Carbon 1000 column. The gas concentrations in the effluent stream were calculated by a prerecorded calibration curve. The absolute flux rate of the effluents was determined by using neon as an internal standard. The relative leakage of O_2 was evaluated by measuring the amount of N_2 in the effluent stream and subtracted from the measured data.

9.2.4. First-principle calculations

The effect of Fe substitution on the formation energy of oxygen vacancies in the $La_{0.6}Ca_{0.4}Co_{1-x}Fe_xO_{3-\delta}$ (LCCF) membranes was also evaluated by first principles calculations. Our calculations are based on the density functional theory (DFT) as implemented in VASP (The Vienna Ab initio Simulation Package) [64], which employs a planewave basis set and the projector augmented-wave method [65]. For the description of the exchange-correlation we have used the generalized gradient approximation of Perdew-Burke-Ernzerhof (PBE-GGA) [66] and the norm-conserving Troullier-Martins pseudopotentials [67]. The cut-off energy of the plane-wave set was set at 520 eV and a 2 × 2 × 2 supercell was adopted to minimize the energy corresponding to the atomic positions. The tolerance for the self-consistent cycle was set at 1×10^{-5} eV per atom for the total energy. A simplified model and the following valence electronic configurations were chosen for the ground state electronic structure calculations: La $5s^2 5p^6 5d^1 6s^2$, Fe $3d^6 4s^2$, O $2s^2 2p^4$, Ca $4s^2$, Co $3d^7 4s^2$. The structure model is based on an ordered distribution of Ca and La as well as Co and Fe in contrast to the experimentally determined random distribution. In this study, we have chosen a 2 × 2 × 2 supercell with a size of approximately 15 Å × 15 Å × 15 Å, which is reasonable and commonly used. Based on a linear relationship of the lattice parameters in the same space group, we have adopted a La/Ca ratio of 6/2 for single oxygen vacancy generation in order to compensate for the charge in our simulation setup. This La/Ca ratio was taken as basis for all calculations of the oxygen vacancy formation energy and the energy barrier of the oxygen migration. Regarding the Co/Fe ratio, our measurements reveal a better membrane performance with a lower Co/Fe ratio (0.3/0.7). The experiments show that higher Co contents lead to a phase transition from orthorhombic to tetragonal. In order to avoid the phase transition and maintain the orthorhombic symmetry, we investigated Co/Fe ratios up to 0.5/0.5. The presence of one oxygen vacancy per 2 × 2 × 2 supercell was approximated, leading to a composition of $La_6Ca_2Co_{4-x}Fe_{4+x}O_{23}\square_1$ (x = 0, 1, 2, 3, 4) to model a variation in the Co/Fe ratio. The cobalt-free composition with x = 4, was selected as parent structure. Spin-polarized simulations were performed for all structures. The Brillouin zone was determined using a 2 × 2 × 2 k-point grid for geometry optimization, while a 5 × 5 × 5 k-point grid was adopted for calculating the formation energy of the oxygen vacancies.

To simulate the structures, we started from the parent atomic arrangement mentioned above. At step 1, cobalt atoms were gradually added to change the Co/Fe ratio. At step 2, the oxygen vacancy site was varied and an additional relaxation was carried out. Geometry optimization and calculation of the lattice parameters were performed by fitting the energy-volume curves for the respective perovskite structures. Based on the obtained lattice parameters, an oxygen vacancy was formed at different sites in the crystal structure and the formation energy was calculated. For these calculations, the volume of the unit cell was kept constant, while the atoms were allowed to relax. Since the formation energy

represents the ease of oxygen vacancy formation, it is expected to give an insight into the pathways of oxygen permeation and further into the ion conductivity. The formation energy $E_f[V_O^{\cdot\cdot}]$ of an oxygen vacancy was calculated with the following equation:

$$E_f[V_O^{\cdot\cdot}] = E_{tot}[V_O^{\cdot\cdot}] - \sum_i n_i \mu_i - E_{tot}[bulk] \quad (1)$$

Where $E_{tot}[V_O^{\cdot\cdot}]$ is the total energy derived from a supercell calculation containing the defect oxygen vacancy, $E_{tot}[bulk]$ is the total energy of the ideal bulk crystal without a vacancy, n_i is a negative number denoting the removed O atoms, and μ_i corresponds to a chemical potential representing the energy of a reservoir of O atoms, which are being exchanged. Two types of geometry relaxations were performed: (a) the symmetry of the lattice was allowed to vary at step 1 and was then maintained during the second relaxation step. (b) The symmetry of the lattice was fixed at both steps. The formation energies are denoted $E_f^{(a)}$ and $E_f^{(b)}$, respectively.

The nudged elastic band method (NEB) [68,69] was used to find potential diffusion pathways and energy barriers of the oxygen transport. Assuming that the local motion of an oxygen ion is not perturbing the shape and volume of the structure, the lattice parameters and shape were set to those of the geometry relaxation used for calculating the oxygen vacancy formation energies. The LCCF crystals were optimized by fully relaxing the atomic positions until the residual Hellmann-Feynman forces acting on each atom were lower than 0.01 eV/Å. The NEB calculations were performed for 2 × 2 × 2 supercells containing 39 atoms and a single oxygen vacancy. In this way, interactions between the images due to periodic boundary conditions were avoided. At a first approximation, we have only considered ion jumps to nearest (N) neighbor sites. Accordingly, five images were interpolated between pair positions through the NEB method and all atoms were relaxed (ΔF < 0.01 eV/Å). The NEB calculations confirmed the existence of only saddle points along each migration path leading to the potential hopping pathways related to the minimum energy. The barrier energy of oxygen ions jumping to next neighbor sites is defined as the energy difference between transition states (TS) and initial states.

9.3. Results and discussion

9.3.1. Phase structure and morphology

Fig. 1 presents the XRD pattern of $La_{0.6}Ca_{0.4}Co_{1-x}Fe_xO_{3-\delta}$ (x = 0, 0.3, 0.5, 0.7, 1) powders prepared by the reverse co-precipitation method. The XRD reflections revealing a full crystallization were indexed using a perovskite-type structure model. They indicate that changing the Co/Fe ratio does not induce major changes in the crystal structure. The indexing was based on a pseudo-cubic perovskite-type cell. The broadening and shape of the 211 reflection points to a lower symmetry, most likely an orthorhombic unit cell. With increasing Fe content, the position of the 111 reflection is shifted to a lower angle. This trend is observed because iron ($r(Fe^{3+})$ = 0.645 Å) [60] has a larger ionic radius than cobalt ($r(Co^{3+})$ = 0.61 Å) [60] at the same oxidation state and coordination number, causing an expansion of the unit cell. The synthesis of $La_{0.6}Ca_{0.4}Co_{0.5}Fe_{0.5}O_{3-\delta}$ powder was successfully up-scaled to 50 g per batch. According to the XRD pattern, a single-phase perovskite-type structure was obtained (Fig. S1). Fig. 2 presents SEM micrographs of the freshly prepared $La_{0.6}Ca_{0.4}Co_{1-x}Fe_xO_{3-\delta}$ (x = 0.3, 0.5, 0.7) membranes. The surfaces of the investigated membranes with a relative density of around 90% are compact without any cracks. The substitution of Fe for Co results in a slight increase of the average grain size. EDXS analysis reveals that the elements including La, Ca, Co, Fe, O are distributed uniformly on the membrane surface (Fig. S2).

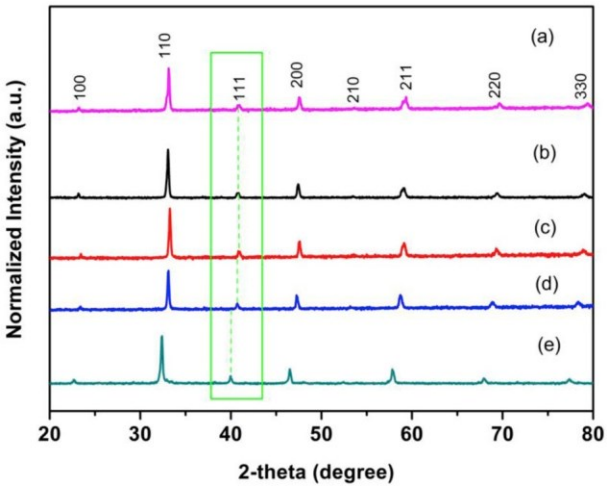

Fig. 1. XRD patterns of $La_{0.6}Ca_{0.4}Co_{1-x}Fe_xO_{3-\delta}$ (x = 0, 0.3, 0.5, 0.7, 1) powders (a) x = 0; (b) x =0.3; (c) x =0.5; (d) x = 0.7; (e) x = 1.

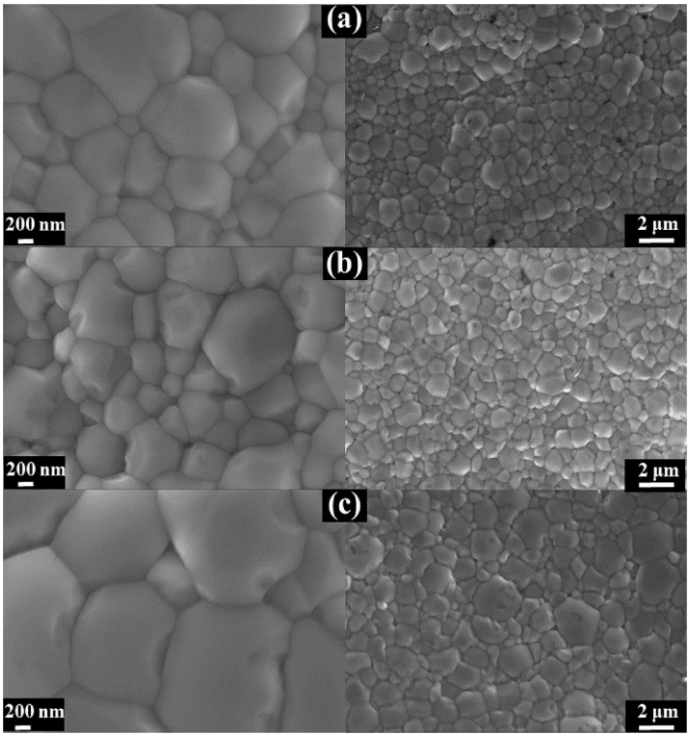

Fig. 2. SEM micrographs of fresh LCCF membranes (a) $La_{0.6}Ca_{0.4}Co_{0.7}Fe_{0.3}O_{3-\delta}$, (b) $La_{0.6}Ca_{0.4}Co_{0.5}Fe_{0.5}O_{3-\delta}$ and (c) $La_{0.6}Ca_{0.4}Co_{0.3}Fe_{0.7}O_{3-\delta}$.

9.3.2. Oxygen permeation behavior of membranes swept by He or CO_2

The oxygen permeation flux through the membranes was measured in 50 K steps in the temperature range of 1023 K and 1223 K in Air/He and Air/CO_2 gradients, respectively, as shown in Fig. 3. As expected, the oxygen permeation fluxes of all membranes increased with increasing temperature, since higher temperatures facilitate both surface exchanges and oxygen bulk diffusion. The oxygen permeation fluxes increased in the following order: $La_{0.6}Ca_{0.4}Co_{0.3}Fe_{0.7}O_{3-\delta}$ > $La_{0.6}Ca_{0.4}Co_{0.5}Fe_{0.5}O_{3-\delta}$ > $La_{0.6}Ca_{0.4}FeO_{3-\delta}$ > $La_{0.6}Ca_{0.4}Co_{0.7}Fe_{0.3}O_{3-\delta}$ > $La_{0.6}Ca_{0.4}CoO_{3-\delta}$. This is also in good agreement with the trend of the activation energies of oxygen ion migration presented in Fig. S4. The highest oxygen

permeation flux of 0.8 ml min^{-1} cm^{-2} was obtained at 1223 K for the $La_{0.6}Ca_{0.4}Co_{0.3}Fe_{0.7}O_{3-\delta}$ membrane in Air/He. Changing the sweep gas from He to CO_2, the oxygen permeation fluxes of all membranes decreased but to a different extend. For example, the oxygen permeation flux of $La_{0.6}Ca_{0.4}Co_{0.3}Fe_{0.7}O_{3-\delta}$ decreased from 0.76 ml min^{-1} cm^{-2} to 0.5 ml min^{-1} cm^{-2} at 1173 K. These declines can be attributed to chemically adsorbed CO_2 at the oxygen vacancy sites of the membrane suppressing the surface-exchange reaction. It is striking that the decrease of oxygen permeation flux of $La_{0.6}Ca_{0.4}Co_{0.5}Fe_{0.5}O_{3-\delta}$ is much smaller than that of other membranes. The oxygen flux was constant within the error margin for more than 6 h in pure CO_2 atmosphere, indicating a weaker CO_2 poisoning effect for this composition.

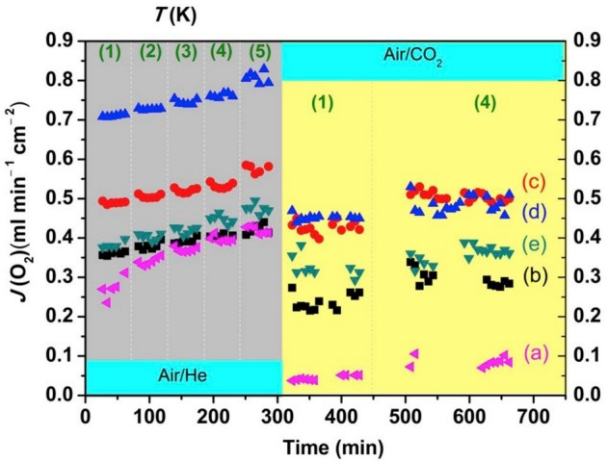

Fig. 3. Oxygen permeation fluxes of $La_{0.6}Ca_{0.4}Co_{1-x}Fe_xO_{3-\delta}$ (x =0, 0.3, 0.5, 0.7, 1) in Air/He and Air/CO_2. Conditions: sweeping gas flow rate He or CO_2 =29 ml min^{-1}, Ne= 1ml min^{-1}; feeding gas flow rate synthetic air =150 ml min^{-1} (80 vol.% N_2, 20 vol.% O_2); membrane thickness: 1 mm; (1) 1023 K; (2) 1073 K; (3) 1123 K; (4) 1173 K; (5) 1223 K; (a) x = 0; (b) x = 0.3; (c) x = 0.5; (d) x = 0.7; (e) x = 1.

DFT was used to understand the impact of Fe substitution on the LCCF transport properties. In order to avoid phase transitions and keep the same orthorhombic symmetry in our simulations we have used lower Co/Fe ratios than in the experiments. The calculated lattice parameters and the closely related experimental values derived from the XRD patterns (cf. Fig. 1) are in very good agreement (deviation ≤ 2.1%) and summarized in Table 1. This agreement allows us to further elucidate the trend of the oxygen vacancy formation energies. However, the fact that simulations and experiments were performed at different temperatures will result in deviations. Both methods reveal a slight overall increase of the lattice parameters when substituting Co with Fe (c.f. Table 1). The results suggest that Fe substitution may reduce the electrical conductivity due to a reduced orbital overlap, which is supported by the experimental findings displayed in Fig. 4. Accordingly, even our simulation results based on a simplistic $La_6Ca_2Co_{4-x}Fe_{4+x}O_{23}\square_1$ model are useable for further investigations of the LCCF systems.

Table 1 Calculated and experimental lattice parameters of the LCCF perovskites.

Co/Fe ratio	Formula	a(Å)	b(Å)	c(Å)
Simulations				
0.500 : 0.500	$La_6Ca_2Co_4Fe_4O_{23}$	3.842	3.733	3.805
0.375 : 0.625	$La_6Ca_2Co_3Fe_5O_{23}$	3.852	3.863	3.822
0.250 : 0.750	$La_6Ca_2Co_2Fe_6O_{23}$	3.864	3.864	3.817
0.125 : 0.875	$La_6Ca_2Co_1Fe_7O_{23}$	3.865	3.865	3.823
0.000 : 1.000	$La_6Ca_2Fe_8O_{23}$	3.874	3.874	3.820
Experiments				
0.700 : 0.300	$La_{0.6}Ca_{0.4}Co_{0.7}Fe_{0.3}O_{3-\delta}$	3.827	3.827	3.827
0.500 : 0.500	$La_{0.6}Ca_{0.4}Co_{0.5}Fe_{0.5}O_{3-\delta}$	3.831	3.831	3.789
0.300 : 0.700	$La_{0.6}Ca_{0.4}Co_{0.3}Fe_{0.7}O_{3-\delta}$	3.844	3.863	3.799
0.000 : 1.000	$La_{0.6}Ca_{0.4}FeO_{3-\delta}$	3.897	3.901	3.900

9.3.3. Conductivity of $La_{0.6}Ca_{0.4}Co_{1-x}Fe_xO_{3-\delta}$ membranes

The temperature dependent total conductivity of $La_{0.6}Ca_{0.4}Co_{1-x}Fe_xO_{3-\delta}$ (x = 0, 0.3, 0.5, 0.7, 1) in He is shown in Fig. 4.

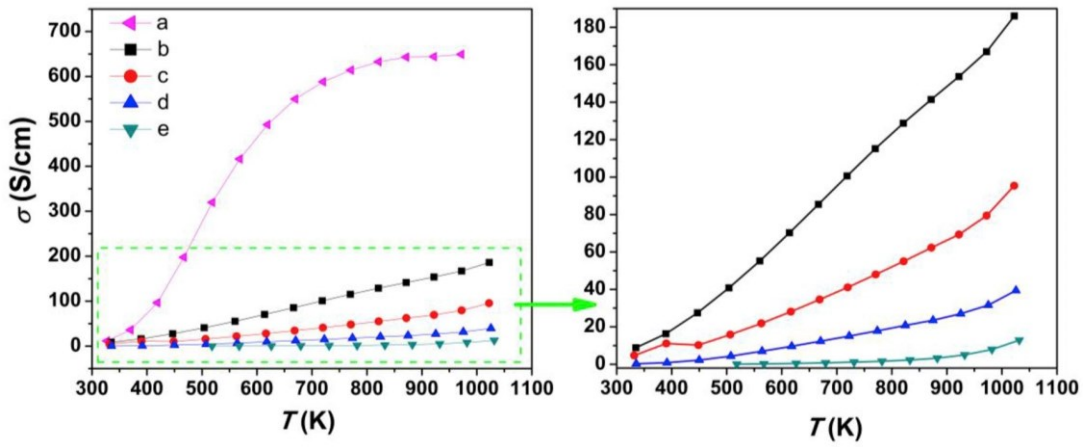

Fig. 4. Temperature dependence of the total conductivity of $La_{0.6}Ca_{0.4}Co_{1-x}Fe_xO_{3-\delta}$ (x = 0, 0.3, 0.5, 0.7, 1) membranes. (a) x =0; (b) x = 0.3; (c) x = 0.5; (d) x = 0.7; (e) x = 1.

In general, the electronic component of the total conductivity is 100–1000 times higher than the ionic conductivity of mixed oxygen-ion and electronic ceramic materials [40]. Thus, the measured total electrical conductivity approximately equates to the electronic conductivity. As shown in Fig. 4, the conductivity increases with increasing temperature for all samples. Fig. S3 shows the temperature dependence of the Seebeck coefficient of $La_{0.6}Ca_{0.4}Co_{1-x}Fe_xO_{3-\delta}$. Over the entire investigated temperature range, the Seebeck coefficient is positive, indicating that the major mobile charge carriers are holes. $La_{0.6}Ca_{0.4}CoO_{3-\delta}$ oxides demonstrate a high conductivity of 650 S cm^{-1} similar to metals. With increasing Fe concentration the electronic conductivity decreases. This can be linked to the increased hopping distance between neighboring octahedral sites with increasing Fe content. The oxygen ionic conductivity is often less than 1 S cm^{-1} [40]. It reasonably assumes that the electronic conductivity had a negligible effect on the oxygen permeability of the different investigated samples since the electronic conductivity still overwhelmed the oxygen ionic conductivity in this study, which agrees well with others' work [40]. $La_{0.6}Ca_{0.4}Co_{0.3}Fe_{0.7}O_{3-\delta}$ possesses a higher oxygen permeation than $La_{0.6}Ca_{0.4}CoO_{3-\delta}$ probably due to its higher oxygen ionic conductivity, although the total conductivity of $La_{0.6}Ca_{0.4}CoO_{3-\delta}$

is much larger than that of $La_{0.6}Ca_{0.4}Co_{0.3}Fe_{0.7}O_{3-\delta}$. Overall, the transport of oxygen ions through membranes with low or negligible ionic conductivity can be significantly hindered. A balance between ionic and electronic conductivities is important for high oxygen permeation.

9.3.4. Formation energy of oxygen vacancies

In order to further understand the oxygen ion migration in the LCCF $La_6Ca_2Co_{4-x}Fe_{4+x}O_{23}\square_1$ system, which is mainly promoted through oxygen vacancies, the oxygen vacancy formation energies were calculated by DFT. The results are based on the simplistic structure model $La_6Ca_2Co_{4-x}Fe_{4+x}O_{23}\square_1$ and the definition given in Eq. (1). The obtained values for both relaxation types (a) and (b) mentioned in the experimental section are summarized in Table 2.

Table 2 Calculated formation energies for both relaxation types (a) and (b) (see Experimental Section) of one oxygen vacancy in the $La_6Ca_2Co_{4-x}Fe_{4+x}O_{23}\square_1$ system. The vacancy sites are sketched in Fig. 5.

Co/Fe ratio	Systems	Oxygen vacancy site	Formation energy $E_f^{(a)}\left(E_f^{(b)}\right)$ (eV)
0.500 : 0.500	$La_6Ca_2Co_4Fe_4O_{23}\square_1$	Fe–O–Fe	2.78 (2.89)
		Fe–O–Fe	2.80 (2.88)
		Fe–O–Co	2.89 (2.85)
		Fe–O–Co	2.55 (2.63)
		Fe–O–Co	2.71 (2.83)
		Fe–O–Co	2.55 (2.65)
		Fe–O–Co	2.65 (2.83)
		Fe–O–Co	2.81(2.68)
		Fe–O–Co	2.82 (2.87)
		Fe–O–Co	2.80 (2.72)
		Co–O–Co	2.83 (2.92)
		Co–O–Co	2.74 (2.68)
0.375 : 0.625	$La_6Ca_2Co_3Fe_5O_{23}\square_1$	Fe–O–Fe	2.84 (2.82)
		Fe–O–Fe	2.89 (2.90)
		Fe–O–Co	2.92 (2.94)
		Fe–O–Co	2.77 (2.78)
		Fe–O–Co	2.67 (2.76)
		Fe–O–Co	2.59 (2.73)
		Fe–O–Co	2.65 (2.79)
		Fe–O–Co	2.89 (2.87)
		Fe–O–Co	2.94 (2.98)
		Co–O–Co	2.96 (2.98)
0.250 : 0.750	$La_6Ca_2Co_2Fe_6O_{23}\square_1$	Fe–O–Fe	2.99 (2.95)
		Fe–O–Co	2.90 (2.80)
0.125 : 0.825	$La_6Ca_2Co_1Fe_7O_{23}\square_1$	Fe–O–Fe	2.98 (2.95)
		Fe–O–Co	2.94 (2.95)
0.000 : 1.000	$La_6Ca_2Fe_8O_{23}\square_1$	Fe–O–Fe	3.01 (3.05)

For the calculation of the formation energies of oxygen vacancies, different oxygen vacancy sites were investigated as depicted in Fig. 5.

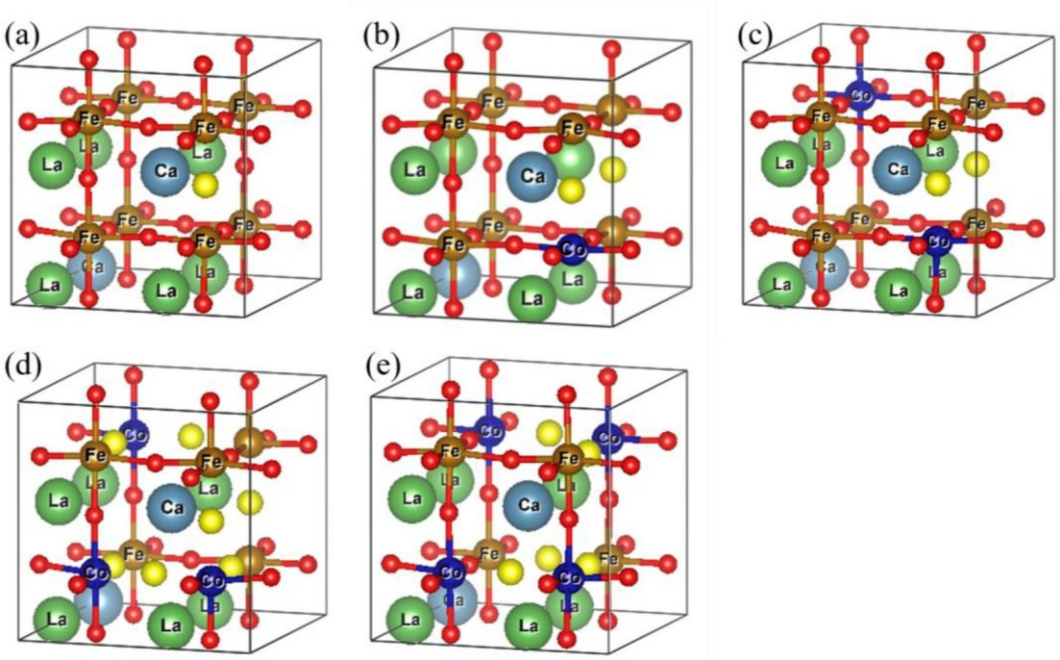

Fig. 5. Simplified lattice models for the $La_6Ca_2Fe_8O_{23}\square_1$ and $La_6Ca_2Co_{4-x}Fe_{4+x}O_{23}\square_1$ (x = 0, 1, 2) systems with the oxygen vacancy formed in the Fe–O–Fe, Fe–O–Co and Co–O–Co bonds. The possible oxygen vacancy sites with different chemical environment are colored in yellow. The different panels correspond to (a) $La_6Ca_2Fe_8O_{23}\square_1$, (b) $La_6Ca_2Co_1Fe_7O_{23}\square_1$, (c) $La_6Ca_2Co_2Fe_6O_{23}\square_1$, (d) $La_6Ca_2Co_3Fe_5O_{23}\square_1$, and (e) $La_6Ca_2Co_4Fe_4O_{23}\square_1$. (For interpretation of the references to color in this figure legend, the reader is referred to the Web version of this article.)

Accordingly, each vacancy is placed in a different atomic environment. Table 2 reveals that the two types of relaxations eventually lead to similar trends. As shown in Table 2, the oxygen vacancy formation energies of $La_6Ca_2Co_{4-x}Fe_{4+x}O_{23}\square_1$ (x = 0, 1, 2, 3, 4) are calculated with values of 2.55–3.05 eV. Such values are similar with other reported $La_{1-x}Sr_xCo_{0.8}Fe_{0.2}O_{3-\delta}$ based materials [70,71], which demonstrates that our simulation results based on a simplistic $La_6Ca_2Co_{4-x}Fe_{4+x}O_{23}\square_1$ model are reliable. It is important to mention that the simplified models in this study are only expected to supply trends about the influence of the *B*-site cation on the oxygen vacancy formation energy. Increasing the Fe content leads to a larger formation energy, implying that the formation of an oxygen vacancy becomes more favorable with increasing Co/Fe ratio. Comparing the various vacancy sites, the lowest formation energies are found on Fe–O–Co sites. Accordingly, the formation of an oxygen vacancy in $La_6Ca_2Co_4Fe_4O_{23}\square_1$ is energetically more favorable on these sites. The highest formation energies, denoting less favorable vacancy sites, are found on Fe–O–Fe sites and for the lowest Co/Fe ratio. Regarding the most favorable vacancy site for a given Co content, no clear trend could be found. For a Co/Fe ratio up to 0.750 : 0.250, the formation energy decreases from a Fe–O–Fe to a Fe–O–Co to a Co–O–Co site, but this trend is reversed when further increasing the cobalt content. It seems that a balance between structural disorder (Co vs. Fe) and the redoxactivity of the *B*-site cations is required to minimize the oxygen vacancy formation energy. In general, a lower oxygen vacancy formation energy next to Co would be expected, since Co favors a lower oxidation state in comparison to Fe (Co^{2+} vs. Fe^{3+}).

Besides the formation of oxygen vacancies, the analysis of the mobility of oxygen vacancies via different pathways is crucial to advance the understanding of the oxygen permeability of LCCF depending on the Co/Fe ratio. Five different possible migration pathways were modelled and analyzed in the $La_6Ca_2Fe_8O_{23}\square_1$ and $La_6Ca_2Co_2Fe_6O_{23}\square_1$ simplified systems. The different locations accessible to the oxygen vacancy can be seen in Fig. S5. The resulting specific energy barriers are summarized in Table 3.

Table 3 Energy barriers for the possible oxygen ion migration pathways.

System	Transport route	Energy barrier (eV)
$La_6Ca_2Fe_8O_{23}\square_1$	$V_{o1} \rightarrow V_{o5}$	0.76
	$V_{o1} \rightarrow V_{o3}$	0.52
$La_6Ca_2Co_2Fe_6O_{23}\square_1$	$V_{o1} \rightarrow V_{o4}$	0.81
	$V_{o1} \rightarrow V_{o5}$	0.77
	$V_{o1} \rightarrow V_{o2}$	0.61
	$V_{o1} \rightarrow V_{o3}$	0.62
	$V_{o2} \rightarrow V_{o3}$	0.80

These are energetic differences between two states, the initial and the transition states (TS). The energy barrier for the jump of the oxygen ions in the $La_6Ca_2Co_2Fe_6O_{23}\square_1$ system is higher than that in $La_6Ca_2Fe_8O_{23}\square_1$, indicating that Co-substitution makes the oxygen ion migration difficult. Together with the oxygen formation energies as shown in Table 2, these calculations show that partial Co substitution can promote the formation of oxygen vacancies while at the same time limiting the migration ability of the oxygen anions. Therefore, a suitable Co/Fe ratio can balance the formation of oxygen vacancies and migration ability of the oxygen ions. From a geometry point of view, there are five possible unique oxygen migration paths between the different oxygen vacancy sites and neighboring oxygen atoms, as shown in Fig. 6.

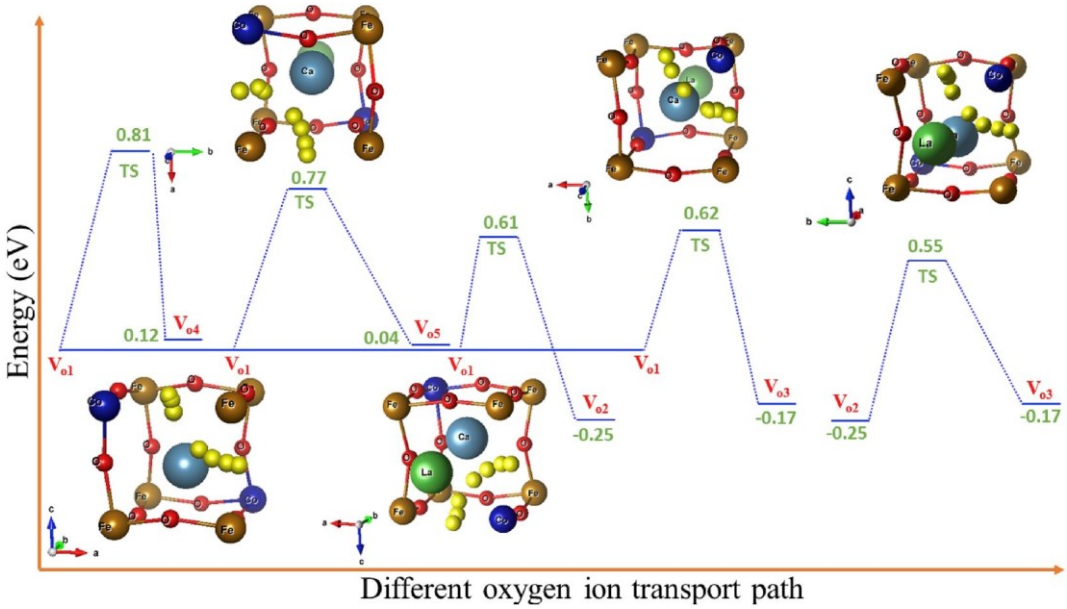

Fig. 6. Potential energy diagram for the oxygen ion migration via different paths in the $La_6Ca_2Co_2Fe_6O_{23}\square_1$ system. TS: Transition state

Since an influence of the Co/Fe ratio on the oxide ion migration was expected, the geometry of the BO_6 octahedra in $La_6Ca_2Co_{4-x}Fe_{4+x}O_{23}\square_1$ was also studied. The results are given in Table S1 and Fig. S6. Increasing the Co content leads to the decrease of La–O and Ca–O bond lengths. These results indicate a higher stability of the LaO_{12} and CaO_{12} polyhedra at higher Co contents. Accordingly, the oxygen ion cannot easily leave the Ca–O or La–O bond. A higher Co content decreases the oxygen vacancy formation energy, while it simultaneously hinders the migration ability of the oxygen anions. This leads to an increased energy barrier of the oxygen ion in the lattice with Co-substitution as shown in Table 3. These findings are in good agreement with previous experimental and theoretical studies [21] and support the above stated experimental data (Fig. 3) of the oxygen permeability. Further ongoing theoretical studies are expected to lead to a better understanding of the oxygen transport process in (La,Ca)(Co,Fe)$O_{3-\delta}$ systems. In addition, since Fe and Co can exist in different valence states (+4, +3, or +2), charge compensation can occur by oxygen vacancy formation in the (La,Ca)(Co,Fe)$O_{3-\delta}$ perovskite-type structure. This is expected to be beneficial to the oxygen permeation process. This behavior, expressed by Eqs. (2) and (3) for (La,Sr)(Co,Fe)$O_{3-\delta}$ perovskites, was already shown by *Oishi* et al. [72].

$$\frac{1}{2}O_2 + V_o^{\cdot\cdot} + 2 \rightarrow O_o^x + 2Fe_{\acute{F}e} \tag{2}$$

$$\frac{1}{2}O_2 + V_o^{\cdot\cdot} + 2Fe_{\acute{F}e} \rightarrow O_o^x + 2Fe_{Fe}^X \tag{3}$$

where Fe_{Fe}^X refers to Fe^{3+} on Fe^{3+} sites, $Fe_{\acute{F}e}$ refers to Fe^{4+} on Fe^{3+} sites, $Fe_{\acute{F}e}$ refers to Fe^{2+} on Fe^{3+} sites, O_o^x refers to an oxygen ion on oxygen vacancy sites, and $V_o^{\cdot\cdot}$ refers to an oxygen vacancy with two positive charges.

9.3.5. Characterizations and analysis

The formation of carbonates has been considered to be responsible for the inactivation of barium- or strontium-containing perovskite-type membranes such as (Ba,Sr)(Co,Fe)$O_{3-\delta}$ and Sr(Co,Fe)$O_{3-\delta}$ [12–14]. The surfaces of the LCCF membranes were investigated to study the reason for the reduction of the oxygen permeation flux of $La_{0.6}Ca_{0.4}Co_{1-x}Fe_xO_{3-\delta}$ (x = 0.3, 0.5, 0.7). Fig. 7 shows the XRD patterns of the air feed side and the CO_2 sweep side of the three membranes after about 11 h operation.

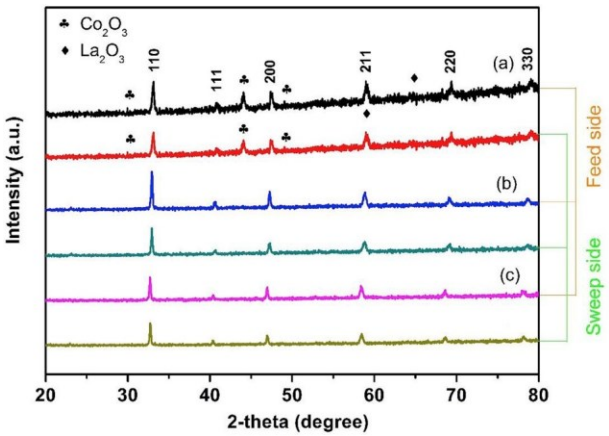

Fig. 7. XRD patterns of the feed side (air) and the sweep side (pure CO_2) of the membranes after O_2 permeation measurements: (a) $La_{0.6}Ca_{0.4}Co_{0.7}Fe_{0.3}O_{3-\delta}$; (b) $La_{0.6}Ca_{0.4}Co_{0.5}Fe_{0.5}O_{3-\delta}$; (c) $La_{0.6}Ca_{0.4}Co_{0.3}Fe_{0.7}O_{3-\delta}$.

It was found that most of the membranes retained their perovskite-type structure. No formation of carbonates on any of the membranes was observed by XRD. These results are in a good agreement with other studies on (La,Ca)(Co,Fe) $O_{3-\delta}$ and (La,Sr)(Co,Fe)$O_{3-\delta}$ membranes [37,41,51]. The stability

of metal oxides in a CO_2-containing atmosphere was estimated using Ellingham diagrams [51]. These diagrams demonstrate that lanthanum, cobalt, calcium, and iron carbonate formation is not preferred. On the other hand, barium and strontium carbonate may easily form above 1073 K dependent on temperature, CO_2 partial pressure, and chemical potential. Accordingly, the absence of barium and strontium in the LCCF membranes may account for the good CO_2 resistance. However, a few weak Co_2O_3 and La_2O_3 reflections can be observed on both the air feed side and the CO_2 sweep side of the tested $La_{0.6}Ca_{0.4}Co_{0.7}Fe_{0.3}O_{3-\delta}$ membrane. This can be attributed to the fact that a perovskite-type MIEC material with a higher Co content usually shows only poor structural stability owing to the easy (partial) reduction of the Co cations [10,11].

Surface morphologies and elemental distributions of the feed side (air) and the sweep side (CO_2) of the tested $La_{0.6}Ca_{0.4}Co_{0.5}Fe_{0.5}O_{3-\delta}$ membrane are presented in Fig. 8.

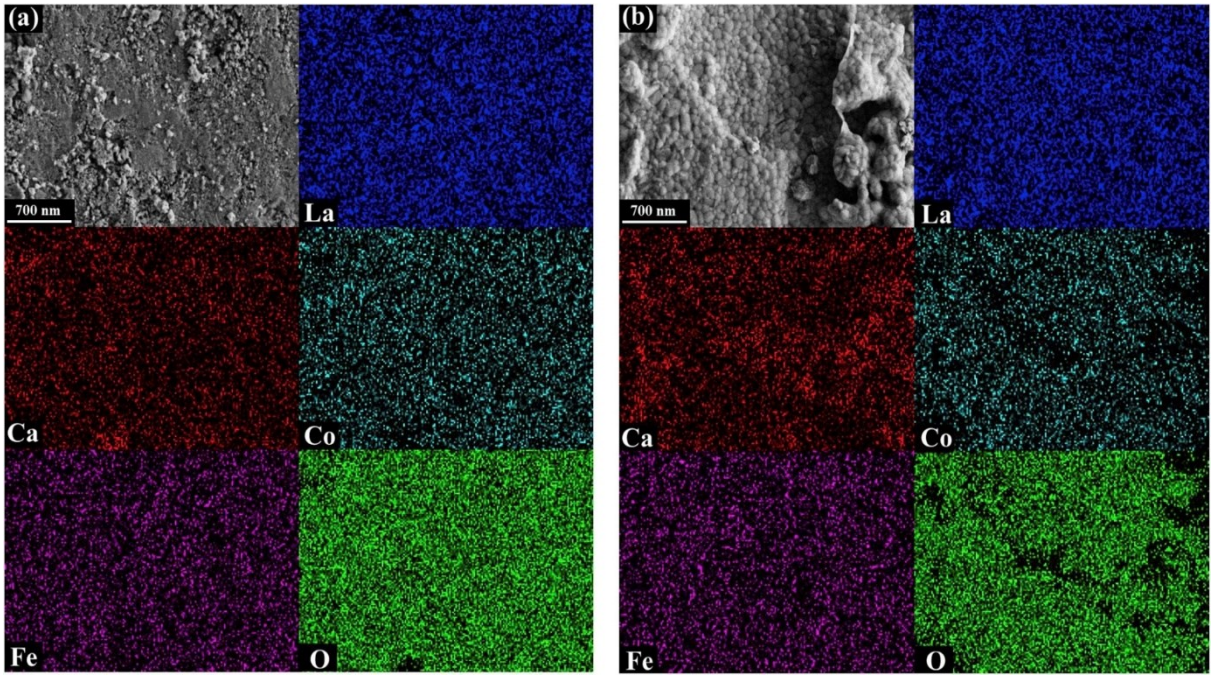

Fig. 8. SEM images and EDXS elemental distribution of the $La_{0.6}Ca_{0.4}Co_{0.5}Fe_{0.5}O_{3-\delta}$ membrane after 11 h operation. The panels depict (a) the feed side (air) and (b) the sweep side (CO_2).

No carbonate particles were found, which is well in agreement with the XRD results. EDXS analysis reveals that the elements La, Ca, Co, Fe, and O are distributed uniformly on both sides of membrane surface after 11 h oxygen permeation experiment. The microstructure and uniform elemental distribution were also observed for $La_{0.6}Ca_{0.4}Co_{0.7}Fe_{0.3}O_{3-\delta}$ and $La_{0.6}Ca_{0.4}Co_{0.3}Fe_{0.7}O_{3-\delta}$ membranes as shown in Figs. S7 and S8.

The oxygen vacancies on the membrane surface play a crucial role for the oxygen capture [73,74]. The concentration of oxygen vacancies depends largely on the temperature and oxygen partial pressure $p(O_2)$ of the surrounding atmosphere. The higher the temperature and the lower $p(O_2)$, the more oxygen vacancies are formed. Theoretical and experimental studies consistently show that the CO_2 adsorption, activation, and dissociation processes were significantly enhanced by the presence of oxygen vacancies [75–78]. Therefore, CO_2 can be chemically bond to an oxygen vacancy site of the membrane surface when used as a sweep gas. As a result, the surface-exchange reaction on interface between $V_{o^{\cdot\cdot}}$ and lattice oxygen is suppressed due to the occupation of the oxygen vacancy site by CO_2 [37]. Thus, the CO_2 affinity of the membrane is an important factor influencing oxygen permeation.

TGA in flowing Ar and CO_2 was carried out to investigate oxygen vacancy formation, potential carbonate formation as well as adsorption of CO_2 to LCCF powders. The results are shown in Fig. 9.

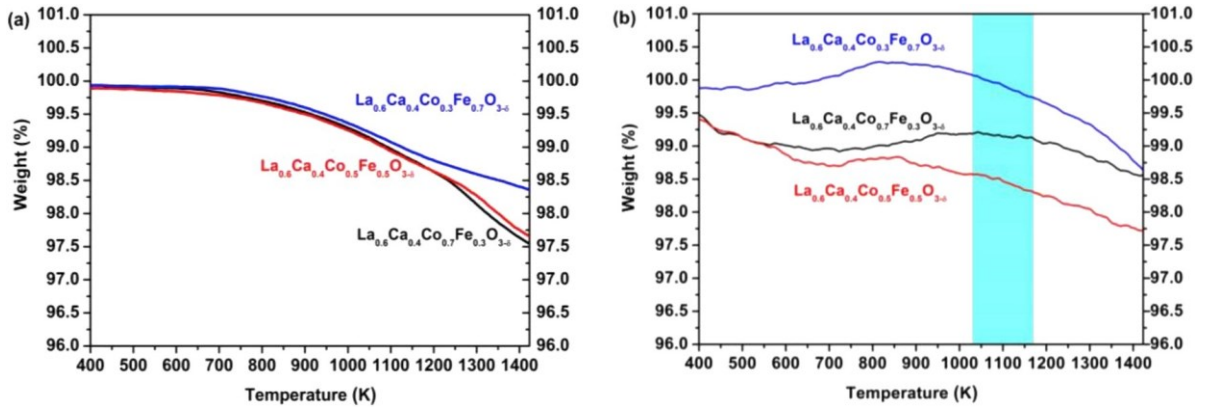

Fig. 9. TG-curves of LCCF fresh powders at 10 K min^{-1} under flowing Ar (a) and CO_2 (b) atmospheres. CO_2 flow rate is 50 ml min^{-1}. Light cyan area: investigated temperature range for oxygen permeation.

In Ar, the weight loss of the samples gradually set in above 651 K. This weight loss was attributed to the beginning formation of additional oxygen vacancies by thermal reduction. Above 873 K, the reduction process accelerated noticeably. As expected from the Co/Fe ratio and the accompanying oxidation state of the *B*-site cations, $La_{0.6}Ca_{0.4}Co_{0.3}Fe_{0.7}O_{3-\delta}$ and $La_{0.6}Ca_{0.4}Co_{0.7}Fe_{0.3}O_{3-\delta}$ showed the smallest and the largest weight loss at high temperatures, respectively. The values of $La_{0.6}Ca_{0.4}Co_{0.5}Fe_{0.5}O_{3-\delta}$ lay in-between (Fig. 9(a)). In CO_2 (Fig. 9(b)), no sharp and significant mass gain was observed in the entire investigated temperature range (up to 1473 K), corroborating the results from the Ellingham diagrams [51] and the XRD measurements. This manifests the superior CO_2-tolerance of the LCCF membranes with respect to the typically observed damage by alkaline earth metal carbonate (e.g. $CaCO_3$) formation. A mass loss due to a release of surface adsorbed species such as H_2O was observed up to about 673 K for all investigated powder samples. This mass loss was more pronounced in the case of $La_{0.6}Ca_{0.4}Co_{0.7}Fe_{0.3}O_{3-\delta}$ (Δm = −1.0%) and $La_{0.6}Ca_{0.4}Co_{0.5}Fe_{0.5}O_{3-\delta}$ (Δm = −1.5%) than for $La_{0.6}Ca_{0.4}Co_{0.3}Fe_{0.7}O_{3-\delta}$ (Δm = −0.2%). Above 723 K a more or less significant mass gain was obtained for all samples. This can be mainly attributed to chemisorption of CO_2 on the LCCF surface as previously reported [54]. The observed mass gain increased in the following order: $La_{0.6}Ca_{0.4}Co_{0.5}Fe_{0.5}O_{3-\delta}$ (Δm = 0.13%), $La_{0.6}Ca_{0.4}Co_{0.7}Fe_{0.3}O_{3-\delta}$ (Δm = 0.3%), and $La_{0.6}Ca_{0.4}Co_{0.3}Fe_{0.7}O_{3-\delta}$ (Δm = 0.9%).

$La_{0.6}Ca_{0.4}Co_{0.5}Fe_{0.5}O_{3-\delta}$ showed the smallest mass gain of all three samples. This indicates a very weak chemisorption of CO_2 also reflected by the fact that at 873 K the weight has reverted to the level before chemisorption, i.e. nearly all CO_2 has been released from the material. However, a contribution of oxygen vacancy formation to the weight change cannot be completely excluded, although in stronger reductive Ar atmosphere significant thermal reduction was only observed above 873 K. At higher temperatures, the weight loss can be attributed mainly to thermal reduction. These observations are in agreement with the only slight decrease of the oxygen permeation flux when switching the sweep gas from He to CO_2. In contrast, $La_{0.6}Ca_{0.4}Co_{0.7}Fe_{0.3}O_{3-\delta}$ and $La_{0.6}Ca_{0.4}Co_{0.3}Fe_{0.7}O_{3-\delta}$ showed a much stronger decline of the oxygen permeation flux of almost 40% (c.f. Fig. 3) suggesting a stronger blocking of oxygen vacancy sites by CO_2 [37]. Indeed, both samples showed a significantly higher mass gain during the thermal treatment in CO_2 pointing to a stronger chemisorption of CO_2 to these materials. Another indicator for a stronger chemisorption was the higher temperatures needed to reach the same weight as before the CO_2 chemisorption. For both samples, $La_{0.6}Ca_{0.4}Co_{0.7}Fe_{0.3}O_{3-\delta}$ (T = 1223 K) and $La_{0.6}Ca_{0.4}Co_{0.3}Fe_{0.7}O_{3-\delta}$ (T = 1173 K), these temperatures were in the range used for oxygen

permeation measurements. Therefore, referring the performance loss of these membrane materials to CO_2-blocked oxygen vacancies seems plausible.

9.3.6. Long-term CO_2 resistance and comparison

Fig. 10 shows the XRD patterns of $La_{0.6}Ca_{0.4}Co_{0.5}Fe_{0.5}O_{3-\delta}$ powder (a) before and (b) after exposure to pure CO_2 for 260 h at 1173 K. The results show that the perovskite structure remains intact. After the CO_2 treatment, all reflection intensities were substantially reduced. This was also observed with other ceramic membranes exposed to a reducing atmosphere [37,54], which implies that the initial coherence of the crystallites was deteriorated by the test. No carbonate formation was observed by the XRD measurements. Therefore, the $La_{0.6}Ca_{0.4}Co_{0.5}Fe_{0.5}O_{3-\delta}$ membrane appears to be a promising candidate for oxygen separation applications owing to its high CO_2 resistance and structural stability together with a relatively high oxygen permeation flux.

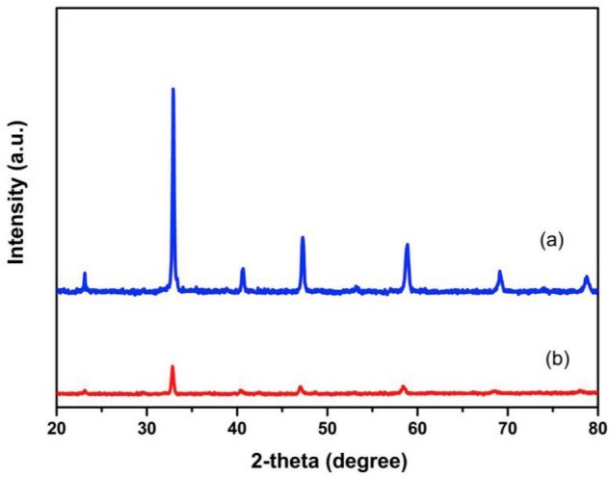

Fig. 10. XRD patterns of $La_{0.6}Ca_{0.4}Co_{0.5}Fe_{0.5}O_{3-\delta}$ powder (from 50 g batch) (a) before and (b) after exposure to pure CO_2 for 260 h at 1173 K. The CO_2 flow rate was 30 ml min^{-1}.

Table 4 compares the oxygen permeation flux values of this work to literature data of several types of membranes. It is well known that oxygen permeation is significantly influenced by the membrane thickness. Several microscopic measures can be adopted to improve the oxygen permeation flux such as constructing hollow fibers and coating of porous supports. Thus, the permeability is considered as a differentiating parameter for a reasonable comparison. At 1173 K, the LCCF membranes studied in this work possess a three times higher oxygen permeability than other published CO_2-tolerant membranes under similar conditions. In addition, the potentially low material costs and the scalable preparation method are conducive to a future commercialization.

Table 4 Summary of oxygen permeation parameters of various membranes swept by pure CO_2 at 1173 K.

Sample	Feed side (Air) (ml min^{-1} cm^{-2})	Sweep side (CO_2) (ml min^{-1} cm^{-2})	$J(o_2)$ (ml min^{-1} cm^{-2})	d (mm)	Permeability (ml min^{-1} cm^{-2} mm)	Method	Configurations	Ref
LCCF	150	29	0.155	1	0.16	sol-gel	Dense disk	51
LSCFN	unknown	100	0.14	0.9	0.13	sol-gel	Dense disk	42
SDC-LSF	unknown	40	0.14	1.1	0.15	sol-gel	Dense disk	33
PSCF	150	50	0.65	0.6	0.39	sol-gel	Dense disk	45
CGC-LCF	100	30	0.44	0.5	0.22	sol-gel	Dense disk	27
LCCF	**150**	**29**	**0.5**	**1**	**0.5**	**CP**	**Dense disk**	**
SFT	120	60	1.15	~0.25	0.29	SSR	MHF	48
SFT	120	60	0.85	~0.21	0.18	SSR	MHF	48
LCF	100	100	0.23	0.25	0.06	sol-gel	Hollow fiber	41
LSCG	100	100	2.22	~0.15	0.33	sol-gel	Hollow fiber	44
LSCF	200	150	0.26	0.32	0.08	sol-gel	Hollow fiber	37

LCCF: $La_{0.6}Ca_{0.4}Co_{0.8}Fe_{0.2}O_{3-\delta}$
LSCFN: $La_{0.6}Sr_{0.4}Co_{0.2}Fe_{0.6}Nb_{0.2}O_{3-\delta}$
SDC-LSF: $Ce_{0.8}Sm_{0.2}O_{2-\delta}$ - $La_{0.9}Sr_{0.1}O_{3-\delta}$
PSCF: $Pr_{0.6}Sr_{0.4}Co_{0.2}Fe_{0.8}O_{3-\delta}$.
CGC-LCF: $Ce_{0.85}Gd_{0.1}Cu_{0.05}O_{2-\delta}$ - $La_{0.6}Ca_{0.4}FeO_{3-\delta}$
LCCF: $La_{0.6}Ca_{0.4}Co_{0.5}Fe_{0.5}O_{3-\delta}$
SFT: $SrFe_{0.9}Ta_{0.1}O_{3-\delta}$
LCF: $(La_{0.8}Ca_{0.2})_{1.01}FeO_{3-\delta}$
SFT: $SrFe_{0.9}Ta_{0.1}O_{3-\delta}$
LSCG: $La_{0.6}Sr_{0.4}Co_{0.8}Ga_{0.2}O_{3-\delta}$
LSCF: $La_{0.6}Sr_{0.4}Co_{0.8}Fe_{0.2}O_{3-\delta}$
d: Thickness; CP: Co-precipitation; SSR: Solid-state reaction; MHF: Multichannel Hollow fiber; **: This work.

9.4. Conclusion

$La_{0.6}Ca_{0.4}Co_{1-x}Fe_xO_{3-\delta}$ (x = 0, 0.3, 0.5, 0.7, 1) membranes were prepared using a scalable reverse co-precipitation method. The experimental and simulation results show that the Co/Fe ratio has a significant effect on the phase stability under CO_2 atmosphere, morphology, electrical conductivity, and CO_2 affinity. All these properties strongly influence the oxygen permeability of the membrane. Increasing the Fe content leads to a decrease in the electrical conductivity, which is non-critical since it still remains much higher than the ionic conductivity. With increasing Co content, a decrease of the oxygen vacancy formation energy corresponding to a rising tendency to form these vacancies was found. However, the actual migration ability of the oxygen anions is decreased in Co-rich compounds probably due to the stronger binding between Co and O. The oxygen permeation flux of the membranes initially increases and then decreases with increasing of the Fe content. The $La_{0.6}Ca_{0.4}Co_{0.3}Fe_{0.7}O_{3-\delta}$ membrane possesses the highest permeation flux, achieving 0.76 ml min^{-1} cm^{-2} under an Air/ He gradient at 1173 K, while the $La_{0.6}Ca_{0.4}Co_{0.5}Fe_{0.5}O_{3-\delta}$ membrane showed the highest CO_2 tolerance, reaching about 0.4 ml min^{-1} cm^{-2} at 1023 K and 0.5 ml min^{-1} cm^{-2} at 1173 K under an Air/CO_2 gradient. The CO_2 affinity of the membrane can be an important factor influencing the oxygen permeation. The poisoning of LCCF by CO_2 is mainly attributed to the strong chemical adsorption of CO_2 to the membrane surface, especially to the active oxygen vacancy sites, and not to the decomposition of the membrane materials by alkaline earth metal carbonate formation, as often observed. It is not one of the abovementioned factors alone (morphology, electrical conductivity, oxygen vacancy concentration), but the combined effect of these factors that determines the convincing oxygen

permeability of the LCCF membranes. Based on our findings, this LCCF material appears to be a promising candidate for high temperature oxygen separation applications owing to its structural stability in a CO_2 atmosphere together with a relatively high oxygen permeation flux.

9.5. Acknowledgements

The financial support of the Federal Ministry of Education and Research of Germany in the framework of the Kopernikus projects for the Energiewende within the project "Plasma-induced CO2-conversion" (PiCK, project number: 03SFK2S3B) is highly acknowledged. G. Chen is grateful to Frank Hack, Dr. Angelika Veziridis, Dr. Dirk Rothenstein and M. Sc. Binjie Tang for their kind supports during the experiments and discussions. The simulations presented in this work were performed on the computational resource For HLR II funded by the Ministry of Science, Research and the Arts Baden-Württemberg and the Deutsche Forschungsgemeinschaft.

9.6. Apendix A. Supplementary Data

Supplementary data to this article can be found online at https:// doi.org/10.1016/j.memsci.2019.05.007.

9.7. References

[1] J. Fang, X. Jin, K. Huang, J. Membr. Sci. 549 (2018) 142.

[2] J. Wu, Y. Huang, W. Ye, Y. Li, Adv. Sci. 4 (2017) 1700194.

[3] S.R. Lingampalli, M.M. Ayyub, C.N.R. Rao, ACS Omega 2 (6) (2017) 2740.

[4] G. Chen, T. Silva, V. Georgieva, T. Godfroid, N. Britun, R. Snyders, M.P. Delplancke-Ogletree, Int. J. Hydrogen Energy 40 (2015) 3789.

[5] N. Britun, T. Silva, G. Chen, T. Godfroid, J. Mullen, R. Snyders, J. Phys. D Appl. Phys. 51 (2018) 144002.

[6] A.P.H. Goede, W.A. Bongers, M.F. Graswinckel, M.C.M. van de Sanden Richard, M. Leins, J. Kopecki, A. Schulz, M. Walker, EPJ Web Conf. 79 (2014) 01005, , https://doi.org/10.1051/epjconf/20147901005.

[7] A.H. Bork, M. Kubicek, M. Struzik, J.L.M. Rupp, J. Mater. Chem. A 3 (2015) 15546.

[8] C. Graves, S.D. Ebbesen, M. Mogensen, K.S. Lackner, Renew. Sustain. Energy Rev. 15 (2011) 1.

[9] S. Yoon, M. Gaul, S. Sharma, K. Son, H. Hagemann, D. Ziegenbalg, U. Schwingenschlogl, M. Widenmeyer, A. Weidenkaff, J. Solid State Sci. 78 (2018) 22.

[10] J. Sunarso, S. Baumann, J.M. Serra, W.A. Meulenberg, S. Liu, Y.S. Lin, J.C. Diniz da Costa, J. Membr. Sci. 320 (1–2) (2008) 13.

[11] C. Zhang, J. Sunarso, S. Liu, Chem. Soc. Rev. 46 (10) (2017) 2941.

[12] J. Hoon Park, J. Pyo Kim, S. Hwan Son, Energy Procedia 1 (1) (2009) 369.

[13] X. Li, T. Kerstiens, T. Markus, J. Membr. Sci. 438 (2013) 83.

[14] M.A. Alaee, M.M. Movahednia, T. Mohammadi, J. Chem. Eng. Data 54 (11) (2009) 3082.

[15] Y. Lu, H. Zhao, X. Chang, X. Du, K. Li, Y. Ma, S. Yi, Z. Du, K. Zheng, K. Świerczek, J. Mater. Chem. A 4 (27) (2016) 10454.

[16] J. Martynczuk, F. Liang, M. Arnold, V. Šepelák, A. Feldhoff, Chem. Mater. 21 (8) (2009) 1586.

[17] K. Efimov, T. Halfer, A. Kuhn, P. Heitjans, J. Caro, A. Feldhoff, Chem. Mater. 22 (4) (2010) 1540.

[18] W. Yao, H. Cheng, H. Zhao, X. Lu, X. Zou, S. Li, C. Li, J. Membr. Sci. 504 (2016) 251.

[19] J. Liu, H. Cheng, B. Jiang, X. Lu, W. Ding, Int. J. Hydrogen Energy 38 (25) (2013) 11090.

[20] T. Schiestel, M. Kilgus, S. Peter, K.J. Caspary, H. Wang, J. Caro, J. Membr. Sci. 258 (1–2) (2005) 1.

[21] F. Yang, H. Zhao, J. Yang, M. Fang, Y. Lu, Z. Du, K. Świerczek, K. Zheng, J. Membr. Sci. 492 (2015) 559.

[22] Z. Yáng, J. Martynczuk, K. Efimov, A.S. Harvey, A. Infortuna, P. Kocher, L.J. Gauckler, Chem. Mater. 23 (13) (2011) 3169.

[23] Y. Lu, H. Zhao, X. Cheng, Y. Jia, X. Du, M. Fang, Z. Du, K. Zheng, K. Świerczek, J. Mater. Chem. A 3 (2015) 6202.

[24] K. Li, H. Zhao, Y. Lu, Y. Ma, Z. Du, Z. Zhang, J. Membr. Sci. 550 (2018) 302.

[25] H. Cheng, N. Zhang, X. Xiong, X. Lu, H. Zhao, S. Li, Z. Zhou, ACS Sustain. Chem. Eng. 3 (9) (2015) 1982.

[26] H. Luo, H. Jiang, T. Klande, Z. Cao, F. Liang, H. Wang, J. Caro, Chem. Mater. 24 (11) (2012) 2148.

[27] W. Fang, F. Liang, Z. Cao, F. Steinbach, A. Feldhoff, Angew. Chem., Int. Ed. Engl. 54 (16) (2015) 4847.

[28] J. Garcia-Fayos, M. Balaguer, J.M. Serra, ChemSusChem 8 (24) (2015) 4242.

[29] S. Cheng, M. Sogaard, L. Han, W. Zhang, M. Chen, A. Kaiser, P.V. Hendriksen, Chem. Commun. (Camb) 51 (33) (2015) 7140.

[30] J. Garcia-Fayos, M. Balaguer, S. Baumann, J.M. Serra, J. Membr. Sci. 548 (2018) 117.

[31] W. Fang, F. Steinbach, C. Chen, A. Feldhoff, Chem. Mater. 27 (22) (2015) 7820.

[32] X. Bi, X. Meng, P. Liu, N. Yang, Z. Zhu, R. Ran, S. Liu, J. Membr. Sci. 522 (2017) 91.

[33] Z. Wang, W. Sun, Z. Zhu, T. Liu, W. Liu, ACS Appl. Mater. Interfaces 5 (21) (2013) 11038.

[34] J. García-Fayos, R. Ruhl, Laura Navarrete, H.J.M. Bouwmeester, J.M. Serra, J. Mater. Chem. A 6 (2018) 1201.

[35] Y. He, L. Shi, F. Wu, W. Xie, S. Wang, D. Yan, P. Liu, M.R. Li, J. Caro, H. Luo, J. Mater. Chem. A 6 (2018) 84.

[36] H. Luo, T. Klande, Z. Cao, F. Liang, H. Wang, J. Caro, J. Mater. Chem. A 2 (2014) 7780.

[37] X. Tan, N. Liu, B. Meng, J. Sunarso, K. Zhang, S. Liu, J. Membr. Sci. 389 (2012) 216.

[38] J. Yi, M. Schroeder, M. Martin, Chem. Mater. 25 (6) (2013) 815.

[39] X. Tan, Z. Wang, K. Li, Ind. Eng. Chem. Res. 49 (6) (2010) 2895.

[40] K. Zhang, R. Ran, L. Ge, Z. Shao, W. Jin, N. Xu, J. Membr. Sci. 323 (2) (2008) 436.

[41] D. Yang, N. Yang, B. Meng, X. Tan, C. Zhang, J. Sunarso, Z. Zhu, S. Liu, Energy Fuel. 31 (4) (2017) 4531.

[42] L. Gui, Y. Wan, R. Wang, Z. Wang, B. He, L. Zhao, J. Alloys Compd. 644 (2015) 788.

[43] Z. Wang, N. Dewangan, S. Das, M.H. Wai, S. Kawi, Separ. Purif. Technol. 201 (2018) 30.

[44] Y. Kathiraser, Z. Wang, N.-T. Yang, S. Zahid, S. Kawi, J. Membr. Sci. 427 (2013) 240.

[45] K. Partovi, B. Geppert, F. Liang, C.H. Rüscher, J. Caro, Chem. Mater. 27 (8) (2015) 2911.

[46] Z. Zhang, D. Chen, F. Dong, X. Xu, Y. Hao, Z. Shao, J. Membr. Sci. 519 (2016) 11.

[47] J.M. Polfus, W. Xing, G. Pećanac, A. Fossdal, S.M. Hanetho, Y. Larring, J. Malzbender, M.L. Fontaine, R. Bredesen, J. Membr. Sci. 499 (2016) 172.

[48] K. Partovi, F. Liang, O. Ravkina, J. Caro, ACS Appl. Mater. Interfaces 6 (2014) 10274.

[49] T. Klande, O. Ravkina, A. Feldhoff, J. Membr. Sci. 437 (2013) 122.

[50] Y. Teraoka, T. Nobunaga, N. Yamazoe, Chem. Lett. 17 (3) (1988) 503.

[51] K. Efimov, T. Klande, N. Juditzki, A. Feldhoff, J. Membr. Sci. 389 (2012) 205.

[52] J. Stevenson, T. Armstrong, R. Carneim, L.R. Pederson, W. Weber, J. Electrochem. Soc. 143 (9) (1996) 2722.

[53] S. Diethelm, J. Van Herle, P.H. Middleton, D. Favrat, J. Power Sources 118 (1–2) (2003) 270.

[54] M. Salehi, M. Søgaard, V. Esposito, S.P.V. Foghmoes, E.S. Persoon, M. Schroeder, P.V. Hendriksen, J. Membr. Sci. 542 (2017) 245.

[55] F. Schulze-Küppers, U.V. Unije, H. Blank, M. Balaguer, S. Baumann, R. Mücke, W.A. Meulenberg, J. Membr. Sci. 564 (2018) 218.

[56] T. Yang, X. Jin, K. Huang, J. Membr. Sci. 568 (2018) 47.

[57] J. Yi, M. Schroeder, T. Weirich, J. Mayer, Chem. Mater. 22 (2010) 6246.

[58] H. Luo, K. Efimov, H. Jiang, A. Feldhoff, H. Wang, J. Caro, Angew. Chem. Int. Ed. 50 (2011) 759–763.

[59] H. Luo, H. Jiang, T. Klande, F. Liang, Z. Cao, H. Wang, J. Caro, J. Membr. Sci. 423 (2012) 450–458.

[60] R.D. Shannon, Acta Crystallogr. A32 (1976) 751.

[61] A. Weidenkaff, S.G. Ebbinghaus, T. Lippert, Chem. Mater. 14 (2002) 1797.

[62] A. Weidenkaff, S.G. Ebbinghaus, T. Lippert, M.J. Montenegro, C. Soltmann, R. Wessicken, Cryst. Eng. 5 (2002) 449.

[63] H. Wang, C. Tablet, A. Feldhoff, J. Caro, J. Membr. Sci. 262 (1–2) (2005) 20.

[64] G. Kresse, J. Furthmüller, Comput. Mater. Sci. 6 (1) (1996) 15.

[65] P.E. Blöchl, Phys. Rev. B 50 (24) (1994) 17953.

[66] J.P. Perdew, K. Burke, M. Ernzerhof, Phys. Rev. Lett. 77 (18) (1996) 3865.

[67] N. Troullier, J.L. Martins, Phys. Rev. B 43 (3) (1991) 1993.

[68] G. Henkelman, B.P. Uberuaga, H.A. Jónsson, J. Chem. Phys. 113 (2000) 9901.

[69] H. Jónsson, G. Mills, K.W. Jacobsen, Nudged elastic band method for finding minimum energy paths of transitions, in: B.J. Berne, G. Ciccotti, D.F. Coker (Eds.), Classical and Quantum Dynamics in Condensed Phase Simulations, World Scientific, Singapore, 1998, p. 385.

[70] Y.A. Mastrikov, R. Merkle, E.A. Kotomin, M.M. Kukljab, J. Maier, Phys. Chem. Chem. Phys. 15 (2013) 911.

[71] Z. Wang, R. Peng, W. Zhang, X. Wu, C. Xia, Y. Lu, J. Mater. Chem. A 1 (2013) 12932.

[72] M. Oishi, K. Yashiro, K. Sato, J. Mizusaki, T. Kawada, J. Solid State Chem. 181 (11) (2008) 3177.

[73] S. Gupta, M.K. Mahapatra, P. Singh, Mater. Sci. Eng. R 90 (2015) 1.

[74] P.-M. Geffroy, E. Blond, N. Richet, T. Chartier, Chem. Eng. Sci. 162 (2017) 245.

[75] G. Chen, N. Britun, T. Godfroid, R. Snyders, M.-P. Delplancke-Ogletree, J. Phys. D Appl. Phys. 50 (2017) 084001.

[76] G. Chen, V. Georgieva, T. Godfroid, R. Snyders, M.-P. Delplancke-Ogletree, Appl. Catal. B Environ. 190 (2016) 115.

[77] L. Liu, Y. Li, Aerosol Air. Qual. Res. 14 (2014) 453.

[78] G. Chen, T. Godfroid, V. Georgieva, N. Britun, M.-P. Delplancke-Ogletree, R. Snyders, Appl. Catal. B Environ. 214 (2017) 114.

9.8. Supplementary Information

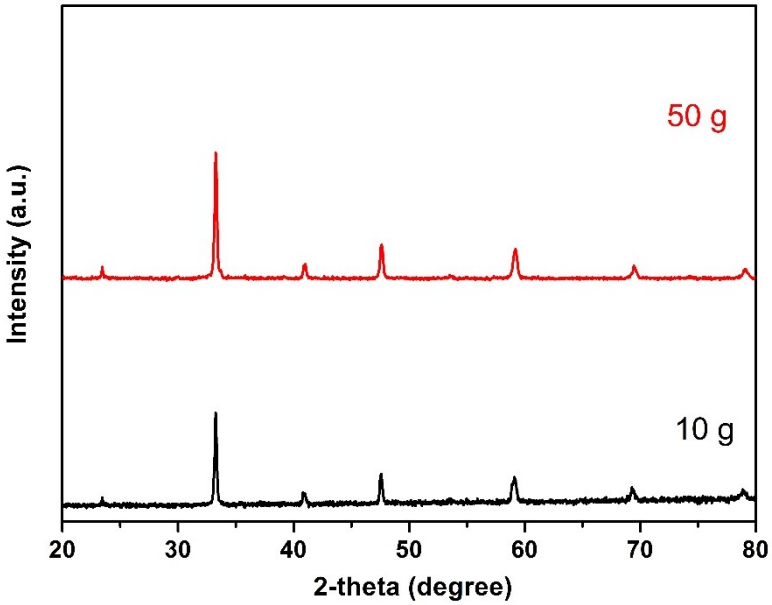

Figure S1. Comparison of XRD patterns of $La_{0.6}Ca_{0.4}Co_{0.5}Fe_{0.5}O_{3-\delta}$ powder synthesized in small or large amount.

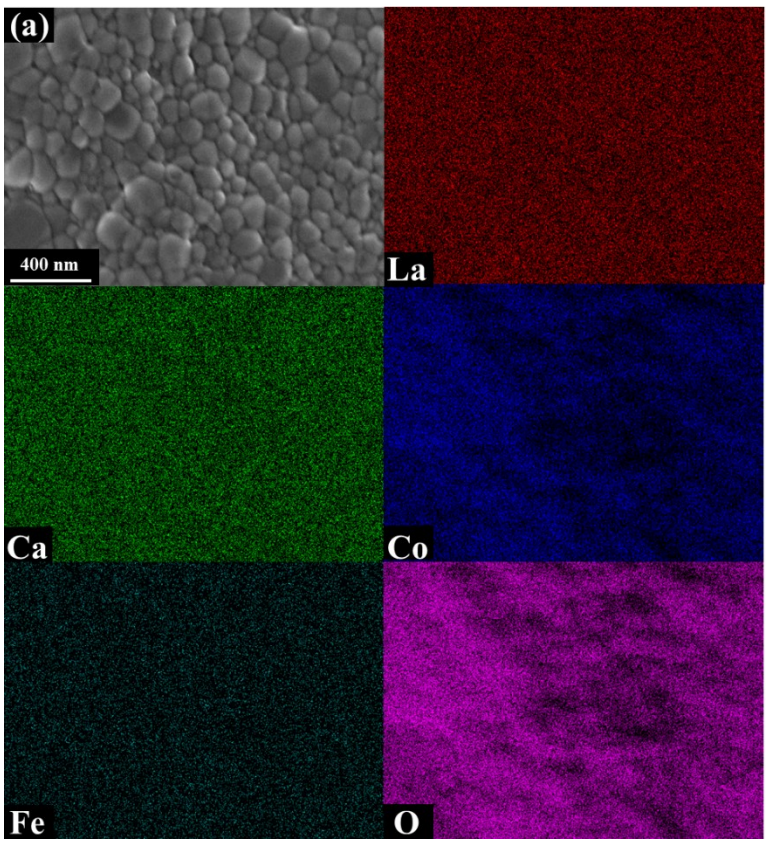

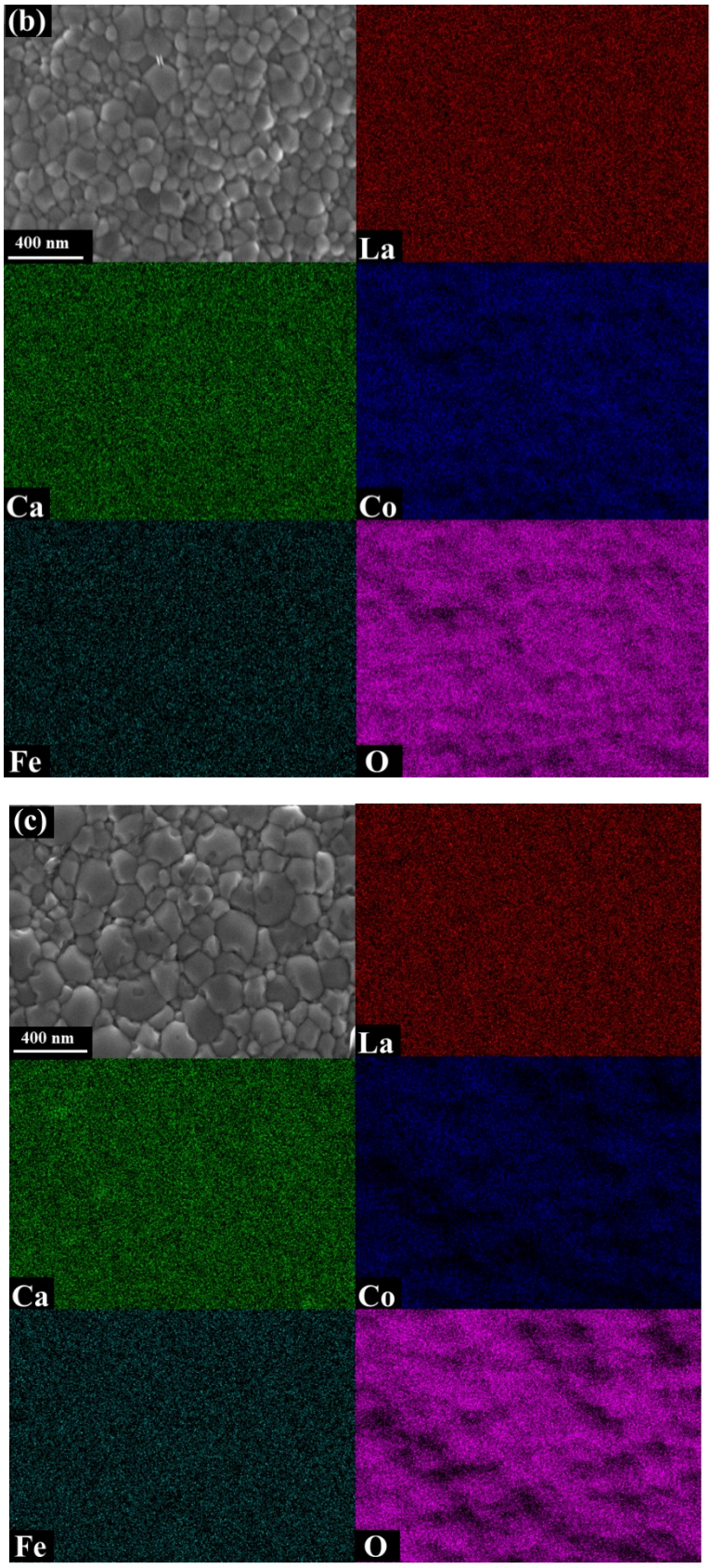

Figure S2. SEM images and EDS elemental distributions of fresh LCCF membranes (a) $La_{0.6}Ca_{0.4}Co_{0.7}Fe_{0.3}O_{3-\delta}$, (b) $La_{0.6}Ca_{0.4}Co_{0.5}Fe_{0.5}O_{3-\delta}$ and (c) $La_{0.6}Ca_{0.4}Co_{0.3}Fe_{0.7}O_{3-\delta}$.

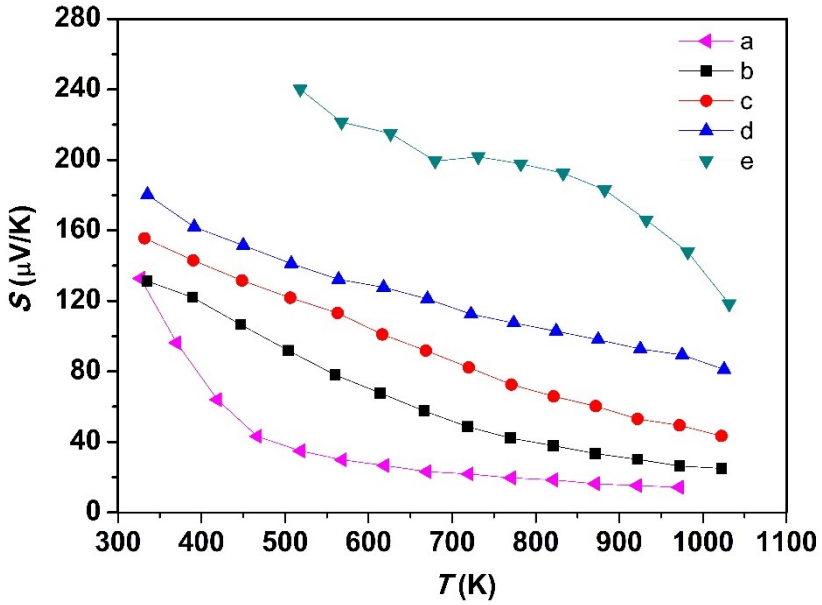

Figure S3. Temperature dependence of the Seebeck coefficient S of sintered bulk $La_{0.6}Ca_{0.4}Co_{1-x}Fe_xO_{3-\delta}$ (x = 0, 0.3, 0.5, 0.7, 1) samples: (a) x = 0; (b) x = 0.3; (c) x = 0.5; (d) x = 0.7; (e) x = 1.

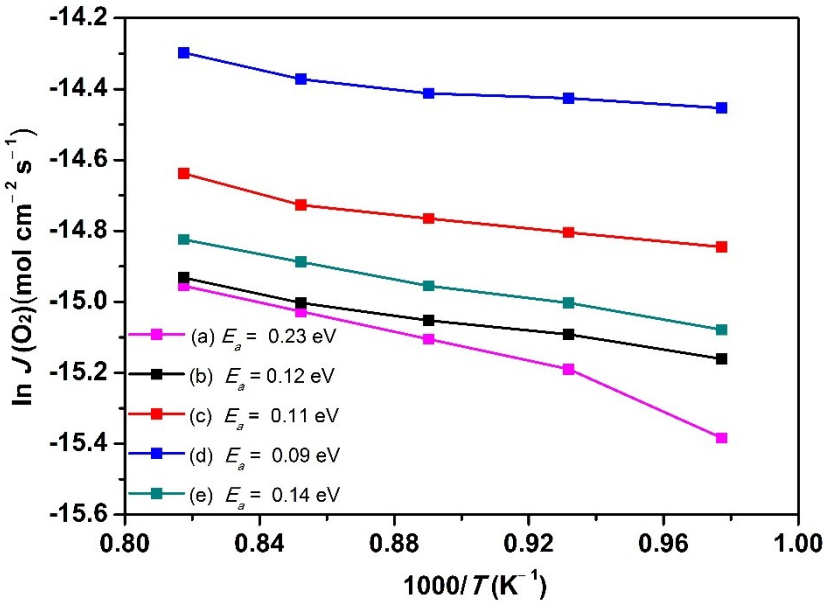

Figure S4. Temperature dependence of oxygen permeation fluxes through $La_{0.6}Ca_{0.4}Co_{1-x}Fe_xO_{3-\delta}$ (x = 0, 0.3, 0.5, 0.7, 1) membranes: (a) x = 0; (b) x = 0.3; (c) x = 0.5; (d) x = 0.7; (e) x = 1.

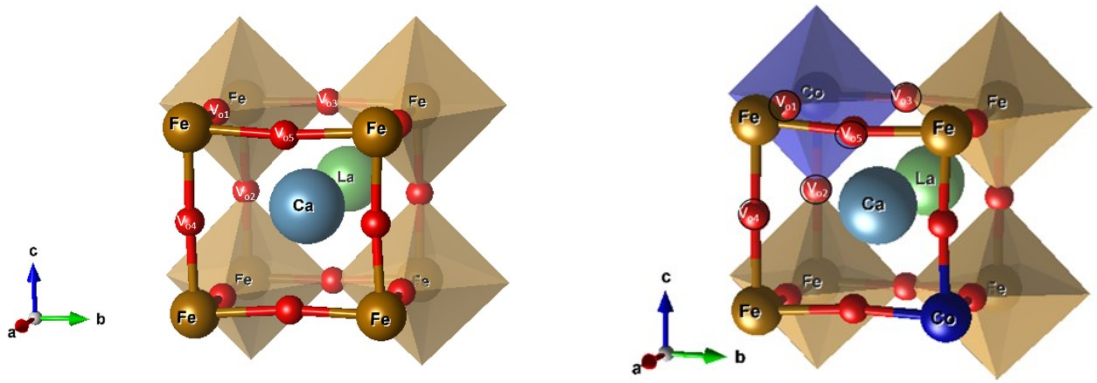

Figure S5. First principles calculation model of $La_6Ca_2Fe_8O_{23}\square_1$ (a) and $La_6Ca_2Co_2Fe_6O_{23}\square_1$ (b). The V_{o1}, V_{o2}, V_{o3}, V_{o4}, and V_{o5} are denoted as different possible sites for oxygen occupation.

Table S1. Calculated bond lengths in the $La_6Ca_2Co_{4-x}Fe_{4+x}O_{23}\square_1$ system.

Co/Fe ratio / Bond length (Å)	0.000 : 1.000	0.125 : 0.825	0.250 : 0.750	0.375 : 0.625	0.500 : 0.500
La-O (1)	2.83	2.82	2.83	2.73	2.28
La-O (2)	--	2.65	2.67	2.57	2.70
La-O (3)	--	--	--	2.66	2.31
La-O (4)	--	--	--	2.37	--
Ca-O (1)	2.67	2.65	2.65	2.61	2.48
Ca-O (2)	--	2.66	2.68	2.55	--
Ca-O (3)	2.77	2.77	2.77	2.45	2.41
Ca-O (4)	--	--	--	2.44	2.58
Ca-O (5)	--	--	--	2.55	2.45
Ca-O (6)	--	--	--	--	2.62
Fe-O (1)	1.87	1.88	1.87	1.89	1.91
Fe-O (2)	1.99	1.88	1.87	1.88	1.88
Fe-O (3)	--	--	--	1.90	1.89
Fe-O (4)	--	--	--	1.87	1.92
Co-O (1)	--	1.89	1.90	1.92	1.87
Co-O (2)	--	1.89	1.90	1.94	1.97
Co-O (3)	--	--	--	1.96	1.98
Co-O (4)	--	--	--	1.91	1.86

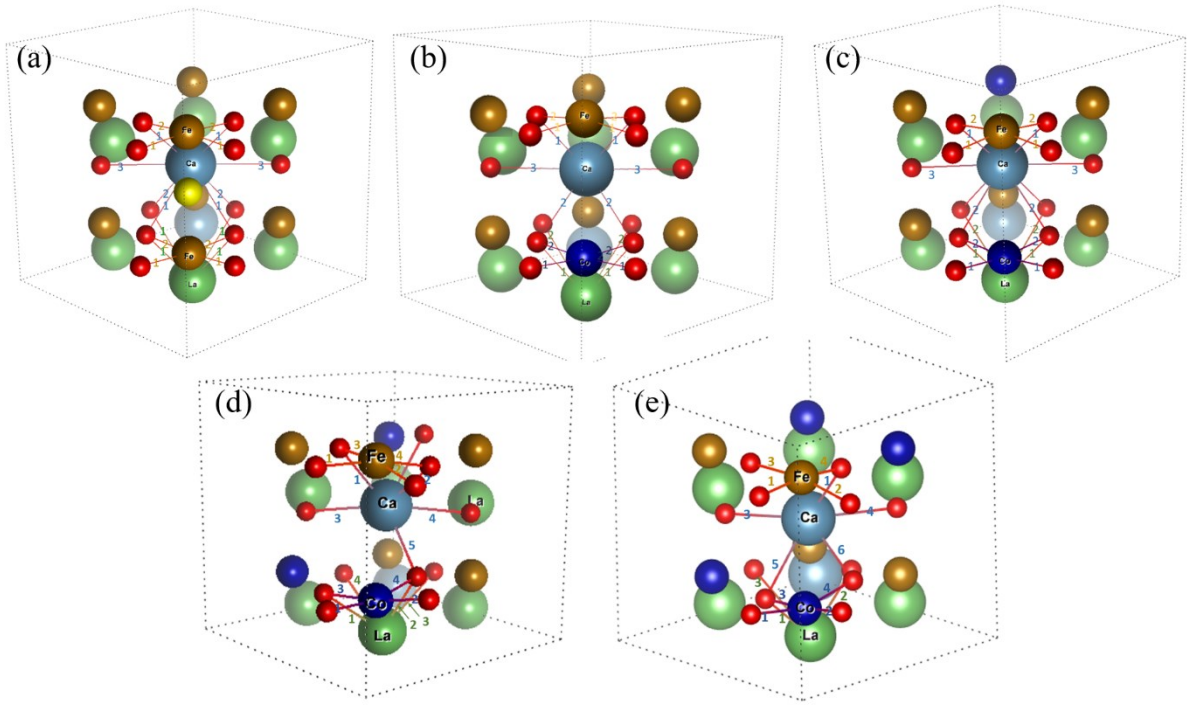

Figure S6. Calculated bond lengths at different sites in the simplified $La_6Ca_2Co_{4-x}Fe_{4+x}O_{23}\square_1$ model. The different panels correspond to (a) $La_6Ca_2Fe_8O_{23}\square_1$, (b) $La_6Ca_2Co_1Fe_6O_{23}\square_1$, (c) $La_6Ca_2Co_2Fe_6O_{23}\square_1$, (d) $La_6Ca_2Co_3Fe_5O_{23}\square_1$, and (e) $La_6Ca_2Co_4Fe_4O_{23}\square_1$.

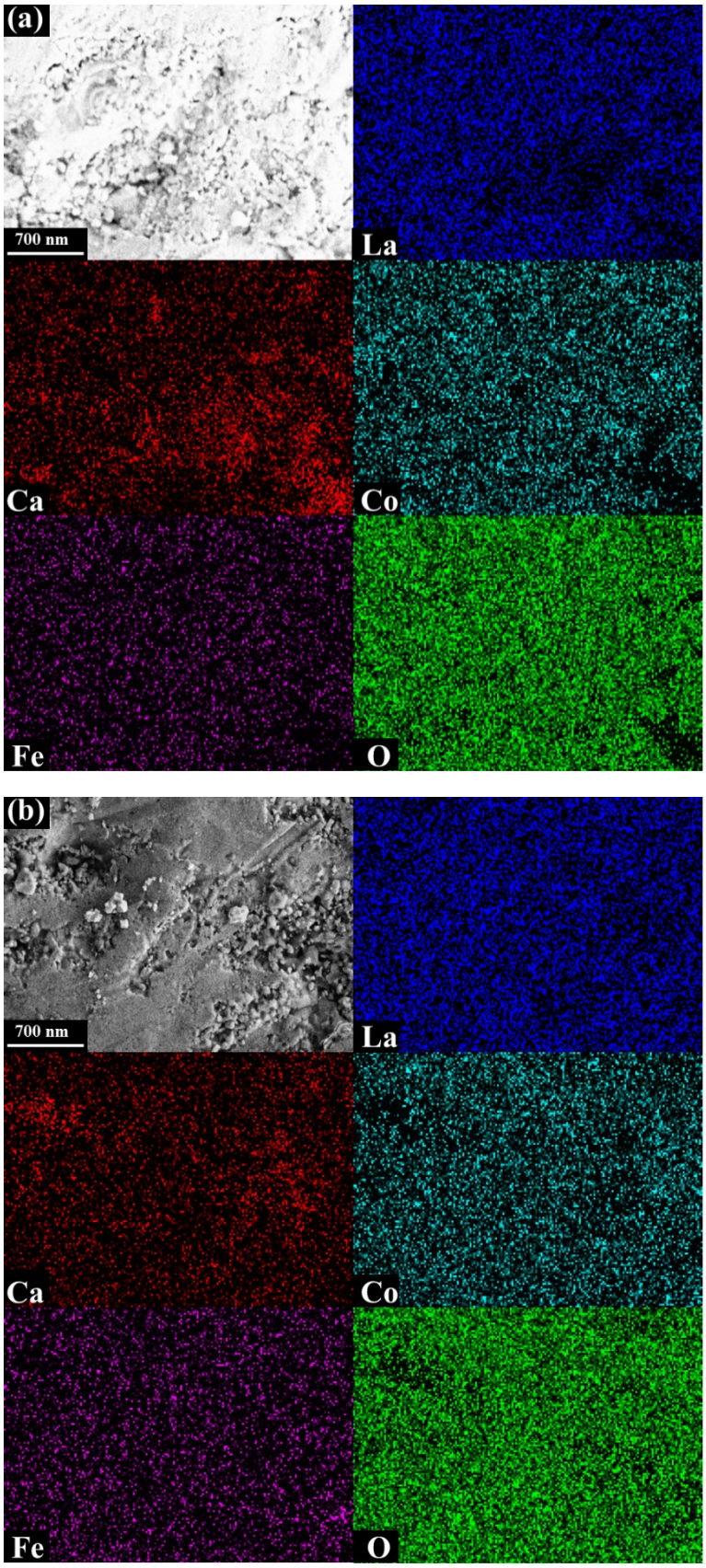

Figure S7. SEM images and EDS elemental distributions of used $La_{0.6}Ca_{0.4}Co_{0.7}Fe_{0.3}O_{3-\delta}$ membrane after 6 h experiment using pure CO_2 as sweep gas. (a) Feed side; (b) Sweep side.

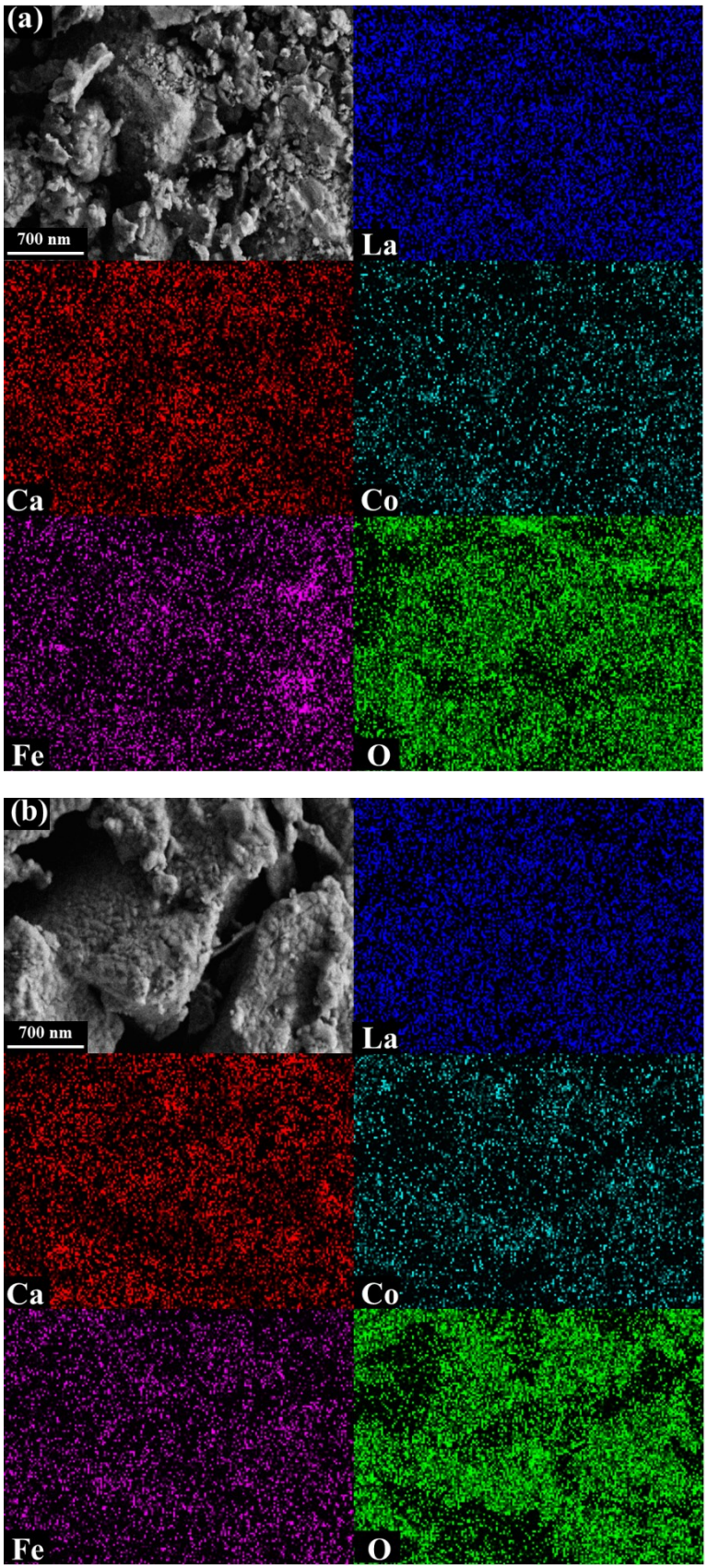

Figure S8. SEM images and EDS elemental distributions of used $La_{0.6}Ca_{0.4}Co_{0.3}Fe_{0.7}O_{3-\delta}$ membrane after 6 h experiment using pure CO_2 as sweep gas. (a) Feed side; (b) Sweep side.

10. Summary

This work was dedicated to develop before unknown perovskite-type oxynitrides with promising physical properties and the advance of understanding their formation. Concerning this, future desired physical properties of perovskite-type oxynitrides can be precisely adjusted. The study yielded a targeted *A*-, *B*-, and *X*-site substitution in $LaTa(O,N)_3$ leading to the before unknown perovskite-type oxynitrides $LaTa^{IV}O_2N$, $La_{1-x}Y_xTa^{IV}O_2N$ (x = 0.1, 0.25, 0.3), and $LaTa_{1-x}Co_x(O,N)_{3-\delta}$ (x = 0.01, 0.03, 0.05) exhibiting bright powder colors from dark red (E_G = 1.7 eV) *via* red (E_G = 1.8 eV) to orange (E_G = 2.0 eV). Additionally, the highest so far reported weight fraction of the very labile $YTa(O,N)_3$ (82(2) wt%) could be synthesized. To understand the formation of the synthesized perovskite-type oxynitrides, parameters for an *in situ* ammonolysis *via* TGA were developed. By performing *in situ* ammonolysis the formation of an unusual oxidation state (Ta^{IV}) and a before unknown O : N ratio of 2 : 1 in $La_{1-x}Y_xTa(O,N)_3$ (x = 0, 0.1, 0.25, 0.3) was elucidated. It could be shown that the precursors' microstructure – crystallinity, particle size, and specific surface area – besides the ammonia concentration, is a very important parameter to modify the product composition, oxidation states, and physical properties. In the synthesis of $LaTa_{1-x}Co_x(O,N)_{3-\delta}$ (x = 0.01, 0.03, 0.05) anionic vacancies in the oxide precursor play an additional role in adjusting the O : N ratio and the oxidation state of Ta. All synthesized materials were investigated by PXRD, TGA, HGE, ICP-OES, DRS, and SEM. More specific characterization techniques to investigate the individual physical properties of the materials were chosen. The materials' specific achieved results are listed in the following:

I) $LaTa^{IV}O_2N$ and $La_{1-x}Y_xTa^{IV}O_2N$ (x = 0.1, 0.25, 0.3): XANES revealed additional to XPS the existence of Ta^{IV} of the bulk in $La_{0.9}Y_{0.1}Ta^{IV}O_2N$. Hence, it is also assumed for $La_{1-x}Y_xTa^{IV}O_2N$ (x = 0, 0.25, 0.3). Conducted DRS measurements showed an unexpected trend for the optical bandgap ($E_{G,x=0.3} \approx E_{G,x=0} < E_{G,x=0.1} < E_{G,x=0.25}$). By performing DFT calculations, the orthorhombic strain as main descriptor was clarified. Because, Ta^{IV}–containing materials were assumed to be black or bluish in color the bright red (E_G = 1.8 eV) or orange (E_G = 2.0 eV) colors of the materials were rather unexpected. Additional DFT calculations revealed a transparent conductor-like behavior ("degenerate semiconductor") of the materials that can explain the observed colors. SPS measurements revealed a *n*-type semiconducting behavior of the materials with effective bandgaps of ~1.75 eV irrespective of the Y^{3+} content. By increasing the Y^{3+} content the photovoltage values increased suggesting an improved charge carrier generation and separation, whereas the timescales for charge carrier generation/decay slowed down. This suggests also trap states in the materials. Based on the obtained results, reduced *B*-site cations such as Ta^{IV} have a significantly weaker impact than classically assumed and the synthesized materials seem to have promising physical properties for light-driven applications such as SWS.

II) $LaTa_{1-x}Co_x(O,N)_{3-\delta}$ (x = 0.01, 0.03, 0.05): Structural and magnetic investigations (SQUID, XAS/XMCD) revealed the first observation of a significant bulk HT-FM with $T_C \sim 600$ K in a DMS system. Hence, $LaTa_{1-x}Co_x(O,N)_{3-\delta}$ (x = 0.01, 0.03, 0.05) is – to the best of one's knowledge – the first diluted ferromagnetic semiconducting perovskite-type oxynitride. The powder colors (from bright red *via* red to dark red) suggested also a semiconducting behavior (E_G = 1.7 eV – 1.9 eV). The sample magnetizations were even large enough to observe direct attracting forces by conventional permanent magnets. The observed physical properties are promising for the application in spintronics.

To conclude the part for the oxynitrides, the here gained achievements can help to develop further before unknown perovskite-type oxynitride family members with desired physical properties for future applications.

Furthermore, perovskite-type oxides were synthesized and their physical properties were investigated in combination with a targeted *B*-site substitution. It was found that the Co/Fe ratio has a strong impact on the phase stability, morphology, electrical conductivity, and CO_2 affinity. Additionally, all these properties affect the oxygen permeability in a significant way. A higher iron content made the oxygen transport membrane material $(La,Ca)Co_{1-x}Fe_xO_{3-\delta}$ more sustainable by reducing the use of the critical elemental cobalt. Simultaneously the electrical conductivity decreased. However, this is non-critical for the oxygen permeation, since it still remained significantly higher than the ionic conductivity. In contrast, if the Co content was increasing, the oxygen vacancy formation energy was decreasing but expectedly the actual migration ability of the oxide ions decreased due to the induced structural relaxations and potential small polaron formation. In contrast, the oxygen permeation flux of the membranes was initially increasing whereas by higher Fe content the flux was decreasing.

Hence, for the perovskite-type oxides also physical properties such as the electrical conductivity can be tuned by a targeted *B*-site substitution. The observed results in this part can be used to improve the performance of this class of materials for future applications such as CCU.

11. Outlook/future work

A future task before bringing the herein presented materials into application is a dedicated evaluation of their environmental impact by standardized scientific methods such as life cycle assessment. This is needed to ensure that the intended energy conversion process and the used materials for it are sustainable. Typically, the sustainability of a material can be improved *via* three main parameters: i) a more-energy efficient production route (*e.g*. microwave-heated processes), ii) using secondary raw materials from recycling processes as starting materials of the chemical reactions, and iii) reducing as much as possible the content of critical elements, while ideally improving the functional performance. The latter has been indicated by the partial replacement of Ca and La by Fe and Ca in $(La,Ca)_{Co1-x}Fe_xO_{3-\delta}$. A similar idea might be applicable for $LaTa(O,N)_3$ by considering $(La,Ca)(Ta,Ti)(O,N)_3$.

12. Acknowledgements

Herein, I would like to thank all the people who supported me during the period of my PhD thesis:

First of all, I would like to thank my supervisor Prof. Dr. Anke Weidenkaff for giving me the opportunity to do the PhD thesis in her group, her great support and patience she gave me and my work.

I thank very much Prof. Dr. Gisela Schütz, who has agreed to take over as co-referee and with it for her great support.

I would like to thank Dr. Marc Widenmeyer for the help and fruitful discussions during the preparation time of the first two papers (LTON and LYTON). Thanks to you, I learned a lot in XRD and ND.

PD Dr. Eberhard Goering, without whom the whole LTCON study would not have been possible. Thank you so much for your great support and fruitful discussions! Thanks to you, I learned a lot in magnetism, solid state physics, and about diluted magnetic semiconductors.

I acknowledge all my cooperation partners (co-authors and technicians) all over the world, especially, Prof. Dr. Frank E. Osterloh (University of California, Davis), and Mr. Samir Hammoud (MPI for Intelligent Systems), for their support, help and fruitful discussions during my PhD period.

Dr. Stefan Kilper and Dr. Nina Blumenstein: Thank you very much for your patience and fruitful discussions. Also, for the great friendship and climbing together.

Additionally, I would like to thank all my colleagues who supported me during my PhD. Especially, Dr. Benjamin Balke, Dr. Songhak Yoon, Dr. Wenjie Xie, Dr. Xingxing Xiao, Dr. Zaklina Burkhardt, Dr. Dirk Rothenstein, Dr. Petia Anatasova, Dr. Giulia Santomauro, Dr. Andrea Knöller, Dr. Timotheus Jahnke, Frank Hack, and Juliane Kränzl.

Last but not least my family – my parents, my sister, my brother-in-law, and our dogs Feli and Momo – I thank you so much for your love and support. Thank you very much!

13. Declaration of the authorship

Statutory declaration

I hereby declare that I have prepared the present work independently and only with the aids and sources listed here. All information taken from sources are marked as such. This work has not yet been submitted to any examination office in the same or similar form.

Eidesstattliche Erklärung

Hiermit erkläre ich, dass ich die vorliegende Arbeit selbstständig und nur mit den hier aufgelisteten Hilfsmitteln und Quellen angefertigt habe. Alle Angaben, die aus Quellen entnommen wurden, sind als solche kenntlich gemacht. In gleicher oder ähnlicher Form hat diese Arbeit noch keiner Prüfungsbehörde vorgelegen.

Darmstadt, den .....

Ort, Datum/Place, Date

……..... …….....

Name/Name Unterschrift/Signature